



Une contribution au chaos ondulatoire expérimental

Fabrice Mortessagne

► To cite this version:

| Fabrice Mortessagne. Une contribution au chaos ondulatoire expérimental. Analyse de données, Statistiques et Probabilités [physics.data-an]. Université Nice Sophia Antipolis, 2006. tel-00120405

HAL Id: tel-00120405

<https://theses.hal.science/tel-00120405>

Submitted on 14 Dec 2006

HAL is a multi-disciplinary open access archive for the deposit and dissemination of scientific research documents, whether they are published or not. The documents may come from teaching and research institutions in France or abroad, or from public or private research centers.

L'archive ouverte pluridisciplinaire **HAL**, est destinée au dépôt et à la diffusion de documents scientifiques de niveau recherche, publiés ou non, émanant des établissements d'enseignement et de recherche français ou étrangers, des laboratoires publics ou privés.

Habilitation à Diriger des Recherches

Fabrice MORTESSAGNE

Laboratoire de Physique de la Matière Condensée

Université de Nice-Sophia Antipolis & CNRS

11 décembre 2006

Jury

Roger Maynard	Président, rapporteur	Professeur, Université Joseph Fourier
Patricia Lebœuf	Rapporteur	Directeur de recherches, CNRS
Richard L. Weaver	Rapporteur	Professeur, University of Illinois, Urbana-Champaign
G. George Batrouni	Examinateur	Professeur, Université de Nice-Sophia Antipolis
Pierre Coullet	Examinateur	Professeur, Université de Nice-Sophia Antipolis
Jacques Treiner	Examinateur	Professeur, Université Pierre et Marie Curie

À Marie-Cé...

Une contribution au chaos ondulatoire expérimental

Fabrice Mortessagne

Laboratoire de Physique de la Matière Condensée
CNRS & Université de Nice-Sophia Antipolis, UMR 6622

Au travers d'une sélection d'articles, ce document propose de suivre le parcours de l'auteur dans le vaste et riche domaine du chaos ondulatoire. L'accent est en particulier mis sur les activités expérimentales dont il a été l'initiateur, et qu'il anime actuellement. Le lecteur parcourra ainsi plusieurs ordres de grandeur de longueurs d'onde : de quelques centaines de nanomètres à la dizaine de centimètres, et croisera des objets aussi simple, en apparence, qu'une boîte en cuivre, ou de plus haute technologie, comme une fibre optique amplificatrice à double cœur ! Il verra des comportements universels à l'œuvre, mais aussi des attitudes viollement atypiques, comme font montre les *scars* et les *modes localisés*. Et, si l'objectif du document est atteint, il sortira de sa lecture convaincu que les travaux menés par l'auteur concourent efficacement à un seul et même objectif : comprendre les mécanismes de propagation des ondes dans les milieux complexes.

Contents

I. Avant-propos	3
II. Chaos ondulatoire en optique guidée	5
A. Fibroscopie du chaos ondulatoire	5
B. Speckle statistics in a chaotic multimode fiber, <i>Physical Review E</i> 65 , 056223 (2002)	8
C. Light scarring in an optical fiber, <i>Physical Review Letters</i> 88 , 014102 (2002)	24
D. Optimized absorption in a chaotic double-clad fiber amplifier, <i>Optics Letters</i> 26 , 872 (2001)	29
E. Amplification optique des scars : vers le chaos ondulatoire non linéaire	33
1. Contexte	33
2. Mise en évidence de l'amplification sélective	34
F. Annexes	36
1. Modélisation de l'amplification	36
2. Calcul du spectre en nombre d'onde	37
3. La Beam Propagation Method	38
III. Cavités micro-ondes « semiclassiques »	41
A. Un diffuseur (quasi-)ponctuel dans une cavité	41
B. Semiclassical analysis of spectral correlations in regular billiards with point scatterers, <i>Physical Review E</i> 55 , 7741 (1997)	45
C. Diffractive orbits in the length spectrum of a two-dimensional microwave cavity with a small scatterer, <i>Physical Review E</i> 74 , 046219 (2006)	50
IV. Diffusion chaotique en milieux ouverts	59
A. Paradigme des milieux ouverts : cavité micro-ondes à température ambiante	59
B. Complete <i>S</i> -matrix in a microwave cavity at room temperature, <i>Physical Review E</i> 71 , 016205 (2005)	62
C. Inhomogeneous resonance broadening and statistics of complex wave functions in a chaotic microwave cavity, <i>Europhysics Letters</i> 70 , 162 (2005) & Inhomogeneous losses and wave function complexity, <i>Europhysics Letters</i> 76 , XXX (2006)	74
D. Gel de la diffusion : modes localisés	88
V. Postface	91

I. AVANT-PROPOS

En 1997, deux ans après ma nomination au poste de Maître de Conférences, j'ai proposé de créer une équipe s'intéressant au chaos quantique expérimental (on ne parlait pas encore de chaos ondulatoire). Malgré mon passé de théoricien, le pari a été relevé par la direction du LPMC. C'est donc avec ce cahier des charges que l'équipe *Propagation des Ondes en Milieux Complexes* a été créée. Je crois que l'on peut, sans réserve, dire que le pari a été gagné : que ce soit en termes de publications, de reconnaissance internationale, d'accueil d'étudiants en thèse, de post-docs, etc. Il faut remarquer que les équipes qui s'intéressent au chaos ondulatoire expérimental ne sont pas légions dans le monde : deux équipes utilisant des cavités micro-ondes en Allemagne (le groupe de Achim Richter et celui de Hans-Jürgen Stöckmann), et deux aux États-Unis (autour de Srinivas Sridhar et de Steve Anlage), on y trouve également les expériences menées par Richard Weaver dans le domaine de l'acoustique au sens large (y compris élastodynamique), dans ce domaine on trouve une activité au Danemark, initiée par Clive Ellegaard, et une équipe française, celle de Mathias Fink. Ce contexte expérimental souffreteux tient, pour l'essentiel, au caractère très fondamental du chaos ondulatoire, donc peu propice aux applications à court terme, réduisant ainsi les possibilités de financement de projets expérimentaux ambitieux. Cet examen rapide de la situation internationale donne encore plus de relief à la réussite de l'équipe POMC.

Créer une activité expérimentale *ex nihilo* est une lourde tâche, c'est pourquoi les premiers résultats ont été obtenus dans le cadre de l'optique guidée (chapitre II). En effet, cette activité a bénéficié de l'environnement favorable du LPMC, où les compétences et les savoir-faire sont importants dans ce domaine. Cette activité continue à nous distinguer internationalement, et le projet en cours (voir II.E) devrait renforcer notre position. C'est pourtant dans les micro-ondes que les premières « protomanips » ont été réalisées. Cette activité a été plus lente à émerger, car nous ne disposions localement d'aucune aide

pour éviter les erreurs de débutants. D'autre part, les situations « simples » ayant déjà été traitées par les équipes allemandes, nous nous sommes « attaqués » au délicat problème des milieux ouverts (chapitre IV) ! Les fruits du gros travail de fond de ces dernières années se récoltent depuis peu. La reconnaissance internationale est acquise. La récente, mais extrêmement prometteuse orientation vers l'étude de la localisation (voir IV.D) traduit la maturité atteinte par cette activité. Le savoir-faire dont nous disposons permet de revisiter des études numériques anciennes et d'en proposer des extensions vers des applications (chapitre III).

Les trois chapitres qui suivent proposent, chacun après une première section introductory, une sélection d'articles : un article long qui pose la problématique générale et expose en détails les travaux effectués, et un ou deux articles de type « lettre », présentant des résultats particulièrement marquant. Ces sélections d'articles sont suivies, pour les chapitres II et IV, d'une section sur les développements en cours. Si l'ancre de mes travaux est résolument fondamental, le lecteur pourra distinguer une volonté d'ouverture vers des applications potentielles (voir III.C) ou avérées (voir II.D). Un nom est associé à tous les travaux présentés ici : celui d'Olivier Legrand. Ayant tous les deux une activité d'enseignements importante, nous trouvons dans la constitution d'un « binôme » un moyen efficace de mener de front nos enseignements et une recherche dynamique. Même si, par goût, je m'imagine davantage dans les activités expérimentales, nous restons indissociables dans les idées, et je tiens à associer son nom à ce document.

En dehors des fautes involontaires de grammaire, d'orthographe et de goût, le lecteur trouvera dans ces lignes des fautes de « franglais » assumées : *speckle* pour tavelures et *scar* pour balafre.

II. CHAOS ONDULATOIRE EN OPTIQUE GUIDÉE

Bien que chronologiquement la deuxième voie expérimentale que j'ai développée – la première étant celle des cavités micro-ondes, qui sera traitée dans les deux sections suivantes –, c'est en optique guidée que les premiers résultats de chaos ondulatoire expérimental ont été obtenus. Le travail n'était pas plus simple, mais les forces vives plus nombreuses : les compétences dans ce domaine sont fortes au LPMC. Ainsi, la première thèse expérimentale que j'ai encadrée, celle de Valérie Doya, s'appuyait sur une fibre optique multimode à section chaotique « maison ». Cette fibre chaotique est maintenant devenue un emblème de l'équipe, et son apport au chaos ondulatoire expérimental est unanimement reconnu. Les trois articles choisis pour illustrer

cette partie de mon activité traduisent ma démarche générale, avec un article de fond (II.B), une lettre sur un résultat marquant (II.C), et une lettre « exogène » portant à l'attention de la communauté telecom optique la potentialité pratique de nos études fondamentales (II.D). Il ne faudrait pas croire que cette activité reste dans le souvenir de son (glorieux) passé. Bien au contraire, l'un de mes axes principaux de recherche reste dans l'optique guidée et constitue l'ossature du projet ANR *Chaos ondulatoire non linéaire* (« Chaos on line ») ; les premiers résultats obtenus dans le cadre de ce projet sont présentés en II.E. Mais avant de rentrer dans la lecture (guidée) des articles et des paragraphes originaux, je vais synthétiser l'essentiel de mon propos.

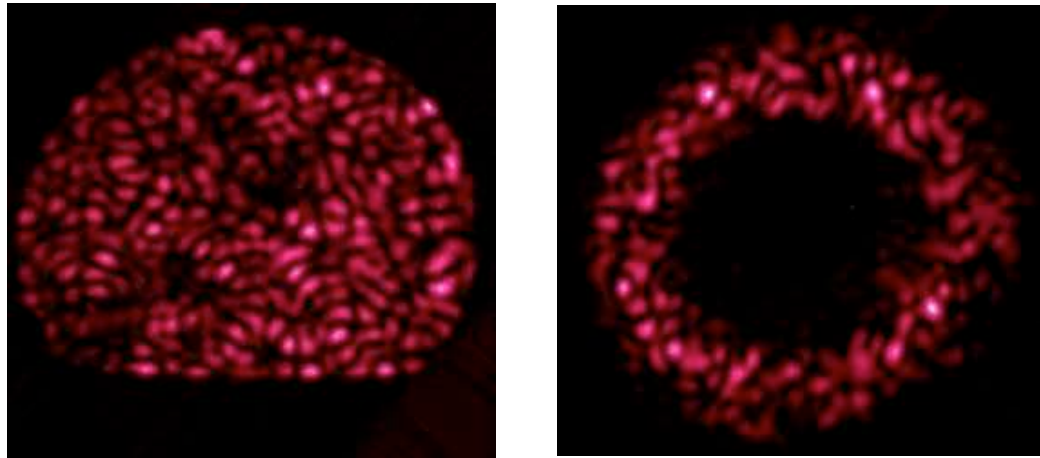


FIG. 1 Images obtenues en sortie d'une fibre chaotique en forme de cercle tronqué pour une excitation (presque) quelconque : à gauche, le champ proche, qui présente l'allure familière d'un champ de tavelures, à droite, le champ lointain, qui illustre l'absence de directions privilégiées dans l'espace des vecteurs d'onde.

A. Fibroscopie du chaos ondulatoire

Dans le cadre des travaux de thèse de Valérie Doya (co-encadrée avec Olivier Legrand), et en collaboration avec Christian Miniatura, nous avons conçu et réalisé une expérience visant à étudier les propriétés spatiales de la lumière transmise dans une fibre optique hautement multimode. Grâce à la forme non circulaire du cœur, cette étude s'est inscrite dans le domaine du chaos ondulatoire, où les expériences ne sont pas légion (atomes de Rydberg, cavités micro-ondes ou blocs vibrants) et où bien peu permettent d'accéder de façon directe à la répartition spatiale de l'onde. En effet, la plupart explorent les spectres de résonances afin d'y mettre en évidence les comportements statistiques universels décrits soit par des théories de matrices aléatoires, soit par des approches semi-

classiques. La fibre que nous avons réalisée au LPMC, grâce à la collaboration de Gérard Monnom et Bernard Dussardier de l'équipe *Fibres Optiques Actives*, présente une section en forme de disque tronqué. L'évolution des rayons, projetée sur la section transverse, est chaotique, ce qui se traduit par le fait que presque tous les modes guidés par cette fibre ont une répartition d'intensité de type speckle (comme le montre la figure 1). Les conditions expérimentales d'illumination de la fibre ne permettent pas d'exciter un mode unique, mais davantage une superposition de modes, centrée autour d'un nombre d'onde transverse moyen. Par une analyse statistique des distributions d'intensité et des corrélations spatiales du champ proche, nous avons confirmé l'hypothèse de statistique gaussienne des modes. Grâce aux images en champ lointain, nous avons fourni, pour la première fois, une vi-

sualisation directe d'une conjecture proposée par Berry dans les années 70 : les statistiques spatiales d'un mode d'une structure chaotique sont identiques à celles obtenues par une superposition aléatoire d'ondes planes. En

pratique, comme le montre la figure 1, le champ lointain forme un cercle dont le rayon est fixé par le nombre d'onde unique de la superposition (et la largeur par l'ouverture numérique de la fibre).

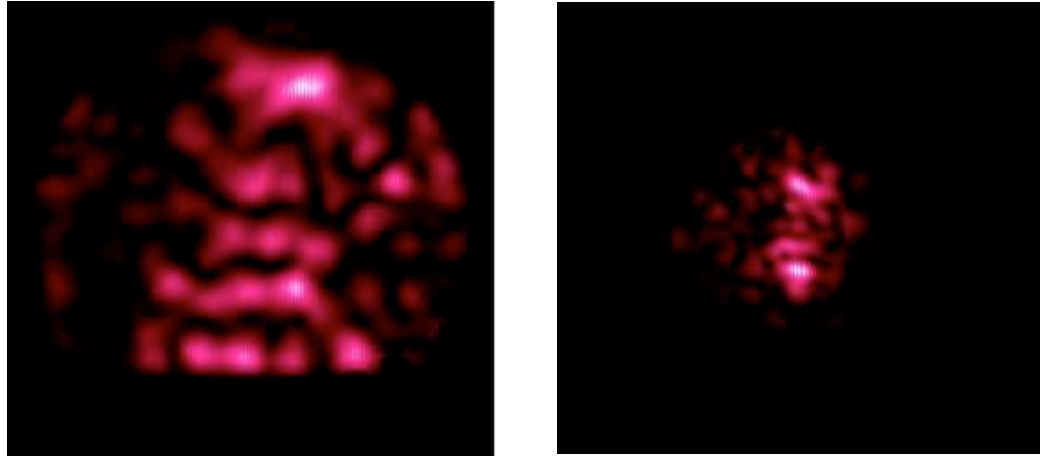


FIG. 2 Images obtenues en sortie d'une fibre chaotique en forme de cercle tronqué pour une excitation particulière : à gauche, le champ proche, où l'on constate la localisation préférentielle de l'énergie lumineuse le long de la verticale, à droite, le champ lointain, où les deux directions principales de propagation apparaissent comme deux spots lumineux.

Si le comportement de type speckle constitue la norme pour la plus grande partie des modes guidés de la fibre, certains d'entre eux présentent des surintensités localisées au voisinage de trajectoires périodiques de rayons. Ces modes particuliers, baptisés « scars » révèlent de manière spectaculaire la capacité des ondes à geler le développement de la dynamique chaotique par le jeu des interférences. Les scars constituent une singularité fascinante dans le domaine du chaos ondulatoire qui motive un grand nombre de travaux ; ils restent néanmoins mal connus (une description unifiée reste à établir) et constituent un défi expérimental pour la communauté. Pour la première fois dans une fibre optique, nous avons observé ce phénomène le long d'une orbite périodique à 2 rebonds (voir la figure 2). Pour fournir une analogie optique, la situation peut s'interpréter en termes d'un « Fabry-Perot » effectif où le résonateur instable est constitué d'un miroir plan et d'un miroir concave. L'observation de tels scars est possible si la norme du vecteur d'onde transverse vérifie une relation de quantification fixée par la réponse spectrale du résonateur.

Il est important de noter que la motivation purement fondamentale à l'origine de ces travaux, n'a pas empêché, grâce à une collaboration opportune avec l'IRCOM Limoges, de proposer des solutions pertinentes au problème de l'optimisation des amplificateurs tout-optiques à double cœur. En effet, en nous basant sur le caractère ergodique de ces modes, nous avons pro-

posé d'optimiser les performances d'amplificateurs à fibre à double cœur, dont le cœur monomode est dopé aux terres rares. Dans de tels dispositifs, nous avons montré théoriquement et numériquement que l'efficacité de l'amplification peut être sensiblement accrue en optimisant le recouvrement de l'onde de pompe multimode avec le cœur dopé, guidant le signal amplifié. Concernant l'absorption de la pompe, ces résultats ont été validés expérimentalement au sein du groupe Optique Guidée et Intégrée (OGI) de l'IRCOM, à Limoges, lors du séjour post-doctoral de Valérie Doya.

Bien qu'invoquant le chaos, le chaos ondulatoire reste une physique linéaire ; c'est la dynamique sous-jacente des rayons qui est non linéaire. Mais la dynamique des ondes est décrite, certes avec difficulté, par des équations purement linéaires. Que devient le chaos ondulatoire dans un milieu non linéaire ? Des effets non linéaires peuvent-ils être inhibés ou, au contraire, exacerbés par le chaos ondulatoire ? Pour tenter de répondre à ces questions où physique fondamentale et appliquée ne sont jamais très éloignées, un projet jeune chercheuse, porté par Valérie Doya, intitulé « Chaos On Line » (pour Chaos ondulatoire non linéaire) a été soumis à l'ANR, et accepté fin 2005. Ce projet traduit la maturité atteinte par l'activité expérimentale que j'ai lancée il y a quelques années. Il s'articule autour de trois axes :

- (i) Amplification sélective des scars dans des fibres chaotiques ;

- (ii) Effets non linéaires dans des fibres cristallines chaotiques ;
- (iii) Chaos et interactions paramétriques dans des guides d'ondes optiques.

L'effort initial s'est naturellement porté sur le premier axe, pour lequel les attentes (et le savoir-faire) de l'équipe sont les plus importantes. En effet, les investigations menées dans la fibre chaotique ont, certes, prouvé que cette dernière constituait un système modèle pour l'analyse des propriétés spatiales des modes de propagation, en particulier des modes de type scar. Mais il faut, cependant, admettre la grande difficulté à manipuler un scar unique, ou même une famille donnée de scars, en raison de l'impossibilité à réaliser une excitation sélective.

Fort de ce constat, nous avons décidé de mettre en œuvre un procédé dynamique de sélection d'un (ou d'une famille de) scar(s). La démarche employée s'est inspirée de travaux réalisés dans le domaine des lasers aléatoires. Il a, en effet, été montré numériquement que l'ajout d'un gain dans un milieu suffisamment désordonné se traduisait par l'amplification des modes localisés du système passif. La sélection d'un mode particulier s'effectuant par la localisation spatiale de la zone à gain. S'appuyant sur les compétences du LPMC en matière de dopage des fibres optiques, nous développons une expérience d'amplification optique dans une fibre multimode chaotique localement dopée par un milieu à gain, l'ytterbium, en l'occurrence.

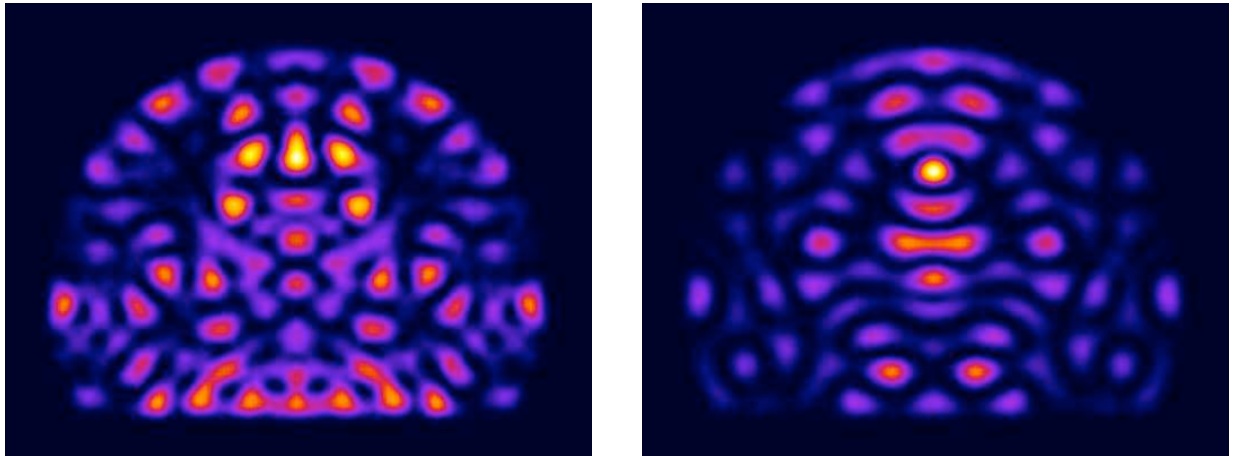


FIG. 3 Images obtenues en sortie d'une fibre chaotique en forme de cercle tronqué : à gauche, on simule la propagation dans une fibre passive, le résultat est une répartition de type speckle de l'intensité, à droite, la simulation intègre une zone dopée, une amplification sélective de (quelques) modes scars s'opère alors ; les conditions initiales sont identiques dans les deux cas.

Parallèlement à la fabrication de la fibre, nous avons étudié numériquement l'influence d'un gain localisé sur les scars. En localisant la zone dopée sur un point auto-focal¹ de la trajectoire périodique sur laquelle se construit le scar et en injectant le signal suivant la direction de cette même orbite périodique, nous avons observé une amplification sélective du mode scar (voir la figure II.A). Dans un milieu linéaire le poids des modes de type scar par rapport aux modes génériques de type speckle est faible. En contribuant à amplifier préférentiellement les scars, l'introduction d'un gain localisé permet de

réaliser une sélection modale de ces derniers, facilitant par conséquent leur observation. En collaboration avec Wilfried Blanc, du LPMC, nous avons réalisé une fibre en silice à section tronquée avec une zone dopée aux ions ytterbium à la position du point auto-focal de l'orbite périodique la plus courte à deux rebonds. Le dispositif expérimental est en cours d'installation : le pompage optique se fera à l'aide d'une diode laser à la longueur d'onde de $\lambda_p = 980 \text{ nm}$ et l'injection du signal à la longueur d'onde $\lambda_s = 1020 \text{ nm}$.

¹ Un ensemble de trajectoires voisines d'une orbite périodique issu d'un point auto-focal se refocalise sur ce point après avoir effectué une période.

B. Speckle statistics in a chaotic multimode fiber, Physical Review E 65, 056223 (2002)

Ce long article de 15 pages est en quelque sorte l'acte de naissance de l'optique guidée dans le champ du chaos ondulatoire. Il a été rédigé avec le soucis d'être complet et digeste, et de servir de socle aux publications ultérieures. Après une première section d'introduction, la section II établit au niveau formel l'analogie entre la propagation de la lumière (polarisée) le long de la fibre et l'évolution dans le temps d'une fonction d'onde quantique ; on y délimite le domaine de validité de cette équivalence, ce qui revient à fournir celui de l'approximation paraxiale. C'est donc une section importante qui pose le modèle utilisé. La section III dans laquelle « [...] we will address the implications of chaotic ray motion on the statistical spatial properties of guided modes. » peut être omise par les spécialistes. En revanche, le lecteur peu familier avec les méthodes semiclassiques et les résultats principaux de la théorie des matrices aléatoires trouvera certainement dans cette visite guidée de quelques pages de quoi satisfaire sa curiosité. Outre sa fonction pédagogique, cette section permet de rappeler les expressions des distributions du champ et d'intensité, ainsi que celles des fonctions d'autocorrélation, attendues pour un champ gaussien. Enfin, on présente les grandes lignes de la construction du spectre de longueur – ce concept sera revu en profondeur dans la partie III.C – de la cavité formée par la section transverse de la fibre ; on y identifie les orbites périodiques du billard équivalent, certaines sont montrées. Pour la petite histoire, le calcul des orbites périodiques du cercle tronqué est loin d'être évident, et ce n'est que grâce aux conseils avisés de Dominique Delande (et un peu de travail...) que j'y suis parvenu. La section IV présente les résultats expérimentaux ; on y construit les diverses diverses distributions présentées dans la section précédente, et un parfait accord avec les prédictions des statistiques gaussiennes est constaté. Une attention particulière pourra être portée sur l'utilisation détournée et féconde de l'intensité en champ lointain pour obtenir les corrélations spatiales du champ en sortie de fibre (figures 19 à 24, relations (43) à (48)). La courte section V est une ouverture vers les applications, mais nous y reviendrons plus largement en II.D.

Speckle statistics in a chaotic multimode fiber

Valérie Doya, Olivier Legrand, and Fabrice Mortessagne

Laboratoire de Physique de la Matière Condensée, CNRS UMR 6622, Université de Nice Sophia-Antipolis, 06108 Nice, France

Christian Miniatura

Laboratoire Ondes et Désordre, CNRS FRE 2302, 1361 Route des Lucioles, Sophia-Antipolis, 06560 Valbonne, France

(Received 21 December 2001; published 23 May 2002)

Wave chaos is devoted to the study of wave motion when the geometrical limit of rays is chaotic. Imprints of ray chaos may be found either in spectral and spatial properties of modes or in spatio-temporal evolution of wave packets. In this paper, we present a thorough experimental and theoretical analysis of field statistics for light propagating in a multimode fiber with a noncircular cross section. This optical fiber serves as a powerful tool to image waves in a system where light rays exhibit a chaotic dynamics. We show that, in the speckle regime, the experimentally measured statistical properties of intensity patterns are well accounted for by a “random Gaussian” hypothesis. A comparison is also made in the case of regular ray motion by using a circular optical fiber. Possible extensions and applications of the tools and concepts of wave chaos are mentioned in modern communication technology.

DOI: 10.1103/PhysRevE.65.056223

PACS number(s): 05.45.Mt, 42.81.-i

I. INTRODUCTION

After three decades of studies in the field of *quantum chaos*, the nature of quantum eigenstates of systems whose classical limit is chaotic is still an active subject of research. In classical Hamiltonian dynamics, chaos is explained in terms of exponential instability of trajectories with respect to initial conditions, leading to mixing and ergodicity. Thus, the application of probability theory to these deterministic systems is justified [1]. It is crucial to realize that asymptotic (long-time) limits of dynamical averages are essential in classical ergodic theory. In contrast, bounded classically chaotic quantum systems show different behaviors since, their frequency spectrum being discrete, all phase-space information is essentially obtained after a finite amount of time. This conflicting situation reveals the subtle and singular nature of the semiclassical limit (boldly implemented as the famous “ $\hbar \rightarrow 0$ ” limit) whose understanding is precisely the subject of quantum chaos. In this limit, wave functions are uniformly distributed over the whole available phase space, which is ergodically explored by the classical trajectories, thus locally resulting in a random superposition of plane waves. Tracking fingerprints of classical phase-space structures in quantum properties (distribution of eigenfrequencies, statistical properties of eigenmodes, Green’s functions, and time evolution) led to major advances in the field, such as random matrix theory, and periodic orbit theory, dynamical localization [2]. In fact, these advances rapidly proved to be relevant for other wave systems sharing close analogies with quantum systems (e.g., microwave or acoustic systems), giving rise to *wave chaos*. For these systems, the goal is to understand the fate of interference in the geometrical limit (wavelength $\lambda \rightarrow 0$) when the ray motion is chaotic. Connections were also found with disordered systems [3]. Wave and quantum chaos are thus now well documented topics [2,4,5] covering a wide variety of physical systems, such as complex atomic nuclei [6], Rydberg atoms [7], electrons in quantum dots [8], cold atoms [9], surface waves [10], elastodynamics [11], acoustics

[12], microwaves [13], and optical cavities [14]. Despite their interesting potentialities [15], wave chaos experiments with visible light, in particular in optical fibers, have been largely underestimated. Indeed, the huge advantage of light in optical fibers resides in the fact that it can be most easily imaged, thus enabling one to achieve very precise measurements of intensity patterns. Recently, using a chaotic optical fiber with a D-shaped transverse section, we have observed and analyzed scarred patterns [16]. While spectacular, this behavior is exceptional in such chaotic optical fibers, and a random field is more generally obtained. The differences between these behaviors can be evidenced through an analysis of the field in terms of spatial statistics and correlations. The aim of the present paper is to provide the first experimental characterization of wave intensity in multimode fibers in the speckle regime, together with a theoretical analysis in terms of wave chaos.

This paper is organized as follows. In Sec. II, we present a theoretical approach based on a modal decomposition to describe light propagation along a multimode fiber. To establish an analogy with quantum systems, we introduce the paraxial approximation, which we show to be valid in the system we consider. In Sec. III, we start from a Hamiltonian formalism for wave propagation to briefly describe the geometrical limit of rays and introduce the concept of chaotic billiards relevant to our study. Then semiclassical arguments are briefly reviewed and used to predict Gaussian statistics of guided modes. A brief mention of periodic orbit theory is made to illustrate the close connection between modes and periodic ray motion. In Sec. IV, our experiment is described, starting with the fabrication of a specially designed multimode fiber. The experimental setup is then presented, followed by an analysis of the measurements of wave intensity. We show the relevance of a Gaussian analysis for a wave pattern resulting from the superposition of ergodic guided modes. A special emphasis is placed on spatial correlations of the near-field using the information contained in the far-field intensity pattern. We cannot conclude without mention-

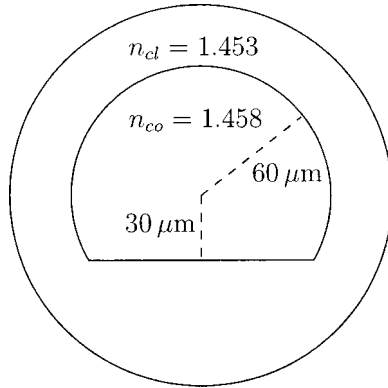


FIG. 1. Sketch of the transverse section of the multimode fiber studied in the paper. The cladding of the actual fiber is thicker than shown here.

ing that, in the current context of rapidly growing optical communications, the understanding and fine control of complex wave propagation in multimode fibers will constitute an indispensable issue in future transmission systems.

II. THE MODEL FOR PROPAGATION ALONG THE FIBER

We postpone to Sec. IV, dedicated to experimental results, the details of fabrication of the fiber we use. Here, we simply give those of its characteristics which justify the approximations of our model. We use a highly multimode step-index fiber, with respective indices of the core and of the cladding, $n_{co}=1.458$ and $n_{cl}=1.453$. The transverse shape of the core is a truncated disk (see Fig. 1) invariant along the fiber.

Since we are dealing with a case of weak guidance [$(n_{co}-n_{cl})/n_{cl} \ll 1$], it is expected that one can construct modes whose transverse field is essentially polarized in one direction. Indeed, in weakly guiding waveguides, though the index nonuniformity is essential to ensure total internal reflection, one may neglect it as far as polarization effects are concerned [17]. In spite of the edges of the transverse section, we checked that the linear polarization of light issued from our laser is indeed fairly well preserved throughout the fiber. We therefore will use the scalar approximation in the following theoretical approach.

A. Modal decomposition

We denote by z the position along the axis of the fiber and by \mathbf{r} the position in the transverse plane. Using the translational invariance $n(\mathbf{r}, z) = n(z)$, the three-dimensional (3D) Helmholtz stationary equation

$$(\Delta + \partial_{zz})\psi(\mathbf{r}, z) + n^2(\mathbf{r})k_0^2\psi(\mathbf{r}, z) = 0, \quad (1)$$

where Δ is the transverse Laplacian, can be reduced to

$$\Delta\phi(\mathbf{r}; \beta) + [n^2(\mathbf{r})k_0^2 - \beta^2]\phi(\mathbf{r}; \beta) = 0, \quad (2)$$

where $k_0 = 2\pi/\lambda$ (λ is the vacuum wavelength of the source) and

$$\psi(\mathbf{r}, z) = \int d\beta \phi(\mathbf{r}; \beta) e^{i\beta z}. \quad (3)$$

For $\beta_{cl}^2 \equiv n_{cl}^2 k_0^2 \leq \beta^2 \leq \beta_{co}^2 \equiv n_{co}^2 k_0^2$, Eq. (2) is solved at discrete values, β_n , called the propagation constants of the guided modes. This eigenvalue problem can be written in a form

$$\left[-\frac{1}{2}\Delta + \frac{\beta_{co}^2 - n^2(\mathbf{r})k_0^2}{2} \right] \phi = \frac{\beta_{co}^2 - \beta^2}{2} \phi, \quad (4)$$

which, by writing $V(\mathbf{r}) = [\beta_{co}^2 - n^2(\mathbf{r})k_0^2]/2$, emphasizes the formal equivalence between Eq. (2) and a stationary Schrödinger equation

$$\left[-\frac{1}{2}\Delta + V(\mathbf{r}) \right] \phi = E\phi. \quad (5)$$

The eigenenergy E takes on discrete values E_n , related to the β_n 's through

$$\beta_n^2 = \beta_{co}^2 - 2E_n. \quad (6)$$

Using the basis generated by the eigenmodes ϕ_n of the Schrödinger equation (5), the solution of Eq. (1) can be written as

$$\begin{aligned} \psi(\mathbf{r}, z) &= \sum_n c_n \phi_n(\mathbf{r}) \exp(i\beta_n z) \\ &= \sum_n c_n \phi_n(\mathbf{r}) \exp(i\sqrt{\beta_{co}^2 - 2E_n} z), \end{aligned} \quad (7)$$

where the sum should generically include the continuum states (nonguided modes with imaginary β 's).

Defining $E_n = \kappa_n^2/2$, to each mode can be associated an angle θ_n with respect to the z axis defined by $\tan \theta_n = \kappa_n/\beta_n$ (or, equivalently, by $\sin \theta_n = \kappa_n/\beta_{co}$). The cutoff angle for guided modes is given by $\sin \theta_{max} = \sqrt{1 - (n_{cl}/n_{co})^2}$ (around 5° with the values of the indices given above), which corresponds to the maximum value $\kappa_{max} = \sqrt{\beta_{co}^2 - \beta_{cl}^2}$. This value is related to the total number of guided modes [18]. Indeed, the number of allowed values β_n in the interval $[\beta_{cl}, \beta_{co}]$ (for a given polarization) is given by the Thomas-Fermi formula, which, in our context, reads

$$\begin{aligned} N(\beta) &= \frac{1}{2\pi} \int_{E > V} d\mathbf{r} [E - V(\mathbf{r})] = \frac{1}{2\pi} \int_{core} d\mathbf{r} \frac{n^2(\mathbf{r})k_0^2 - \beta^2}{2} \\ &= \frac{S}{4\pi} (\beta_{co}^2 - \beta^2) = \frac{S\kappa^2}{4\pi}, \end{aligned} \quad (8)$$

where S is the area of the core. This expression yields the well-known formula [19] for a cylindrical fiber of radius a : $N = v^2/2$, with $v = ak_0(n_{co}^2 - n_{cl}^2)^{1/2}$, when allowing for both polarizations. In our exotic fiber, the total number of modes (with a given polarization) is approximately 1500.

B. The paraxial approximation

Many of the theoretical results in the field of wave chaos have been obtained in the quantum context [7,18]. Though the introduction of the quantum formalism is not theoretically indispensable, it is quite convenient to our purposes and is easily performed through the following transformation. Starting from Eq. (5), one can write a pseudo-time-dependent Schrödinger equation

$$i\beta_{\text{co}}\partial_z\varphi(\mathbf{r};z) = [-\frac{1}{2}\Delta + V(\mathbf{r})]\varphi(\mathbf{r};z) \quad (9)$$

which can be viewed as an evolution equation along z . Any solution $\varphi(\mathbf{r};z)$ of the above equation can also be decomposed on the ϕ_n 's,

$$\varphi(\mathbf{r};z) = \sum_n c_n \phi_n \exp\left(-i\frac{E_n}{\beta_{\text{co}}}z\right). \quad (10)$$

Note that Eq. (9) corresponds to the paraxial (or parabolic) approximation performed on Eq. (1). Indeed, if one writes

$$\psi(\mathbf{r},z) = \zeta(\mathbf{r};z)e^{i\beta_{\text{co}}z}, \quad (11)$$

Eq. (1) becomes

$$\begin{aligned} i\beta_{\text{co}}\partial_z\zeta(\mathbf{r};z) &= \left[-\frac{1}{2}\Delta + \frac{\beta_{\text{co}}^2 - n^2(\mathbf{r})k_0^2}{2}\right] \zeta(\mathbf{r};z) \\ &\quad - \frac{1}{2} \partial_{zz}\zeta(\mathbf{r};z) \end{aligned} \quad (12)$$

which is equivalent to Eq. (9) insofar as one may neglect the second order z derivative of ζ (paraxial or slowly varying amplitude approximation):

$$|\partial_{zz}\zeta| \ll |\beta_{\text{co}}\partial_z\zeta|. \quad (13)$$

This neglect amounts to approximate the exact solution (7) of Eq. (1) by

$$\varphi(\mathbf{r};z)e^{i\beta_{\text{co}}z} = \sum_n c_n \phi_n(\mathbf{r}) \exp\left(i\frac{\beta_{\text{co}}^2 - E_n}{\beta_{\text{co}}}z\right). \quad (14)$$

The validity of this approximation is easily established in our experimental context. Indeed, by comparison of Eqs. (7) and (14), corresponding terms of each sum are close if the difference between their phases remains much smaller than 2π , i.e.,

$$\hat{\delta\beta} = \beta_{\text{co}} - \frac{E_n}{\beta_{\text{co}}} - \sqrt{\beta_{\text{co}}^2 - 2E_n} \simeq \frac{1}{2}\beta_{\text{co}}\left(\frac{E_n}{\beta_{\text{co}}^2}\right)^2 \ll \frac{2\pi}{z}. \quad (15)$$

Condition (15) leads to values of θ somewhat smaller than the cutoff angle θ_{max} , when allowing for the actual length of the fiber. Therefore, this condition amounts to restricting the sum in Eq. (14) to the first few hundreds of guided modes.

III. FROM RAYS TO WAVE

We now consider the geometrical limit of rays and propose to do so by deriving the eikonal equation in the paraxial approximation. This is technically much simpler than deriving the eikonal equation directly from the 3D Helmholtz equation without restricting the generality of the ensuing results [20]. We are then naturally led to investigate a problem of *chaotic billiards* [21,22]. Then we will address the implications of chaotic ray motion on the statistical spatial properties of guided modes.

A. Chaotic ray motion

Starting from the parabolic equation (9), if one substitutes

$$\varphi(\mathbf{r};z) = A(\mathbf{r};z)\exp[i\beta_{\text{co}}\mathcal{L}(\mathbf{r};z)], \quad (16)$$

two equations are obtained,

$$-2\partial_z\mathcal{L} = (\nabla\mathcal{L})^2 + \left(1 - \frac{n^2(\mathbf{r})}{n_{\text{co}}^2}\right) - \frac{1}{\beta_{\text{co}}^2} \frac{\Delta A}{A}, \quad (17)$$

$$\partial_z(A^2) = -\nabla \cdot (A^2 \nabla \mathcal{L}). \quad (18)$$

Equation (18) is simply a conservation equation for the “density” A^2 , with “current” $A^2 \nabla \mathcal{L}$, whereas Eq. (17) is not the eikonal equation since it allows for diffraction effects through the last term of the right-hand side. Indeed, the true eikonal equation, associated to geometrical optics, is obtained by neglecting $\beta_{\text{co}}^{-2}\Delta A/A$, consistently with condition (13). It therefore reads

$$-\partial_z\mathcal{L} = H(\mathbf{r}, \nabla\mathcal{L}), \quad (19)$$

where

$$H(\mathbf{r}, \mathbf{p}_\perp) = \frac{\mathbf{p}_\perp^2}{2} + \frac{1}{2} \left(1 - \frac{n^2(\mathbf{r})}{n_{\text{co}}^2}\right) \quad (20)$$

is the Hamiltonian and \mathbf{p}_\perp is the transverse momentum. The rays of the geometrical limit are the characteristic curves $(\mathbf{r}(z), \mathbf{p}_\perp(z))$ of the Hamilton-Jacobi equation and satisfy the Hamilton equations

$$\frac{d\mathbf{r}}{dz} = \frac{\partial H}{\partial \mathbf{p}_\perp}, \quad (21)$$

$$\frac{d\mathbf{p}_\perp}{dz} = -\frac{\partial H}{\partial \mathbf{r}}. \quad (22)$$

These equations are straightforwardly solved for our fiber. Indeed, inside the uniform core, H is reduced to its “kinetic” part, $\mathbf{p}_\perp^2/2$, which can be related to the angle θ defined above through $\mathbf{p}_\perp^2 = \sin^2 \theta$. At the boundaries between core and cladding, if $\sin^2 \theta < (1 - n_{\text{cl}}^2/n_{\text{co}}^2)$, the ray is reflected back to the core. Between two consecutive specular reflections, the ray consists of a straight segment. We have thus reduced the initial wave problem to the dynamics of a point particle inside a domain with perfectly rigid walls: a billiard [23].

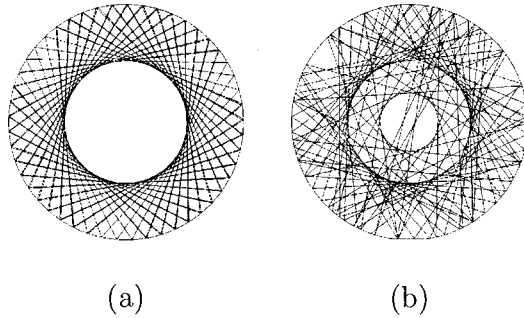


FIG. 2. Examples of a single ray trajectory after a propagation of 150 in units of the radius R : (a) inside a circular billiard, where a caustic is clearly observed; (b) inside a circular billiard cut by a small straight segment of length $10^{-2}R$. The caustic is destroyed due to the chaotic motion.

Here, the dynamics refers to the evolution along z and can be most easily visualized by projecting the ray trajectories onto the transverse plane. From now on, we will restrict our study of the motion to the two-dimensional (2D) projected motion.

Without going into technicalities, we wish now to illustrate the particular dynamics of chaotic billiards. Let us first recall the regular motion of rays in the billiard with the shape of a circle. Figure 2(a) shows a typical trajectory within such a billiard after a propagation length of 150 in units of the radius R . One can clearly observe the presence of a caustic. The latter encloses a region of space that this trajectory never visits (whatever the number of reflections). This kind of structure is destroyed in chaotic billiards. This is exemplified by considering the following modification of the previous billiard. A new shape is obtained by cutting a small straight segment of length $10^{-2}R$. Whereas the change of boundary is not visible in Fig. 2(b), its effect on the dynamics is dramatic: for the same initial conditions (position and direction), the formerly forbidden region is invaded after a finite number of reflections. In the theory of Hamiltonian chaos, it is shown that this effect stems from the *extreme sensitivity to initial conditions*, which appears for any nonvanishing size of the cut (excepted for a cut of length R , which corresponds to the semicircular billiard).

The qualification of chaos is more conveniently studied through a phase-space representation. A common representation in billiards consists in restricting the dynamics to the knowledge, at each impact, of the curvilinear abscissa, s , and of the sine of the angle of reflection, α , with respect to the inward boundary normal (see Fig. 3). Thus, at j th reflection, defining $\hat{\mathbf{t}}_j$ the unit vector tangent to the oriented boundary at abscissa s_j , and $\hat{\mathbf{n}}_j$ the inward normal unit vector, the transverse momentum reads $\mathbf{p}_\perp = \hat{\mathbf{t}}_j \sin \theta \sin \alpha_j + \hat{\mathbf{n}}_j \sin \theta \cos \alpha_j$. The same trajectories as in Fig. 2 are shown in the phase space $(s, \sin \alpha)$ in Fig. 4: the regular motion is associated to the conservation of α in the circular billiard [Fig. 4(b)], while in the truncated billiard, which is chaotic, the whole phase space is eventually uniformly covered by almost any trajectory [Fig. 4(b)] shows the trajectory after a finite number of bounces, i.e., at finite time]. It should be mentioned here that there exist particular trajectories which do not fit into this scheme, namely, the periodic orbits. These orbits are

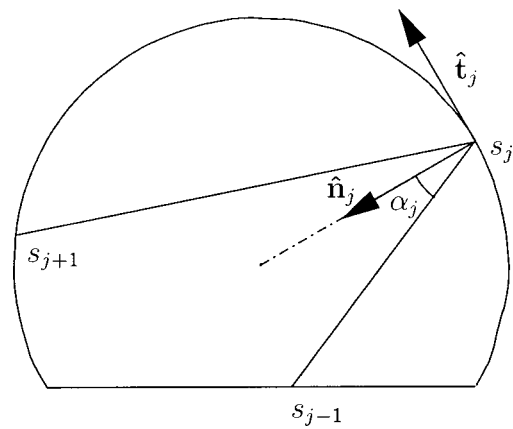


FIG. 3. Representation of the dynamics in a billiard through the coordinates associated, at each rebound, to the curvilinear abscissa s along the boundary, and the sine of the angle of reflection α with respect to the inward boundary normal.

trajectories which close upon themselves in phase space (hence also in real space). For a chaotic system they must, of course, be unstable in the sense that any small initial deviation from it must diverge exponentially with time. To be complete, the proper way of evidencing chaos in billiards is by considering the behavior of a collection of initial conditions. In Fig. 5, this set is initially shown as a dark disk in the phase space associated to the geometry of our actual fiber. Rapidly (exponentially with the number of reflections) the initial conditions will spread over the whole surface. This behavior is precisely the sign of Hamiltonian chaos.

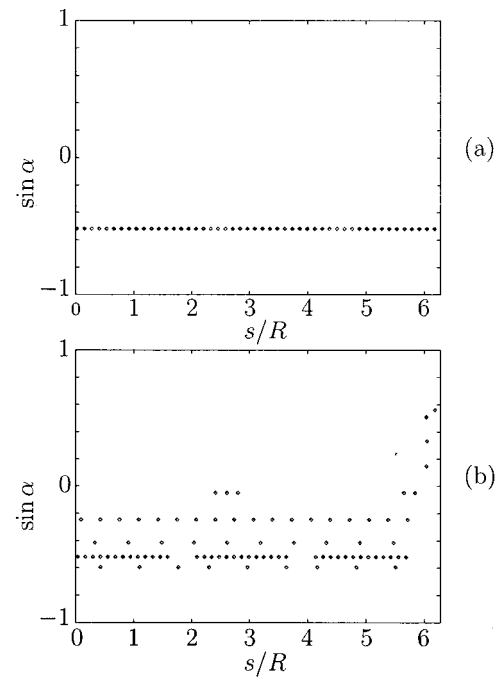


FIG. 4. Same trajectories as in Fig. 2 using the phase-space coordinates $(s, \sin \alpha)$ introduced in Fig. 3. (a) The regular motion in the circular billiard is associated to the conservation of α ; (b) in the chaotic billiard, the whole phase space is asymptotically uniformly covered by almost any ray trajectory.

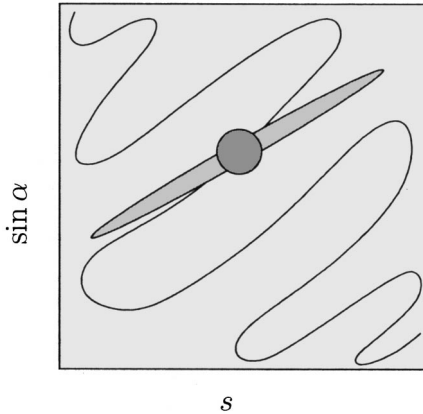


FIG. 5. Sketch of the typical evolution in phase space of a subset of initial conditions. Starting from an initial disk, subsequent stretching and folding are depicted at larger and larger times.

B. Gaussian statistics of ergodic guided modes

In the following, we will use the quantum terminology of semiclassical techniques to designate what is otherwise referred to as the geometrical theory of diffraction [24]. Thus, using the quantum analog of our optical waveguide, the geometrical limit of rays corresponds to the classical limit of a quantum problem. In our case, the small parameter for semiclassical expansions is $(\kappa L)^{-1}$, where $\kappa^2 = \beta_{co}^2 - \beta^2 = 2E$ and $L \sim \sqrt{S}$ is the typical size of the core [25], and ray trajectories have to be viewed as a genuine skeleton of wave motion [26]. In particular, the features of uniformity and isotropy resulting from the chaotic exploration of phase space by rays, as illustrated in the last section (Fig. 5), should be expected to govern, likewise, the statistical distribution of eigenmodes. The ergodicity of eigenmodes can be rigorously shown [27] and may be formally stated in writing down the *local density of states*,

$$\rho_0(\mathbf{r}; \kappa) = \frac{\int d\mathbf{p}_\perp \delta(\kappa^2/2 - \beta_{co}^2 H(\mathbf{r}, \mathbf{p}_\perp))}{\int d\mathbf{r}' d\mathbf{p}'_\perp \delta(\kappa^2/2 - \beta_{co}^2 H(\mathbf{r}', \mathbf{p}'_\perp))} \equiv \lim_{\kappa L \rightarrow \infty} \langle |\phi(\mathbf{r})|^2 \rangle_\kappa, \quad (23)$$

where the average reads

$$\langle |\phi(\mathbf{r})|^2 \rangle_\kappa = \frac{1}{N} \sum_n |\phi_n(\mathbf{r})|^2, \quad (24)$$

the sum running over N eigenmodes centered around $E = \kappa^2/2$. This average is meaningful provided that the energy interval is large enough to ensure a large value of N , but small enough for the density of states to be approximately constant within this interval [28]. In practice, an average over a few modes is adequate, and the ergodic behavior can even become a generic feature of individual eigenmodes when $(\kappa L)^{-1}$ tends to zero. In Fig. 6, the squared amplitude of such an ergodic mode is shown. It has been obtained by numerically solving by

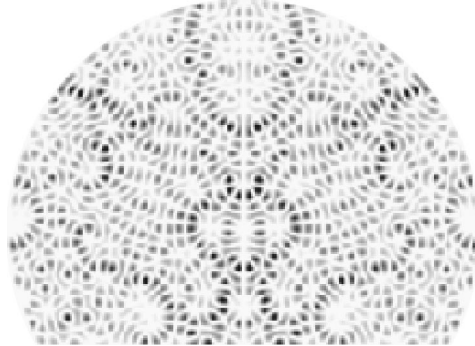


FIG. 6. A typical *ergodic* eigenmode (squared amplitude), solution of Eq. (25) with Dirichlet boundary conditions, in the truncated chaotic billiard with $\kappa R = 87.89$. Apart from the obvious symmetry, such an eigenmode can be viewed as a superposition of plane waves at a given κ with random phases and directions.

$$\begin{aligned} (\Delta + \kappa^2) \phi &= 0 && \text{inside the core} \\ \phi &= 0 && \text{on the boundary.} \end{aligned} \quad (25)$$

The above eigenvalue problem (with Dirichlet conditions) is a good approximation of Eq. (4) for low-lying guided modes. Nevertheless, the following qualitative arguments concerning the statistics of eigenmodes do not rely on this approximation. In Sec. IV, to analyze our experimental results, we will not use it. In Fig. 6, $\kappa = 87.89$ (in units of inverse radius of the billiard). This figure illustrates the fact that a typical eigenmode can be viewed as a random superposition of 2D plane waves of different phases and directions but with the same wave number κ [29].

If one views a typical specklelike guided mode locally as the superposition of plane waves with random directions, it may be shown that the field autocorrelation function

$$C_\phi(\mathbf{r}, \mathbf{r}_0; \kappa) = \langle \phi^*(\mathbf{r} - \frac{1}{2}\mathbf{r}_0) \phi(\mathbf{r} + \frac{1}{2}\mathbf{r}_0) \rangle_\kappa, \quad (26)$$

where $\langle \dots \rangle_\kappa$ is to be understood as an ensemble (energy) average in the asymptotic limit $\kappa L \gg 1$, has the expected value [30,31] [following the microcanonical result (23)]

$$\begin{aligned} C_\phi(\mathbf{r}, \mathbf{r}_0; \kappa) &= \frac{\int d\mathbf{p}_\perp \exp[i\beta_{co} \mathbf{p}_\perp \cdot \mathbf{r}_0] \delta(\kappa^2/2 - \beta_{co}^2 H(\mathbf{r}, \mathbf{p}_\perp))}{\int d\mathbf{r}' d\mathbf{p}'_\perp \delta(\kappa^2/2 - \beta_{co}^2 H(\mathbf{r}', \mathbf{p}'_\perp))}. \end{aligned} \quad (27)$$

In the case of a 2D billiard, where $H(\mathbf{r}, \mathbf{p}_\perp) = \mathbf{p}_\perp^2/2$ in its interior, the Dirac δ function only fixes the norm of \mathbf{p}_\perp . Equation (27) thus amounts to the well-known result [31]

$$C_\phi(\mathbf{r}, \mathbf{r}_0; \kappa) = J_0(\kappa r_0), \quad (28)$$

where $J_0(x)$ is the zero-order Bessel function and r_0 is the norm of \mathbf{r}_0 . Using an ergodic hypothesis, the average in Eq. (26) can be replaced by a spatial average over the midpoint \mathbf{r} ,

which, in practice, should be evaluated over a domain encompassing a sufficiently large number of oscillations [30].

In the asymptotic limit, a random superposition of plane waves with random uncorrelated phases is expected to yield a Gaussian random field. In the case of real eigenmodes, this implies that the probability $P(\phi)d\phi$ that the eigenfunction has a value between ϕ and $\phi+d\phi$ is given by

$$P(\phi) = \frac{1}{\sqrt{2\pi\langle\phi^2\rangle}} \exp\left(-\frac{\phi^2}{2\langle\phi^2\rangle}\right), \quad (29)$$

where $\langle\cdots\rangle$ denotes a spatial average on the surface of the fiber section [32]. One should note that a Gaussian distribution does not imply the stronger requirement (27). The result (29) is also recovered by random matrix theory (RMT) for the Gaussian orthogonal ensemble of real symmetric $N\times N$ matrices in the limit $N\rightarrow\infty$ [28]. Indeed, RMT leads to the so-called Porter-Thomas distribution for the squared eigenvector components. The latter distribution is obtained from Eq. (29) for the intensity $I=\phi^2$ and reads

$$P(I) = \frac{1}{\sqrt{2\pi I\langle I\rangle}} \exp\left(-\frac{I}{2\langle I\rangle}\right). \quad (30)$$

To check this behavior, we first numerically solve the propagation equation (25) with Dirichlet boundary conditions using a plane-wave decomposition method. This method [33] has allowed the calculation of the first 2000 eigenmodes of the D-shaped billiard. Because of Dirichlet boundary conditions, the eigenmodes are chosen to be real.

Using these calculated modes, we have evaluated the radial field autocorrelation function $C_\phi(r_0; \kappa)$,

$$C_\phi(r_0; \kappa) = \frac{1}{2\pi} \int_0^{2\pi} d\theta C_\phi(r_0; \kappa) \quad (31)$$

with θ the polar angle and where the field autocorrelation function $C_\phi(r_0; \kappa)$ is equivalent to Eq. (26) with a spatial average over \mathbf{r} ,

$$C_\phi(r_0; \kappa) = \langle \phi^*(\mathbf{r} - \frac{1}{2}\mathbf{r}_0) \phi(\mathbf{r} + \frac{1}{2}\mathbf{r}_0) \rangle_r, \quad (32)$$

where the average $\langle\cdots\rangle_r$ reads $\iint_{\mathcal{D}} \cdots dr / \iint_{\mathcal{D}} |\phi(\mathbf{r})|^2 dr$, with \mathcal{D} the domain of integration.

In Fig. 7, we have represented one typical high-energy eigenmode (amplitude) of the D-shaped billiard for a value of κ equal to 87.89 in units of inverse radius R , its probability distribution and the corresponding radial field autocorrelation function following Eqs. (31) and (32). The assumption of a random superposition of plane waves is confirmed by the good agreement between the probability distribution $P(\phi)$ and the Gaussian distribution, as can be seen in Fig. 7(b). The radial autocorrelation function $C_\phi(r_0; \kappa)$ is compared to the expected zero-order Bessel function $J_0(\kappa r_0)$ for $\kappa R = 87.89$. Note that the prediction (28) is perfectly verified. From the oscillatory nature of the autocorrelation function, one should define a correlation length deduced from the

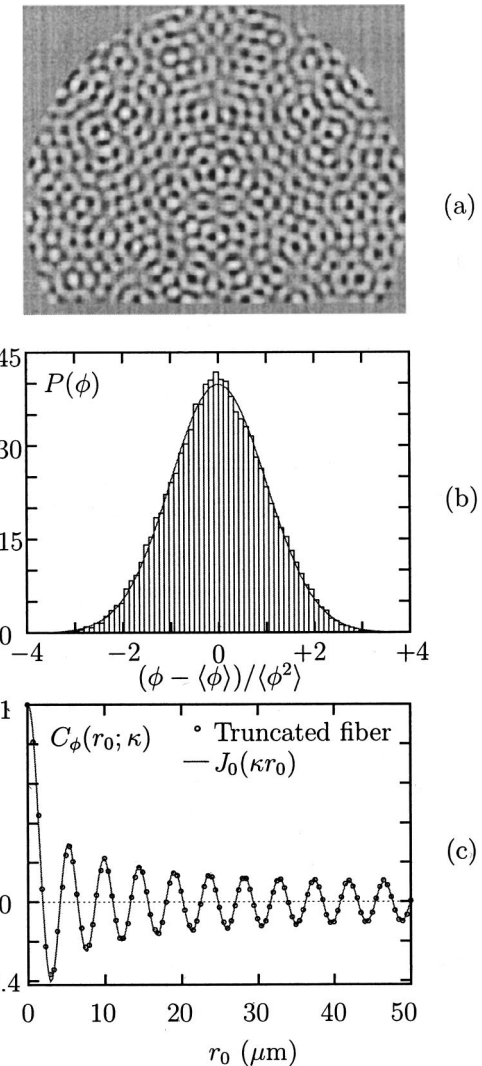


FIG. 7. (a) A high-energy eigenmode (amplitude) with $\kappa R = 87.89$ in the truncated chaotic billiard, (b) its associated probability distribution $P(\phi)$, compared to a Gaussian distribution (continuous line), and (c) the radial field autocorrelation function $C_\phi(r_0; \kappa)$.

quasiperiod of the autocorrelation function. This correlation length is related to the typical size of the speckle grain which is of the order of κ^{-1} .

In order to reveal the ergodic behavior of the chaotic eigenmodes of the D-shaped billiard, we have compared the previous results with those obtained for a typical high-energy mode of the circular billiard. For large values of the quantized number m associated to the number of zeros in the radial direction, there exists a simple relation between the couple of quantized numbers (l, m) associated to the regular eigenmode of the circular billiard and the value of κ given by [34]

$$\kappa \approx (l+2m) \frac{\pi}{2R}, \quad m \gg 1. \quad (33)$$

The resolution of Eq. (25) for the circular fiber yields solutions of the form

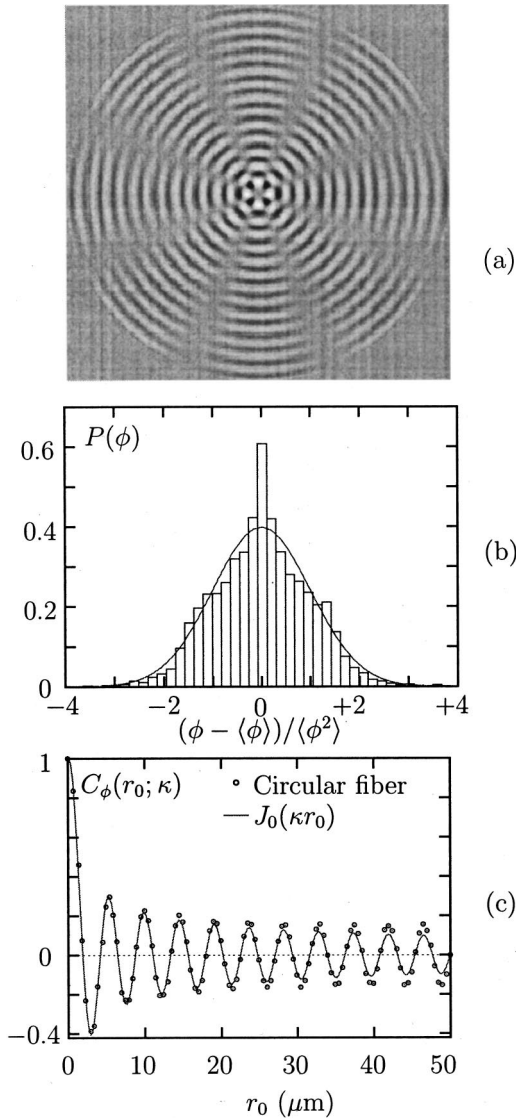


FIG. 8. (a) A high-energy eigenmode with $\kappa R = 87.0$ in the regular circular billiard, (b) its associated probability distribution $P(\phi)$, compared to a Gaussian distribution (continuous line), and (c) the radial field autocorrelation function $C_\phi(r_0; \kappa)$.

$$\phi_{l,m}(\mathbf{r}) = J_l(\kappa_m r) \times \begin{cases} \cos(l\vartheta) & \text{even solution} \\ \sin(l\vartheta) & \text{odd solution,} \end{cases} \quad (34)$$

where $J_l(\kappa_m R) = 0$ and ϑ is the angular variable in the circular coordinates. Using these relations, we have calculated one eigenmode of the circular billiard, for a value of $\kappa R \approx 87.0$, shown in Fig. 8(a). The associated probability [Fig. 8(b)] and the corresponding radial field autocorrelation function [Fig. 8(c)] deviate from the theoretical predictions (28) and (29) pertaining to ergodic modes. This is not surprising since the regular eigenmodes are obviously nonergodic. Indeed, in this context, a good test of ergodicity relies on the independence of the above statistical quantities on the spatial domain \mathcal{D} introduced in Eq. (32) [30]. This domain defines the statistical sample used for the evaluation of the distribution probability. For the eigenmodes of the D-shaped fiber,

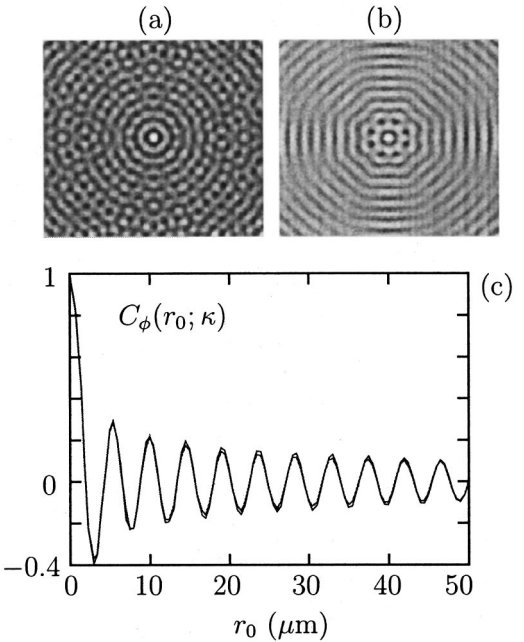


FIG. 9. Field autocorrelation functions for (a) an eigenmode of the truncated billiard, (b) an eigenmode of the circular billiard, and (c) their associated radial representations.

we have checked this independence. On the contrary, in the circular fiber, wide variations are observed from one sample to another. Surprisingly enough, for particular domains of this regular fiber, one can even observe that the behavior of the radial field autocorrelation function is very close to the zero-order Bessel function (Fig. 9). It does not necessarily follow from this result that the field autocorrelation function $C_\phi(r_0; \kappa)$ (32) is isotropic, as implied by Berry's prediction (28) for ergodic eigenmodes. As an illustration, Fig. 9 displays the behavior of the field autocorrelation functions calculated for eigenmodes, with similar values of κ , of the D-shaped (a) and of the circular (b) fibers. Note that, while the *radial* autocorrelation functions for these two modes are nearly indistinguishable [Fig. 9(c)], only the ergodic eigenmode exhibits isotropic correlations.

C. Periodic orbit theory

As any prediction concerning average behaviors, the results presented in the previous section suffer rare but important exceptions. Indeed, inspecting Fig. 10(a), a clear deviation from ergodicity is seen, which is in fact associated to a particular periodic orbit (superimposed as a solid line). This intensity enhancement in the vicinity of a single periodic orbit (p.o.) is coined *scarring* [33,35]. This unexpected behavior has led the quantum chaos community to reconsider the semiclassical limit (23). They have established that the semiclassical skeleton of eigenmodes is built on all the periodic orbits of the system. Thus the one-to-one relationship shown in Fig. 10, between an eigenmode and a periodic orbit, has to be considered as an exception, since, as the number of p.o.'s proliferates exponentially with their lengths, eigenmodes must build upon many of them. The crucial role of p.o.'s had already been exemplified by the famous *trace*

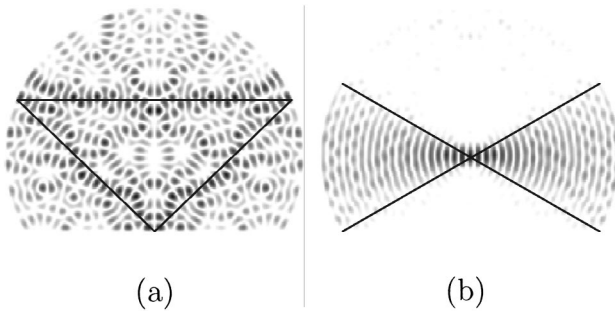


FIG. 10. Examples of eigenmodes displaying an intensity enhancement in the vicinity of (a) an unstable periodic orbit (superimposed as a solid line) and (b) the continuous family of diameters (boundaries shown as solid lines).

formula [36], which establishes the semiclassical expression of the density of states $n(\kappa) = dN/d\kappa$,

$$n_{sc}(\kappa) = n_0(\kappa) + \sum_p \ell_p w_p \exp(i \kappa \ell_p). \quad (35)$$

In the above equation, the sum is running over the periodic orbits, including multiple traversals, and ℓ_p is the total transverse length of orbit p . The quantity w_p encompasses a classical amplitude related to the stability of the orbit and a phase associated to caustics and reflections. The smooth part of the density (for the Dirichlet case) is given by the so-called Weyl formula [37]

$$n_0(\kappa) = \frac{S}{2\pi} \kappa - \frac{P}{4\pi}, \quad (36)$$

where P is the perimeter of the billiard and S is its surface. Note that the leading term of the above expression is directly obtained by differentiating Eq. (8). Considering the actual density of states $n(\kappa) = \sum_j \delta(\kappa - \kappa_j)$, Eq. (35) suggests that its Fourier transform provides a *length spectrum*, which dis-

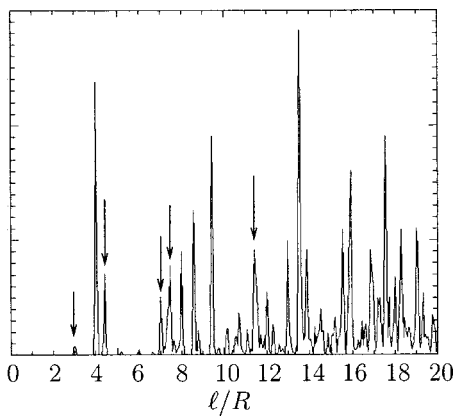


FIG. 11. The *length spectrum* or Fourier transform of the density of states $n(\kappa)$, for the eigenvalue problem (25) in the truncated chaotic billiard shown in Figs. 6 and 10. The *trace formula* permits us to show that the length spectrum should have peaks at the period lengths of the periodic orbits. Arrows indicate lengths corresponding to the periodic orbits shown in Fig. 12.

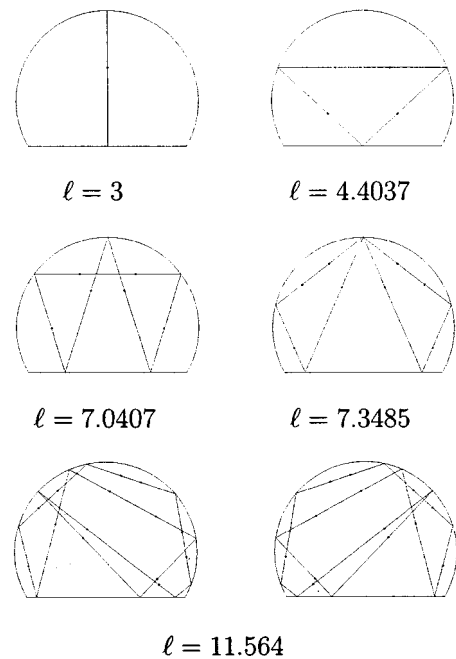


FIG. 12. A few periodic orbits whose periods correspond to peaks of the length spectrum shown in Fig. 11.

plays peaks located at the lengths of the p.o.'s. In Fig. 11, we show the length spectrum of the above considered billiard. A few orbits among the shortest are indicated by arrows and are displayed in Fig. 12. Remark that the vast majority of periodic orbits contribute to the generic ergodic behavior described in the previous section. Interestingly enough, formula (35) allows us to recover many of the predictions of RMT [38]. Nonetheless, the least unstable periodic orbits or the continuous family of diameters which survived the truncation, and constitute marginally unstable periodic orbits, are responsible for the non-Gaussian statistics of the eigenmodes shown in Fig. 10.

IV. EXPERIMENTS

A. Fiber design

The fiber designed and fabricated in our lab for the experiment is now briefly described. Its transverse section is a truncated disk (see Fig. 1): a silica bar of 1-cm diameter is cut and polished and the fiber is pulled at a temperature low enough to avoid smoothing of the edges. This process ensures a small roughness (a few nanometers) of the planar surface. Moreover, since we only use lengths of the order of 10 cm, a high translational invariance is achieved (less than 3% error on the fiber diameter). The final dimensions are 120 μm for the diameter of the disk and 90 μm for the truncated diameter (Fig. 13). The cladding is composed of 40% of a black silicon (Rhodorsil RTV 1523 A) and 60% of transparent silicon (Rhodorsil RTV 1523 B). We use a black silicon cladding in order to avoid propagation of light in the cladding which could complicate the far-field intensity pattern. The indices are, respectively, $n_{co} = 1.458$ in the core and $n_{cl} = 1.453$ in the cladding. To prevent mode coupling due to bends or stresses, we keep the fiber straight by embedding it

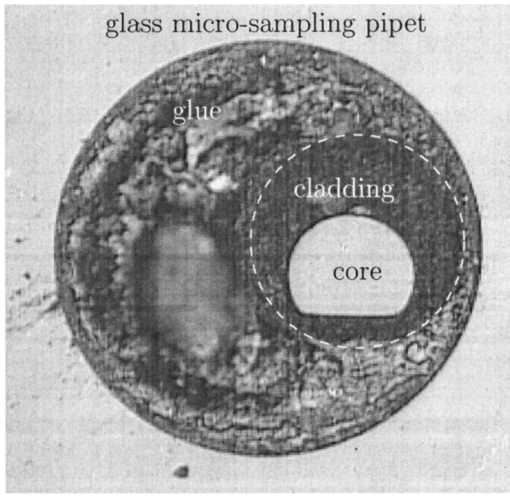


FIG. 13. Microscope observation of the transverse section of the fiber embedded in a glass microcapillary pipet.

in a glass microcapillary pipet. The set is kept together in a dural tube. A circular multimode fiber of 120- μm diameter with a black silicon cladding has been fabricated in the same way to compare spatial distributions of intensity for a chaotic and a regular billiardlike system.

B. Experimental setup

For our experiments, we use a He-Ne laser source ($\lambda = 632.8 \text{ nm}$) with output power of 1 mW. The experimental setup is illustrated in Fig. 14. The laser beam of 1-mm diameter is first spatially filtered and expanded to obtain a 5-mm-diam beam. As a result, the final diameter is large compared with the 120- μm -diam fiber so that the laser beam may be viewed as a plane wave. We also performed another type of illumination by using a $\times 10$ microscope objective to focus the filtered and expanded beam on the fiber input.

The key parameter of the experiment is the incident direction of the beam given by the angle θ_0 between the beam and the fiber axis (Fig. 15). The incident angle of the beam on the fiber input fixes the mean order of the excited modes by the way of the following simple relation:

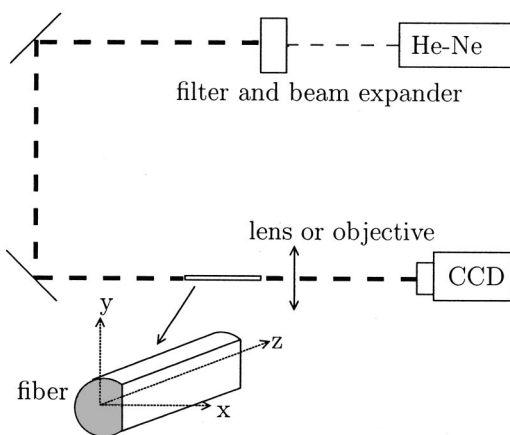


FIG. 14. Experimental setup.

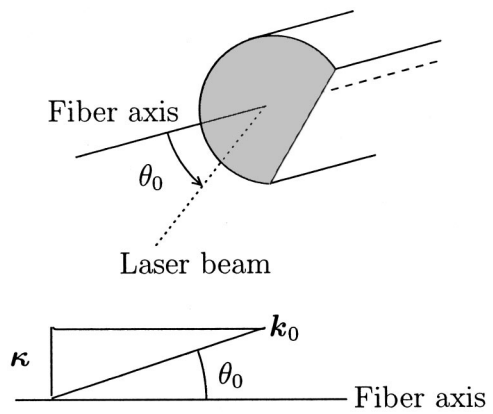


FIG. 15. Relation between the incident angle on the fiber and the transverse wave vector κ .

$$\kappa_c = k_0 \sin \theta_0, \quad (37)$$

where $k_0 = 2\pi/\lambda$. Indeed, it should be kept in mind that, even with an ideal plane wave, the propagating wave in the fiber is essentially decomposed over a certain number of guided modes whose eigenvalues are centered on κ_c .

For the detection, we use a Sony CCD Camera of 398×288 pixel size. The CCD is used in its most sensitive regime (between 0.6 μm and 0.7 μm). At the output of the fiber, we detect either the near-field intensity or the far-field intensity. The near-field intensity is obtained by imaging the fiber output with a $\times 20$ microscope objective, whereas the far-field intensity is observed in the focal plane of a 2-cm-focal-length lens in the detection cell. Figure 16 shows typical near-field (a) and far-field (b) experimental intensity patterns at the fiber output for a quasi-plane-wave illumination.

C. Analysis of experimental results

Here, we propose an analysis of our observations based on the random Gaussian character of eigenmodes in the D-shaped fiber. The patterns of Fig. 16 are associated to a superposition of eigenmodes for a value of the transverse wave number $\kappa_c R$ equal to 36. This value is deduced from the mean radius of the ring in the far-field intensity observation. The far-field intensity $\tilde{I}(\kappa, \Theta)$ is essentially the squared modulus of the spatial Fourier transform $T_F\{\psi(r)\}$ of the

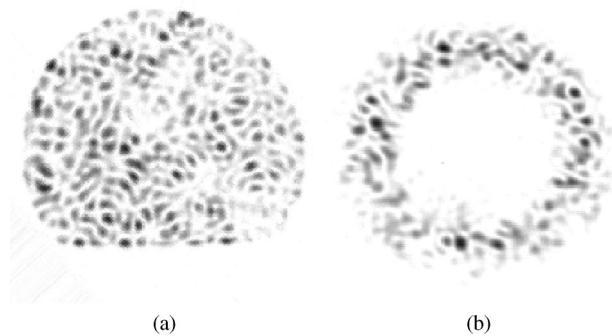


FIG. 16. (a) Experimental near-field and (b) far-field intensity patterns for $\kappa_c R \approx 36.0$ for a quasi-plane-wave illumination.

field at the output of the fiber. The width of the ring in Fig. 16(b) gives an estimate of the number of excited modes. In practice, this number is evaluated by assuming a Gaussian shape for the radial envelope of the far-field intensity. Its full width at half-maximum fixes the κ interval around κ_c and yields 175 modes. The ring width we observe is more important than what we can theoretically expect from a plane-wave illumination. It is mainly due to the initial excitation: we do not have a perfect plane wave at the fiber input, so that several modes are excited.

Thus, the complex field $\psi(\mathbf{r}, z)$ for a propagation length z reads

$$\psi(\mathbf{r}, z) = \sum_{n=1}^N a_n \phi_n(\mathbf{r}) \exp(-i\beta_n z), \quad (38)$$

where a_n is the weight of mode ϕ_n in the superposition, given by the projection of the initial condition on the eigenmodes basis $\{\phi_n\}$,

$$a_n = \int \int_S \phi_m^*(\mathbf{r}) \psi(\mathbf{r}, z=0) d\mathbf{r} / S \quad (39)$$

with S the surface of the transverse section of the fiber and β_n the propagation constant associated to ϕ_n . The section of the fiber we study presents a symmetry axis. The eigenmodes basis is therefore naturally decomposed into even- and odd-parity modes which correspond to two independent spectra [18].

Here we use a concept inspired from quantum mechanics: In close analogy with the Heisenberg time [39], the *Heisenberg length* is defined as

$$z_H = 2\pi/\Delta\beta, \quad (40)$$

where $\Delta\beta = 4\pi/(S\beta_{co})$ is the mean modal spacing for a given parity. Beyond this length, the guided modes can be considered as individually resolved leading to uncorrelated phases between modes in the decomposition (38). For a propagation length z longer than the Heisenberg length z_H , the products $a_n e^{-i\beta_n z}$ may be viewed as independent random variables. Indeed, this condition implies that the phase difference between two neighboring guided modes is greater than 2π . It is interesting to note that, in our system, the Heisenberg length

$$z_H = \frac{\beta_{co} S}{2} = n_{co} \frac{\pi S}{\lambda} \quad (41)$$

may be viewed as an *effective* Rayleigh length [40]. For a Gaussian laser beam propagating out of the waist w_0 , the Rayleigh length $z_R = \pi(w_0)^2/\lambda$ delineates the borderline between the Fresnel near-field and the Fraunhofer far-field regions. At distances large compared to the Rayleigh length, the full Fourier content of the laser beam is thus angularly resolved as are the individual modes fully resolved in our situation for distances large compared to the Heisenberg length.

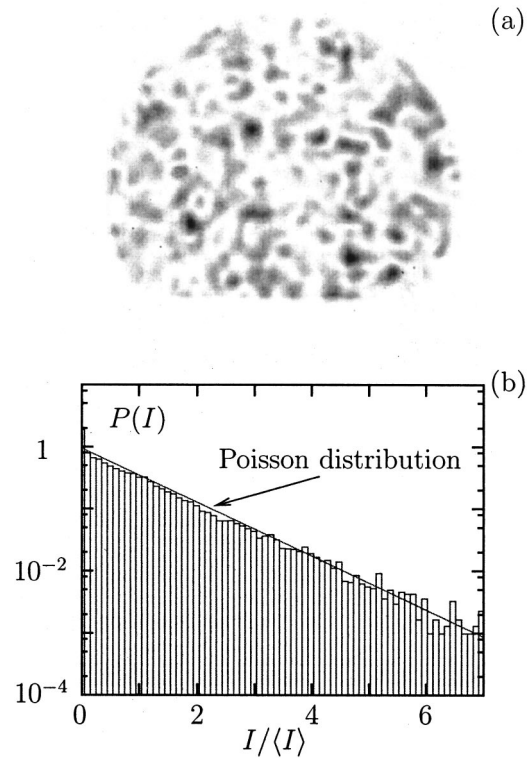


FIG. 17. (a) Mode superposition in the case of a focused excitation for the D-shaped fiber and (b) its intensity probability compared to the expected Poisson distribution.

Combining the expression (38) of the complex field with the previous assumption on the random behavior of the eigenmodes and of the terms $a_n \exp(-i\beta_n z)$, we deduce that the real and imaginary parts of the complex field $\psi(\mathbf{r}, z)$ are themselves independent random Gaussian variables. This cannot be verified from the experimental results because we do not have experimental measurements of the complex field in the fiber. Nevertheless, using this Gaussian analysis, we can derive a prediction for the behavior of the probability distribution of the intensity and thus compare it to the results deduced from the measured intensity.

If we separate the intensity of the field $I = |\psi|^2$ using the real and imaginary part of the field assumed to be equivalent independent random Gaussian variables, we can derive the expression of the intensity probability $P(I)dI$ from the joint probability distribution. Its evaluation leads to the Poisson distribution

$$P(I) = \exp(-I/\langle I \rangle) / \langle I \rangle. \quad (42)$$

Figure 17(b) illustrates the good agreement between the Poisson distribution issued from our Gaussian analysis and the intensity probability calculated from the measured near-field intensity of the superposition of modes presented in Fig. 17. The initial illumination is a focused beam with a $\times 10$ microscope objective. This experimental result agrees with our assumption on the Gaussian statistics of the eigenmodes of the truncated and chaotic fiber. A validation of this as-

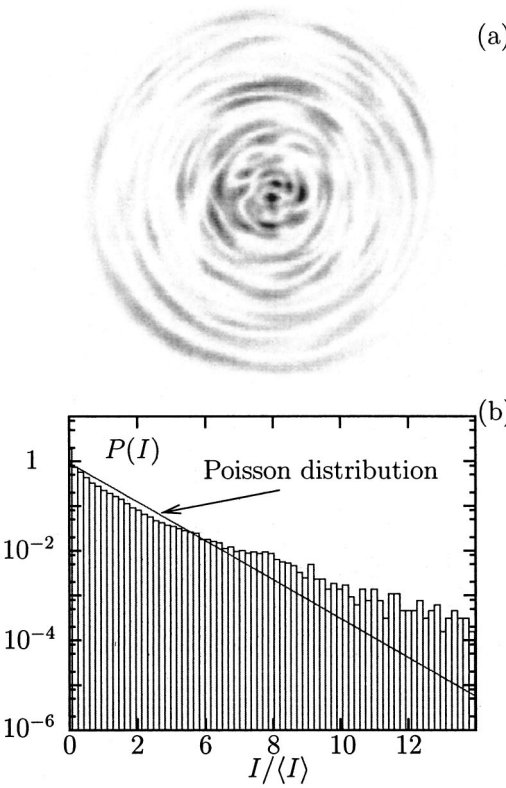


FIG. 18. (a) Mode superposition in the case of a focused excitation for the circular fiber and (b) its intensity probability compared to the Poisson distribution.

sumption will be provided by the investigations on the spatial autocorrelation functions which are much more sensitive to the nature of eigenmodes.

We now turn to compare this probability distribution to the one calculated for the near-field intensity pattern at the output of the circular fiber represented in Fig. 18(a) for a focused excitation by a $\times 10$ microscope objective. As seen before, we cannot use the Gaussian analysis to describe the behavior of the eigenmode of the circular fiber so that we do not expect a Poisson distribution for the intensity probability. In Fig. 18(b), we have plotted the intensity probability associated to the above intensity distribution. We can observe a large deviation from the Poisson distribution, thus confirming that the Gaussian analysis is only relevant for the description of chaotic systems.

We are now interested in evaluating the field autocorrelation function of a superposition of modes as measured in our experiment. Although the complex field at the fiber output cannot be measured directly, we deduce some of its properties from the far-field intensity. Indeed, the far-field intensity is proportional to the Fourier transform of the complex near field as the detector is placed in the focal plane of a lens.

The field autocorrelation function is deduced from the far-field intensity using the well-known Fourier transform relation

$$C_\psi(\mathbf{r}_0, z; \kappa_c) = \mathcal{T}_F^{-1}\{\tilde{I}(\kappa, \Theta)\}, \quad (43)$$

where (κ, Θ) are the coordinates of the far-field space.

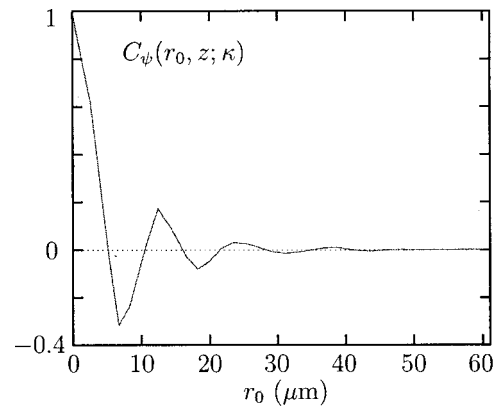


FIG. 19. The radial field autocorrelation function for $\kappa_c R \approx 30.0$ derived from the far-field intensity pattern of Fig. 16.

The autocorrelation function is thus obtained from the experimental observation by the way of a simple inverse Fourier transform performed on the far-field intensity. The radial function $C_\psi(r_0, z; \kappa_c)$ is then calculated from the vectorial function $C_\psi(\mathbf{r}_0, z; \kappa_c)$ using the angular integration (31) and is presented in Fig. 19. One should notice that the radial field autocorrelation still oscillates with a quasiperiod but quickly decreases as r_0 increases. It implies that long-range correlations within the complex field are reduced due to the superposition of several modes. As before, we use our Gaussian analysis to derive a prediction for the behavior of the field autocorrelation function for a superposition of modes. This analysis is original in the sense that we apply a modal approach to describe our experimental results.

The field autocorrelation function is defined as

$$C_\psi(\mathbf{r}_0, z; \kappa_c) = \langle \psi(\mathbf{r} + \mathbf{r}_0, z) \psi^*(\mathbf{r}, z) \rangle_r. \quad (44)$$

If one substitutes $\psi(\mathbf{r}, z)$ by its expression (38), the field autocorrelation function reads

$$\begin{aligned} C_\psi(\mathbf{r}_0, z; \kappa_c) &= \sum_{n,n'=1}^N \langle a_n a_n'^* \phi_n(\mathbf{r} + \mathbf{r}_0) \phi_n^*(\mathbf{r}) e^{-i\beta_n z} e^{i\beta_{n'} z} \rangle_r \\ &= \sum_{n=1}^N |a_n|^2 \langle \phi_n(\mathbf{r} + \mathbf{r}_0) \phi_n^*(\mathbf{r}) \rangle_r. \end{aligned} \quad (45)$$

The distinct eigenmodes are assumed to be statistically independent to derive the second expression. In relation (45) one can recognize the definition of the field autocorrelation function $C_\phi(\mathbf{r}_0; \kappa)$ [Eq. (32)] associated to an individual mode ϕ_n . Then, using the expression (28), we deduce the expression of the field autocorrelation function

$$C_\psi(\mathbf{r}_0, z; \kappa_c) = \sum_{n=1}^N |a_n|^2 J_0(\kappa_n r_0). \quad (46)$$

As a consequence, the Gaussian analysis yields a field autocorrelation function written as a weighted sum of zero-order

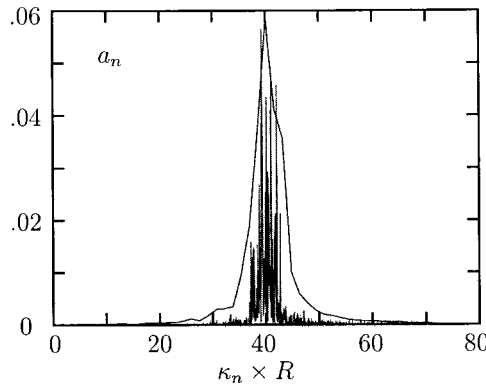


FIG. 20. Distribution of the coupling coefficients for a plane-wave illumination with $\kappa_0 R = 40.0$ and $\Theta = 17^\circ$.

Bessel functions evaluated at each value of κ_n . Expression (46) thus includes the contribution of each eigenmode of the superposition (38) to the field correlations.

To calculate the right-hand side of Eq. (46), one needs to know the value of the square $|a_n|^2$ of the coupling coefficients which are defined by the condition of illumination (39). Experimentally, these terms cannot be perfectly evaluated. Indeed, only a smoothed version $b(\kappa)$ can be deduced from the measured far-field intensity

$$b(\kappa) = \frac{1}{2\pi} \int_0^{2\pi} \tilde{I}(\kappa, \Theta) d\Theta, \quad (47)$$

Θ being the angular variable in the spatial frequencies space (κ_x, κ_y).

To each eigenmode ϕ_n corresponds a ring pattern in the far field with mean radius κ_n . The width of each ring is ideally determined by the finite size of the section of the fiber and fixes the scale over which the weighted density $\sum |a_n|^2 \delta(\kappa - \kappa_n)$ is smoothed to yield $b(k)$. Provided that the experimental resolution be sufficient, the evaluation of the $|a_n|^2$'s through $b(k)$ is thus intrinsically limited by diffraction. Nevertheless, we can numerically confirm the validity of our Gaussian analysis for the description of the field autocorrelation function using the calculated eigenmodes

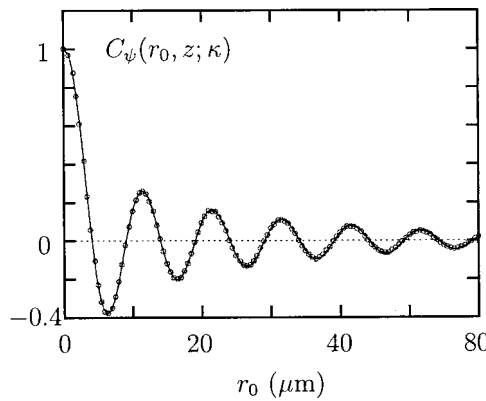


FIG. 21. Comparison between the experimental field autocorrelation function (circle) and the prediction derived from the Gaussian analysis (line).

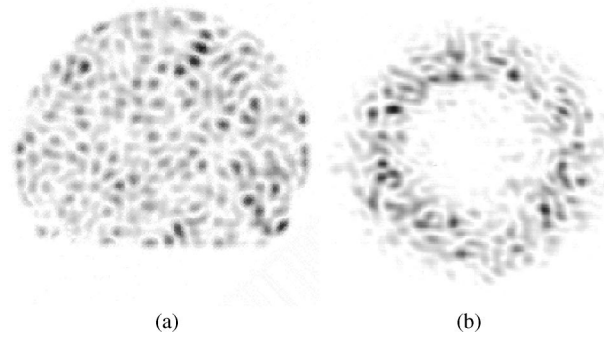


FIG. 22. (a) Near field and (b) far field at the output of a truncated fiber for $\kappa_c R \approx 29.0$.

(see Sec. III B). To do this, we project a plane wave $\exp(-i\kappa_0 \cdot \mathbf{r})$ for a given value of κ_0 on the basis of the eigenmodes and we propagate this initial condition along the fiber by multiplying each eigenmode ϕ_n by the phase factor in the paraxial approximation $\exp(-i\beta_n z) \approx \exp[-i(E_n/\beta_{co})z]$. The expression of the field for a given length of propagation z is thus given by the relation

$$\psi(\mathbf{r}, z) = \sum_{n=1}^N a_n \phi_n(\mathbf{r}) \exp\left(-i \frac{E_n}{\beta_{co}} z\right). \quad (48)$$

The coupling coefficients a_n are then derived from the projection of the initial condition $\exp(-i\kappa_0 \cdot \mathbf{r})$ on the eigenmodes basis $\{\phi_n\}$ (39). In Fig. 20, we have plotted the distribution of the coupling coefficients associated to a plane-wave illumination with $\kappa_0 R = 40$ ($\kappa_0 = |\kappa_0|$). The corresponding smooth $b(\kappa)$ is also shown to exemplify the diffraction limit.

One can note that the distribution of the coupling coefficients is centered on the initial condition $\kappa_c R = \kappa_0 R = 40$. Using the coupling coefficients, we can evaluate the prediction (46) deduced from the Gaussian analysis. In Fig. 21, we have represented the field autocorrelation function calculated from the far-field intensity (43) compared with the evaluation of the expression (46). The agreement between the two curves is excellent, thus validating the choice of our modal Gaussian approach.

Even though the Gaussian analysis of the experimental field autocorrelation function is intrinsically spoiled by dif-

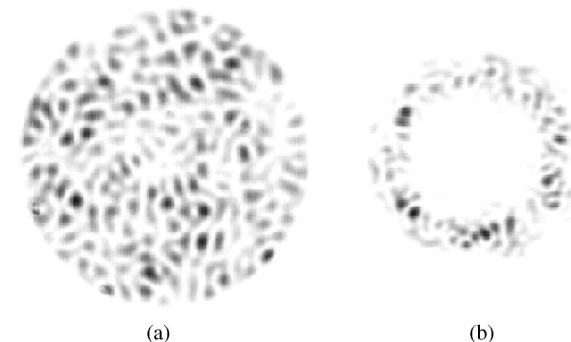


FIG. 23. (a) Near field and (b) far field at the output of a circular fiber for $\kappa_c R \approx 29.0$.

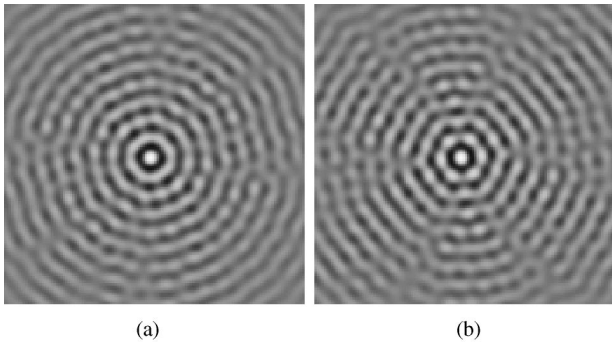


FIG. 24. Autocorrelation functions associated to filtered far fields (see text) for (a) the chaotic D-shaped fiber (far-field intensity patterns shown in Fig. 22) and (b) the regular circular fiber (Fig. 23). Note the hexagonal structure which is strongly marked near the origin in the nonergodic case.

fraction, one can nonetheless extract from it some information on the nature of the field. In particular, we can try to illustrate the essential difference in nature between the fields in the regular (circular) fiber and in the chaotic (truncated) fiber. We first consider the intensity patterns at the output of both fibers for a plane-wave illumination (Figs. 22 and 23). These intensity patterns correspond to the superposition of several modes around a central value of $\kappa_c R$ equal to 29. In order to extract the contribution to $C_{\psi}(\mathbf{r}_0, z; \kappa_c)$ of only a few eigenmodes, we perform a κ filtering by multiplying the far-field intensity pattern by a Gaussian ring. The width of the ring is fixed to $0.4/R$ (corresponding to the pixel size and approximately comprising nine modes) for both types of fiber (regular and chaotic) and its mean radius to $\kappa_c R \approx 29$. We then calculate the autocorrelation functions associated to these filtered far-field intensity patterns by performing an inverse Fourier transform (43). The resulting autocorrelation functions are presented in Fig. 24. One can clearly see the isotropic behavior of the autocorrelation function associated to the field in the D-shaped fiber [Fig. 24(a)]. Indeed, this behavior is the signature of the ergodic nature of the chaotic eigenmodes of this truncated fiber. On the contrary, in the case of the circular fiber [Fig. 24(b)], privileged directions of high correlations mark the autocorrelation function. This nonisotropy results from the spatial distribution of the regular eigenmodes of the circular fiber which are characterized by a finite and well-defined number of zeros in the radial and angular coordinates.

So far we have only considered the ergodic nature of the chaotic eigenmodes. Deviations from this generic behavior are nevertheless observed that can be related to specific periodic ray motion associated to the short least unstable orbits of the system, leading to the so-called scarring phenomenon. A *scared* eigenmode displays intensity enhancement along short periodic orbits (see Sec. III). The spatial localization of light induces strong correlations for both field and intensity and the resulting autocorrelation function exhibits strong anisotropy [16].

V. APPLICATION TO DOUBLE-CLAD FIBER AMPLIFIERS

Since the first appearance of erbium-doped fiber amplifiers (EDFA) in 1987, a novel way of using optical fibers has

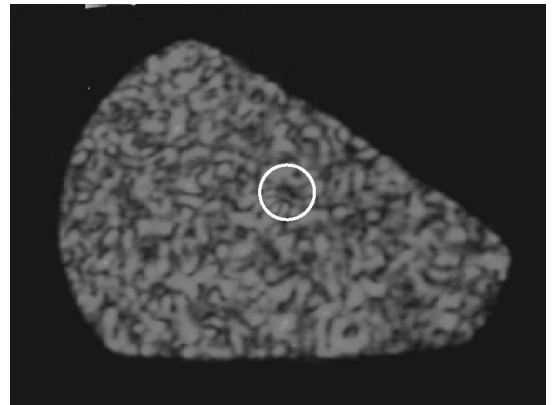


FIG. 25. Near-field intensity pattern at the output of a double-clad fiber with a doubly truncated inner cladding. The white circle delimits a chromium-doped core (IRCOM, Limoges).

proven its relevance and efficiency in optical telecommunications [41]. These EDFA's are now commonly used to restore optical signals in long-haul optical links. As applications in this domain require more and more powerful signals, high pump power levels are consequently needed. Double-clad fibers permit us to couple high pump power into the doped core. In these fibers, the doped amplifying single-mode (for the wavelength of the signal to be amplified) core is embedded in a multimode (for the pump wavelength) inner cladding where the pump is injected. Amplification is achieved by a transfer of the pump power from the inner cladding into the core as it propagates along the fiber. By using an inner cladding with the shape of a chaotic billiard, one may optimize the overlap of the pump field with the core along the propagation, thus reducing the differential modal absorption of the pump generally observed in standard circular double-clad fibers. Indeed, in a regular circular fiber, the overlap of guided modes varies widely from one mode to the other, thus leading to fluctuating transfer rates from the inner cladding into the core between modes. On the contrary, for the ergodic modes of a chaotic fiber, the overlap with the core region is essentially a constant. In a recent paper [42], we have proposed a quantitative theory for such an optimized pump absorption and provided numerical results in fair agreement with the predictions of our theory. The latter essentially relies on the fact that ergodic motion ensures a maximal and constant overlap of the pump intensity with the doped absorbing core along the fiber. We have also shown that suppression of marginally stable orbits can significantly improve the absorption characteristics of such double-clad EDFA's. Experimental demonstration of pump absorption optimization in a doubly truncated double-clad fiber has been recently achieved [43]. As an illustration, we show in Fig. 25 the experimental near-field intensity pattern of a chromium-doped double-clad fiber obtained by Ph. Leproux, Ph. Roy, J.-M. Blondy, and D. Pagnoux of the Guided and Integrated Optics group from Institut de Recherche en Communications Optiques (IRCOM) Limoges, France.

VI. CONCLUSION

In conclusion, we have provided the first complete theoretical and experimental characterization of wave intensity in

a chaotic multimode optical fiber in terms of spatial statistics and correlations. We have been able to confirm the validity of a Gaussian analysis for the statistics of the wave pattern in the speckle regime. Special attention was paid to the near-field autocorrelation function, which is obtained through the measurement of the far-field intensity, thus giving a dual way of characterizing the amount of randomness in the propagated field pattern. Starting from the above experiment, further progress is envisaged along the following directions: selective excitation of modes and parametric correlations in the frequency domain through the use of tunable laser sources.

This original experiment in multimode optical fibers provides interesting prospects to the applications of wave chaos concepts to modern technology as recently exemplified in

optical fiber amplifiers based on double-clad chaotic fibers [42]. Furthermore, multimode optical fibers have recently received renewed interest in the context of optical multiplexing in transmission systems [44]. The feasibility of such network applications strongly relies on a proper understanding of propagation of light in complex fibers. The present work aims to serve this objective.

ACKNOWLEDGMENTS

The authors gratefully acknowledge useful discussions with Eric Picholle and helpful numerical materials from Anne Vigouroux. It is a pleasure to thank Gérard Monnom and his team for the fabrication of the chaotic fiber.

-
- [1] A.J. Lichtenberg and M.A. Lieberman, *Regular and Stochastic Motion* (Springer-Verlag, New York, 1983).
 - [2] *Chaos and Quantum Physics*, edited by M.-J. Giannoni, A. Voros, and J. Zinn-Justin, Les Houches 89, Session LII (North-Holland, Amsterdam, 1991).
 - [3] A. Altland, C.R. Offer, and B.D. Simons, *Quantum Chaos: Lessons from Disordered Metals*, in *Supersymmetry and Trace Formulae: Chaos and Disorder*, edited by I.V. Lerner, J.P. Keating, and D.E. Khmelnitskii (Kluwer Academic, New York, 1999).
 - [4] *Mesoscopic Quantum Physics*, edited by A. Akkermans, G. Montambaux, J.-L. Pichard, and J. Zinn-Justin, Les Houches 94, Session LXI (North-Holland, Amsterdam, 1995).
 - [5] H.-J. Stöckmann, *Quantum Chaos: An Introduction* (Cambridge University Press, Cambridge, England, 1999).
 - [6] C.E. Porter, *Statistical Theories of Spectral Fluctuations* (Academic Press, New York, 1965).
 - [7] D. Delande, *Chaos in Atomic and Molecular Physics*, in *Chaos and Quantum Physics*, edited by M.-J. Giannoni, A. Voros, and J. Zinn-Justin, Les Houches 89, Session LII (North-Holland, Amsterdam, 1991).
 - [8] P.B. Wilkinson, T.M. Fromhold, L. Eaves, F.W. Sheard, N. Miura, and T. Takamasu, *Nature* (London) **380**, 608 (1996); L.P. Kouwenhoven, C.M. Marcus, P.L. McEuen, S. Tarucha, R.M. Westervelt, and N.S. Wingreen, *Electron Transport in Quantum Dots*, in *Proceedings of the Summer School on Mesoscopic Electron Transport* (Kluwer, Dordrecht, 1997).
 - [9] C.F. Bharucha, J.C. Robinson, F.L. Moore, B. Sundaram, Q. Niu, and M.G. Raizen, *Phys. Rev. E* **60**, 3881 (1999); D.A. Steck, W.H. Oskay, and M.G. Raizen, *Science* **293**, 274 (2001); W.K. Hensinger, H. Häffner, A. Browaeys, N.R. Heckenberg, K. Helmerson, C. McKenzie, G.J. Milburn, W.D. Phillips, S.L. Rolston, H. Rubinsztein-Dunlop, and B. Upcroft, *Nature* (London) **412**, 52 (2001).
 - [10] A. Kudrolli, M.C. Abraham, and J.P. Gollub, *Phys. Rev. E* **63**, 026208 (2001).
 - [11] R.L. Weaver, *J. Acoust. Soc. Am.* **85**, 1005 (1989); R.L. Weaver and O.I. Lobkis, *Phys. Rev. Lett.* **84**, 4942 (2000).
 - [12] J. de Rosny, A. Tourin, and M. Fink, *Phys. Rev. Lett.* **84**, 1693 (2000).
 - [13] S. Sridhar, *Phys. Rev. Lett.* **67**, 785 (1991); C. Dembowski, H.-D. Gräf, A. Heine, R. Hofferbert, H. Rehfeld, and A. Richter, *ibid.* **84**, 867 (2000); J. Stein, and H.-J. Stöckmann, *ibid.* **68**, 2867 (1992).
 - [14] J.U. Nöckel and A.D. Stone, *Nature* (London) **385**, 45 (1997).
 - [15] J. Krug, *Phys. Rev. Lett.* **59**, 2133 (1987); R.E. Prange and S. Fishman, *ibid.* **63**, 704 (1989); B. Fischer and A. Rosen, *Opt. Lett.* **24**, 1463 (1999).
 - [16] V. Doya, O. Legrand, F. Mortessagne, and Ch. Miniatura, *Phys. Rev. Lett.* **88**, 014102 (2002).
 - [17] A.W. Snyder and J.D. Love, *Optical Waveguide Theory* (Chapman and Hall, London, 1983).
 - [18] O. Bohigas, *Random Matrices and Chaotic Dynamics*, in *Chaos and Quantum Physics*, edited by M.-J. Giannoni, A. Voros, and J. Zinn-Justin, Les Houches 89, Session LII (North-Holland, Amsterdam, 1991).
 - [19] D. Gloge, *Appl. Opt.* **10**, 2252 (1971).
 - [20] S.S. Abdullaev, *Chaos and Dynamics of Rays in Waveguide Media* (Gordon and Breach Science Publishers, Amsterdam, 1993).
 - [21] L.A. Bunimovich, *Commun. Math. Phys.* **65**, 295 (1979).
 - [22] S. Ree and L.E. Reichl, *Phys. Rev. E* **60**, 1607 (1999).
 - [23] O. Bohigas, M.J. Giannoni, and Ch. Schmit, *Phys. Rev. Lett.* **52**, 1 (1984).
 - [24] J.B. Keller, *J. Opt. Soc. Am.* **52**, 116 (1962).
 - [25] The semiclassical limit $\kappa L \gg 1$ has to be consistent with the paraxial hypothesis which, for the fiber we use, amounts to $\kappa L \lesssim 50$.
 - [26] F. Mortessagne, O. Legrand, and D. Sornette, *Europhys. Lett.* **33**, 417 (1996).
 - [27] A. Voros, *Lect. Notes Phys.* **93**, 326 (1979).
 - [28] F. Haake, *Quantum Signatures of Chaos* (Springer-Verlag, Berlin Heidelberg, 1991).
 - [29] M.V. Berry, *Semiclassical mechanics of Regular and Irregular Motion*, in *Chaotic Behaviour of Deterministic Systems*, edited by R.H.G. Helleman and G. Ioss, Les Houches 82, Session XXXVI (North-Holland, Amsterdam, 1983).
 - [30] M. Srednicki and F. Stiernelof, *J. Phys. A* **29**, 5817 (1996).
 - [31] M.V. Berry, *J. Phys. A* **10**, 2083 (1977).
 - [32] J.W. Goodman, *Statistical Properties of Laser Speckle Pat-*

- terns, in *Laser Speckle and Related Phenomena*, edited by C. Dainty, Topics in Applied Physics Vol. 9 (Springer, Berlin, 1984).
- [33] E.J. Heller, *Wave Packet Dynamics and Quantum Chaology*, in *Chaos and Quantum Physics*, edited by M-J. Giannoni, A. Voros, and J. Zinn-Justin, Les Houches 89, Session LII (North-Holland, Amsterdam, 1991).
- [34] B.E.A. Saleh and M.C. Teich, *Fundamentals of Photonics* (John Wiley & Sons, New York, 1991).
- [35] E. Bogomolny, Physica D **31**, 169 (1988).
- [36] M.C. Gutzwiller, *Chaos in Classical and Quantum Mechanics* (Springer-Verlag, New-York, 1990).
- [37] R. Balian and C. Bloch, Ann. Phys. (N.Y.) **63**, 582 (1971).
- [38] M.V. Berry, *Some Quantum-To-Classical Asymptotics*, in *Chaos and Quantum Physics*, edited by M-J. Giannoni, A. Voros, and J. Zinn-Justin, Les Houches 89, Session LII (North-Holland, Amsterdam, 1991).
- [39] D. Delande, *The Semiclassical Approach for Chaotic Systems, in Waves and Imaging through Complex Media*, edited by P. Sebbah (Kluwer Academic Publisher, Dordrecht, 2001).
- [40] A.E. Siegman, *Lasers* (University Science Books, Mill Valley, 1986), p. 668.
- [41] E. Desurvire, *Erbium Doped Fiber Amplifiers* (Wiley Interscience, New York, 1994).
- [42] V. Doya, O. Legrand, and F. Mortessagne, Opt. Lett. **26**, 872 (2001).
- [43] Ph. Leproux, Ph.D. dissertation, Université de Limoges, France, 2001.
- [44] H.R. Stuart, Science **289**, 281 (2000).

C. Light scarring in an optical fiber, Physical Review Letters 88, 014102 (2002)

Depuis leur découverte en 1984 par Eric Heller², les scars demeurent des objets toujours aussi fascinants. Ces vilaines « balafres » dans le paysage quasi étale des modes d'une cavité chaotique, par le biais desquelles font soudain irruption quelques orbites périodiques instables, ont en effet de quoi surprendre. La fascination qu'ils exercent tient certainement aussi beaucoup à l'acharnement qu'ils mettent à résister à une description théorique unique³, sans parler de leur statut mathématique très incertain⁴.

Nous n'avons pas échappé au pouvoir de séduction des scars. Bien au contraire, cette lettre est le fruit de mois d'efforts constants pour améliorer le dispositif expérimental présenté dans l'article précédent, et notamment la technique d'illumination de la fibre. Et pour la première fois une fibre optique montre ses cicatrices ! Bien sûr, abstraction faite des échelles caractéristiques et des longueurs d'onde très différentes, le passage de la figure 1 (a) à la figure 1 (b) peut s'observer, par exemple, dans une cavité micro-ondes. En revanche, on peut à nouveau souligner l'originalité apportée par la mesure de l'intensité en champ lointain. Que ce soit dans l'observation directe de la brisure d'ergodicité (figures 1 (b) et 3 (b)) ou dans l'apparition nette d'une direction privilégiée de propagation dans les auto-corrélations spatiales du champ proche (figures 2 et 4).

² E. J. Heller, Phys. Rev. Lett. **53**, 1515 (1984).

³ E.B. Bogomolny, Physica D **31**, 169 (1988); M.V. Berry, Proc R. Soc. Lond. Ser. A **423**, 219 (1989); O. Agam, S. Fishman, Phys. Rev. Lett. **73**, 806 (1994); L. Kaplan, E.J. Heller, Phys. Rev. E **59**, 6609 (1999).

⁴ Voir, par exemple, dans la littérature récente : E. Lindenstrauss, Ann. of Math. **163**, 165 (2006); F. Faure, S. Nonnenmacher, and S. De Bievre, Commun. Math. Phys. **239**, 449 (2003); F. Faure and S. Nonnenmacher, Commun. Math. Phys. **245**, 201 (2004).

Light Scarring in an Optical Fiber

Valérie Doya, Olivier Legrand, and Fabrice Mortessagne

Laboratoire de Physique de la Matière Condensée, CNRS UMR 6622, Université de Nice Sophia-Antipolis, 06108 Nice, France

Christian Miniatura

Laboratoire Ondes et Désordre, CNRS FRE 2302, 1361 route des Lucioles, Sophia-Antipolis, F-06560 Valbonne, France

(Received 31 July 2001; published 18 December 2001)

We report the first experimental study of wave scarring in an optical fiber with a noncircular cross section. This optical multimode fiber serves as a powerful tool to image waves in a system where light rays exhibit a chaotic dynamics. Far-field intensity measurements are used to provide a better identification of scars in the Fourier domain. This first experimental characterization of scarring effect in optics demonstrates the relevance of such an optical waveguide for novel experiments in wave chaos.

DOI: 10.1103/PhysRevLett.88.014102

PACS numbers: 05.45.Mt, 42.81.-i

Classical fields (electromagnetic, acoustic, etc.) or quantum amplitude probabilities share the same interesting statistical features when, in the corresponding geometrical or classical limits, the dynamics of rays or trajectories exhibit chaos [1]. In recent years, *wave chaos* in non-quantal wave experiments [1] has provided a productive alternative to mostly theoretical studies in *quantum chaos*. In wave cavities for which the limit of rays exhibits chaos, wave function statistics is generally expected to follow the predictions of random matrix theory. According to this theory, wave functions are uniformly distributed over the whole available phase space which is ergodically explored by the rays, thus locally resulting in a random superposition of plane waves [2]. Nonetheless, some eigenmodes of classically chaotic systems are known to show anomalous enhancement of intensity along weakly unstable periodic orbits, a phenomenon called scarring [3,4]. This concentration is particularly counterintuitive since chaotic motion of rays should lead to rapid spreading of any localized initial wave packet. Semiclassical theories of scars were proposed by Heller [3], and also by Bogomolny [5] or Berry [6], which rely on linearized dynamics in the vicinity of unstable periodic orbits. While generically the long time evolution yields a specklelike field characterized by the well-known isotropic autocorrelation function [2,7], scarring introduces strong anisotropy which is related to localization not only in configuration space but also in momentum space.

Two alternative approaches are generally considered to study the influence of short unstable periodic orbits on wave statistics in chaotic wave cavities. One is dynamical as it is based on the evolution of wave packets launched along periodic orbits [4,8] while the other is devoted to the analysis of individual scarred eigenstates [3]. In this Letter, we demonstrate that multimode optical waveguides are particularly well adapted to a quantitative analysis of scarring since they naturally provide a connection between both approaches. To this aim, we have designed and fabricated a multimode optical fiber with a noncircular cross section for which it has been proven that the transverse

motion of rays is chaotic in the strongest sense [9]. The propagation along the fiber is the optical analog of wave function evolution in a quantum billiard. By properly illuminating the input of the fiber, we are therefore able to control the initial condition.

The fiber we use has the D-shaped cross section that can be seen in Fig. 1(a). The multimode core of this fiber has a $2R = 127 \mu\text{m}$ diameter and is made of pure silica with index $n_{\text{co}} = 1.458$ surrounded by a cladding composed of mixed silicon elastomers (40% Rhodorstyl RTV 1523A, 60% Rhodorstyl RTV 1523B including a black dye in order to avoid propagation in the cladding) with index $n_{\text{clad}} = 1.453$, thus implying weak guidance. The largest width perpendicular to the flat part is $107 \mu\text{m}$. The transverse shape of the fiber may be considered as invariant along its length, which is 8.5 cm for the results presented below. This fiber was fabricated in LPMC [10] according to an original protocol. A centimeter-sized silica rod is first cut and polished to obtain the D-shaped transverse section. Then a homothetic fiber is obtained by pulling the rod at a sufficiently low temperature. The fiber is rigidly maintained along its axis to preserve it from any strain

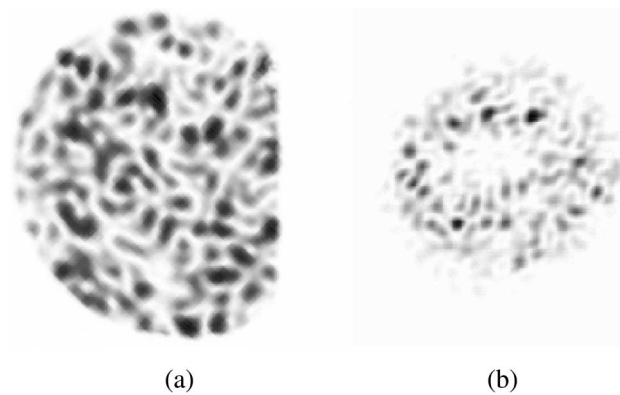


FIG. 1. Typical specklelike experimental intensity pattern at the output of a chaotic D-shaped fiber for a plane wave illumination at central wave vector $\kappa_c = 19.0R^{-1}$. (a) Near-field intensity; (b) far-field intensity.

or bending. With the above-mentioned technical features under control, we have checked that our fiber fairly well preserves the polarization of the input illumination, thus enabling us to use a scalar model for the optical propagation. For negligible bending, the dynamics of rays in the fiber may be restricted to the two-dimensional (2D) motion in the transverse section, the coordinate along the axis playing the role of time in analogous quantum billiard systems.

We denote by z the position along the axis and by \mathbf{r} the position in the transverse plane. Using the translational invariance $n(\mathbf{r}, z) = n(\mathbf{r})$, the scalar three-dimensional Helmholtz stationary equation,

$$(\Delta_{\perp} + \partial_{zz})\psi(\mathbf{r}, z) + n^2(\mathbf{r})k_0^2\psi(\mathbf{r}, z) = 0, \quad (1)$$

where Δ_{\perp} is the transverse Laplacian and $k_0 = 2\pi/\lambda$ (λ is the vacuum wavelength of the source), can be reduced to a stationary Schrödinger equation,

$$[-\frac{1}{2}\Delta_{\perp} + V(\mathbf{r})]\phi = E\phi, \quad (2)$$

where ϕ is given by $\psi(\mathbf{r}, z) = \int d\beta \phi(\mathbf{r}; \beta)e^{i\beta z}$, the potential $V(\mathbf{r}) = [\beta_{co}^2 - n^2(\mathbf{r})k_0^2]/2$ with $\beta_{co} \equiv n_{co}k_0$, and the “eigenenergy” $E = \frac{1}{2}(\beta_{co}^2 - \beta^2)$ which takes on discrete values E_n associated to guided modes ϕ_n .

Any guided solution $\psi(\mathbf{r}, z)$ of Eq. (1) can be decomposed on the basis generated by the eigenstates ϕ_n of the Schrödinger equation (2) and reads

$$\begin{aligned} \psi(\mathbf{r}, z) &= \sum_n c_n \phi_n(\mathbf{r}) \exp(i\beta_n z) \\ &= \sum_n c_n \phi_n(\mathbf{r}) \exp(i\sqrt{\beta_{co}^2 - 2E_n} z). \end{aligned} \quad (3)$$

A He-Ne linearly polarized laser beam ($\lambda = 632.8$ nm) is focused through a microscope lens and the fiber intercepts the diverging beam at a large distance (a few centimeters) from the focus. Hence, due to the small transverse size of the fiber, the illumination at the input is, to a good approximation, equivalent to a plane wave. By translating the microscope lens, we select a particular wave vector which is decomposed into its component along the longitudinal axis of the fiber and the orthogonal component. The modulus κ_c of the latter transverse component fixes the central “energy” $E_c = \kappa_c^2/2$ of the superposition of modes injected into the fiber. We then have two complementary ways of measuring light at the output of the fiber: either by imaging the near-field intensity at the output surface [see Fig. 1(a)], or by producing the far-field intensity pattern obtained in the focal plane of a lens [see Fig. 1(b)]. In either case, we use a 398×288 pixels CCD camera to capture eight-bit encoded pictures. In Fig. 1, a typical specklelike pattern is shown, that is obtained for a central value of $\kappa_c \approx 19.0R^{-1}$. The corresponding far-field intensity shown in Fig. 1(b) has the typical shape of a ring whose mean radius is given by κ_c and width is related to the number of modes, which dominate the decomposition

of the input illumination. Note that a ring with a similar speckled structure would be observed if one could excite a single mode. For a value of $\kappa_c \approx 19R^{-1}$, the transverse broadening due to diffraction by the finite aperture of the fiber has a width $\delta\kappa \approx \pi/R$, which corresponds to a number of modes,

$$\delta N = (S/2\pi)\kappa_c \delta\kappa, \quad (4)$$

of the order of 30, where S is the area of the core. The observation of a ring, which is a little broader than the above estimate, is due to slight departures from a plane wave input. Another important point concerning the possible impact of the source linewidth is in order. If we could illuminate the fiber with an ideal plane wave, the linewidth (1.5 GHz) is not broad enough to introduce any uncertainty about which mode is predominantly excited. This justifies the monochromatic assumption made above. We should also remark that the guided modes with the highest values of κ correspond to $\kappa_{max} = \sqrt{n_{co}^2 - n_{clad}^2} k_0 \approx 76R^{-1}$. Hence, the modes contributing to the patterns shown in Fig. 1 are *low-lying* modes, and a possible contribution of leaky modes can be ignored, as assumed in Eq. (3).

One of the key predictions concerning the ergodic modes of chaotic billiards is the isotropic field autocorrelation function, given by the zero-order Bessel function [2,11],

$$\langle \phi_n^*(\mathbf{r} + \mathbf{s})\phi_n(\mathbf{r}) \rangle = J_0(\kappa_n s). \quad (5)$$

In this Letter, the average $\langle \dots \rangle$ in Eq. (5) is to be understood as a spatial average over \mathbf{r} . Since we are not able to measure the complete optical near field (amplitude and phase), we use the far-field intensity, which essentially is the spatial 2D Fourier transform (FT) of the near-field autocorrelation function. Hence, in practice, we just perform an inverse FT of the far-field data to obtain the field autocorrelation function. In the case of Fig. 1, the 2D field autocorrelation is shown in Fig. 2. Its isotropy is clearly seen—contour lines roughly form circles—but it cannot be directly compared to Eq. (5) since it results from the superposition of modes over a finite range of κ values about κ_c , thus yielding an autocorrelation function, which decreases faster than the single $J_0(\kappa_c s)$. Indeed, it is easily shown that, for a field given by expression (3), where each mode is supposed to satisfy Eq. (5) and where statistical independence of distinct modes is assumed, the autocorrelation function reads [7]

$$\langle \psi^*(\mathbf{r} + \mathbf{s})\psi(\mathbf{r}) \rangle = \sum_n |c_n|^2 J_0(\kappa_n s). \quad (6)$$

This prediction does not include the smoothening due to the finite aperture of the fiber, which makes the retrieval of the c_n coefficients from the experimental data a nontrivial task. Indeed, it may be shown that each mode of the superposition will produce a far-field pattern located on a ring with a diffraction limited resolution, therefore mixing more and more contributions from modes as higher and higher values of κ are considered.

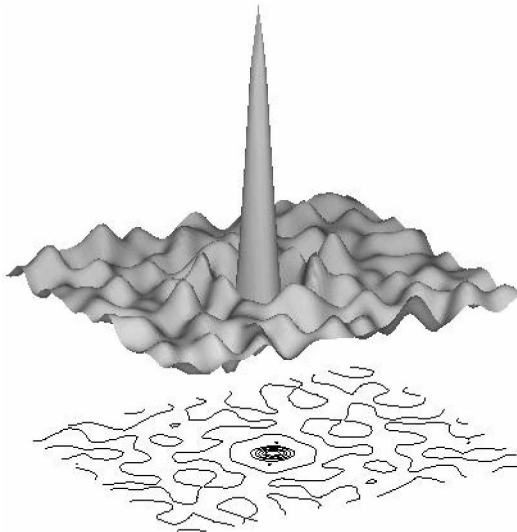


FIG. 2. Near-field autocorrelation function in the case of the specklelike pattern of Fig. 1, calculated through the inverse Fourier transform of the far-field intensity. An isotropic Bessel-like behavior is observed as evidenced by the displayed contour lines.

We have nevertheless evaluated these coefficients through the numerical simulation of a paraxial approximation of Eq. (1). Indeed, it can be shown that this approximation is valid in our experimental context [7]. We have thus successfully tested the validity of prediction (6) even in the case of an initial condition consisting of very few modes [7]. Here, it should be noted that the effective length of the fiber under study is of the order of the so-called Heisenberg length $z_H = \beta S$ where $\beta \approx \beta_{\text{co}}$. Beyond this length, the guided modes can be considered as individually resolved leading to uncorrelated phases between modes in the decomposition (3). In this regime, a semiclassical or eikonal approximation is no longer expected to describe the system properly.

To obtain a scarring effect in this fiber, the best choice is to start with an initial condition consisting of a wave packet along the shortest, least unstable periodic orbit in the D-shaped billiard, namely, the two-bounce orbit (2BO) perpendicular to the cut [see the dashed line in Fig. 3(a)]. This wave packet should also be centered on a transverse wave vector with a modulus κ_c such that a Bohr-Sommerfeld-type condition be fulfilled:

$$\kappa_c L - \delta\varphi - \frac{\pi}{2} = 2p\pi, \quad (7)$$

where L is the transverse period length of the 2BO, and $\delta\varphi$ is the dephasing due to reflections at the discontinuities of the optical index (essentially π at each reflection for the lowest lying modes) and p is an integer. Expression (7) may alternatively be viewed as a resonance condition for an unstable Fabry-Perot resonator [12]. The 2BO also has the advantage of lying on the symmetry axis of the fiber so that any initial condition being even with respect to this

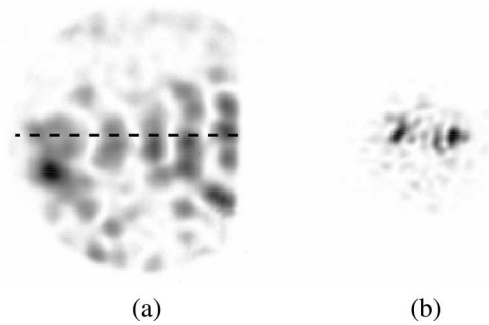


FIG. 3. Scar pattern for a plane wave illumination at central wave vector $\kappa_c = 11.4R^{-1}$ along the 2BO (see text): (a) Near-field intensity, (b) far-field intensity.

axis will select only even guided modes. In Fig. 3(a), a scarred pattern is shown that is obtained with a plane wave illumination centered on $\kappa_c = 11.4R^{-1}$, the incident wave vector lying within the symmetry plane of the fiber. The observed value of κ_c corresponds to a value $p = 5$ in the quantization formula (7). This is confirmed by comparison with the result of a numerical simulation of the propagation of an exact plane wave illumination with the exact value of κ given by Eq. (7) for $p = 5$, accounting for the exact value of $\delta\varphi$ [12]. It is recalled that the length of our fiber is much larger than the length corresponding to the first classical recurrences along the 2BO and practically of the order of the Heisenberg length, implying that the observed effect cannot simply be accounted for by a (semiclassical) ray-based approach. In the far field, two spots are clearly seen [Fig. 3(b)], which are related to two opposite wave vectors building the sinelike pattern. One should remark here that this pattern is still the result of a superposition of modes, among which one has strongly enhanced intensity in the vicinity of the 2BO. This localization in the Fourier domain was first recognized in a numerical study of acoustic radiation from membranes by Sornette and Delande in the case of a narrow band excitation [13].

Another strong evidence for scarring in this case is obtained by considering the autocorrelation function calculated through the inverse FT of the far-field intensity shown in Fig. 3(b). It is shown in Fig. 4 where the single direction oriented pattern is clearly evidenced and bears no resemblance with the ergodic prediction (6). One should still be careful to note that a 2D view such as the one in Figs. 2 and 4 is absolutely necessary to discriminate between ergodic and scar behaviors. Indeed, when integrating the autocorrelation function shown in Fig. 4 over the polar angle, one recovers a function of the radial distance in striking accord with $J_0(\kappa_c s)$, as it should from the very definition of the zero-order Bessel function itself [14].

Scars have already been observed experimentally in microwave experiments [15], capillary or Faraday waves [16,17]. However, to our knowledge, they have always been concerned with the evidence of wave enhancement in patterns obtained through a continuous forcing of the

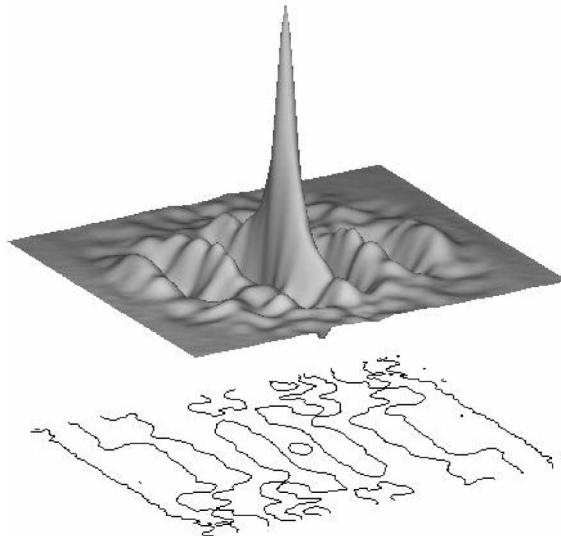


FIG. 4. Near-field autocorrelation function in the case of the scar pattern of Fig. 3, calculated through the inverse Fourier transform of the far-field intensity.

system at a given frequency. Our experiment in a multimode optical fiber is the first experiment to exhibit the scar phenomenon as resulting from an initial condition, thereby establishing a link with the dynamical approach of scars [4,8]. Moreover, the types of measurements involved in this experiment allow a dual characterization of scarring, which results from amplitude localization in the neighborhood of periodic orbits both in the configuration and momentum spaces. By an appropriate input illumination concentrated on a few guided modes, we are able to observe this localization in the near-field and far-field patterns and to identify the order of the quantization condition (7). This new kind of experiment in multimode optical fibers also has the advantage of bringing together quantum chaos and applied modern technology, as recently illustrated in optical amplifiers based on chaotic double-clad fibers [18].

The authors gratefully acknowledge useful discussions with Dominique Delande and helpful numerical materials from Anne Vigouroux.

- [1] H.-J. Stöckmann, *Quantum Chaos: An Introduction* (Cambridge University Press, Cambridge, England, 1999).
- [2] M. V. Berry, J. Phys. A **10**, 2083 (1977).
- [3] E. J. Heller, Phys. Rev. Lett. **53**, 1515 (1984).
- [4] L. Kaplan, Phys. Rev. Lett. **80**, 2582 (1998).
- [5] E. B. Bogomolny, Physica (Amsterdam) **31D**, 169 (1988).
- [6] M. V. Berry, Proc. R. Soc. London A **423**, 219 (1989).
- [7] V. Doya, O. Legrand, F. Mortessagne, and Ch. Miniatura (to be published).
- [8] L. Kaplan and E. J. Heller, Phys. Rev. E **59**, 6609 (1999).
- [9] L. A. Bunimovich, Commun. Math. Phys. **65**, 295 (1979); S. Ree and L. E. Reichl, Phys. Rev. E **60**, 1607 (1999).
- [10] Laboratoire de Physique de la Matière Condensée, CNRS UMR 6622, Université de Nice Sophia-Antipolis, 06108 Nice, France. It is a pleasure to thank Gérard Monnom and his team for the fabrication of the chaotic fiber.
- [11] M. Srednicki, Phys. Rev. E **54**, 954 (1996).
- [12] V. Doya, Ph.D. dissertation, Université de Nice-Sophia Antipolis, Nice, France, 2000.
- [13] D. Delande and D. Sornette, J. Acoust. Soc. Am. **101**, 1793 (1997).
- [14] M. Abramovitz and I. A. Stegun, *Handbook of Mathematical Functions* (Dover, London, 1965).
- [15] J. Stein and H.-J. Stöckmann, Phys. Rev. Lett. **68**, 2867 (1992); S. Sridhar and E. J. Heller, Phys. Rev. A **46**, R1728 (1992); A. Kudrolli, V. Kidambi, and S. Sridhar, Phys. Rev. Lett. **75**, 822 (1995).
- [16] R. Blümel, I. H. Davidson, W. P. Reinhardt, H. Lin, and M. Sharnoff, Phys. Rev. A **45**, 2641 (1992).
- [17] A. Kudrolli, M. C. Abraham, and J. P. Gollub, Phys. Rev. E **63**, 026208 (2001).
- [18] V. Doya, O. Legrand, and F. Mortessagne, Opt. Lett. **26**, 872 (2001).

D. Optimized absorption in a chaotic double-clad fiber amplifier, Optics Letters 26, 872 (2001)

Dans cette lettre, nous tentons de promouvoir une approche « chaos ondulatoire » du très concret problème de l'amélioration des performances d'un amplificateur tout-optique fibré. Schématiquement, ces amplificateurs sont constitués de deux fibres concentriques de diamètres et de compositions très différents ; la plus interne, d'un diamètre typique de moins de 10 microns, guide le « signal » telecom ; l'externe, d'un diamètre de l'ordre de 100 microns, propage le signal de « pompe », qui cède son énergie au signal via le milieu à gain qui constitue la fibre interne. Le message principal de cet article est synthétisé dans la figure 2 : l'efficacité de l'absorption de l'énergie de la pompe est très nettement améliorée par la géométrie de plus en plus chaotique du cœur externe. Ces résultats numériques ont été confirmés expérimentalement grâce à une collaboration avec l'IRCOM de Limoges⁵ ; La figure 25 de l'article présenté en II.B est issue de cette collaboration.

Au cœur du raisonnement développé dans cet article, on trouve la loi de Sabine : loi empirique qui prédit une décroissance exponentielle de l'énergie sonore dans une salle ! Son invocation ici (via les références 9 et 15) n'est pas incongrue car mon travail de thèse l'avait très clairement analysée en termes de chaos, classique et quantique – on ne parlait pas encore de chaos ondulatoire. Quel lien avec un problème de décroissance de l'énergie lumineuse dans une fibre ? Dans les deux cas il s'agit d'un problème de propagation d'ondes dans un milieu complexe, présentant, *mutatis mutandis*, de fortes analogies.

⁵ P. Leproux, V. Doya, P. Roy, D. Pagnoux, O. Legrand, and F. Mortessagne, Opt. Commun. **218**, 249 (2003).

Optimized absorption in a chaotic double-clad fiber amplifier

Valérie Doya, Olivier Legrand, and Fabrice Mortessagne

Laboratoire de Physique de la Matière Condensée, Centre National de la Recherche Scientifique Unité Mixte de Recherche 6622,
Université de Nice Sophia-Antipolis, Parc Valrose, 06108 Nice, France

Received January 29, 2001

Double-clad fibers with a doped single-mode core and a noncylindrical multimode chaotic cladding are shown to provide optimal pump-power absorption in power amplifiers. Based on the chaotic dynamics of rays in such fibers, we propose a quantitative theory for the pump-absorption ratio and favorably compare the predictions of the theory with numerical results obtained through an adapted beam-propagation scheme. © 2001 Optical Society of America

OCIS codes: 030.6140, 060.2320, 080.2740, 250.4480.

Optical fiber amplifiers, and more specifically erbium-doped fiber amplifiers (EDFAs), are now commonly used to restore optical signals in long-haul optical links.¹ To overcome the difficulty of coupling high pump power into the doped core, Snitzer *et al.* proposed the widely applied solution of double-clad fibers (DCFs).² In DCF amplifiers, a high saturation power requires strong pump power. To decrease the required amount of pump power, one needs to optimize the shape of the inner cladding. Design optimization has clearly established that the standard circular geometry cannot provide very high absorption efficiency,^{2,3} as exemplified by DCFs with eccentric cores⁴ or rectangular inner claddings.⁵ Yet, to our knowledge, a systematic tool of analysis for predicting the absorption characteristics of nonstandard double-clad geometries is not currently available. The inner cladding can be viewed as an external multimode fiber, and recently, for what is believed to be the first time, nonstandard multimode fibers were investigated,⁶ both theoretically and experimentally, within the framework of wave chaos,⁷ which provides powerful novel tools for their analysis. This original approach has been quite successful in adding to the understanding of the semiclassical properties of waves in bounded systems, such as microwave cavities,⁷ elastic waves in thin plates or blocks,⁸ or sound in rooms,⁹ in which the ray dynamics is generically chaotic. Multimode optical fibers provide ideal experimental systems for investigating the spatial properties of the diffuse field induced by chaotic ray dynamics.⁶ We also believe that, with the help of wave chaos techniques, more-efficient devices can be designed.

In this Letter we propose to show how pump-power absorption in double-clad EDFAs can be optimized by resort to the chaotic two-dimensional (2-D) motion of rays when they are projected onto the transverse section of the fiber. Indeed, in the case of a chaotic ray dynamics, the uniformity and isotropy of the diffuse field can be established. From these we deduce a theoretical prediction of the pump decrease, which is found to rapidly become uniform along the fiber. This prediction is then successfully tested against the results of numerical simulations of the true wave character of light propagation, performed through an

adapted beam-propagation scheme including absorption within the doped core via a complex nonlinear index. Through the use of wave chaos concepts we identify parameters relevant to optimized pump-power absorption.

2-D closed systems in which rays propagate are known as billiards. In a billiard with the shape of a truncated disk (a D-shaped billiard), the dynamics of rays has been shown to be fully chaotic in the strongest sense¹⁰ (i.e., with exponential sensitivity to initial rays' coordinates and directions). This particular billiard belongs to the family of chaotic focusing billiards studied by Bunimovich.¹¹ The geometrical limit of the transverse motion of rays in a multimode fiber is a billiard problem. In a D-shaped multimode fiber, the ray dynamics will therefore be chaotic. As an illustration, Fig. 1(a) shows a typical single ray trajectory projected onto the transverse section, which tends to visit any part of the section after a long enough propagation length. In this situation the theory of chaotic billiards establishes that a typical ray trajectory tends to cover the whole available phase space¹² (i.e., position and direction) uniformly without building caustics, which are generally found in regularly shaped waveguides. This property led Berry¹³ to conjecture that, in chaotic wave cavities, almost all modes

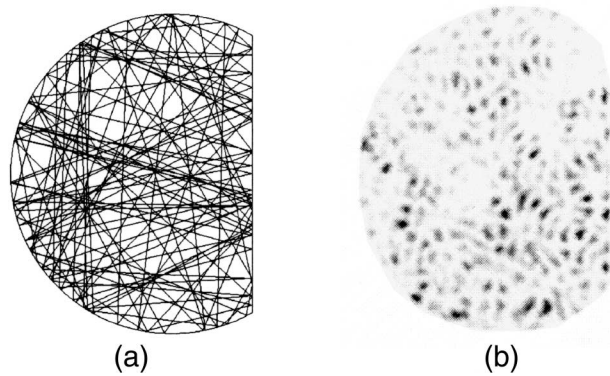


Fig. 1. (a) Typical chaotic ray trajectory in the transverse section of a D-shaped fiber. (b) Typical specklelike near-field intensity actually measured at the output of an optical multimode fiber.

are local results of a superposition of plane waves with random directions that yields a specklelike pattern. This conjecture implies that each individual mode is statistically uniformly distributed over the section of the fiber. Since a wave propagating through the fiber is naturally decomposed over these modes, it inherits their statistical properties.¹⁴ The speckle pattern in Fig. 1(b) is a typical near-field intensity distribution (inverse video) actually measured at the output of an optical multimode fiber specially designed and fabricated in our laboratory for study of the statistical properties of the transmitted light.⁶ The multimode core of this fiber has a 120-μm diameter and is made of pure silica with index $n_1 = 1.458$, surrounded by an outer cladding composed of mixed silicon elastomers with index $n_2 = 1.453$, thus implying weak guidance. The width perpendicular to the flat part is 90 μm.

In double-clad EDFAs, the signal launched into the single-mode doped core is amplified as a result of the absorption of the pump power injected into a multimode inner cladding. Since a D-shaped inner cladding ensures a statistically uniform distribution of the field over its section, it should permit us to achieve maximal overlap of the pump power with the doped core, thus yielding efficient pump absorption. We now demonstrate this qualitative influence by analyzing the pump-absorption characteristics of a DCF with an Er³⁺-doped 5-μm-diameter core of index n_0 at the center of a D-shaped inner cladding with index n_1 and the same dimensions as given above (see the middle inset in Fig. 2). Guidance is obtained through step-index profiles with the linear index of the core $n_0 = 1.468$, the index of the inner clad $n_1 = 1.458$, and the index of the outer silicon clad $n_2 = 1.43$.

The main point of the following argument stems from the fact that the deterministic 2-D ray dynamics is so strongly chaotic that it mimics a truly random process with no memory.¹¹ Therefore, provided that the fraction α of energy absorbed from a ray per passage through the doped core is small, it can be shown that the power-decay length along the fiber is given by the following expression (the so-called Sabine's law)¹⁵:

$$L = \frac{\langle l \rangle}{\alpha} \tan \theta, \quad (1)$$

where θ is the mean angle of the rays with respect to the axis of the fiber and $\langle l \rangle$ is the mean transverse path between successive encounters of the core and is expressed as

$$\langle l \rangle = \frac{\pi A_{\text{clad}}}{P_{\text{core}}}; \quad (2)$$

A_{clad} is the area of the inner cladding and P_{core} is the perimeter of the core. Then, if χ is the inverse length of absorption along the core, α reads as

$$\alpha = \chi l_{\text{core}} \tan \theta', \quad (3)$$

where $n_1 \sin \theta = n_0 \sin \theta'$ and $l_{\text{core}} = \pi A_{\text{core}}/P_{\text{core}}$ is the mean transverse path across the core, given in terms

of the area of the core, A_{core} , and of its perimeter, P_{core} . Of course, expression (3) relies on the complete transverse isotropy of light resulting from the chaotic motion of rays. In practice, for values of θ as high as 0.1 rad and an index mismatch of the order of $n_0 - n_1 = 0.01$, to an excellent approximation, $\tan \theta' = (n_1/n_0)\tan \theta$. The inverse decay length thus reduces to

$$L^{-1} = \chi \frac{A_{\text{core}}}{A_{\text{clad}}} \frac{n_1}{n_0}. \quad (4)$$

This simple expression is local, in the sense that it may depend on the coordinate along the fiber and can therefore allow for a nonlinear dependence of the χ factor (as, for instance, in the case of saturable absorption). Equation (4) also has the rather intuitive interpretation of an inverse decay length being in proportion to the fraction of light intensity localized in the core, assuming a uniform distribution of intensity over the total cross section of the DCF. One should also keep in mind that the 2-D analysis presented above assumes negligible bending, which is reasonable for a bend radius far larger than the cladding radius.

To check the validity of the mean field theory presented above, we model the true wave nature of light propagation in the DCF with the beam-propagation method (BPM), modified by allowing for the introduction of a saturable imaginary part of the index in the core. For the nondiffractive part of the propagation scheme of the BPM, this amounts to writing an equation for the pump intensity within the core, $dI_p/dz = -\chi I_p$, where $\chi = \sigma_p N_t/(1 + \tilde{I}_p)$; σ_p is the absorption cross section, N_t is the concentration of Er³⁺ per unit volume, and \tilde{I}_p is the normalized pump intensity in units of threshold intensity, $I_{p0} = h\nu_p/(\sigma_p t_{sp})$. Obviously, these two equations are valid in the case of a weak signal intensity. For all our simulations, the following parameters were used: pump wavelength $\lambda_p = 980$ nm, erbium-ion concentration $N_t = 2 \times 10^{26} \text{ m}^{-3}$, absorption cross section $\sigma_p = 2.5 \times 10^{-25} \text{ m}^2$, spontaneous lifetime $t_{sp} = 10^{-2} \text{ s}$, and initial pump power a little above the threshold.

For all the numerical simulations presented here, the input is chosen to be a quasi-plane wave with a mean angle θ of $\sim 6^\circ$. Figure 2 displays the pump-power decrease (in logarithmic scale) along 20 m of DCF for

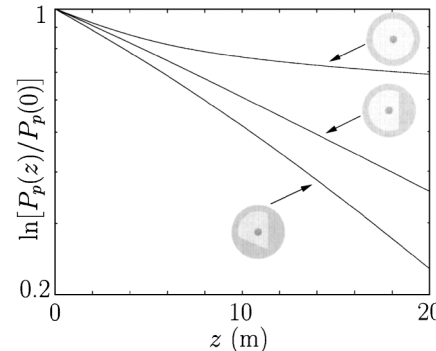


Fig. 2. Pump-power decreases on a logarithmic scale along 20 m of a double-clad EDFA for three different geometries, indicated as insets. The two chaotic (truncated) geometries lead to nonsaturating absorption.

three different geometries, as shown by the insets. For the standard circular fiber (with the total area of the guiding cross section, including core and inner cladding, equal to $1.38 \times 10^{-8} \text{ m}^2$), the decrease saturates very rapidly, owing to the rapid exhaustion of the small fraction of modes of the inner cladding that have a nonnegligible overlap with the core. For the D-shaped fiber with parameters as indicated above (total guiding area $1.19 \times 10^{-8} \text{ m}^2$), the decrease does not saturate and the visible curvature is essentially due to the nonlinear dependence of the absorption parameter, χ . Another source of curvature is known to originate in the existence of the continuous family of special ray trajectories that pass through the center of the fiber and do not hit the cut. These so-called marginally unstable trajectories may drastically slow down the exploration of phase space and therefore induce a long-term nonexponential decrease.¹⁵ These are certainly the main reasons for the 10% discrepancy between the numerically obtained slope after 20 m and the prediction given by Eq. (4), with χ being evaluated at the corresponding intensity level. The slope deduced from the modified BPM scheme is, in this case, equal to 0.055 m^{-1} , whereas the predicted value is 0.060 m^{-1} . For the double-truncated fiber, the geometry of the inner cladding is designed with two cuts (total guiding area $0.91 \times 10^{-8} \text{ m}^2$), thus suppressing the above-mentioned special trajectories while preserving the chaotic character of the ray dynamics¹¹ and therefore leading to excellent agreement between the numerical result (0.083 m^{-1}) and the theoretical prediction (0.086 m^{-1}). Here it should be remarked that even the short distance decrease (at $\sim 1 \text{ m}$) is observed to agree fairly well with the prediction, thereby indicating that ergodicity is established over shorter distances (typically distances of a few centimeters are sufficient to randomize almost any initial input).⁶

In conclusion, noting that multimode fibers with nonstandard transverse shapes generically induce chaotic dynamics of rays, we have proposed studying chaotic DCFs in the framework of wave chaos. We showed that ergodicity of the ray dynamics can result in an important improvement of pump absorption, owing to a maximal overlap of the pump intensity with the doped absorbing core. We provided a theoretical argument to estimate the inverse decay length and, through fine control of the relevant parameters of the fiber (notably by suppression of nonchaotic ray trajectories), were able to optimize the absorption characteristics of a double-clad EDFA. We then tested

our prediction against numerical results obtained through a modified BPM scheme. The agreement is excellent and illustrates the potentially important role of wave chaos in designing double-clad EDFA. Relying on these theoretical and numerical results, we are currently involved in the experimental realization of such an amplifier in collaboration with the Institut de Recherche en Communications Optiques et Microondes (IRCOM) Limoges.

The authors acknowledge fruitful discussions with Ph. Leproux, D. Pagnoux, and Ph. Roy from the group Guided and Integrated Optics of IRCOM Limoges and are grateful to G. Monnom of Laboratoire de Physique de la Matière Condensée Nice for his collaboration in the fabrication of the chaotic fiber. V. Doya's e-mail address is doya@bacchus.unice.fr.

References

1. E. Desurvire, *Erbium-doped Fiber Amplifiers* (Wiley Interscience, New York, 1994).
2. E. Snitzer, H. Po, F. Hakimi, R. Tumminelli, and B. C. McCollum, in *Optical Fiber Sensors*, Vol. 2 of 1988 OSA Technical Digest Series (Optical Society of America, Washington, D.C., 1988), paper PD5.
3. A. Liu and K. Ueda, *Optics Commun.* **132**, 511 (1996).
4. R. A. Hayward, W. A. Clarkson, P. W. Turner, J. Nilsson, A. B. Grudinin, and D. C. Hanna, in *Digest of Conference on Lasers and Electro-Optics* (Optical Society of America, Washington, D.C., 2000), paper CFH2.
5. S. T. Jackson and T. A. King, *Opt. Lett.* **25**, 1462 (2000).
6. V. Doya, "Du speckle aux scars: une expérience de chaos ondulatoire dans une fibre optique," Ph.D dissertation (Université de Nice Sophia-Antipolis, Nice, France).
7. H.-J. Stöckmann, *Quantum Chaos: An Introduction* (Cambridge U. Press, Cambridge, 1999).
8. R. L. Weaver and O. I. Lobkis, *Phys. Rev. Lett.* **84**, 4942 (2000).
9. F. Mortessagne, O. Legrand, and D. Sornette, *Chaos* **3**, 529 (1993).
10. S. Ree and L. E. Reichl, *Phys. Rev. E* **60**, 1607 (1999).
11. L. A. Bunimovich, *Commun. Math. Phys.* **65**, 295 (1979).
12. M. V. Berry, *Eur. J. Phys.* **2**, 91 (1981).
13. M. V. Berry, *J. Phys. A* **10**, 2083 (1977).
14. V. Doya, O. Legrand, F. Mortessagne, and Ch. Miniatura are preparing a manuscript to be called "Speckle statistics in a chaotic multimode fiber."
15. F. Mortessagne, O. Legrand, and D. Sornette, *J. Acoust. Soc. Am.* **94**, 154 (1993).

E. Amplification optique des scars : vers le chaos ondulatoire non linéaire

Cette section sera difficilement accessible au lecteur qui n'aurait pas lu les trois articles précédent. En effet, nous ne revenons pas ici sur les concepts clefs et sur la modélisation. Tous les détails, plus ou moins techniques, liés à cette partie ont été renvoyés dans les annexes II.F.

1. Contexte

Les travaux présentés précédemment ont montré (*i*) que les scars étaient présents dans une fibre optique chaotique passive, mais (*ii*) que leur accès était très délicat. Faire émerger des modes particuliers d'un milieu passif où l'excitation sélective est quasi-impossible est un défi déjà relevé sur une autre facette du chaos ondulatoire : la diffusion multiple. C'est, en effet, l'une des observations réalisées sur lasers aléatoires⁶. Dans ce contexte, le rôle des modes scars est joué par les modes localisés. Ces deux types de modes doivent leur existence à des très importants effets de cohérence, et affichent des propriétés statistiques communes⁷. Christian Vanneste et Patrick Sebbah ont clairement montré dans leurs simulations numériques que les modes amplifiés dans un laser aléatoire correspondaient aux modes localisés du milieu passif⁸. De plus, ils ont mis en évidence qu'une excitation sélective de modes localisés pouvait être réalisée en localisant spatialement le gain⁹. Tant que la matrice passive n'est pas absorbante, la région active peut même avoir une extension beaucoup plus réduite que la taille de mode sur lequel s'effectue l'amplification laser¹⁰.

Avant d'envisager de réaliser un laser fibré sur les modes scars (un « lascar » !), les lasers aléatoires nous indiquent le chemin à suivre à plus court terme : utiliser un milieu à gain pour amplifier les scars au détriment des autres modes. Ce faisant nous mettons un pied dans le chaos ondulatoire non linéaire. Terrain très peu défriché. En effet, il faut noter que dans les expériences dans lesquelles des scars ont été observés¹¹, comme d'ailleurs dans la plupart des études relevant du chaos ondulatoire, la physique des ondes mise en jeu reste linéaire, seule la dynamique des rayons géométriques est non linéaire. Récemment, Kudrolli et ses collaborateurs ont développé une expérience sollicitant les ondes non linéaires de Faraday à la surface d'un container en forme de stade de Bunimovich¹². Ils ont notamment montré une sélection

de quelques familles de scars, que Agam et Altshuler ont ensuite clairement identifiée comme un effet de la non linéarité de l'équation d'onde¹³. Dans les microcavités lasers, les propriétés particulières des scars, notamment leur grand facteur de qualité, ont déjà été exploitées¹⁴. Ces lasers d'une taille typique d'une centaine de microns, et réalisés dans des semiconducteurs ou dans des matériaux diélectriques¹⁵, sont de plus en plus présents en photonique. On attend d'eux une bonne directivité d'émission et un faible seuil. Les scars remplissent ce cahier des charges en constituant, dans la plupart des cas, les modes de plus grand facteur de qualité, et une directivité fine donnée par la structure du mode dans l'espace des phases. Souvent seul un petit nombre de modes efficaces de ce type sont présents dans ces microcavités¹⁶.

Comme nous l'avons montré en II.D, la fibre optique multimode en forme de cercle tronqué – en forme de « D », pour faire plus court – est idéale pour réaliser un amplificateur optique. De fait, les amplificateurs de puissance dit à double cœur utilisent cette géométrie en D pour le cœur externe¹⁷. Soulignons tout de suite deux aspects importants et délicats pour la suite. Tout d'abord, un amplificateur standard possède une zone active dont l'indice optique est plus élevé que le cœur externe, et ce afin de continuer à guider le signal (monomode) utile qui sera, après amplification, réinjecté dans le réseau télécom constitué de fibres monomodes. Deuxièmement, ce cœur actif est, pour des raisons pratiques, situé au centre du cercle dans lequel s'inscrit le D du cœur externe. Or, nous voulons évidemment éviter un quelconque guidage dans une zone réduite de la fibre, et, par analogie avec le comportement des lasers aléatoires, il serait judicieux de placer la zone dopée sur une sur-intensité du mode scar dont on veut réaliser l'amplification. Le calcul des plusieurs milliers de modes d'une cavité en forme de cercle tronqué avec des conditions aux limites de Dirichlet (cavité métallique), nous incite à localiser la zone active autour du point auto-focal de l'orbite périodique à 2 re-

026208 (2001).

¹³ O. Agam and B. L. Altshuler, Physica A **302**, 310 (2001).
¹⁴ C. Gmachl, F. Capasso, E. E. Narimanov, J. U. Nöckel, A. D. Stone, J. Faist, D. L. Sivco, and A. Y. Cho, Science **280**, 1556 (1998); C. Gmachl, E. E. Narimanov, F. Capasso, J. N. Baillargeon, and A. Y. Cho, Opt. Lett. **27**, 824 (2002); T. Harayama, T. Fukushima, P. Davis, P. O. Vaccaro, T. Miyasaka, T. Nishimura, and T. Aida Phys. Rev. E **67**, 015207 (2003).

¹⁵ Voir également les références suivantes pour l'intéressante voie des microlasers en polymère : M. Lebental, J. S. Lauret, R. Hierle, and J. Zyss, Appl. Phys. Lett. **88**, 031108 (2006); M. Lebental, J. S. Lauret, J. Zyss, C. Schmit, and E. Bogomolny, arXiv :physics/0609009.

¹⁶ W. Fang, A. Yamilov, and H. Cao, Phys. Rev. A **72**, 023815 (2005).

¹⁷ Une petite remarque pour le lecteur curieux et non-spécialiste qui irait jeter un œil sur la littérature spécialisée : les fibres à double cœur, en français, deviennent à double gaine (double-clad), en anglais ; ainsi, en passant à l'anglais, le cœur externe devient-il un « inner cladding » !

⁶ Voir la référence suivante pour une revue récente et accessible de ce très productif domaine : H. Cao, J. Phys. A : Math. Gen. **38**, 10497 (2005).

⁷ P. Pradhan and S. Sridhar, Phys. Rev. Lett. **85**, 2360 (2000).

⁸ P. Sebbah and C. Vanneste, Phys. Rev. B **66**, 144202 (2002).

⁹ C. Vanneste and P. Sebbah, Phys. Rev. Lett. **87**, 183903 (2001).

¹⁰ H. Cao, J. Phys. A : Math. Gen. **38**, 10497 (2005).

¹¹ Voir les références dans l'article présenté en II.C

¹² A. Kudrolli, M. C. Abraham, and J. P. Gollub, Phys. Rev. E **63**,

bonds la plus courte.

Comme nous le verrons dans la partie suivante, la première difficulté a été surmontée grâce à l'équipe *Fibres Optiques Actives* du LPMC, et notamment grâce à la collaboration de Wilfried Blanc et Michèle Udé. Le décentrage du cœur a été réalisé par Pavel Oupicky à l'institut de Physique des Plasmas de Turnov, en République Tchèque. Avant la phase expérimentale qui devrait débuter début 2007, une campagne de simulations les plus plus réalistes possibles est en cours. Les premiers résultats que je vais présenter sont extrêmement encourageants et semblent montrer que l'amplification sélective d'un, ou quelques, modes scar est possible dans une fibre optique. Outre l'intérêt en soi de réaliser cette sélection par le gain, nous disposerons donc bientôt de scars « propres » qui pourront être injectés dans des fibres, diélectriques ou cristallines aux diverses propriétés non linéaires : χ^2 , χ^3 , Brillouin, etc.

2. Mise en évidence de l'amplification sélective

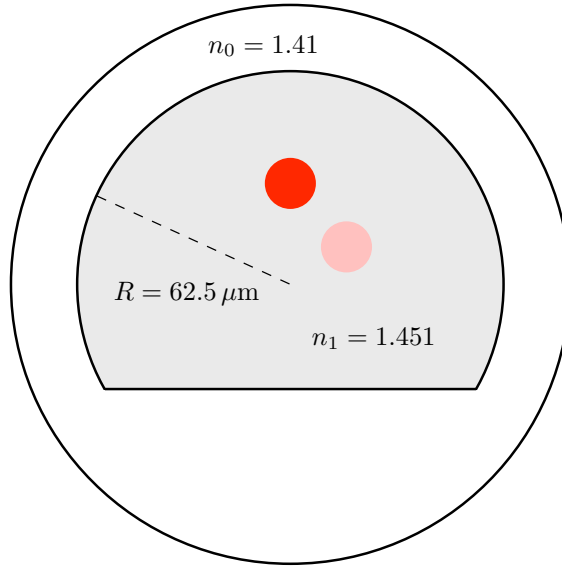


FIG. 4 Représentation schématique de la fibre amplificatrice. Le disque plein représente la zone dopée localisée à la position du point auto-focal de l'orbite verticale à 2 rebonds ; en plus clair apparaît une deuxième position de la zone utilisée dans les simulations.

Décrivons tout d'abord la fibre utilisée. Comme le montre la figure 4, nous avons conservé dans cette étude une fibre avec pour forme de section transverse un cercle tronqué à la moitié de son rayon. Le diamètre de la fibre est de $125 \mu\text{m}$ et les indices optiques sont $n_0 = 1.41$ pour la gaine mécanique et $n_1 = 1.451$ pour le cœur tronqué. Ainsi, l'ouverture numérique de la fibre $\sin \theta_{\max} = (n_1^2 - n_0^2)^{1/2}$ est égale à 0.34. À cet angle limite correspond un nombre d'onde maximum $k_t^{\max} = (2\pi/\lambda_s) \sin \theta_{\max}$, où λ_s est la longueur d'onde dans le vide. Pour $\lambda_s = 1020 \text{ nm}$,

on trouve environ 3500 modes guidés dans la fibre. La zone dopée est localisée autour du point auto-focal de l'orbite verticale à 2 rebonds. Elle couvre un disque de diamètre $15 \mu\text{m}$ (figure 4). Son indice optique n_2 , qui, idéalement, devrait être le même que celui de la fibre tronquée, est, en pratique, légèrement supérieur

$$n_2 = n_1 + 2 \times 10^{-4}$$

Toutes les valeurs d'indice ont été fournies par Wilfried Blanc – et confirmées par le Service Central d'Analyses du CNRS. L'équipe « fibres » a fabriqué une fibre cylindrique dopée à l'ytterbium, en modifiant la procédure habituelle de façon à minimiser la différence d'indice entre la zone centrale à gaine et le cœur externe. Une attention particulière a été portée au dopage de la préforme – barreau de silice initial d'un diamètre de l'ordre du centimètre¹⁸ – dont le profil d'indice est représenté sur la figure 5. La procédure de tirage ne modifie pas la forme globale du profil d'indice de la région à gain, et en réduit même légèrement l'élévation, comme le montre la figure 6. Contrairement au cahier des charges initial, la fibre possède donc une zone active d'un indice supérieur à la matrice environnante. Mais, fort heureusement, cette élévation modérée et progressive de l'indice ne s'accompagne pas de l'existence d'un mode guidé dans la région dopée. En transposant dans un contexte quantique, on montre facilement qu'un puits de potentiel 2D de cette forme ne contient pas d'états liés. En pratique dans les simulations, nous avons approché le profil triangulaire par une Gaussienne (essentiellement pour éviter des discontinuités dans la dérivée du profil).

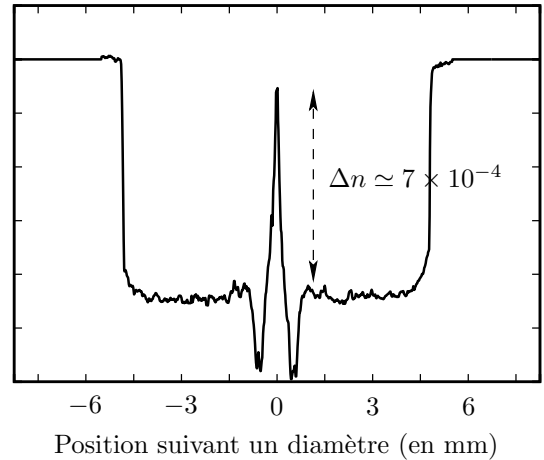


FIG. 5 Profil d'indice de la préforme réalisé au LPMC. On notera la forme triangulaire du profil dans la partie centrale dopée à l'ytterbium et la faible valeur de l'élévation d'indice.

¹⁸ Pour une présentation générale de la fabrication des fibres optiques voir : *Optical Fiber Communications : Fiber Fabrication*, Tingye Li, Academic Press (1985).

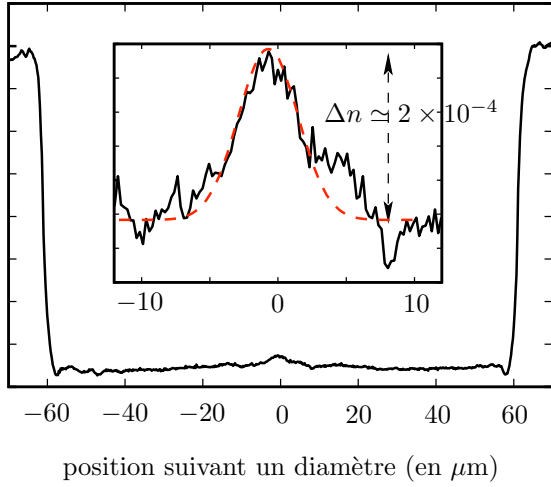


FIG. 6 Profil d'indice de la fibre (cylindrique) réalisée au LPMC. Le profil de la zone dopée reste grossièrement triangulaire; la Gaussienne en pointillés représente le profil utilisé dans la simulation.

Rappelons la règle de quantification pour les scars localisés le long de l'orbite verticale à deux rebonds, ou, de manière équivalente, la condition de stationnarité dans une cavité Fabry-Pérot constituée d'un miroir plan et d'un miroir concave :

$$k_t L - \Delta\phi - \frac{\pi}{2} = 2\pi p \quad (1)$$

où L est la longueur de l'orbite, p l'ordre du mode scar, $\Delta\phi$ le déphasage de l'onde qui se réfléchit sur l'interface cœur/gaine. Le déphasage de $\frac{\pi}{2}$ s'acquierte à la traversée du point auto-focal. Dans le cas d'une cavité métallique (puits quantique infini), chaque réflexion entraîne un déphasage de π et $\Delta\phi = 2\pi$; lorsque, comme ici, le saut d'indice est plus modéré, l'expression du déphasage est la suivante

$$\Delta\phi = 4 \arctan \sqrt{\frac{n_1^2 - n_0^2}{k_t^2} \left(\frac{2\pi}{\lambda_s} \right)^2 - 1} \quad (2)$$

où λ_s la longueur d'onde de l'onde qui se propage dans la fibre.

Nous utilisons dans la simulation une excitation de type onde plane comme présentée en II.C. En raison de la diffraction liée à la taille finie de la fibre, il est impossible de n'injecter qu'un seul module de vecteur d'onde dans la fibre, mais on doit s'accommoder d'une dispersion en nombres d'onde de l'ordre de $6R^{-1}$, soit une cinquantaine de modes avec les paramètres utilisés dans les simulations. Nous effectuons tout d'abord une simulation de référence, sans amplification, en utilisant une onde plane de nombre d'ondes correspondant au scar $p = 10$, soit $k_t R \simeq 23.5$. Après 22 m de propagation, nous obtenons, comme attendu, une figure en champ proche de type speckle et un champ lointain construisant presque parfaitement un cercle au trait épais par la diffraction initiale

(figure 7). La figure 7 montre également le « spectre en nombres d'onde » (voir l'annexe II.F.2) de la fibre passive. On voit nettement l'effet de la diffraction initiale par l'ouverture finie de la fibre dans le nombre de modes effectivement excités dans la fibre. Le scar d'ordre 10, dont le nombre d'onde correspond à celui de l'onde plane injectée, ne domine pas suffisamment le spectre pour dominer le comportement du signal.

La simulation de la fibre passive ne présente pas un caractère nouveau car cette situation est celle traitée par les études expérimentales présentées en II.B et II.C. Il était tout de même important de s'assurer de la pertinence de la méthode numérique (voir annexe II.F.3). Mais, surtout, les résultats présentés sur la figure 7 vont servir de points de comparaison pour la simulation, originale, de la fibre amplificatrice. La même onde plane que précédemment est injectée dans la fibre représentée schématiquement sur la figure 4; la zone dopée à l'ytterbium couvre un disque de $15 \mu\text{m}$ de diamètre. La figure 8 montre des comportements totalement différents du cas passif : (i) le spectre est beaucoup plus limité et dominé par le scar d'ordre 10, qui, (ii), imprime sa structure aux champs proche et lointain. On peut fournir une autre preuve de la domination du scar d'ordre 10 en effectuant un filtrage du champ lointain pour ne conserver qu'un anneau centré sur $k_t R = 23.5$, et en effectuant une transformée de Fourier inverse du champ contenu dans l'anneau (la simulation numérique donne accès au champ, et pas uniquement à l'intensité). La figure 9 montre, en haut à gauche, le résultat de cette opération. La structure spatiale obtenue se superpose presque parfaitement à la structure du scar du même ordre calculé dans une cavité métallique comme le montre la figure 9. On devine également sur la figure de champ lointain deux spots symétriques dont une mesure montrent qu'ils sont situés à une distance $k_t R = 10.9$ du centre du champ lointain. Cette valeur de nombre d'onde correspond à celle du scar d'ordre 4, qui possède une forte surintensité sur le point auto-focal. La même opération de filtrage du champ lointain est donc effectuée, avec un anneau de rayon moyen $k_t R = 10.9$. Son résultat apparaît en bas à gauche de la figure 9 : la structure spatiale du scar d'ordre 4 apparaît nettement. Bien évidemment, les mêmes opérations ont été effectuées sur le champ lointain de la fibre passive et aucune structure identifiable n'en est sortie.

Une simulation effectuée dans les mêmes conditions mais avec une zone dopée placée hors de l'axe (figure 4), n'a révélé aucun effet d'amplification préférentiel du mode scar. Le rôle favorable du bon recouvrement spatial entre la zone dopée et la région où le mode présente une forte amplitude est donc souligné. La robustesse de l'effet d'amplification sélective semble être importante. En effet, revenant à la configuration initiale, des simulations effectuées à partir d'un « bruit » constitué par une superposition d'ondes planes aléatoire de modules et de directions aléatoires, semblent montrer un effet d'amplification sur les scars dont la surintensité est la plus marquée sur le point auto-focal. Les premiers résultats

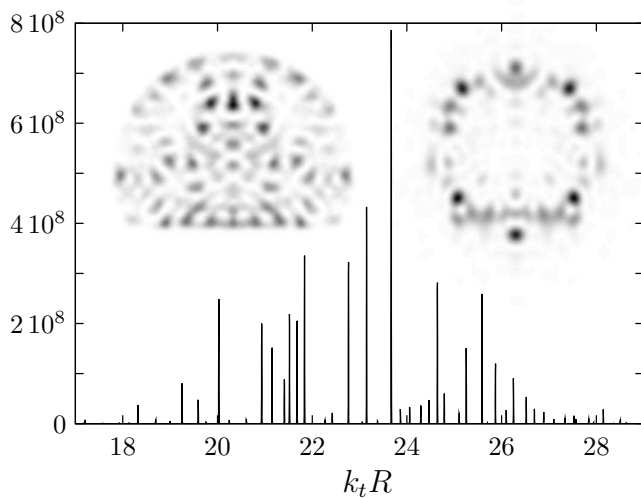


FIG. 7 Simulation dans une fibre passive. Spectre en nombres d'onde pour une excitation par une onde plane se propageant verticalement avec $k_t \simeq 23.5 R^{-1}$, après 22 mètres de propagation. Les images en champ proche (à gauche) et en champ lointain (à droite) montrent un comportement de type speckle.

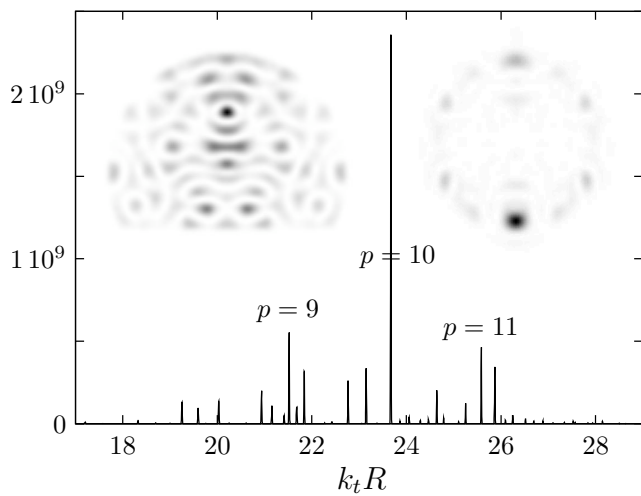


FIG. 8 Simulation dans une fibre amplificatrice. Spectre en nombres d'onde pour une excitation par une onde plane se propageant verticalement avec $k_t \simeq 23.5 R^{-1}$, après 22 mètres de propagation ; l'amplification a favorisé quelques modes, notamment les scars d'ordre $p = 9, 10, 11$. Les images en champ proche (à gauche) et en champ lointain (à droite) confirment la prégnance du scar d'ordre $p = 10$.

présentés ici ne permettent pas d'affirmer complètement que le phénomène d'amplification sélective d'un scar dans une fibre optique amplificatrice a été validé. Ils sont, en revanche, indéniablement encourageants. Jusqu'à présent les simulations ont été effectuées avec une valeur initiale de la puissance de pompe juste au dessus du seuil d'amplification (1 W), et avec un signal faible ($1 \mu\text{W}$). Une

nouvelle campagne de simulations va maintenant être entamée avec les valeurs de puissance délivrées par les lasers qui vont être utilisés dans l'expérience : 3 W pour la pompe (bien au dessus du seuil) et 100 mW pour le signal

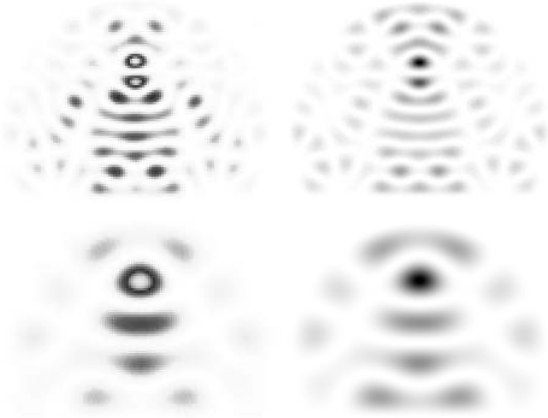


FIG. 9 À gauche : images de champ proche obtenues par transformée de Fourier inverses après filtrage du champ lointain par un anneau centré en $k_t R = 23.5$ (en haut) et $k_t R = 10.9$ (en bas) : à droite les modes scars $p = 10$ et $p = 4$ calculés dans une cavité métallique.

F. Annexes

1. Modélisation de l'amplification

Parmi les ions de terre rare utilisés dans les amplificateurs optiques, notre choix s'est porté sur l'ytterbium. Il possède une structure à quatre niveaux d'énergie (figure 10) qui peut se traiter comme un système à deux niveaux¹⁹, avec une émission à 1020 nm et une absorption à 980 nm. Les spectres d'absorption et d'émission de l'ytterbium laissent supposer une excellente efficacité de transfert d'énergie en utilisant une pompe à 980 nm et un signal à 1020 nm (figure 10). Il ne serait pas judicieux d'utiliser l'émission forte à 980 nm car le signal serait trop facilement réabsorbé.

Dans l'approximation du système à deux niveaux, on appelle N_1 la densité de population du « fondamental » (niveau $2F^{7/2}$) et N_2 celle du « niveau excité » (niveau $2F^{5/2}$) : $N_1 + N_2 = N_t$. On montre facilement²⁰

$$\frac{dN_1}{dt} = -\frac{\sigma_{pa} I_p}{h\nu_p} N_1 + \frac{\sigma_{sa} I_s}{h\nu_s} (\eta_s N_2 - N_1) + \frac{N_2}{\tau_{sp}} \quad (3)$$

¹⁹ R. Paschotta, J. Nilsson, A.C. Tropper, D.C. Hanna, IEEE Journal of Quantum Electronics **33**, 1049 (1997)

²⁰ Facilement, car le calcul se trouve dans les bons ouvrages, par exemple dans : *Introduction to fiber optics*, A.Ghatak, K.Thyagarajan, Cambridge University Press (1998).

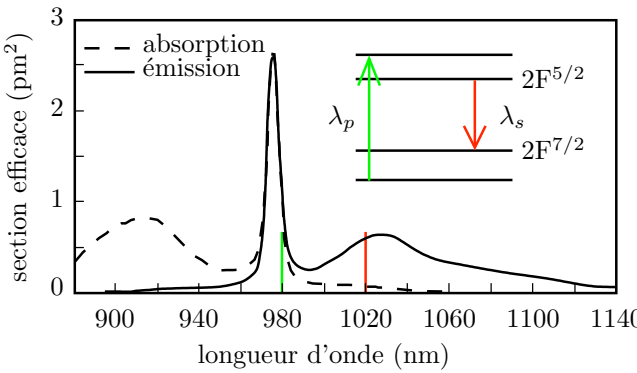


FIG. 10 Spectres d'émission et d'absorption de l'ytterbium et schéma des niveaux atomiques sollicités : le meilleur compromis est obtenu pour des longueurs d'onde à 980 nm, pour l'absorption, et 1020 nm, pour l'émission

où I_p représente l'intensité de la pompe et I_s celle du signal ; $\eta_s = \sigma_{se}/\sigma_{sa}$ représente le rapport de la section efficace d'émission à 1020 nm, σ_{se} , sur la section efficace d'absorption à 1020 nm, σ_{sa} ; σ_{pa} est la section efficace d'absorption à 980 nm ; ν_p et ν_s les fréquences respectivement associées aux transitions à 980 nm et 1020 nm ; τ_{sp} représente la durée de vie du niveau excité quand on mesure l'émission spontanée à 1020 nm.

La solution stationnaire de l'équation (3) est donnée par

$$\begin{aligned} N_1(x, y, z) &= \frac{1 + \frac{\eta_s}{1 + \eta_s} \frac{I_s}{I_{s0}} N_t}{1 + \frac{I_p}{I_{p0}} + \frac{I_s}{I_{s0}}} \\ N_2(x, y, z) &= \frac{\frac{I_p}{I_{p0}} + \frac{1}{1 + \eta_s} \frac{I_s}{I_{s0}}}{1 + \frac{I_p}{I_{p0}} + \frac{I_s}{I_{s0}}} N_t \end{aligned} \quad (4)$$

où I_{p0} est l'intensité de saturation de la pompe (intensité en dessous de laquelle la pompe ne contribue plus à l'inversion de population $\eta_s N_2 > N_1$) et I_{s0} représente l'intensité de saturation du signal (intensité au dessus de laquelle le système entre en régime de saturation).

Il reste maintenant à passer des évolutions spatiales des densités de population à celles des intensités de la pompe et du signal. On appelle ξ_p^{abs} le nombre de photons de pompe absorbés sur une distance dz , par unité de temps et de surface :

$$\xi_p^{\text{abs}} = \frac{\sigma_{pa} I_p(z) N_1}{\nu_p} dz \quad (5)$$

On définit de même ξ_s^{abs} pour les photons de signal. Pour l'émission stimulée, on introduit ξ_s^{em} , qui représente le nombre de photons de signal émis par unité de temps et de surface, sur une distance dz et à la longueur d'onde

du signal

$$\xi_s^{\text{em}} = \frac{\sigma_{se} I_s(z) N_2}{\nu_s} dz \quad (6)$$

L'énergie absorbée par unité de temps et de surface sur la distance dz s'écrit alors, pour le signal et pour la pompe

$$dE_p = \sigma_{pa} I_p N_1 dz \quad (7)$$

$$dE_s = \sigma_{sa} I_s (N_1 - \eta_s N_2) dz \quad (8)$$

Or cette différence d'énergie par unité de temps et de surface peut s'écrire

$$-\frac{dI_{s,p}}{dz} dz \quad (9)$$

soit encore

$$\frac{dI_p}{dz} = -\sigma_{pa} N_1(z) I_p(z) \quad (10)$$

$$\frac{dI_s}{dz} = \sigma_{sa} (\eta_s N_2 - N_1) I_s(z) \quad (11)$$

Ces équations décrivent le processus d'échange énergétique entre la pompe et le signal, c'est-à-dire le processus d'amplification ; ce sont elles qui sont implémentées par la méthode numérique décrite en II.F.3.

2. Calcul du spectre en nombre d'onde

Cette annexe présente la méthode utilisée pour calculer le spectre de l'onde qui se propage dans la fibre²¹.

Rappelons l'expression de la décomposition du champ sur les modes de propagation de la fibre :

$$\psi(x, y, z) = \sum_n c_n \phi_n(x, y) e^{i\beta_n z} \quad (12)$$

avec

$$\iint dx dy |\phi_n|^2 = 1, \quad \iint dx dy \phi_m^* \phi_n = \delta_{nm} \quad (13)$$

La fonction d'autocorrélation (en pseudo-temps) du champ s'écrit

$$\mathcal{C}(z) = \iint dx dy \psi^*(x, y, 0) \psi(x, y, z) \quad (14)$$

$$\mathcal{C}(z) = \sum_n |c_n|^2 e^{i\beta_n z} \quad (15)$$

Elle correspond au recouvrement du champ $\psi(x, y, z)$ avec sa condition initiale $\psi(x, y, 0)$.

²¹ M.D. Feit and J.A. Fleck, Applied Optics **19**, 1154 (1980).

Pour éviter les traditionnels problèmes rencontrés dans l'utilisation des algorithmes de FFT, il faut « adoucir » les bords de la fonction $\mathcal{C}(z)$. On choisit une apodisation par une Gaussienne $f(z)$ qui permet de ramener les extrémités de la fonction à des valeurs très faibles, de manière continue. *In fine*, on obtient l'expression suivante de la fonction d'autocorrélation

$$\begin{aligned}\mathcal{C}(k) &= \int dz f(z) \sum_n |c_n|^2 e^{i\beta_n z} e^{-ikz} \\ \mathcal{C}(k) &= \int dz f(z) \sum_n |c_n|^2 e^{i(\beta_n - k)z}\end{aligned}$$

qui peut encore s'écrire

$$\begin{aligned}\mathcal{C}(k) &= \text{TF}[f(z)] * \sum_n |c_n|^2 \int dz e^{i(\beta_n - k)z} \\ \mathcal{C}(k) &= \text{TF}[f(z)] * \sum_n |c_n|^2 \delta(\beta_n - k)\end{aligned}\quad (16)$$

où $*$ représente un produit de convolution.

Nous obtenons donc une fonction qui présente des résonances lorsque $k = \beta_n$, où les β_n sont les vecteurs d'onde qui correspondent aux modes sur lesquels se décompose le champ qui se propage. En se rappelant qu'à l'intérieur de la fibre, l'onde peut s'écrire

$$\Psi(x, y, z) = \psi(x, y, z) e^{i\beta z} \quad (17)$$

et que $n_1^2 |\vec{k}_s|^2 = \beta^2 + k_t^2$ nous pouvons passer du vecteur d'onde β_n au nombre d'onde transverse ; en effet, en écrivant k_t comme

$$k_t^2 = (n_1 k_s)^2 - (n_1 k_s + \beta_n)^2 \quad (18)$$

il vient

$$k_t^2 = -(2n_1 k_s \beta_n + \beta_n^2) \quad (19)$$

Et apparaît, ainsi, le spectre en nombre d'onde de l'onde qui se propage dans la fibre.

3. La Beam Propagation Method

Cette annexe n'est pas à interpréter comme l'expression d'une maladroite tentative d'appropriation de cette méthode numérique, d'un usage très répandue parmi les opticiens. Mais, justement, en raison de sa popularité, le lecteur n'en trouvera aucune présentation, même succincte, dans les articles collectés ici – ni d'ailleurs dans le reste de ma littérature. J'ai donc jugé opportune la présente annexe²².

La « Beam Propagation Method » est une méthode numérique très couramment utilisée qui permet de simuler la propagation d'une onde scalaire dans un guide à deux dimensions. Le principe de base de cette méthode consiste à distinguer la propension naturelle d'une onde à se propager dans tout l'espace, c'est-à-dire la diffraction, de l'effet guidant du milieu de propagation, d'extensions spatiales finies. La première étape se traitera dans l'espace des vecteurs d'onde, la deuxième dans l'espace réel.

Le champ $\Psi(x, y, z)$ s'écrit comme le produit d'une amplitude complexe, $\psi(x, y, z)$, et d'un terme de propagation selon la direction longitudinale :

$$\Psi(x, y, z) = \psi(x, y, z) e^{i\beta z} \quad (20)$$

L'équation d'Helmholtz prend alors la forme

$$(\Delta_{\perp} - \beta^2 + \partial_{zz} + 2i\beta\partial_z + n^2 k^2) \psi(x, y, z) = 0 \quad (21)$$

Rappelons que nous nous plaçons toujours dans le domaine de validité de l'approximation paraxiale où les variations du champ selon z sont petites sur une échelle de l'ordre de la longueur d'onde. Il est, ainsi, légitime de négliger le terme en dérivée seconde pas rapport à la dérivée première. L'équation (21) se ramène alors à l'équation de Fresnel :

$$-\Delta_{\perp} \psi(x, y, z) - (n^2 k^2 - \beta^2) \psi(x, y, z) = 2i\beta\partial_z \psi(x, y, z) \quad (22)$$

L'analogie avec l'équation de Schrödinger

$$-\frac{1}{2} \Delta \psi + V(x, y) \psi = i\hbar\partial_t \psi \quad (23)$$

permet de définir un opérateur d'évolution longitudinale, tel que

$$i\partial_z \psi = (D + P)\psi \quad (24)$$

où le terme $D = -\frac{1}{2\beta} \Delta_{\perp}$ est associé à la diffraction et le terme $P = -(n^2 k^2 - \beta^2)/2\beta$ à la propagation guidée.

On peut ainsi décrire l'évolution selon la direction longitudinale du champ :

$$\psi(z + \delta z) = \psi(z) e^{-i(D+P)\delta z} \quad (25)$$

sur une distance de propagation δz .

Dans le cas général, il faudrait développer $e^{(D+P)}$ selon la formule de Baker-Hausdorff

$$e^A e^B = \exp(A + B + \frac{1}{2}[A, B] + \frac{1}{12}[A - B, [A, B]] + \dots) \quad (26)$$

mais dans la mesure où on considère une distance δz suffisamment petite, seul le terme e^{A+B} n'est pas négligeable. On peut alors écrire

$$\psi(z + \delta z) = \psi(z) e^{-iD\delta z} e^{-iP\delta z} \quad (27)$$

Les deux étapes de diffraction et de propagation guidée peuvent donc être traitées séparément.

(i) Diffraction

²² J'ai fait de larges emprunts à un récent rapport de stage de Claire Michel, elle-même très largement inspirée par la thèse de Valérie Doya, elle-même fortement influencée par... etc.

Considérons une décomposition en ondes planes de l'onde $\psi(x, y, z)$ se propageant dans la fibre. Soit $\tilde{\psi}(k_x, k_y, z)$ la transformée de Fourier dans le plan transverse de la fibre de $\psi(x, y, z)$. L'étape

$$D\psi(z) = -\frac{\Delta_\perp}{2\beta}\psi(z) \quad (28)$$

s'écrit alors

$$D\tilde{\psi}(k_x, k_y, z) = \frac{k_x^2 + k_y^2}{2\beta}\tilde{\psi}(k_x, k_y, z) \quad (29)$$

En intégrant (27), nous obtenons

$$\tilde{\psi}(k_x, k_y, z + \delta z) = \tilde{\psi}(k_x, k_y, z) \exp\left(-i\frac{k_x^2 + k_y^2}{2\beta}\delta z\right) \quad (30)$$

On note $k_x^2 + k_y^2 = k_t^2$. Le champ de l'onde diffractée s'écrit alors

$$\psi(x, y, z + \delta z) = \text{TF}^{-1}\left[\tilde{\psi}(k_x, k_y, z) \exp\left(i\frac{k_t^2}{2\beta}\delta z\right)\right] \quad (31)$$

(ii) Propagation guidée

L'étape de propagation guidée peut maintenant être appliquée au champ $\psi_{\text{diff}}(x, y, z + \delta z)$. On applique alors la relation

$$i\partial_z\psi(z + \delta z) = P\psi(z) \quad (32)$$

dans laquelle

$$P\psi(z) = -\frac{n^2 k_0^2 - \beta^2}{2\beta}\psi(z) \quad (33)$$

où $k_0 = 2\pi/\lambda_0$, λ_0 étant la longueur d'onde dans le vide. L'évolution guidée du champ sur un pas de propagation prend donc la forme

$$\begin{aligned} \psi(x, y, z + \delta z) &= \\ &\psi(x, y, z) \exp\left(i\frac{n^2 k_0^2 - \beta^2}{2\beta}\delta z\right) \end{aligned} \quad (34)$$

Ce qui permet d'écrire l'expression finale du champ en $z + \delta z$

$$\begin{aligned} \psi(x, y, z + \delta z) &= \text{TF}^{-1}\left[\tilde{\psi}(k_x, k_y, z) \exp\left(i\frac{k_t^2}{2\beta}\delta z\right)\right] \\ &\times \exp\left(i\frac{n^2 k_0^2 - \beta^2}{2\beta}\delta z\right) \end{aligned} \quad (35)$$

La distance δz considérée, en pratique, est telle que $\frac{\delta z}{\lambda} \simeq 0.5$; le critère de validité de l'approximation paraxiale est donc bien vérifié

Pour un traitement complet de l'amplification, il faudrait simuler les évolutions concomitantes et liées de la pompe (à 980 nm) et du signal (à 1020 nm). Cependant,

comme le montre l'étude présentée dans la partie II.D, dans une fibre optique chaotique la puissance de la pompe décroît exponentiellement avec la distance de propagation

$$P_p(x, y, z) = P_p(x, y, z = 0)e^{-\alpha_p z} \quad (36)$$

où z est la direction de propagation dans la fibre optique.

Cela donne une équation pour l'évolution de l'intensité de pompe, $I_p(z)$

$$I_p(x, y, z) = \frac{P_p(x, y, z)}{S}e^{-\alpha_p z} \quad (37)$$

où S est l'aire de la section transverse du cœur externe. Dans ces conditions, il n'y a plus qu'une seule équation qui modélise l'amplification : celle qui simule l'amplification du signal et son interaction avec la pompe. Cela s'écrit à l'aide du facteur d'amplification α_{ampli} :

$$\alpha_{\text{ampli}} = \sigma_{sa}(\eta_s N_2 - N_1) \quad (38)$$

et qui devient

$$\alpha_{\text{ampli}} = \alpha_p N_t \frac{\eta_s \frac{I_p}{I_{p0}} - 1}{1 + \frac{I_p}{I_{p0}} + \frac{I_s}{I_{s0}}} \quad (39)$$

en remplaçant N_1 et N_2 par leurs expressions données par les équations (4). L'intégration de l'équation

$$\frac{\partial I_s}{\partial z} = \alpha_{\text{ampli}} I_s \quad (40)$$

se fait alors en supposant que l'évolution de $I_p(x, y, z)$ est connue.

En pratique, les simulations sont effectuées avec une modélisation plus fine de la pompe. En raison de l'effet de saturation, l'évolution de la pompe exhibe deux régimes exponentiels, avec deux valeurs distinctes pour α_p . Il était plus simple de décrire uniquement la modélisation pour une exponentielle pure, mais la méthode s'adapte, sans difficulté, à la situation véritablement traitée.

III. CAVITÉS MICRO-ONDES « SEMICLASSIQUES »

Les trajectoires classiques (rayons géométriques) forment le squelette des méthodes semiclassiques. Plus précisément, si l'on s'intéresse au spectre d'un système, ce sont les orbites périodiques qui vont jouer un rôle clef. Pour les modes, les scars sont des évidences du rôle particulier et inattendu – du point de vue des théories « globales », comme la théorie des matrices aléatoires – joué par certaines orbites périodiques dans le domaine ondulatoire. Tout aussi inattendue est l'influence que peut avoir un simple diffuseur ponctuel sur le spectre d'un système, intégrable ou chaotique. Des études numériques ont en effet montré, il y a quelques années, que les statistiques spectrales d'un système possédant un défaut quasi-ponctuel étaient, d'une part, très différentes des statistiques du système vierge, et d'autre part, pouvaient s'interpréter en termes de la famille particulière d'orbites périodiques qui heurtent le diffuseur et que l'on appelle, dans ce cas, des « orbites diffractives ». Ma contribution à cet effort de recherches est présenté en III.B. Cet article offre une introduction au sujet et présente l'influence des orbites diffractives sur le facteur de forme.

Le problème du diffuseur ponctuel est resté très longtemps quasi académique, car inaccessible aux expériences, et sans application évidente. Grâce au savoir-faire acquis au cours de la thèse de Jérôme Barthélémy (voir la section IV), j'ai proposé de vérifier expérimentalement la prégnance des orbites diffractives dans une situation où le diffuseur est de plus d'un ordre de grandeur inférieur en taille à la plus petite des longueurs d'onde se propageant dans le système, en l'occurrence une cavité micro-onde. Outre l'aspect fondamental, l'idée est de promouvoir une technique semiclassique de détection non invasive de défauts. L'objectif à moyens termes de la thèse de David Laurent, financée par la DGA, était la démonstration de cet effet. Il faut en effet parler au passé car nous avons pu récemment mettre en évidence des signatures franches de la présence du petit diffuseur dans le « spectre de longueur » de la cavité ; cette dernière quantité, qui s'obtient à partir de la connaissance précise du spectre, fournit un catalogue de toutes les longueurs associées aux orbites périodiques du billard équivalent. Bien que de moindre amplitude, les orbites diffractives y apparaissent très nettement et fournissent même un moyen, comme nous l'avons vérifié, de suivre l'évolution du défaut constitué par le diffuseur. Ces résultats constituent l'essentiel de l'article présenté en III.C.

A. Un diffuseur (quasi-)ponctuel dans une cavité

Le « cœur dur » du message que j'aimerais faire passer dans ce chapitre est contenu dans les deux articles proposés en III.B et III.C, et surtout dans le deuxième. Je

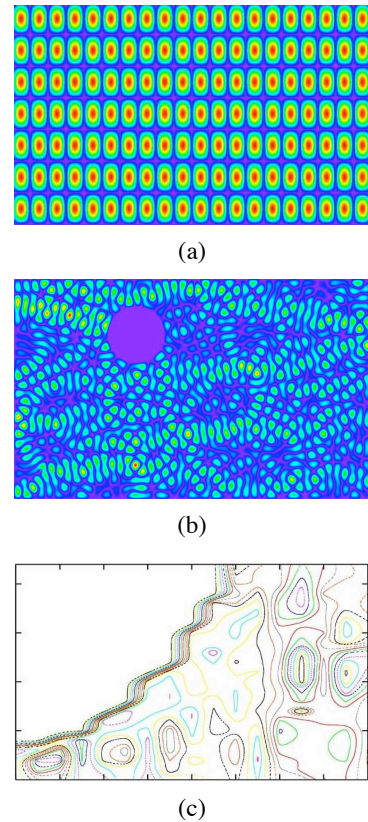


FIG. 11 (a) et (b) Modes calculés numériquement dans une cavité rectangulaire vide (a) ou en présence d'un diffuseur de taille finie (b) ; mode mesuré expérimentalement dans une cavité de Sinai (c). Les structures spatiales sont représentatives des deux grandes familles de cavités : les cavités intégrables (a) et les cavités chaotiques (b) et (c).

souhaite simplement ici donner un avant-goût de la richesse d'une situation physique que l'on pourrait penser pauvre : un diffuseur ponctuel dans une cavité ! Le niveau technique est volontairement léger, contrairement aux deux articles qui suivent. Le lecteur spécialiste y trouvera des illustrations, parfois originales, de concepts connus, le lecteur simplemement « averti » pourra le lire comme une introduction en images au sujet.

Le spectre et les modes d'une cavité rectangulaire métallique (conditions aux bords de Dirichlet) de dimension $L_x \times L_y$ sont étiquetés par un couple d'indices (de « nombres quantiques ») (n, m) , avec $n, m \in \mathbb{N}^*$. La donnée du couple (n, m) est, en effet, suffisante pour exprimer la fréquence propre ou le nombre d'onde propre

$$k_{nm} = \sqrt{\left(n \frac{\pi}{L_x}\right)^2 + \left(m \frac{\pi}{L_y}\right)^2} = \frac{1}{c} \omega_{nm} \quad (41)$$

ainsi que la fonction d'onde

$$\psi_{nm}(x, y) = \frac{2}{\sqrt{L_x L_y}} \sin\left(n \frac{\pi x}{L_x}\right) \sin\left(m \frac{\pi y}{L_y}\right) \quad (42)$$

La figure 11 (a) montre, par exemple, le mode (20,7) : la structure spatiale est d'une grande simplicité. En revanche, lorsqu'un diffuseur de taille finie est introduit dans la cavité, la carte de champ devient très chahutée (figure 11 (b)). On a construit une cavité chaotique, et le chapitre précédent a suffisamment discuté de la richesse des modes d'une structure chaotique, pour que je n'ai pas à y revenir ici. Une question intéressante, qui a été posée dès le début des années 90, est de savoir quelle famille, celle des modes réguliers ou celle des modes chaotiques, adopte une cavité intégrable perturbée par un « petit » diffuseur²³. Gardons, pour l'instant, un flou sur l'influence et la taille du diffuseur, nous leurs donnerons un sens précis dans quelques lignes.

La figure 12 représente de manière schématique les modes d'une cavité rectangulaire aux fréquences correspondant à des dimensions $L_x = 20 \text{ cm}$ et $L_y = 12.4 \text{ cm}$. Une mesure expérimentale du mode (5,2), dans une cavité micro-ondes, est également présentée. Rapidement, la mesure consiste à suivre le décalage en fréquence du maximum de la courbe de résonance d'un mode donné, consécutif au déplacement en fréquence d'une bille métallique à l'intérieur de la cavité. Pour cette figure, la technique est très sommaire, la bille étant déplacée « à la main » par l'intermédiaire d'un aimant extérieur à la cavité. La taille de l'aimant interdit de parcourir l'ensemble de la cavité, ce qui explique l'absence de mesures sur les bords. Cette technique a été, depuis, « professionnalisée » et sera revue en IV.D. La figure 11 (c) montre la carte d'intensité, ainsi obtenue, d'un mode d'une cavité de type billard de Sinaï.

Les cartes d'intensité représentées sur la figure 13 sont obtenues alors qu'un diffuseur métallique de diamètre 6 mm est introduit dans la cavité micro-ondes. Rappelez que 5 GHz correspond à une longueur d'onde de 6 cm et que le champ ne pénètre pas dans le diffuseur. Les deux modes apparaissant aux fréquences les plus voisines de la fréquence du mode (5,2) de la cavité vide sont représentés. On peut remarquer que les fréquences n'atteignent pas les valeurs des deux modes voisins de (5,2) dans la cavité vide ; ce constat est en fait une règle, comme le montrera, plus bas, le calcul du spectre. La qualité atteinte par les cartes d'intensité ne permet pas une analyse quantitative, mais elle est suffisante pour constater le comportement surprenant du système. Tout d'abord, loin d'une simple modification locale de la structure du mode (5,2), on observe des structures totalement différentes. Cependant, une réminiscence de la structure des modes réguliers est nettement visible : on pourrait qualifier le mode à 4.33 GHz de quasi-(4,2) et celui à

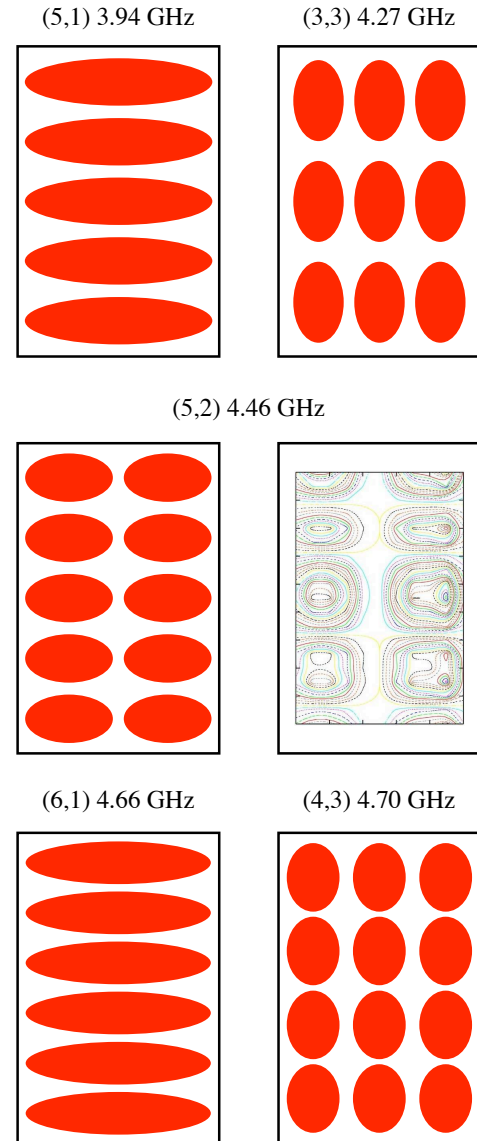


FIG. 12 Représentations schématiques de quelques modes d'une cavité micro-ondes rectangulaire ($L_x = 20 \text{ cm}$, $L_y = 12.4 \text{ cm}$) autour du mode (5,2) à 4.46 GHz ; la carte d'intensité obtenue expérimentalement est également montrée, pour ce mode.

4.47 GHz de quasi-(2.5,3) (le concept de nombre quantique fractionnaire dans ce contexte reste à définir...) En fait, les structures observées peuvent s'obtenir par une superposition linéaire des modes réguliers, voisins du mode (5,2) (figure 12). Cet effet de couplage des résonances – qui s'observe en mécanique quantique de base avec le double puits de potentiel – a été étudié expérimentalement dans une cavité micro-ondes rectangulaire par l'équipe de Marburg²⁴

²³ P. Seba, Phys. Rev. Lett. **64**, 1855 (1990) ; T. Shigehara, Phys. Rev. E **50**, 4357 (1994) ; voir également les références citées dans les introductions des deux articles III.B et III.C.

²⁴ U. Kuhl, E. Persson, M. Barth, and H.-J. Stöckmann, Eur. Phys. J. B **17**, 253 (2000). Dans cette étude, c'est l'antenne de mesure

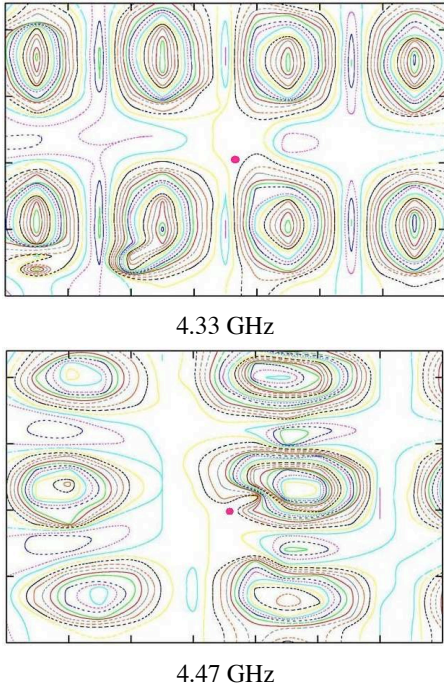


FIG. 13 Cartes d'intensité du champ micro-ondes dans la cavité perturbée par un diffuseur quasi-ponctuel (point rouge sur les cartes)

Intéressons-nous maintenant aux spectres d'une cavité perturbée par un petit diffuseur. Pour ce faire, je vais introduire brièvement le modèle numérique utilisée en III.B et, dans une moindre mesure, en III.C. Ce faisant, nous allons préciser, ce que la communauté entend par diffuseur ponctuel. Le « modèle standard » consiste à utiliser un diffuseur de rayon a dont la taille effective s'annule avec la longueur d'onde. Pour l'équation d'onde en dimension 2, la section efficace du diffuseur qui entraîne cette propriété²⁵ s'écrit

$$\sigma = \frac{4}{\omega(1 + 16\alpha^2)} \quad (43)$$

où α est un paramètre qui contrôle la force du diffuseur. On pourra le prendre constant (avec quelques précautions, voir la discussion en III.B) mais il dépend de k comme

$$\alpha(k) = -\frac{1}{2\pi} \ln \left(\frac{k}{k_0} \right) + \text{const.} \quad (44)$$

où $k_0 = 2/a$ (voir III.C).

qui joue le rôle du diffuseur ponctuel.

²⁵ Attention à la coquille dans l'écriture de la section efficace dans l'équation (1) de l'article III.B. Cette erreur est sans gravité dans cet article où seul le cas $\alpha = 0$ est traité!

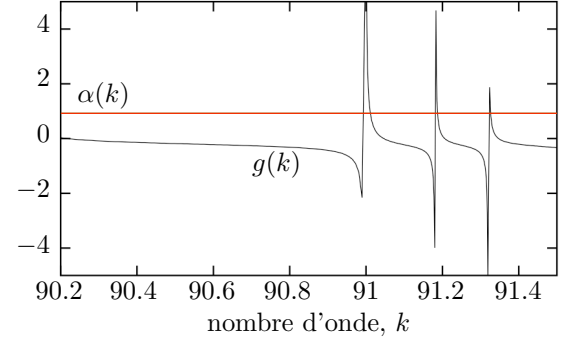


FIG. 14 Calcul des modes de la cavité perturbée par résolution graphique de l'équation (45); à l'échelle de la figure, $\alpha(k)$ dessine une droite presque horizontale.

Le spectre de la cavité perturbée est obtenu²⁶ en déterminant les valeurs de k qui satisfont la contrainte

$$\alpha(k) = g(k) \simeq \sum_{n,m} \psi_{nm}^2(\vec{r}_s) \frac{4k^6}{k^8 - k_{nm}^8} - \frac{1}{4} \quad (45)$$

Cette équation se prête très bien à une résolution graphique, comme le montre la figure 14. Les modes de la cavité rectangulaire fournissent les singularités de la courbe $g(k)$, les modes recherchés se placent donc toujours entre deux modes k_{nm} . Sur la gamme de vecteurs d'onde couverte dans la figure 14, l'évolution du paramètre α est presque parfaitement confondue avec une droite. Cette remarque est vraie pour presque tout le spectre, à l'exception des premiers modes. C'est en ce sens que supposer α constant n'est pas, en pratique, pathogène. Une fois le spectre connu, on peut le passer dans divers cibles statistiques. Parmi les plus couramment utilisés, je ne vais présenter, ici, que le plus simple (une quantité plus complexe est abordé en III.B) : la distribution des écarts entre niveaux voisins²⁷, $P(s)$. Les systèmes intégrables et chaotiques se distinguent, entre autres, par des expressions respectives très différentes de cette distribution, chacune portant le nom d'un physicien célèbre : Poisson, pour les premiers, et Wigner, pour les seconds. Concrètement :

$$\text{Poisson} : P(s) = \exp(-s) \quad (46)$$

$$\text{Wigner} : P(s) = \frac{\pi}{2} \exp\left(-\frac{\pi}{4}s^2\right) \quad (47)$$

Elles sont représentées sur la figure 15 : les différences sont frappantes ! Les nombreuses quasi-dégénescences qui caractérisent un système intégrable (forte probabilité d'écart nul) disparaissent totalement dans un système chaotique. Ce dernier exhibe de la « répulsion de niveaux ». Autre différence caractéristique, la distribution

²⁶ R. L. Weaver and D. Sornette, Phys. Rev. E **52**, 3341 (1995).

²⁷ Pour une présentation simple des diverses distributions ou moments, voir : H.-J. Stöckman, *Quantum Chaos*, Cambridge University Press (1999).

de Wigner est beaucoup plus ramassée que celle de Poisson. La figure 15 montre les distributions d'écart de niveaux obtenues pour différentes forces du diffuseur ponctuel. La distribution de Poisson semble bien représenter la distribution limite atteinte pour un diffuseur « transparent » ($\alpha \rightarrow \infty$). Par contre, dans la limite opposée d'un diffuseur très efficace ($\alpha \rightarrow 0$), le système ne bascule pas franchement dans un comportement chaotique. De la répulsion de niveaux apparaît, mais le comportement au grand espacements s'écarte très sensiblement de la loi de Wigner. Ce résultat n'est pas original ! C'est au tournant du siècle qu'est apparue cette statistique intermédiaire, dont le nom « semi-Poisson²⁸ » ne signale pas un être chimérique, cousin de l'ondin, mais traduit la difficulté de placer les systèmes qui l'arborent dans une catégorie franche. Sa forme canonique est donnée par

$$\text{Semi-Poisson : } P(s) = 4s \exp(-2s) \quad (48)$$

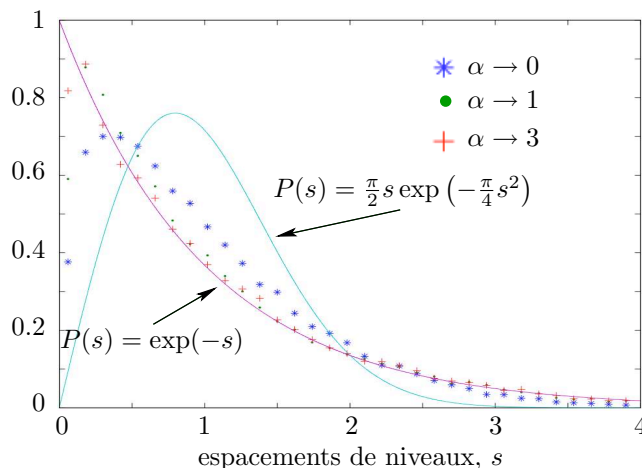


FIG. 15 Distributions $P(s)$ des espacements de niveaux d'une cavité rectangulaire avec un diffuseur ponctuel pour différentes valeurs asymptotiques du paramètre α . Dans la situation où le diffuseur est le plus efficace ($\alpha \rightarrow 0$), $P(s)$ ne suit pas la distribution de Wigner.

Il existe de nombreux travaux sur ce type de statistiques particulières, qui s'obtiennent en supprimant plus ou moins aléatoirement certains niveaux dans un spectre donné ou en construisant un spectre à partir des positions médianes des intervalles entre deux modes consécutifs²⁹. On se rend compte sur la figure 14 que les modes de la cavité perturbée se rapprochent de cette dernière situation

pour $\alpha \rightarrow 0$. Notons pour conclure sur le lien entre diffuseur ponctuel et statistiques spectrales, qu'un modèle où la section efficace ne s'annule pas avec la longueur d'onde conduit, lui aussi, à une distribution intermédiaire³⁰.

Après ce rapide survol des propriétés intéressantes que confère un diffuseur (quasi-)ponctuel à une banale cavité rectangulaire, nous allons, au travers des deux articles suivants, rentrer plus profondément dans le sujet. La quantité centrale dans les deux études présentées est le facteur de forme, à partir duquel on déduit la « conditional number density » (étude numérique présentée en III.B), ou le spectre de longueur (étude expérimentale présentée en III.C).

²⁸ Proposé pour la première fois dans la référence : E. B. Bogomolny, U. Gerland, and C. Schmit, Phys. Rev. E **59**, R1315 (1999).

²⁹ H. Hernández-Saldaña, J. Flores, and T. H. Seligman, Phys. Rev. E **60**, 449 (1999) ; voir également la publication récente suivante et les références s'y trouvant : O. Bohigas and M. P. Pato, Phys. Rev. E **74**, 036212 (2006).

³⁰ Même si le premier à s'intéresser à cette physique des diffuseurs ponctuels a cru distinguer la distribution de Wigner : P. Seba, Phys. Rev. Lett. **64**, 1855 (1990).

B. Semiclassical analysis of spectral correlations in regular billiards with point scatterers, Physical Review E 55, 7741 (1997)

Malgré son ancienneté : il date d'une période antérieure à la création de l'équipe POMC (donc avant le passage au cap expérimental), cet article est totalement d'actualité. Son association avec le suivant, montre comment un thème provisoirement mis en sommeil peut resurgir lorsque des moyens nouveaux sont acquis. Le message se concentre ici sur le facteur de forme spectral d'une cavité rectangulaire « habillée » par un diffuseur ponctuel. Il s'agit, dans cette étude numérique, d'un vrai diffuseur ponctuel dont la section efficace de diffusion est inversement proportionnelle à la fréquence. L'évolution du facteur de forme en fonction de l'espacement moyen entre niveaux (calculés suivant la méthode présentée précédemment) s'écarte sensiblement des prédictions de la théorie des matrices aléatoires. Cet écart est associé à l'existence de deux familles d'orbites périodiques : celles qui heurtent ou pas le diffuseur ponctuel.

Il faut cependant reconnaître un défaut à cet article : le modèle numérique³¹ sur lequel il repose souffre d'une pathologie ! En effet, les modes de la cavité perturbés ne sont pas orthogonaux. L'erreur tient dans le fait d'avoir contrôlé la force du diffuseur par un paramètre constant α . Dans l'annexe de l'article III.C, nous montrons qu'en relâchant cette contrainte on rétablit l'orthogonalité des fonctions propres, dans le même temps que α gagne une dépendance en k . La concession à la réalité physique faite dans le présent article ne remet cependant pas en question les effets mis en exergue. Le spectre de la cavité perturbée est très peu affecté par la dépendance en nombre d'onde du paramètre α .

Je tiens aussi à signaler qu'une des raisons qui m'a poussé à sélectionner cet article est qu'il est le seul écrit en commun avec Richard Weaver. Fait étonnant car depuis notre première rencontre (à l'occasion de ma soutenance de thèse !) nos contacts ont été très réguliers, et j'ai très souvent bénéficié de ses précieux conseils.

³¹ R. L. Weaver and D. Sornette, Phys. Rev. E **52**, 3341 (1995).

BRIEF REPORTS

Brief Reports are accounts of completed research which do not warrant regular articles or the priority handling given to Rapid Communications; however, the same standards of scientific quality apply. (Addenda are included in Brief Reports.) A Brief Report may be no longer than four printed pages and must be accompanied by an abstract. The same publication schedule as for regular articles is followed, and page proofs are sent to authors.

Semiclassical analysis of spectral correlations in regular billiards with point scatterers

Olivier Legrand,¹ Fabrice Mortessagne,¹ and Richard L. Weaver²

¹Laboratoire de Physique de la Matière Condensée, CNRS URA 190, Université de Nice-Sophia Antipolis, Parc Valrose, 06108 Nice Cedex 2, France

²Department of Theoretical and Applied Mechanics, University of Illinois, 104 South Wright Street, Urbana, Illinois 61801

(Received 13 May 1996)

A semiclassical analysis is proposed to elucidate quantitatively the deviations from the predictions of the random matrix theory of the observed conditional number density in rectangular billiards with point scatterers [R. L. Weaver and D. Sornette, Phys. Rev. E **52**, 3341 (1995)]. Using the scattering cross section of the point scatterer, the spectral form factor is shown to be built on two categories of periodic orbits depending whether they are scattered or not. Our quantitative predictions are successfully compared to the observed spectral correlations in various cases of a rectangular billiard with one or several point scatterers. [S1063-651X(97)14106-X]

PACS number(s): 05.45.+b, 03.65.Sq, 03.40.Kf

It has been conjectured that the eigenvalue statistics of generic systems which are classically chaotic are identical to those of random matrices belonging to the Gaussian orthogonal ensemble (GOE). It is also accepted that regular integrable systems should display Poisson statistics. However, many classically integrable systems have been shown to exhibit spectral rigidity which is typical of GOE-like systems [1,2]. A particular example is the singular quantum billiard introduced by Seba [2]. It consists of a rectangular billiard with an isotropic point scatterer. In previous works [3,4], conditions for the appearance of level repulsion or spectral rigidity have been discussed, and a quantitative prediction for the range of GOE-like statistics was proposed in Ref. [3], relying upon a proper definition of the scattering cross section of the scatterer. Here we present a semiclassical analysis of the spectral form factor in order to provide quantitative predictions for the conditional density of levels in rectangular billiards with one or several point scatterers. Those predictions are compared with the statistics of eigenvalues numerically evaluated through the method introduced in Ref. [3].

A regular billiard with a point scatterer remains fully integrable. At finite time, and except for a set of measure zero, the infinitesimal scatterer does not affect ray paths. One might therefore presume that the statistics remain Poissonian. This may be contrasted with the usual asymptotic consideration of the fully chaotic Sinai billiard, in which the wavelength is taken to zero while the radius of the removed arc is kept finite, and the statistics are GOE. If, however, one investigates the *distinguished limit* in which scatterer size is taken to zero at the same rate that wavelength is taken to zero, one recovers a regime of considerable current interest. This is precisely the limit implicit in recent studies [2–4] of the isotropic point scatterer with finite cross section in a rect-

angular billiard. The limit could presumably also be reached by study of a Sinai billiard with small arc at large, but finite, energy. We know of no such studies.

First, we briefly recall that a point scatterer in any dimension $D \geq 2$ cannot be represented through a scattering potential. The scatterer is in fact properly defined by its t matrix in terms of which its cross section is readily obtained. For the Helmholtz wave equation in two dimensions, the latter is a length σ which depends on the frequency ω and on a “strength” dimensionless parameter α as [3]

$$\sigma = 4/(\omega \sqrt{1 + 4\alpha^2}). \quad (1)$$

This form is readily obtained by imposing flux conservation between incident and scattered waves which yields a one-parameter transition strength for the scatterer. In a finite system, this procedure enables one to find the modes of the dressed system (i.e., with the point scatterer) through the modes of the bare system (i.e., without the point scatterer) by using the Lippman-Schwinger equation relating the dressed Green’s function to the undressed Green’s function via the parameter α [see Eqs. (14)–(23) of Ref. [3]]. This one-parameter family of eigenvalues constitute the spectrum of the self-adjoint extensions of the Helmholtz operator in the presence of a point scatterer [4]. The procedure presented in Ref. [3] is extended to the case of several scatterers by the analysis presented in the Appendix.

To study quantitatively the spectral correlations among the eigenvalues associated with the rectangular membrane (Dirichlet boundary condition) with a point scatterer, we follow a semiclassical analysis along the lines proposed by Argaman, Imry, and Smilansky [5]. In the following, we will use the dimensionless frequency variable $x \equiv \omega/\langle \Delta \omega \rangle$, where ω is the angular frequency and $\langle \Delta \omega \rangle$ is the mean frequency

spacing between adjacent modes around ω . This amounts to considering the so-called unfolded spectrum [6]. Now, the commonly considered nearest-neighbor spacing distribution, though revealing a possible level repulsion, is not very sensitive to mid-range or long-range correlations. Instead, the conditional probability $g(s)ds$ of finding a level in the interval $[x+s, x+s+ds]$, given that there is one level at x (assuming here and in the rest that the spectrum is stationary), is a true two-point measure likely to characterize spectral rigidity. The latter notion manifests itself in the slow increase of the variance of the number of levels in a given frequency interval with the mean value of this number [typically, for GOE spectra, $\Sigma^2 \equiv \langle (N - \langle N \rangle)^2 \rangle \approx (2/\pi^2) \ln(2\pi\langle N \rangle)$ for large $\langle N \rangle$ whereas, for uncorrelated Poisson spectra, $\Sigma^2 = \langle N \rangle$] [6]. The conditional number density $g(s)$ is equivalently expressed as $1 - \delta(s) + K(s)$ where $K(s) = \langle (d[x-(s/2)] - 1)(d[x+(s/2)] - 1) \rangle$ is the autocovariance of the spectral density $d(x) = \sum_n \delta(x - x_n)$ (the mean value of which is unity). Defining the spectral form factor as the Fourier transform $\tilde{K}(\tau) = \int ds e^{i\tau s} K(s)$, one may show (see Ref. [5] and also Berry's course in Ref. [7]) that a semiclassical evaluation of the form factor is obtained as a sum over periodic orbits of the corresponding billiard, which reads (in the diagonal approximation)

$$\tilde{K}(\tau) \approx \sum_{\text{p.o.'s}} |A_j|^2 \delta(\tau - \tau_j), \quad (2)$$

where the A_j 's are the amplitudes and the τ_j 's are the dimensionless periods ($\langle \Delta\omega \rangle T = \tau$, with T the true period) of the periodic orbits. This sum rule yields a valid approximation of the spectral form factor for values of τ much larger than $\langle \Delta\omega \rangle T_0$ (with T_0 being the period of the shortest periodic orbit) and still much smaller than 2π . For larger values of τ , another sum rule, proposed by Berry [7], shows that $\tilde{K} \rightarrow 1$ if $\tau \gg 2\pi$. The sum rule given by Eq. (2) has proved to give the correct universal behavior as well in generic regular systems [where $\tilde{K}(\tau) = 1$, yielding the Poisson statistics for uncorrelated spectra, see, for instance, Ref. [8]] as in chaotic systems with or without time reversal invariance [where $\tilde{K}(\tau) \approx \tau/\pi$, which is the small τ leading behavior of the GOE form factor $1 - b_{\text{GOE}}(\tau)$; see, for instance, [7]].

The key to the following argument will be to consider that the wave problem associates a finite size of the order of the cross section to the point scatterer, and that this coarse-grained scale should be taken as the diameter of a virtual disk centered at the position of the scatterer, and fixing an effective range of action of the latter on ray trajectories in the billiard. Thus, when considering the problem of a point scatterer in a regular billiard like the rectangle, one should subdivide the periodic orbits (p.o.'s) into two categories: the first group consists of p.o.'s of the original regular billiard which do not hit the disk associated to a "coarse-grained" scatterer while the other group consists of "new" trajectories which hit this disk at least once, and which are responsible, at large enough times, for the ergodic regime of the wave problem. Here we would like to stress that our approach is concerned with an integrable system with one or a few point scatterers, and not with hyperspherical rigid scatterers placed at random in a hypercubic billiard in the limit of vanishing wavelength

compared to the size of the spheres. The latter problem was recently addressed in Ref. [9], and focused principally on the transition from ballistic to diffusive regimes. If sufficiently many pointlike impurities were placed in the rectangle billiard, one could eventually envisage a diffusive dynamical regime for times intermediate between the ballistic regime and the ergodic one, as considered in Ref. [5].

In a two-dimensional billiard of area S , the rate at which a typical ray hits a disk of diameter σ is given by the expression $\Gamma = \pi\sigma/\pi S$ (see, for instance, Ref. [10]). Using the leading part of Weyl's formula for the modal density at high frequencies, the mean spacing between adjacent eigenfrequencies reads $\langle \Delta\omega \rangle \approx 2\pi/\omega S$, which enables one to define the dimensionless rate

$$\gamma = \Gamma/\langle \Delta\omega \rangle = \frac{\omega\sigma}{2\pi} = \frac{2}{\pi\sqrt{1+4\alpha^2}}. \quad (3)$$

One then proceeds to evaluate the spectral form factor by summing up the contributions associated to the two categories of p.o.'s mentioned above. In the dressed rectangle, the fraction of regular periodic trajectories (belonging to the periodic orbits of the regular undressed billiard) which have not met the scatterer at time τ may be approximated to decay like $\exp(-\gamma\tau)$, thus reducing by an identical factor the amplitude A associated with those orbits in the sum rule (2). Since the sum rule in the integrable billiard yields $\tilde{K}(\tau) \rightarrow A^2(\tau)\rho_b(\tau) = 1$ [8], where $\rho_b(\tau)$ is the density (per unit dimensionless time) of p.o.'s of the bare rectangle, one deduces the "regular part" of the form factor of the dressed rectangle

$$\tilde{K}_d^{\text{reg}}(\tau) \approx e^{-2\gamma\tau}. \quad (4)$$

For the other group of p.o.'s, one can reasonably assume that the corresponding "ergodic part" of the form factor is obtained through the ansatz consisting of multiplying the GOE form factor by the relative fraction of trajectories which have met the coarse-grained scatterer at least once before the time τ

$$\tilde{K}_d^{\text{erg}}(\tau) = (1 - e^{-\gamma\tau})[1 - b_{\text{GOE}}(\tau)]. \quad (5)$$

Indeed, according to Ref. [5], a semiclassical evaluation of the spectral form factor is obtained as (in the case of time-reversal symmetry) $\tilde{K}(\tau) \approx (\tau/\pi)P(\tau)$, where $P(\tau)$ denotes the classical probability for periodic motion. The factor (τ/π) is in fact the so-called diagonal approximation of the GOE spectral form factor $1 - b_{\text{GOE}}(\tau)$, and $P(\tau)$, in the present case, should be given by $(1 - e^{-\gamma\tau})$ for times large enough compared to the time of flight t_f across the billiard. Presumably, there exist deviations from the GOE (see Ref. [11]), and the contribution from the ergodic orbits could be modified to account for them, but they do not concern us as all the levels we study are in the regime $\tilde{g} \gg 1$, where $\tilde{g} \equiv 1/(\langle \Delta\omega \rangle t_f)$ is the so-called dimensionless conductance. By summing both contributions, Eqs. (4) and (5), one obtains our approximation for the complete form factor $\tilde{K}_d(\tau)$ for the dressed rectangle. A numerical inverse Fourier transform then leads to the corresponding conditional number density $g_d(s)$. Our result differs from that obtained by Agam and

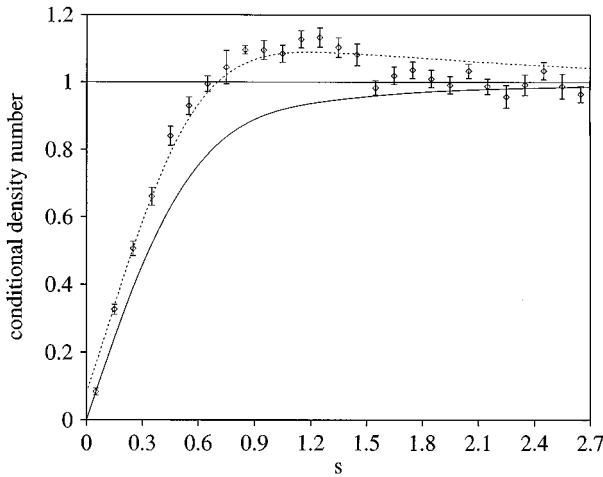


FIG. 1. Conditional number density observed among more than 10^4 even-even modes in the dressed rectangle with a single-point scatterer at the center. It is compared to an evaluation of the conditional density $g_d(s)$ (dotted line) obtained through a numerical inverse Fourier transform of our approximation for the complete form factor $\tilde{K}_d(\tau)$ with $\gamma=2/\pi$. For the sake of comparison, the prediction of the GOE is shown (solid line).

Fishman [9] for two chief reasons: (a) our formula (4) differs by a factor of 2 from the corresponding formula (5) in the first of Ref. [9]; (b) in Ref. [9], their system has the geometry of the torus (leading to the absence of periodic orbits which are scattered only once), whereas ours has Dirichlet boundary conditions: this explains why the fourth term of formula (5.9) in the second of Ref. [9] does not appear in our result. A related result was obtained by Altland and Gefen [12] through a diagrammatic perturbative analysis of nondiffusive disordered electron systems; apart from the term accounting for the orbits that are not scattered, their result [Eq. (32) of Ref. [12]] is identical to that obtained by Agam and Fishman [9], and thus differs from ours in the limit studied in the present paper, namely, the ballistic regime.

In Fig. 1, we plot the conditional density observed among more than 10^4 levels corresponding to even-even modes obtained in ten different rectangles with a single-point scatterer at the center (see Ref. [3]; also see the Appendix, where a discussion of the method by which the numerical data were generated is given in the general case of many scatterers, as well as a short summary of what systems were studied and what the range of eigenvalues examined). The parameter α was chosen to be zero. This numerical result is compared to the inverse transform of the sum of Eqs. (4) and (5) [13] (dotted line) with $\gamma=2/\pi$ and also to the conditional density for GOE spectra, namely, $1 - Y_{2,\text{GOE}}(s)$. The agreement is fair, especially for values of s smaller than unity. For larger values, oscillations are seen in the numerical data which cannot be reproduced by the above ansatz. In Fig. 2, we plot (a) the conditional density observed for levels in a rectangle billiard with three maximum strength scatterers ($\alpha=0$) located at random positions not too near the edge and compare it to our prediction (dotted line) with $\gamma=6/\pi$; and (b) the same for a rectangle billiard with six maximum strength scatterers located at random positions not too near the edge and with $\gamma=12/\pi$. Again, even if numerical data are closer to the GOE behavior, the agreement with our ansatz is still significant.

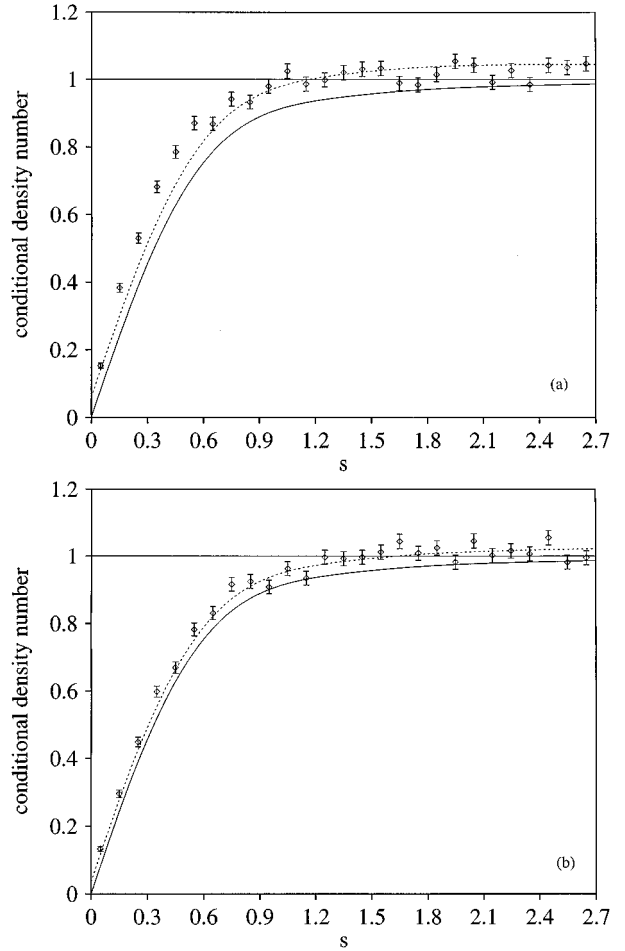


FIG. 2. Same as in Fig. 1 for the cases of a rectangular billiard with (a) three full strength scatterers placed at random, and (b) six full strength scatterers placed at random. The dotted line shows our prediction with (a) $\gamma=6/\pi$ and (b) $\gamma=12/\pi$.

In conclusion, we have proposed a quantitative prediction for the conditional density in rectangle billiards with point scatterers, using a semiclassical analysis of the spectral form factor based on the partition of periodic orbits in two categories: one accounts for the regular behavior of the spectrum correlations at large frequency range, while the other one builds upon scattered orbits which contribute to the ergodic part of the form factor leading to short- and intermediate-range spectral rigidity. This prediction was shown to be in good agreement with numerically observed levels in the rectangular billiard with either a single centered scatterer or a few point scatterers placed at random. It is remarkable that such a simple theory does as well as it does in spite of its limitations.

It is our pleasure to thank D. Sornette for very fruitful discussions on this problem. One of us (O.L.) wishes to acknowledge very stimulating discussions with Eugene Bogomolny.

APPENDIX

We define the bare Green's function, $G^0(\vec{r}, \vec{s})$ as the harmonic (ω) response at position \vec{r} to a unit source at \vec{s} in a rectangular domain without scatterers. The response $G(\vec{r}, \vec{s})$

in the system with j scatterers ($j=1,2,3,\dots,n$) is a superposition of a response which directly propagates by means of G^0 , and several fields, each the bare response to a point source of as yet unknown strengths A_j at positions \vec{b}_j . Thus the total field due to a source at \vec{s} is given by

$$G(\vec{r},\vec{s}) = G^0(\vec{r},\vec{s}) + \sum_j G^0(\vec{r},\vec{b}_j)A_j \quad (\text{A1})$$

for some as-yet-undetermined set of effective source strengths A_j . The quantities A_j in general depend on the source position \vec{s} as well as the positions and scattering strengths of all the scatterers. In the vicinity of scatterer number l , the field is

$$\begin{aligned} G(\vec{r} \approx \vec{b}_l, \vec{s}) &= G^0(\vec{b}_l, \vec{s}) + \sum_{j \neq l} G^0(\vec{b}_l, \vec{b}_j)A_j \\ &+ \left[f(\vec{b}_l) - \frac{i}{4} H_0^{(1)}(\omega \|\vec{r} - \vec{b}_l\|) \right] A_l \end{aligned} \quad (\text{A2})$$

where we have used the form given in Eq. (16) of Ref. [3] to describe the bare Green's function in the vicinity of its singularity in terms of an incident part (due to multiple reflections from the boundary) and an outgoing part. f is given by [3]

$$f(\vec{b}) = \lim_{\vec{r} \rightarrow \vec{b}} \left\{ G^0(\vec{r}, \vec{b}) + \frac{i}{4} H_0^{(1)}(\omega \|\vec{r} - \vec{b}\|) \right\}. \quad (\text{A3})$$

The efficient evaluation of f is discussed in Ref. [3]. The ratio of the coefficient of the outgoing part $H_0^{(1)}$ to the incident part is, by definition, the scattering strength of the scatterer (a property of the scatterer and independent of the system in which it is placed):

$$t_l = A_l / \left[G^0(\vec{b}_l, \vec{s}) + \sum_{j \neq l} G^0(\vec{b}_l, \vec{b}_j)A_j + f(\vec{b}_l)A_l \right]. \quad (\text{A4})$$

The complex scattering strength t_l is related to the real parameter α_l by Eq. (13) of Ref. [3]:

$$t = (i/4 + \alpha)^{-1}. \quad (\text{A5})$$

Equation (A4) may be written as an algebraic relation among the unknown source strengths A_j :

$$A_l[t_l f(\vec{b}_l) - 1] + t_l \sum_{j \neq l} G^0(\vec{b}_l, \vec{b}_j)A_j + t_l G^0(\vec{b}_l, \vec{s}) = 0. \quad (\text{A6})$$

Equation (A6) is a linear algebraic relation for the effective source strengths A_j . It is singular, indicating a resonance in the composite system, whenever the matrix of the coefficients of the A_j 's has a vanishing determinant. This is the criterion used to find the eigenvalues of the composite system.

The elements of the matrix of coefficients of the A_j 's are singular at each of the eigenvalues of the bare systems; thus the matrix can be ill conditioned near these eigenvalues. It may be shown, however, that the determinant has only a simple pole at these eigenvalues. The numerical procedures used to evaluate the determinant were therefore written to take advantage of this feature, and thereby to avoid most of the ill-conditioning.

The conditional densities reported in Fig. 2 were taken from about 22 500 levels for each of the cases (a) and (b). The 22 500 levels were taken from nine sample systems each of about 2500 levels in the range of $50 < \omega < 80$, consisting of rectangles of size $\pi \times \pi / (\sqrt{5} - 1)$. The case of the single scatterer at the center of Fig. 1 was reported in Ref. [3]; the conditional density for this case was based on 10 000 even-even levels in the range $60 < \omega < 100$.

-
- [1] T. Cheon and T. D. Cohen, Phys. Rev. Lett. **62**, 2769 (1989).
[2] P. Seba, Phys. Rev. Lett. **64**, 1855 (1990); S. Albeverio and P. Seba, J. Stat. Phys. **64**, 369 (1991).
[3] R. L. Weaver and D. Sornette, Phys. Rev. E **52**, 3341 (1995).
[4] T. Shigehara, Phys. Rev. E **50**, 4357 (1994).
[5] N. Argaman, Y. Imry, and U. Smilansky, Phys. Rev. B **47**, 4440 (1993).
[6] O. Bohigas, in *Chaos and Quantum Physics*, edited by M. J. Giannoni, A. Voros, and J. Zinn-Justin (Elsevier, Amsterdam, 1991), pp. 87–199.
[7] M. V. Berry, in *Chaos and Quantum Physics* (Ref. [6]), pp. 251–303.
[8] M. V. Berry and M. Tabor, Proc. R. Soc. London Ser. A **356**, 375 (1977).
[9] O. Agam and S. Fishman, Phys. Rev. Lett. **76**, 726 (1996); J. Phys. A **29**, 2013 (1996).
[10] F. Mortessagne, O. Legrand, and D. Sornette, Chaos **3**, 529 (1993).
[11] A. V. Andreev and B. L. Altshuler, Phys. Rev. Lett. **75**, 902 (1995); O. Agam, B. L. Altshuler, and A. V. Andreev, *ibid.* **75**, 4389 (1995); A. V. Andreev, O. Agam, B. D. Simons, and B. L. Altshuler, *ibid.* **76**, 3947 (1996).
[12] A. Altland and Y. Gefen, Phys. Rev. B **51**, 10 671 (1995).
[13] A good approximation of the conditional density number for the dressed billiard $g_d(s)$ can be obtained in the limit of large values of γ simply by replacing the product $e^{-\gamma\tau}(1 - b_{\text{GOE}}(\tau))$ by its leading behavior at small τ , namely, $e^{-\gamma\tau}/(\tau/\pi)$, thus yielding the following expression:

$$g_d(s) \approx 1 - Y_{2,\text{GOE}}(s) - \frac{1}{\pi^2 \gamma^2} \frac{1 - (s/\gamma)^2}{[1 + (s/\gamma)^2]^2}$$

$$+ \frac{1}{2\pi\gamma} \frac{1}{1 + (s/2\gamma)^2}.$$

This is presumably valid at large s , but it is found to be a fair approximation for all but the smallest ranges.

C. Diffractive orbits in the length spectrum of a two-dimensional microwave cavity with a small scatterer, Physical Review E 74, 046219 (2006)

Comme l'ont souligné avec enthousiasme les « referees », cet article offre des résultats expérimentaux nets, sur un sujet où il en existe très peu. La section II donne les quantités semiclassiques utiles pour la suite de l'article. La section III reprend le modèle numérique déjà traité en III.B, mais en corrigeant une pathologie de la version initiale. Les orbites diffractives sont parfaitement identifiées dans le spectre de longueur obtenu (figure 3). Cette section n'a pas volonté à modéliser l'expérience réalisée, mais elle doit être vue comme une démonstration, dans un cas idéal (grand nombre de modes, pas de pertes), de la pertinence des orbites diffractives. Enfin, les résultats expérimentaux obtenus dans une cavité micro-ondes sont présentés. Malgré la difficulté à extraire l'information dans le signal, la présence du diffuseur est nettement visible dans le spectre de longueur expérimental (figures 7 et 8).

Dans l'annexe nous apportons une correction au modèle proposé par Weaver et Sornette afin de rétablir l'orthogonalité des modes propres de la cavité perturbée. Ce faisant, nous mettons un terme à une controverse entre ces auteurs et Shigehara.

Diffractive orbits in the length spectrum of a two-dimensional microwave cavity with a small scatterer

David Laurent, Olivier Legrand, and Fabrice Mortessagne

Laboratoire de Physique de la Matière Condensée, CNRS UMR 6622, Université de Nice-Sophia Antipolis, 06108 Nice, France

(Received 14 July 2006; published 31 October 2006)

In a two-dimensional rectangular microwave cavity dressed with one pointlike scatterer, a semiclassical approach is used to analyze the spectrum in terms of periodic orbits and diffractive orbits. We show, both numerically and experimentally, how the latter can be accounted for in the so-called *length spectrum*, which is retrieved from two-point correlations of a finite-range frequency spectrum. Beyond its fundamental interest, this first experimental evidence of the role played by diffractive orbits in the spectrum of an actual cavity, can be the first step towards a technique to detect and track small defects in wave cavities.

DOI: 10.1103/PhysRevE.74.046219

PACS number(s): 05.45.Mt, 03.65.Sq

I. INTRODUCTION

It has been widely recognized that the semiclassical approach of spectral statistics based on periodic orbits (POs) has met a definite success in chaotic systems (see, e.g., Ref. [1] and references therein). In systems where one or more pointlike scatterers are added, a similar approach is possible, calling for both POs and the so-called diffractive orbits (DOs) [2]. If the unperturbed system is regular (with integrable ray motion), the spectral statistics induced by the presence of scatterers is clearly not predicted by random matrix theory, even if some level repulsion appears. Indeed, at large spacing, the spacing distribution decays exponentially like in a regular system [3,4]. In fully chaotic systems, on the contrary, adding scatterers has been shown to be of practically no effect on the spectral statistics [5].

In the present paper, we will show both numerically and experimentally, how the presence of short DOs can be accounted for in the so-called *length spectrum*, which one can retrieve from two-point correlations of a finite-range frequency spectrum. Our experiments are performed in microwave cavities at room temperature and the limited range of the available spectrum is a practical issue. Nevertheless, in the case of a two-dimensional (2D) rectangular (regular) cavity with one point-scatterer (actually a small scatterer in the experiments), the lengths associated to the shortest DOs are easily identified in our experiments and can be used to locate the scatterer and possibly track its displacements.

II. SEMICLASSICAL EXPANSION AND SPECTRAL DENSITY

We now briefly recall the semiclassical approach of spectral correlations based on a decomposition of the spectral density on POs. It relies on the semiclassical representation of the Green's function $G(\vec{r}, \vec{r}')$, written as a sum over classical trajectories connecting points \vec{r} and \vec{r}' ,

$$G(\vec{r}, \vec{r}') = \sum_{\text{ctr}} A_{\text{tr}}(\vec{r}, \vec{r}') \exp[iS_{\text{tr}}(\vec{r}, \vec{r}')]. \quad (1)$$

By evaluating the trace of $G(\vec{r}, \vec{r})$ through a stationary phase approximation, one obtains a semiclassical trace formula for the modal density ρ [1]. The latter is thus written as an av-

erage smooth density plus an oscillatory part,

$$\rho(k) = \bar{\rho}(k) + \rho^{\text{osc}}(k) = \bar{\rho}(k) + \sum_j A_j e^{ik\ell_j} + \text{c.c.} \quad (2)$$

Here, k is the wave number, ℓ_j is the length of the j th PO, and A_j is its complex amplitude accounting for its stability and possibly depending on k .

In diffractive systems with pointlike singularities, classical trajectories that hit those singularities can be continued in any direction. These can nonetheless be tackled with in the wave description by introducing an isotropic diffraction coefficient \mathcal{D} , which fixes the scattering amplitude at each scatterer. In previous works (see Refs. [6,7]), this diffraction constant has been calculated (with the free Green's function in Ref. [7]) to yield

$$\mathcal{D} = \frac{2\pi}{-\ln(ka/2) - \gamma + i\pi/2}, \quad (3)$$

where γ is the Euler constant and a is a characteristic length, which may be interpreted as the nonvanishing radius of an s -wave scattering disk [6], the above expression being precisely the limiting scattering amplitude for $ka \ll 1$. The semiclassical expansion of the Green's function in the presence of a point scatterer located at \vec{s} therefore reads

$$G(\vec{r}, \vec{r}') = G_0(\vec{r}, \vec{r}') + G_0(\vec{r}, \vec{s})\mathcal{D}G(\vec{s}, \vec{r}'), \quad (4)$$

where G_0 is the unperturbed Green's function. Hence formula (2) for the modal density still holds provided that non-classical contributions due to DOs are included, consistently with the geometrical theory of diffraction, yielding: $\rho^{\text{osc}} = \rho_{\text{po}}^{\text{osc}} + \rho_{\text{do}}^{\text{osc}}$. In a rectangular domain of area \mathcal{A} with a single-point scatterer, contributions from periodic orbits and diffractive orbits respectively read [8]

$$\rho_{\text{po}}^{\text{osc}}(k) = \frac{\mathcal{A}}{\pi} \sum_{\text{po}}' \sum_{r=1}^{\infty} \frac{k}{\sqrt{2\pi rk\ell_{\text{po}}}} \cos(rk\ell_{\text{po}} - rn_{\text{po}}\pi - \pi/4) \quad (5)$$

and

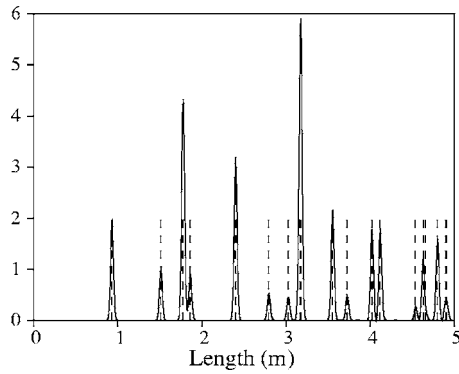


FIG. 1. Length spectrum computed in a rectangular cavity with a single-point scatterer. Approximately 11 000 resonances have been used. Dashed sticks indicate the lengths of the POs listed in Table I.

$$\rho_{do}^{osc}(k) = \sum_{do} \frac{\ell_{do}}{\pi} \frac{D}{\sqrt{8\pi k \ell_{do}}} \cos(k\ell_{do} - n_{do}\pi - 3\pi/4), \quad (6)$$

where Σ' denotes a sum over primitive periodic (diffractive) orbits of length ℓ_{po} (ℓ_{do}) and the number of bounces n_{po} (n_{do}); r is the number of repetitions. In formula (6) only leading order one-scattering events are included, repetitions or concatenations of primitive orbits of order ν being of order $\mathcal{O}(k^{-\nu/2})$ [8].

Note that the contribution of DOs is subdominant with respect to POs due to different k dependences. Nevertheless, the relevance of both POs and DOs is clearly illustrated through a weighted length spectrum [9], which is obtained by calculating the so-called form factor $K(L)$, i.e., the Fourier transform of the spectral autocorrelation $C(\kappa)$ of $\rho^{osc}(k)$:

$$C(\kappa) = \left\langle \rho^{osc}\left(k + \frac{\kappa}{2}\right) \rho^{osc}\left(k - \frac{\kappa}{2}\right) \right\rangle_k. \quad (7)$$

In practice, the local average over k in Eq. (7) can be written

$$\langle f(k) \rangle_k = \int dk' f(k') W_\sigma(k' - k), \quad (8)$$

where the weighing function W_σ is zero centered and of typical width σ . In the following, we will use either Gaussian or Hanning weighing functions.

In the so-called *diagonal approximation* [1], the following expression of the form factor is obtained [10]:

$$K(L) \propto \sum_j |A_j|^2 \delta(L - \ell_j). \quad (9)$$

Ideally, the length spectrum appears as a series of delta peaks located at particular orbit lengths ℓ_i , with real positive amplitudes (see Fig. 1).

For practical reasons, both in numerics and in analyzing our experiments, we will rather use the cumulated density $N(k) = \int_0^k dk' \rho(k')$, which is a staircase function increasing of one unit at each eigenwavenumber. This integrated quantity enables one to evaluate the form factor (9) more readily.

III. NUMERICAL LENGTH SPECTRA

To validate the possibility of identifying the shortest DOs in the short-term nonuniversal part of the length spectrum, we first investigate a numerical model of a rectangular cavity with a point scatterer (hereafter called the *dressed cavity*). To numerically obtain all the eigenfrequencies in a given frequency range for the dressed cavity, we will closely follow the method first introduced by Weaver and Sornette in Ref. [11]. This method provides a clear physical insight of the way the scatterer can be characterized by its transition matrix and scattering cross section. However, following a criticism made by Shigehara and Cheon in Ref. [12], we will correct a pathology of the aforementioned method by restoring the orthogonality of the perturbed eigenfunctions.

In 2D billiards, in the presence of a point scatterer at position \vec{s} , it is possible to write the total field Ψ at the position \vec{r} , in the vicinity of \vec{s} , as the superposition of incoming and outgoing waves,

$$\Psi(\vec{r}) \propto \left[\frac{1}{2} H_0^{(2)}(k|\vec{r} - \vec{s}|) + \left(\frac{1}{2} - i \frac{t}{4} \right) H_0^{(1)}(k|\vec{r} - \vec{s}|) \right], \quad (10)$$

where $H_0^{(1,2)}$ are the Hankel functions of first and second kinds. The parameter $t(k)$ defines the ratio of the strength of the incident field at the scatterer to the strength of the outgoing field in the vicinity of the scatterer. In terms of this parameter the scattering cross section (here a length) is given by $|t|^2/4k$. From the expression (10) for Ψ , energy conservation implies $|\frac{1}{2}|^2 = |\frac{1}{2} - i \frac{t}{4}|^2$ yielding $t = (\alpha + i/4)^{-1}$, α being a real parameter.

In the Appendix, we show how a specific k dependence of α can be established to ensure the orthogonality of the perturbed eigenfunctions. We thus reconcile the seemingly contradictory approaches of Refs. [11,12]. The resulting expression for t [Eq. (A15)] is the same as the diffraction constant in Equation (3).

Note that, apart from a logarithmic correction, the scattering cross section essentially scales as the wavelength, thus making the scatterer equally efficient at all frequencies, which is not the behavior of finite-size scatterers as used in our experiments. However, in practice, we will always be in the limiting case $ka \ll 1$. The resonances of the dressed cavity correspond to the poles of the transition matrix (A2). Practically, the ensuing characteristic equation is solved through a convergence accelerating procedure described in Ref. [11], by equating $\alpha(k) = -[\ln(ka/2) + \gamma]/(2\pi)$ to the function $g(k)$,

$$g(k) = \sum_n \Psi_n^2(\vec{s}) \frac{4k^6}{k^8 - (k_n^{(0)})^8} - \frac{1}{4}. \quad (11)$$

Here, the Ψ_n 's are the solution of the Helmholtz equation and the $k_n^{(0)}$'s are the associated eigenwavenumbers in the empty cavity. The problem of calculating the eigenwavenumbers in the presence of the point scatterer is thus solved by finding the zeroes of $g(k) - \alpha(k)$. Note that $g(k) - \alpha(k)$ has singularities for each $k_n^{(0)}$ and all its zeroes, hereafter denoted

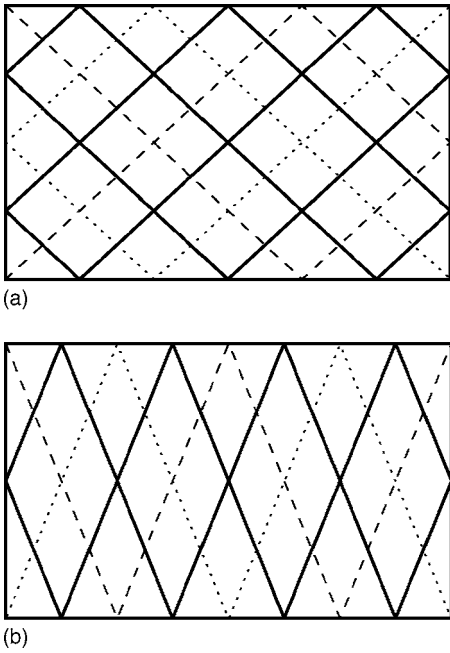


FIG. 2. Periodic orbits representation with indices (a) (2,3) and (b) (1,4). Continuous deformations of the orbit shown in thick black lines lead to the orbits shown in dotted or dashed lines.

k_i , must lie between two consecutive eigenvalues of the empty cavity. This analytical approach allows us to deal with very large frequency ranges.

In practice, we obtain the form factor and the length spectrum by calculating the Fourier transform of the difference $N(k) - \bar{N}(k)$, where the average behavior $\bar{N}(k)$ is given by Weyl's formula,

$$\bar{N}(k) = \frac{\mathcal{A}}{4\pi} k^2 - \frac{\mathcal{L}}{4\pi} k + \frac{1}{4}. \quad (12)$$

Here \mathcal{A} is the total area of the cavity and \mathcal{L} its perimeter.

An example of a length spectrum corresponding to a rectangular cavity with a single-point scatterer is given in Fig. 1. Here, the dimensions of the cavity in which we have performed our calculations are those of the actual cavity we use in our experiments: $L_x=0.7562$ m and $L_y=0.4656$ m, the scatterer is located at $x=46.5$ cm and $y=20$ cm (positions are measured from the upper left corner of the cavity sketched in Figs. 2 and 4), and the value of $a=3$ mm corresponds to the radius of the actual cylindrical scatterer. A large number of resonances (approximately 11 000) have been used so that the length resolution is excellent. To illustrate that such a length spectrum still is dominated by the POs of the empty cavity, it is shown in Fig. 1 with an amplitude scale such that the contributions of the DOs are too small to be seen.

In a rectangular cavity of side lengths L_x and L_y , the POs are identified by two indices n and m indicating the number of steps on a rectangular lattice of basis $(2L_x, 2L_y)$ (see Ref. [13]). They form families of continuously deformable orbits with the same length $\ell=2(n^2L_x^2+m^2L_y^2)^{1/2}$. For the families shown in Fig. 2, the most symmetric representative is displayed, as well as the result of continuous deformations (dot-

TABLE I. Indices and lengths (in meter) of the periodic orbits shown in Fig. 1.

(n,m)	Length	(n,m)	Length	(n,m)	Length	(n,m)	Length
(0,1)	0.931	(0,3)	2.794	(0,4)	3.725	(0,5)	4.656
(1,0)	1.512	(2,0)	3.025	(1,4)	4.020	(2,4)	4.798
(1,1)	1.776	(2,1)	3.165	(2,3)	4.118	(1,5)	4.896
(0,2)	1.862	(1,3)	3.177	(3,0)	4.537	(3,2)	4.905
(1,2)	2.399	(2,2)	3.552	(3,1)	4.632		

ted or dashed) yielding self-retracing orbits hitting two corners. Note that, in polygonal billiards, diffraction occurs only at vertices where the angle is not a submultiple of π [8]. POs are easily identified on the length spectrum shown in Fig. 1 with the help of Table I, which gives the correspondence between indices and lengths for all lengths shorter than 5 m. At first sight, it could even seem that no other contribution is to be seen as if the DOs were absent from it. Somehow, it could even be expected since no long-range correlations are observed in the frequency spectrum, thereby indicating that if the DOs should contribute, especially at short lengths, they should in a negligible way.

This is indeed what one can observe by closely inspecting a typical length spectrum for lengths smaller or of the order of the size of the cavity in the presence of a single-point scatterer. In Fig. 3, the contributions of the DOs are displayed on the length range from 0 to 1.6 m using an enlarged scale for the amplitude of the peaks. Sticks indicate the lengths of the DOs (dotted) and POs (dashed) within this range.

The shortest relevant lengths are those of the elementary self-retracing DOs starting from the scatterer and bouncing once on one of the sides of the rectangle as shown in Fig. 4(a). In Fig. 4(b), some of the shortest self-retracing DOs with one scattering event, two bounces on one side and one bounce in a corner, are drawn. In Fig. 4(c), DOs with one scattering event and three bounces are drawn. All these DOs are listed with their corresponding lengths in Table II.

In Fig. 5, we have used different Gaussian normalized frequency windows with variance $\sigma=2$ GHz centered on 10, 15, and 20 GHz to illustrate the $1/k$ dependence of the

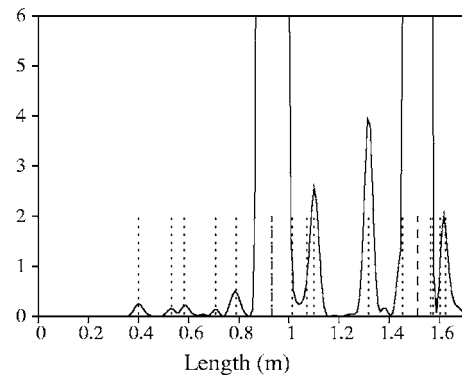


FIG. 3. Zoom ($\times 10^4$) of the length spectrum shown in Fig. 1 on the length range from 0 to 1.6 m using an enlarged scale for the amplitude of the peaks: POs (dashed sticks), DOs (dotted sticks).

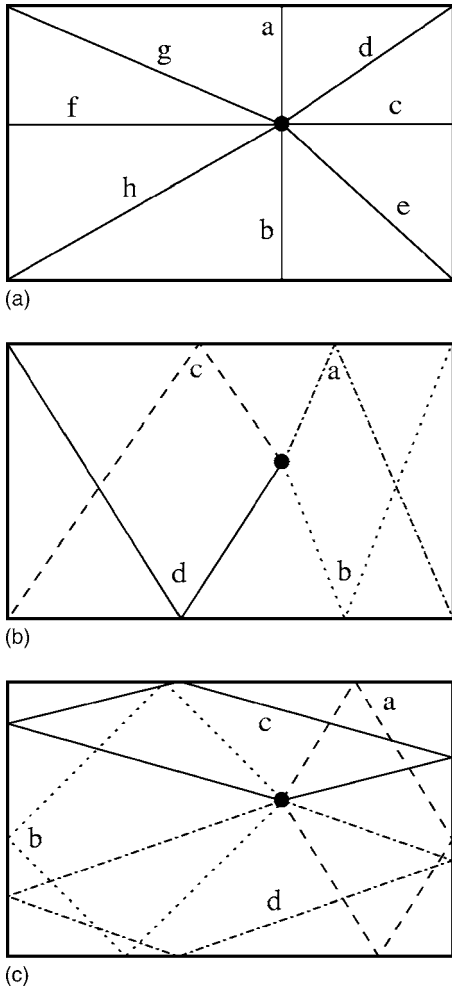


FIG. 4. Three different kinds of one-diffraction event diffractive orbits associated to the position of the scatterer used numerically and experimentally: (a) direct self-retracing DOs (first kind), (b) self-retracing DOs (second kind), (c) three-bounce DOs (third kind).

squared amplitudes associated to the DOs [see formula (6)]. An excellent agreement with the prediction of formula (6) is observed and validates the semiclassical approach. We also have observed the k dependence expected for POs [see formula (5)], but we will not present it here.

In this section we have used a model for a point-scatterer in a cavity to validate the possibility of revealing the presence of DOs in the short-term nonuniversal part of the length spectrum.

TABLE II. Lengths (in meters) of the diffractive orbits shown in Fig. 4; first, second, and third kinds refer to DOs depicted in (a), (b), and (c), respectively.

First kind		Second kind		Third kind
a: 0.400	e: 0.789	a: 1.454	a: 1.099	
b: 0.532	f: 0.930	b: 1.575	b: 1.316	
c: 0.582	g: 1.012	c: 1.625	c: 1.564	
d: 0.706	h: 1.071	d: 1.734	d: 1.603	

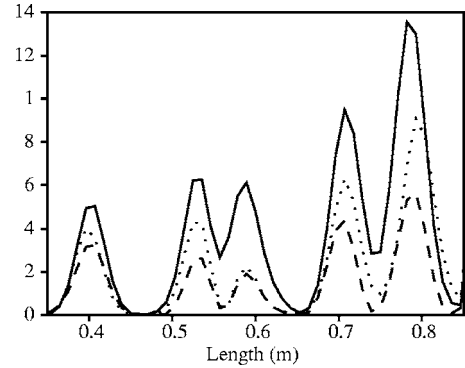


FIG. 5. Scaling law in $1/k$ of the amplitudes of the peaks associated to the DOs. Gaussian normalized frequency windows with equal variances (2 GHz) centered on 10 GHz (solid), 15 GHz (dotted), and 20 GHz (dashed) were used. An excellent agreement with the prediction of formula (6) is observed.

IV. EXPERIMENTAL LENGTH SPECTRA

In our experiments, the frequency spectra are determined from transmission signals measured in a 2D microwave cavity operated at frequencies ranging from 500 MHz to 5 GHz. The rectangular cavity is composed of two copper plates sandwiching a copper rectangular frame of thickness 5 mm and of width 2 cm. The cavity may thus be viewed as the slice of a rectangular waveguide closed at both ends, with perimeter $\mathcal{L}=2.446$ m and area $\mathcal{A}=0.3528$ m². The quality of copper is OFHC to reduce ohmic losses. Due to its height of 5 mm (smaller than half the smallest wavelength used), this cavity only admits transverse magnetic two-dimensional modes of order 0. Through one of the copper plates, ten antennas are introduced with positions determined at random. Optimal coupling was obtained by fixing their penetration length inside the cavity at 2 mm. The details about transmission measurements are described in Ref. [14]. The scatterer is a small copper cylinder of radius 3 mm much smaller than the smallest wavelength of the order of 5 cm. For the results presented here, we used three different couples of antennas to be sure not to miss any resonance frequency in the *dressed* cavity in the range mentioned above (nearly 300 resonances were measured for each position of the scatterer). The cumulated density number $N(k)$ we could deduce from these measurements enabled us to verify that a small level repulsion can be observed as exemplified by the nearest-spacing distribution $P(s)$ whose histogram is shown in Fig. 6. The nearest spacings are as usually obtained by building the sequence of normalized spacings $s_i=\bar{N}(k_{i+1})-\bar{N}(k_i)$, whose average is unity. A comparison is shown with the distribution associated to a semi-Poisson sequence as a guideline. In fact, Bogomolny *et al.* have shown that the statistics of the singular billiard as the one discussed in the previous section, is intermediate between Poisson (uncorrelated spectrum) and semi-Poisson (short-range repulsion) [4].

Once the frequencies of all the resonances in the range mentioned above have been determined with a sufficient precision (better than one tenth of the local spacing), we build an average cumulated density through a polynomial fitting of

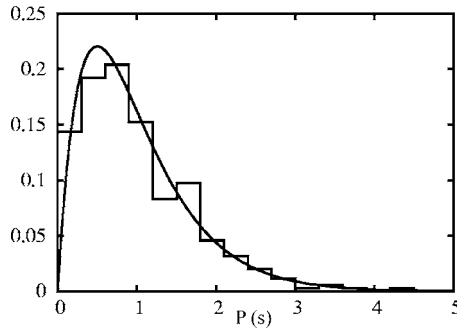


FIG. 6. Experimental histogram of $P(s)$ in the dressed cavity; semi-Poisson law: $P(s)=4se^{-2s}$ (continuous curve).

order two (consistent with Weyl's formula). Hence, an *experimental* length spectrum is evaluated by using the total frequency range at our disposal [here, the weighing function of formula (8) is therefore simply a Hanning window] for the FFT. Figure 7 shows such a length spectrum on a scale where the shortest POs can clearly be identified. Note however the poor resolution compared to the *analytical* length spectrum of Figs. 3 and 5. This is entirely due to the reduced frequency range we were compelled to use. Indeed, above 5 GHz, the ohmic losses are so important that the overlap of neighboring resonances prevents one from properly extracting all the resonance frequencies with the required precision. If one

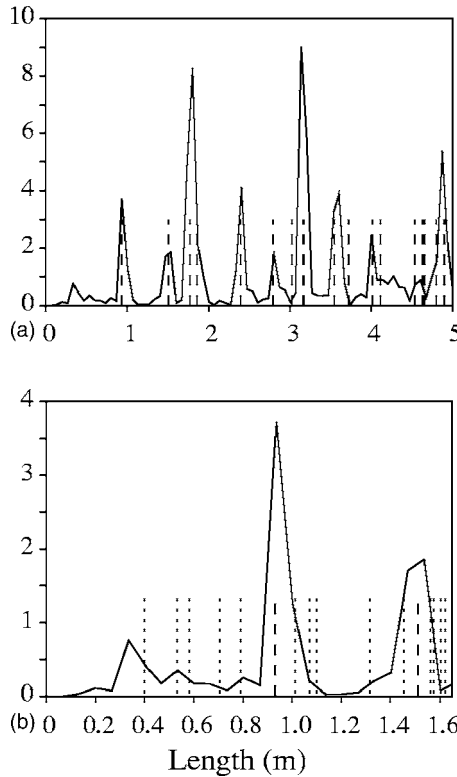


FIG. 7. Experimental length spectrum computed from 300 actual resonances measured from 500 MHz to 5 GHz. The position of the center of the scatterer is the same as in the numerical results of the previous section. (a) Length range from 0 to 5 m, POs indicated by dashed sticks; (b) length range from 0 to 1.6 m; POs indicated by dashed sticks; DOs indicated by dotted sticks.

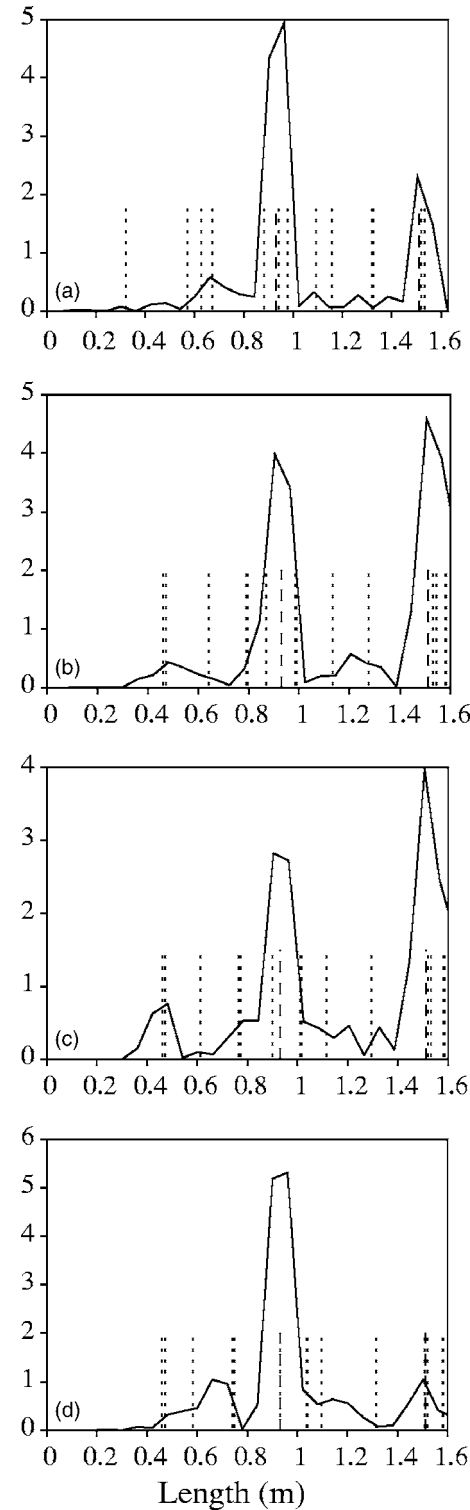


FIG. 8. Experimental length spectrum for four different positions of the scatterer measured from the upper left corner of the rectangular cavity: (a) $x=28.5$ cm, $y=13$ cm; (b) $x=43.5$ cm, $y=23$ cm; (c) $x=45$ cm, $y=23$ cm; (d) $x=46.5$ cm, $y=23$ cm. The corresponding DOs of the three kinds are depicted by dotted sticks. POs are indicated by dashed sticks.

wishes to use frequencies above this limit, the resolution of the length spectrum is not significantly improved whereas the risk of missing many levels is rapidly increasing, thereby

making the appearance of spurious peaks in the length spectrum more probable. These are current limitations when one requires high-precision spectra in such microwave experiments at room temperature. Within this frequency range the resolution is sufficient to identify the shortest (and relevant) DOs, even when only one couple of antennas is used to extract the frequency spectrum.

As in the analytical part, one can note the presence of peaks not centered at the lengths of POs. The important difference with the analytical or numerical approach is that the peaks related to the DOs have amplitudes only one order smaller than those of the POs. This can be accounted by the finite size of the actual scatterer leading to a different k dependence of the amplitudes associated to the DOs. In addition, we have also checked that the displacements of the scatterer within the cavity can be tracked by properly monitoring the lengths of the peaks associated to the shortest DOs contributing to the *experimental* length spectrum. This is illustrated in Fig. 8 where only one couple of antennas was used to extract the frequency spectrum for four different positions of the scatterer. This could constitute the basis of a nondestructive way of detecting the motion of a defect.

V. CONCLUSION

In the present paper, we have shown how a semiclassical approach of spectral statistics, usually based on periodic orbits in chaotic cavities, can be extended to analyze experiments in a 2D rectangular microwave cavity with a small scatterer by including diffractive orbits. More specifically, we have illustrated, through a model of cavity with a point scatterer, how DOs can be clearly identified in the so-called *length spectrum* of the cavity. This length spectrum could be retrieved through the evaluation of the two-point spectral correlations deduced from the cumulated spectral density of around 300 resonances measured in the frequency range (500 MHz, 5 GHz). To our knowledge, this is the first experimental evidence of the unambiguous role played by diffractive orbits in the spectrum of an actual cavity. This is also a clear illustration of how a semiclassical analysis can be used to reveal nonuniversal spectral features of a complex cavity. Our findings show that the length spectrum can be used to locate the scatterer, or any small defect, and, eventually, to track a moving defect.

ACKNOWLEDGMENTS

We wish to thank Charles Poli for the numerical implementation of Eq. (11). F.M. wishes to acknowledge enlightening discussions with Niels Sondergaard during the gathering *Chaotic and Random Wave Scattering in Quantum Mechanics and Acoustics* held in Cuernavaca (Mexico, 2005). D.L. acknowledges financial support from DGA/CNRS Grant No. 2004487.

APPENDIX: ORTHOGONALITY OF THE PERTURBED EIGENFUNCTIONS

We will use the following notations: G_0 is the Green function of the bare cavity, Ψ_n are the eigenfunctions, and E_n are

the corresponding eigenenergies; G is the perturbed Green function of the dressed cavity and Φ_n denotes the eigenfunctions with z_n the corresponding eigenvalues. The two Green functions are related by

$$G(\vec{r}, \vec{r}'; z) = G_0(\vec{r}, \vec{r}'; z) + G_0(\vec{r}, \vec{s}; z) \tau(\vec{s}; z) G_0(\vec{s}, \vec{r}'; z), \quad (\text{A1})$$

where the transition matrix τ is given by

$$\tau(\vec{s}; z) = [t^{-1} - f(\vec{s}; z)]^{-1}, \quad (\text{A2})$$

with $t^{-1} = \alpha + i/4$ [see formula (12) of Ref. [11]) for some real α .

The resonances of the perturbed cavity correspond to the zeroes of $[t^{-1} - f(\vec{s}; z)]$ where

$$f(\vec{s}; z) = \lim_{\vec{r} \rightarrow \vec{s}} \left[G_0(\vec{r}, \vec{s}; z) + \frac{i}{4} H_0^{(1)}(\sqrt{z} \|\vec{r} - \vec{s}\|) \right] = \frac{i}{4} \\ + \lim_{\vec{r} \rightarrow \vec{s}} \left[G_0(\vec{r}, \vec{s}; z) - \frac{1}{2\pi} \left(\gamma + \ln \frac{\sqrt{z} \|\vec{r} - \vec{s}\|}{2} \right) \right]. \quad (\text{A3})$$

One deduces the Φ_n through the residues of G at z_n ,

$$\lim_{z \rightarrow z_n} [G(\vec{r}, \vec{s}; z)(z - z_n)] = \Phi_n(\vec{r}) \Phi_n(\vec{s}). \quad (\text{A4})$$

Thus, according to Eq. (A1) (see Ref. [12]), one has

$$\Phi_n(\vec{r}) = N_n G_0(\vec{r}, \vec{s}; z_n), \quad (\text{A5})$$

where

$$N_n^2 = \left(\sum_{\nu} \frac{\Psi_{\nu}^2(\vec{s})}{(z_n - E_{\nu})^2} \right)^{-1}. \quad (\text{A6})$$

One wishes to calculate $\int \Psi_m(\vec{r}) \Psi_n(\vec{r}) d\vec{r}$. Using

$$G_0(\vec{r}, \vec{s}; z) = \sum_{\nu} \frac{\Psi_{\nu}(\vec{r}) \Psi_{\nu}(\vec{s})}{z - E_{\nu}}, \quad (\text{A7})$$

one gets

$$\int \Phi_m(\vec{r}) \Phi_n(\vec{r}) d\vec{r} \\ = N_m N_n \sum_{\nu, \mu} \frac{\Psi_{\nu}(\vec{s}) \Psi_{\mu}(\vec{s})}{(z_m - E_{\nu})(z_n - E_{\mu})} \int \Psi_{\nu}(\vec{r}) \Psi_{\mu}(\vec{r}) d\vec{r} \\ = N_m N_n \sum_{\nu} \frac{\Psi_{\nu}^2(\vec{s})}{(z_m - E_{\nu})(z_n - E_{\nu})}, \quad (\text{A8})$$

where $\int \Psi_{\nu}(\vec{r}) \Psi_{\mu}(\vec{r}) d\vec{r} = \delta_{\nu\mu}$ was used. If $m = n$, one finds

$$\int \Phi_n^2(\vec{r}) d\vec{r} = N_n^2 \sum_{\nu} \frac{\Psi_{\nu}^2(\vec{s})}{(z_n - E_{\nu})^2}. \quad (\text{A9})$$

If $n \neq m$, one calculates

$$\begin{aligned}
& f(\vec{s}; z_n) - f(\vec{s}; z_m) \\
&= \lim_{\vec{r} \rightarrow \vec{s}} \left[G_0(\vec{r}, \vec{s}; z_n) - G_0(\vec{r}, \vec{s}; z_m) - \frac{1}{4\pi} \ln \left(\frac{z_n}{z_m} \right) \right] \\
&= \sum_{\nu} \frac{\Psi_{\nu}^2(\vec{s})}{(z_n - E_{\nu})(z_m - E_{\nu})} - \sum_{\nu} \frac{\Psi_{\nu}^2(\vec{s})}{(z_m - E_{\nu})} - \frac{1}{4\pi} \ln \left(\frac{z_n}{z_m} \right) \\
&= (z_m - z_n) \sum_{\nu} \frac{\Psi_{\nu}^2(\vec{s})}{(z_n - E_{\nu})(z_m - E_{\nu})} - \frac{1}{4\pi} \ln \left(\frac{z_n}{z_m} \right). \tag{A10}
\end{aligned}$$

At the resonances of G , $f(\vec{s}) = t^{-1}$ assumed to be constant, whence $f(\vec{s}, z_n) = f(\vec{s}, z_m)$, thus implying, if one writes $z_n = k_n^2$,

$$\sum_{\nu} \frac{\Psi_{\nu}^2(\vec{s})}{(z_n - E_{\nu})(z_m - E_{\nu})} = \frac{1}{2\pi(k_m^2 - k_n^2)} \ln \left(\frac{k_n}{k_m} \right) \neq 0, \tag{A11}$$

and finally yielding

$$\int \Phi_m(\vec{r}) \Phi_n(\vec{r}) d\vec{r} = \frac{1}{2\pi N_m N_n} \frac{\ln(k_n/k_m)}{k_m^2 - k_n^2}. \tag{A12}$$

If one allows α to depend on k , then one can restore the orthogonality between the eigenfunctions Φ_n and Φ_m with $m \neq n$. Indeed, it suffices to write

$$\alpha(k_n) - \alpha(k_m) = -\frac{1}{2\pi} \ln \left(\frac{k_n}{k_m} \right), \tag{A13}$$

or, equivalently,

$$\alpha(k) = -\frac{1}{2\pi} \ln \left(\frac{k}{k_0} \right) + \text{const.} \tag{A14}$$

If one puts $k_0 = 2/a$ and $\text{const} = -\gamma/(2\pi)$, γ being the Euler constant, then (see Ref. [6])

$$t = \frac{2\pi}{-\ln \left(\frac{ka}{2} \right) - \gamma + i\frac{\pi}{2}}. \tag{A15}$$

This corresponds to the asymptotic behavior of the diffraction coefficient of a cylindrical s -wave scatterer of radius a . Therefore, in the approach due to Weaver and Sornette [11], the relation (23), which defines the resonances, should read

$$-\frac{1}{2\pi} \ln \left(\frac{ka}{2} \right) = \lim_{\vec{r} \rightarrow \vec{s}} \left\{ G_0(\vec{r}, \vec{s}; z) - \frac{1}{2\pi} \ln \left(\frac{k\|\vec{r} - \vec{s}\|}{2} \right) \right\}, \tag{A16}$$

thus restoring *the orthogonality of the perturbed eigenfunctions as well as the unitarity of the time-evolution operator* [12].

-
- [1] H.-J. Stöckmann, *Quantum Chaos—An Introduction* (Cambridge University Press, Cambridge, 1999).
 - [2] G. Vattay, A. Wirzba, and P. E. Rosenqvist, Phys. Rev. Lett. **73**, 2304 (1994).
 - [3] E. Bogomolny, O. Giraud, and C. Schmit, Phys. Rev. E **65**, 056214 (2002).
 - [4] E. Bogomolny, U. Gerland, and C. Schmit, Phys. Rev. E **63**, 036206 (2001).
 - [5] E. Bogomolny, P. Leboeuf, and C. Schmit, Phys. Rev. Lett. **85**, 2486 (2000).
 - [6] P. Exner and P. Šeba, Phys. Lett. A **222**, 1 (1996).
 - [7] S. Rahav and S. Fishman, Nonlinearity **15**, 1541 (2002).
 - [8] N. Pavloff and C. Schmit, Phys. Rev. Lett. **75**, 61 (1995); **75**, 3779 (1995).
 - [9] D. Biswas, Phys. Rev. Lett. **71**, 2714 (1993).
 - [10] O. Legrand, F. Mortessagne, and R. L. Weaver, Phys. Rev. E **55**, 7741 (1997).
 - [11] R. L. Weaver and D. Sornette, Phys. Rev. E **52**, 3341 (1995).
 - [12] T. Shigehara and T. Cheon, Phys. Rev. E **54**, 1321 (1996).
 - [13] S. R. Jain, Phys. Rev. E **50**, 2355 (1994).
 - [14] J. Barthélémy, O. Legrand, and F. Mortessagne, Phys. Rev. E **71**, 016205 (2005).

IV. DIFFUSION CHAOTIQUE EN MILIEUX OUVERTS

A. Paradigme des milieux ouverts : cavité micro-ondes à température ambiante

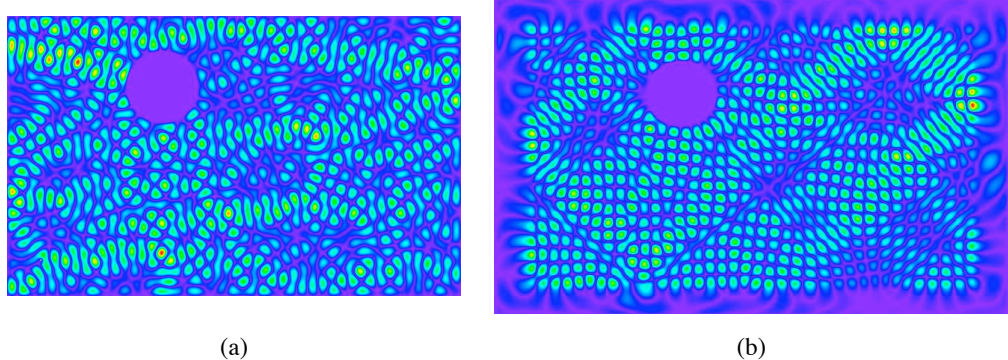


FIG. 16 Cartes d'intensité obtenues numériquement : (a) un mode d'une cavité fermée, (b) même fréquence d'excitation, mais les parois sont rendues perméables.

Dans le cadre des travaux de thèse de Jérôme Barthélémy (co-encadrée avec Olivier Legrand), nous nous sommes intéressés au très délicat problème du transport des ondes en milieu ouvert³². Ce problème reste en effet très peu défriché, aussi bien par les modèles théoriques, que par les expériences. D'un point de vue théorique, en perdant l'hermiticité du problème on perd l'espoir d'une description simple. Expérimentalement, les pertes, en réduisant la qualité du signal mesuré, notamment sa dynamique, constituent une gêne, évacuée au prix de beaucoup d'efforts. Dans les expériences en cavité micro-ondes, elles sont éliminées en utilisant des matériaux supraconducteurs, c'est-à-dire des cavités suffisamment petites pour être immergées dans un cryostat. Les pertes, ou la dissipation, constituent pourtant un ingrédient incontournable quel que soit le type d'ondes considéré : de l'acoustique des salles au transport dans les systèmes mésoscopiques. À titre de simple illustration, la figure IV.A montre comment le passage de bords fermés à des bords perméables modifie en profondeur la répartition spatiale de l'énergie à l'intérieur de la cavité. À l'onde stationnaire se superposent, dans le deuxième cas, des ondes progressives³³.

Nous avons donc réalisé dans une cavité (chaotique) micro-ondes bidimensionnelle, des mesures de diffusion à température ambiante. Notons que la situation physique traitée présente une analogie parfaite avec le problème d'une particule scalaire dans un billard quantique. Dans cette cavité, par le biais d'antennes reliées à un Analyseur de Réseau Vectoriel, sont injectées et mesurées des ondes hyperfréquences dans la gamme des GHz. Nous avons pu décrire complètement la matrice de diffusion (de type Breit-Wigner) de notre problème, c'est-à-dire en tenant compte des différentes sources de perte et de la nature du couplage avec les antennes (voir IV.B). Si les pertes ohmiques sont uniquement dues à la conductivité finie des parois, il faut néanmoins en distinguer deux types. Le premier, qui présente un comportement monotone avec la fréquence, ne dépend pas de la géométrie de la cavité, seulement de son épaisseur. Le deuxième, physiquement plus intéressant, est lié à une dissipation sur les bords de la cavité. Il dépend de la résonance excitée, donc de la géométrie, et fluctue d'un mode à l'autre. Nous avons également étudié l'évolution de la phase des résonances avec la fréquence et son lien avec l'évolution des pertes ohmiques liées aux bords (voir IV.C, article 1). La distribution de la phase est calculée à partir des données expérimentales. Elle est comparée à des prédictions analytiques, ce qui permet de fixer un paramètre qui mesure la taille typique de la partie imaginaire de l'amplitude du champ. Nos données expérimentales montrent très clairement une proportionnalité entre la largeur ohmique due

³² Thèse téléchargeable sur le site du serveur de thèses du CNRS : tel.archives-ouvertes.fr/

³³ La partie stationnaire n'étant pas forcément la même dans les deux cas si les pertes sont fortes.

aux bords et ce paramètre.

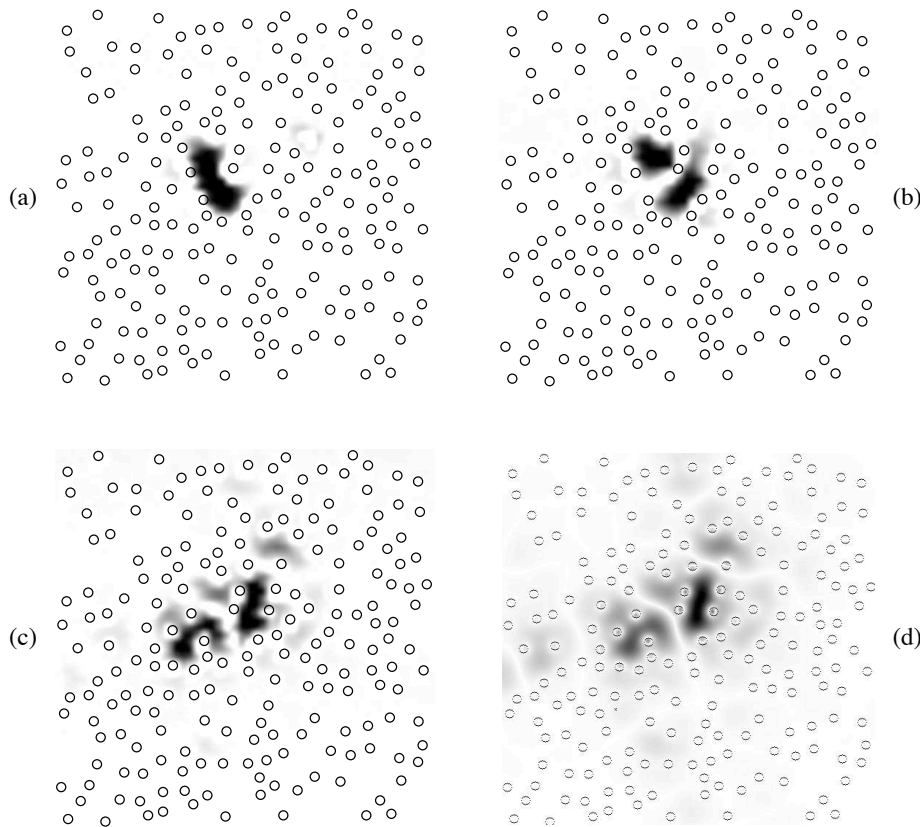


FIG. 17 Amplitude du champ micro-ondes dans une cavité ouverte et désordonnée (25×25 cm, 196 diffuseurs) : (a), (b) et (c) cartes expérimentales correspondant respectivement à des résonances à 5.45 GHz, 5.66 GHz et 7.80 GHz., (d) carte obtenue par simulation numérique pour la résonance à 7.80 GHz.

Récemment, en collaboration avec Dmitry Savin (Department of Mathematical Sciences, Brunel University), qui a bénéficié de deux mois de « professeur invité » en début d'année, nous avons développé un modèle théorique en parfait accord avec nos résultats expérimentaux (voir IV.C, article 2). La thèse que débute Charles Poli s'inscrit dans la continuité de ce travail. Il aura pour objectif ultime d'étendre le modèle, pour l'instant limité aux situations de faible recouvrement modal, à tous les régimes. Ce problème agite actuellement beaucoup la communauté du chaos ondulatoire³⁴.

³⁴ Y. V. Fyodorov and D. V. Savin, J. Phys. A : Math ; Gen. **38**, 10731 (2005) ; U. Kuhl, H.-J. Stöckmann, and R. L. Weaver, *ibid.*, p. 10433. Voir également l'abondante littérature qu'un bon moteur de recherches sur le web trouve avec les mots-clés : « open billiard », « non-orthogonal modes » ou « quasinormal modes ».

Disposant d'un outil expérimental performant et bien contrôlé, et après une première phase présentée en III, le travail de thèse de David Laurent a été orienté vers la mesure indirecte de la répartition spatiale des résonances en régime de diffusion multiple. En pratique, la cavité micro-ondes a été « ouverte », grâce à l'adjonction de matériaux isolants sur son pourtour, et « désordonnée », en disposant, de manière aléatoire, près de 200 petits plots cylindriques constitués d'un matériau diélectrique à haute permittivité (de l'ordre de 37). L'enjeu étant l'observation directe de « modes localisés ». Ces objets constituent une sorte de Graal pour la communauté de la diffusion multiple : la présence de modes spatialement (de manière exponentielle) localisés dans une gamme de fréquences donnée, est très certainement à l'origine du phénomène de localisation forte des ondes, ou localisation d'Anderson, dans le cas des ondes électroniques. Ce phénomène est l'objet de très nombreuses études, théoriques et numériques, et, dans une moindre me-

sure, expérimentales. Les difficultés pour réaliser ces dernières sont grandes, et l'analyse des résultats n'est pas toujours exempte d'ambiguïtés. La première d'entre elles tient au fait que la plupart des expériences sont réalisées dans le domaine temporel, et traquent la signature de la localisation dans une décroissance exponentielle d'un signal de transmission³⁵. Or, un autre effet, totalement inévitable, se traduit également par une décroissance exponentielle d'un signal de transmission au travers d'un milieu : l'absorption – ou pertes, couplages vers l'extérieur³⁶. Une approche « statistique » de la localisation a été proposée dans des systèmes désordonnées (quasi)unidimensionnels³⁷. Mais la localisation en dimension 1 possède un statut un peu particulier ; ces expériences ne constituent donc qu'une étape dans la compréhension du phénomène de localisation. Il faut tout de même reconnaître l'apport de certaines expériences 1D qui permettent d'obtenir des visualisations directes remarquables de couplages entre modes localisés³⁸.

Après une délicate période de mise au point, et grâce à un soutien financier important du laboratoire, nous avons obtenu très récemment les premières cartographies de modes localisés ! Ces derniers satisfont à divers critères de localisation et se comparent parfaitement aux résultats de simulations numériques effectuées en parallèle (voir figure 17). Je présenterai un peu plus en détail ces récents travaux dans la section IV.D.

³⁵ D. S. Wiersma, P. bartolini; A. Lagendijk, and R. Righini, *Nature* **390**, 671 (1997).

³⁶ Voir cependant la référence suivante où l'effet de l'absorption semble être parfaitement discriminé : M. Störzer, P. Gross, C. M. Aegerter, and G. Maret, *Phys. Rev. Lett.* **96**, 063904 (2006).

³⁷ A. A. Chabanov, M. Stoychev, and A. Z. Genack, *Nature* **404**, 850 (2000).

³⁸ P. Sebbah, B. Hu, J. M. Klosner, and A. Z. Genack, *Phys. Rev. Lett.* **96**, 183902 (2006).

B. Complete S -matrix in a microwave cavity at room temperature, Physical Review E 71, 016205 (2005)

Cet article est l'un de ceux présentés dans ce document dont je suis le plus fier : je le crois bien écrit, et il représente l'aboutissement de longues années d'efforts. Que de chemin parcouru depuis les premières mesures réalisées en quasi catimini, avec Patrick Sebbah, sur un analyseur de réseaux de l'ESINSA...

Nous adoptons dans cet article une démarche « perturbative », c'est-à-dire que le modèle est progressivement rendu plus complexe pour atteindre la situation physique voulue. La modélisation de la cavité sans perte et des antennes est exposée dans la section II ; deux points importants, mais plus techniques, l'auto-adjonction du Hamiltonien total et l'expression de la matrice de couplage, sont traités dans l'annexe A. La section III introduit les pertes ohmiques et se conclue, avec l'équation (50), par l'expression analytique complète de la matrice de diffusion. Je souligne que, d'une part, la distinction entre pertes ohmiques homogènes (équation (48)) et inhomogènes (équation (49)), et, d'autre part, la fonction de transfert des antennes (51) et les pertes associées (52), constituaient, à la parution de cet article, des résultats totalement nouveaux. La section IV confronte, enfin, la modélisation aux expériences : les tests sont passés avec un succès remarquable, comme le montrent notamment les figures 4, 5 et 7.

Complete *S* matrix in a microwave cavity at room temperature

Jérôme Barthélémy, Olivier Legrand, and Fabrice Mortessagne

Laboratoire de Physique de la Matière Condensée, CNRS UMR 6622, Université de Nice-Sophia Antipolis, 06108 Nice, France

(Received 9 February 2004; published 6 January 2005)

We experimentally study the widths of resonances in a two-dimensional microwave cavity at room temperature. By developing a model for the coupling antennas, we are able to discriminate their contribution from those of Ohmic losses to the broadening of resonances. Concerning Ohmic losses, we experimentally put to evidence two mechanisms: damping along propagation and absorption at the contour, the latter being responsible for variations of widths from mode to mode due to its dependence on the spatial distribution of the field at the contour. A theory, based on an *S*-matrix formalism, is given for these variations. It is successfully validated through measurements of several hundreds of resonances in a rectangular cavity.

DOI: 10.1103/PhysRevE.71.016205

PACS number(s): 05.45.Mt, 05.60.Gg, 03.65.Nk, 03.65.Yz

I. INTRODUCTION

In the field of quantum chaos, microwave experiments have proven to yield very important breakthroughs in providing versatile analog models of quantum systems in the domain of classical electromagnetic waves [1]. Room-temperature experiments have opened the way [2], rapidly followed by experiments in superconducting cavities [3]. In a first stage, studies have mainly been concerned with the verification of predictions issued from random matrix theory or from semiclassical approaches regarding spectral fluctuations. Losses, which were originally absent from theoretical models, were seen as severe drawbacks in the seminal experiments, especially for an accurate analysis of resonance frequencies (see, e.g., [2–4]). The first account of resonance widths observed in superconducting cavities was related to coupling losses in the absence of Ohmic losses, and measuring widths essentially amounted to measuring intensities at the locations of few antennas [5]. During the past decade, the great flexibility of microwave cavities has led to an important diversification of geometries and configurations in order to investigate the spectral correlations and the spatial distribution of the field, in closed or open, disordered, and/or chaotic cavities (see [1] for a review). Nevertheless, until recent years, the impact of the different loss mechanisms, present in these systems, on their spatial or spectral statistical properties attracted very little consideration. Indeed, as long as losses are weak, resonances can be viewed as isolated. On the contrary, for increasing damping, resonances are no longer easily distinguished due to modal overlapping, and the very description of the wave system in terms of modes loses its pertinence. Since the seminal papers by Ericson in nuclear physics [6] and by Schroeder in room acoustics [7], the regime of large modal overlap has been abundantly studied in the context of quantum chaos [8–10].

The question of intermediate modal overlap for which resonances can be distinguished but broadening is no longer negligible is essentially open as yet (see the excellent review [11]). In the present paper, we propose to help pave the way of a more complete understanding of microwave cavities at room temperature by accounting for the presence of essentially two kinds of loss mechanisms, namely Ohmic damping at the boundaries and coupling to the outside through anten-

nas. To be able to separate their respective contributions to the broadening of resonances, a thorough analysis is required of the way the wave functions are spatially distributed throughout the cavity.

The cavity we have actually used for our experiments is composed of two rectangular OFHC copper plates between which a copper rectangular frame is sandwiched. The rectangular frame has been machined as one piece and serves as the contour of the cavity. The cavity may thus be viewed as the slice of a rectangular waveguide closed at both ends, with contour \mathcal{C} of length $L=2.446$ m, section \mathcal{S} of area $A=0.3528$ m², and thickness $d=5$ mm. As long as the wavelength λ is larger than d , the boundary conditions in the z direction (perpendicular to the top and bottom plates) only admit transverse magnetic (TM) two-dimensional (2D) modes. The whole structure is tightly screwed and 10 holes have been drilled through one of the plates to introduce 10 antennas, which protrude a length l into the cavity. The antennas are monopolar with SMA connectors which are commonly used in the frequency range from 0 to 18 GHz. The positions of the antennas are displayed in Fig. 1. For a measurement, only one antenna at a time is used as a microwave emitter and another (in transmission) or the same (in reflection) as a receiver. The other unused antennas are terminated by 50Ω loads so that all antennas behave the same way regarding the losses they imply. These antennas are linked to an HP 8720 D vector analyzer through flexible cables. All the measurements are performed after a proper calibration to get

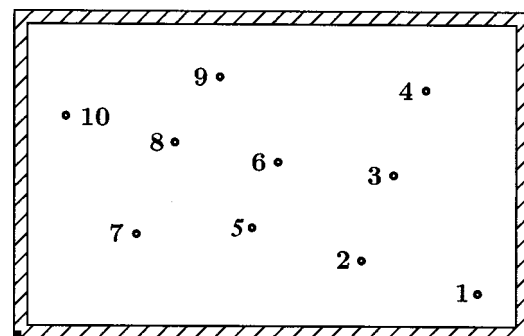


FIG. 1. Schematic view of the microwave cavity with locations of antennas.

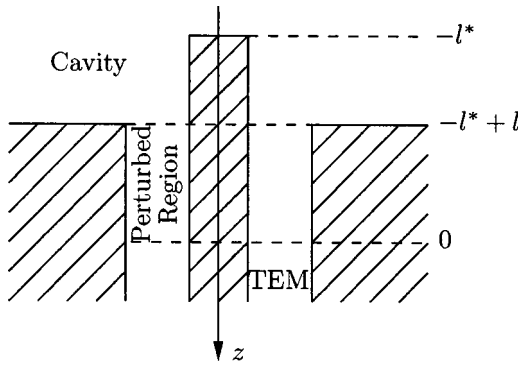


FIG. 2. Schematic cut view of a coupling antenna. Physical regions introduced in our model are displayed along with the associated characteristic lengths.

rid of any parasitic influence of cables and connectors and even of the analyzer itself. The measurements are given in terms of scattering coefficients which form the S matrix $(\begin{smallmatrix} S_{11} & S_{12} \\ S_{21} & S_{22} \end{smallmatrix})$, where $S_{11}(S_{22})$ measures the reflection on port 1 (2) and $S_{12}(S_{21})$ measures the transmission from port 2 (1) to port 1 (2).

In the following section, we develop an S -matrix formulation for an ideal cavity through the introduction of an electromagnetic model of antennas which enables us to write the response of the cavity within the form of a Breit-Wigner decomposition. Then, in the third section, we complete this description with a perturbative evaluation of Ohmic losses at the walls of the cavity. We show that the resulting Ohmic width of each resonance may be decomposed in two qualitatively and quantitatively distinct contributions, one of them being sensitive to the spatial distribution of the wave function at the contour. Then, in Sec. IV, we proceed to an experimental validation of our model in the case of a rectangular cavity. We show that, for each measured resonance, we are able to discriminate quantitatively among the two Ohmic contributions to the total widths and the contribution due to the presence of the antennas.

II. S-MATRIX FORMULATION FOR A CAVITY WITHOUT OHMIC LOSSES

A. Electromagnetic model of antennas

As an antenna, we use the terminal part of the center conductor of a coax (see Fig. 2). Far from this termination, in a coaxial line, only transverse electromagnetic (TEM) modes can propagate and the field results as the superposition of incoming and outgoing parts. In the vicinity of the termination of the line, hereafter called the *perturbed region*, perturbative nonpropagating waves exist [12]. The longitudinal variable z along the line is oriented outward from the cavity and its origin located at the border between the TEM and the perturbed regions, i.e., at a distance l^* from the end of the antenna (see Fig. 2). In the perturbed region, assuming a sinusoidal behavior, we write the stationary current $I_{pert}(z)$ as

$$I_{pert}(z) = I_+ e^{ikz} + I_- e^{-ikz} \text{ for } -l^* < z < 0, \quad (1)$$

the time evolution being conventionally written $\exp(-i\omega t)$.

The current $I(z)$ in the TEM region reads [13]

$$I(z) = \frac{V_0}{Z} (\mathcal{A}_{out} e^{ikz} + \mathcal{A}_{in} e^{-ikz}) \text{ for } z > 0, \quad (2)$$

where Z is the characteristic impedance of the coaxial line. The following continuity conditions are then imposed:

$$\begin{aligned} I_{pert}(-l^*) &= 0, \\ I_{pert}(0) &= I(0). \end{aligned} \quad (3)$$

Therefore,

$$I_{pert}(z) = I(0) \frac{\sin k(l^* + z)}{\sin kl^*} \text{ for } -l^* < z < 0 \quad (4)$$

with

$$I(0) = \frac{V_0}{Z} (\mathcal{A}_{out} + \mathcal{A}_{in}). \quad (5)$$

Inside the cavity, time-independent Maxwell's equations yield the following wave equation for the electric field \vec{E} :

$$\Delta \vec{E} + k^2 \vec{E} = i\omega \mu \vec{J}, \quad (6)$$

where, assuming a pointlike antenna at location \vec{r}_0 , the current density within the plane of the cavity reads

$$\vec{J}(z, \vec{r}) = I(z) \delta(\vec{r} - \vec{r}_0) \hat{z} \text{ for } -l^* < z < 0. \quad (7)$$

The 2D formulation of our problem is obtained by integrating Eq. (6) along z in different ways for the left-hand side and the right-hand side. Indeed, while the left-hand side is easily integrated over the thickness d of the cavity, i.e., for $-l^* + l - d < z < -l^* + l$, the integration of the right-hand side is more involved. To account for the effective coupling of the electric field with the current in the perturbed region, we define a coupling function $f(z)$ on the interval $[-l^*, 0]$ which multiplies the current before integrating. To our knowledge, only numerical approaches of this problem have been published, using FDTD [14] or modal decomposition [15,16]. Here we adopt an effective description by assuming $f(z) = 1$ on the interval $[-l^*, -l^* + l_{eff}]$ and $f(z) = 0$ on the rest of the interval. The length l_{eff} is an adjustable parameter lying between l and l^* , most likely close to l . Hence, for M identical antennas, Eq. (6) becomes

$$\begin{aligned}
(\Delta + k^2)E_z(\vec{r}) \times d &= i\omega\mu_0 \sum_{c=1}^M \delta(\vec{r} - \vec{r}_c) \frac{V_0}{Z} (\mathcal{A}_{out}^c + \mathcal{A}_{in}^c) \\
&\times \int_{-l^*}^{-l^*+l_{eff}} \frac{\sin k(l^* + z)}{\sin kl^*} dz \\
&= \frac{iV_0Z_0}{Z} \frac{\sin^2 \frac{kl_{eff}}{2}}{\sin \frac{kl^*}{2} \cos \frac{kl^*}{2}} \\
&\times \sum_{c=1}^M \delta(\vec{r} - \vec{r}_c) (\mathcal{A}_{out}^c + \mathcal{A}_{in}^c), \quad (8)
\end{aligned}$$

where $Z_0 = \sqrt{\mu_0/\epsilon_0}$ is the vacuum impedance.

B. Breit-Wigner decomposition

We now follow a standard approach in scattering theory to analytically express the S matrix of a microwave cavity coupled to pointlike antennas. This kind of calculation was initiated in nuclear physics [17] and has been reproduced in various contexts since then (see, e.g., Ref. [11,18,19]). The cavity is described as a closed system coupled to M channels, one for each antenna. The complete Hilbert space of the system comprises the cavity and the channels. It is therefore decomposed as the direct sum of Hilbert spaces associated to the inside and the outside of the cavity: $\mathcal{H} = \mathcal{E}_{in} \oplus \mathcal{E}_{out}$. Though the inside Hilbert space is of infinite dimension, we adopt the commonly used simplification of a finite dimension $N \gg 1$ [11]. The Hamiltonian of the cavity \mathcal{H}_{in} is thus represented by an $N \times N$ matrix H . The eigenstates associated to \mathcal{H}_{in} are denoted $|\mu\rangle$. The outside Hilbert space is associated to the M antennas and is written as the direct sum $\mathcal{E}_{out}(E) = \mathcal{E}_1(E) \oplus \dots \oplus \mathcal{E}_M(E)$, where E is the energy of a continuum of scattering states denoted by $|c, E\rangle$ for channel c . Finally, W denotes the coupling matrix of dimension $N \times M$ between the bound states of the cavity and the scattering states of the antennas. As long as the wavelength remains smaller than the distances between antennas, the direct coupling between channels may be neglected. The complete Hamiltonian \mathcal{H} thus reads

$$\begin{aligned}
\mathcal{H} &= \sum_{\mu, \nu=1}^N |\mu\rangle H_{\mu\nu} \langle \nu| + \sum_{c=1}^M \int dE |c, E\rangle E \langle c, E| \\
&+ \sum_{c=1}^M \sum_{\mu=1}^N \left(|\mu\rangle \int dE W_{\mu c}(E) \langle c, E| + \text{H. c.} \right) \\
&= \mathcal{H}_{in} + \mathcal{H}_{out} + \mathcal{W}_{out \rightarrow in} + \mathcal{W}_{in \rightarrow out}. \quad (9)
\end{aligned}$$

The normalization conditions are

$$\langle \nu | \mu \rangle = \delta_{\nu\mu} \text{ and } \langle a, E | b, E' \rangle = \delta_{ab} \delta(E - E'). \quad (10)$$

The space representation of \mathcal{H}_{in} is given by

$$\langle \vec{r} | \mathcal{H}_{in} | \vec{r}' \rangle = -\delta(\vec{r} - \vec{r}') \Delta_{\vec{r}}. \quad (11)$$

Likewise, the space representation of \mathcal{H}_{out} in the coax reads

$$\langle z_a | \mathcal{H}_{out} | z_b \rangle = -\langle z_a | z_b \rangle \frac{d^2}{dz_b^2}. \quad (12)$$

For pointlike antennas, the coupling will be represented by

$$\langle \vec{r} | \mathcal{W}_{out \rightarrow in}(E) | z_c \rangle = t_c(E, z_c) \delta(\vec{r} - \vec{r}_c). \quad (13)$$

Let $\Phi = [\varphi_\alpha(\vec{r}) \varphi_{\beta_1}(z_1) \dots \varphi_{\beta_M}(z_M)]^T$ denote a state of the complete system. Then the eigenvalue problem $\mathcal{H}\Phi = E_0\Phi$ may be written as

$$\begin{aligned}
&- \Delta \varphi_a(\vec{r}) + \sum_{c=1}^M \delta(\vec{r} - \vec{r}_c) \\
&\times \int dz_c t_c(E_0, z_c) \varphi_{\beta_c}(z_c) = E_0 \varphi_a(\vec{r}), \\
&t_1^*(E_0, z_1) \varphi_\alpha(\vec{r}_1) - \varphi_{\beta_1}''(z_1) = E_0 \varphi_{\beta_1}(z_1), \\
&\vdots \\
&t_M^*(E_0, z_M) \varphi_\alpha(\vec{r}_M) - \varphi_{\beta_M}''(z_M) = E_0 \varphi_{\beta_M}(z_M), \quad (14)
\end{aligned}$$

where the prime symbols stand for the ordinary derivative.

According to the electromagnetic description given at the beginning of this section, $t_c(E_0, z_c)$ will be vanishing except in a perturbed region of length l^* from the termination of the antenna. It is therefore quite natural to fix the origin of z_c at the limit of this region. For $z_c > 0$, the field is written as the superposition of ingoing and outgoing waves,

$$\varphi_{\beta_c}(z_c) = \frac{1}{\sqrt{k}} (\mathcal{A}_{out}^c e^{ikz_c} + \mathcal{A}_{in}^c e^{-ikz_c}) \text{ for } z_c > 0, \quad (15)$$

where $k^2 = E_0$. The factor $1/\sqrt{k}$ is required for dimensional and normalization purposes, and \mathcal{A}_{in}^c and \mathcal{A}_{out}^c are dimensionless complex amplitudes. For $z_c \in [-l^*, 0]$, the perturbed field $\phi(z_c)$ in the coupling region is still to be a superposition of plane waves. Continuity conditions in agreement with our electromagnetic description imply

$$\begin{aligned}
\phi_{\beta_c}(-l^*) &= 0, \\
\phi_{\beta_c}(0) &= \varphi_{\beta_c}(0). \quad (16)
\end{aligned}$$

One therefore deduces

$$\phi_{\beta_c}(z_c) = \varphi_{\beta_c}(0) \frac{\sin k(z_c + l^*)}{\sin kl^*} \text{ for } -l^* < z_c < 0. \quad (17)$$

The $M \times M$ S matrix being defined by

$$\mathcal{A}_{out} = S \mathcal{A}_{in}, \quad (18)$$

where $\mathcal{A}_{in} = (\mathcal{A}_{in}^1 \dots \mathcal{A}_{in}^M)^T$ and $\mathcal{A}_{out} = (\mathcal{A}_{out}^1 \dots \mathcal{A}_{out}^M)^T$, only the functions $\varphi_{\beta_c}(z_c)$ for $z_c > 0$ are relevant. Equation (14) can thus be obviously reduced to

$$\begin{aligned}
& -\Delta\varphi\alpha(\vec{r}) + \sum_{c=1}^M \delta(\vec{r} - \vec{r}_c) \\
& \times \int_{-l^*}^0 dz_c t_c(E_0, z_c) \phi_{\beta_c}(z_c) = E_0 \varphi_\alpha(\vec{r}), \\
& -\varphi''_{\beta_1}(z_1) = E_0 \varphi_{\beta_1}(z_1), \\
& \vdots \\
& -\varphi''_{\beta_M}(z_M) = E_0 \varphi_{\beta_M}(z_M), \quad (19)
\end{aligned}$$

where $t_c(E_0, z_c) = 0$ has been used for $z_c > 0$. Here again we introduce the simplification of a nonvanishing constant value $t_c(E_0)$ for $t_c(E_0, z_c)$ only on the interval $[-l^*, -l^* + l_{eff}]$. With this assumption and expression (17), the first equation in Eq. (19) reads

$$-\Delta\varphi_\alpha(\vec{r}) + \sum_{c=1}^M T_c(k) \delta(\vec{r} - \vec{r}_c) \varphi_{\beta_c}(0) = E_0 \varphi_\alpha(\vec{r}), \quad (20)$$

with

$$T_c(k) = \frac{t_c(E_0)}{k} \frac{\sin^2 \frac{kl_{eff}}{2}}{\sin \frac{kl^*}{2} \cos \frac{kl^*}{2}}. \quad (21)$$

Assuming identical antennas, i.e., $T_c(k) \equiv \tilde{T}(k)$, and by identifying Eq. (8) with Eq. (20), one deduces

$$\tilde{T}(k) = i\sqrt{k} \frac{Z_0}{Z} \frac{\sin^2 \frac{kl_{eff}}{2}}{\sin \frac{kl^*}{2} \cos \frac{kl^*}{2}}. \quad (22)$$

In spite of the reduction performed in Eq. (19), by eliminating the source terms associated to the field inside the cavity [18,19], the condition of self-adjointness can be recovered through appropriate boundary conditions. In Appendix A 1, we show that it can be done through the following boundary condition for channel c :

$$\tilde{T}^*(k) \varphi_\alpha(\vec{r}_c) = \varphi'_{\beta_c}(0). \quad (23)$$

We are now in a position to derive an explicit expression for the S matrix. If the energy dependence of the coupling is small on a scale of the order of the mean energy spacing between neighboring modes, the S matrix can be written [11]

$$S_{ab} = \delta_{ab} - 2\pi i \langle a, E | W^\dagger (E - H_{eff})^{-1} W | b, E \rangle, \quad (24)$$

where

$$H_{eff} = H - i\pi W W^\dagger. \quad (25)$$

The S matrix can thus be rewritten

$$S = \frac{1 - iK}{1 + iK}, \quad (26)$$

with

$$K = \pi W^\dagger \frac{1}{E - H} W. \quad (27)$$

Standard linear algebra (see, e.g., Ref. [18]) transforms expression (26) into

$$S = I_M - 2i\pi W^\dagger \frac{1}{k^2 - H + i\pi W W^\dagger} W. \quad (28)$$

Then, assuming a weak coupling, a perturbative expansion to leading order (considering the isolated cavity as the “zeroth order”) yields the following expression for an element of the S matrix:

$$S_{ab} = \delta_{ab} - 2i\pi \sum_{\mu=1}^N \frac{\frac{W_{\mu a}^* W_{\nu b}}{M}}{k^2 - k_\mu^2 + i\pi \sum_{c=1}^M |W_{\mu c}|^2}, \quad (29)$$

where the sum runs over the eigenstates of the isolated cavity with energies k_μ^2 . In Appendix A 2, it is shown that the coupling matrix elements, in the space representation, are given by

$$W_{\mu c} = \frac{\tilde{T}(k) \psi_\mu^*(\vec{r}_c)}{\sqrt{k\pi}}, \quad (30)$$

where $\psi_\mu(\vec{r}) = \langle \vec{r} | \mu \rangle$ is the eigenfunction associated to k_μ^2 . One finally obtains the following explicit expression for the S -matrix elements:

$$\begin{aligned}
S_{ab} = & \delta_{ab} - 2i \frac{|\tilde{T}(k)|^2}{k} \\
& \times \sum_{\mu=1}^N \frac{\psi_\mu(\vec{r}_a) \psi_\mu^*(\vec{r}_b)}{k^2 - k_\mu^2 + \frac{i}{k} |\tilde{T}(k)|^2 \sum_{c=1}^M |\psi_\mu(\vec{r}_c)|^2}. \quad (31)
\end{aligned}$$

III. PERTURBATIVE EVALUATION OF OHMIC LOSSES

In this section, we present the results deduced from a standard first-order perturbation approach whose validity is restricted to nondegenerate modes (see Jackson’s textbook [20]). The power dP dissipated (Ohmic losses) by a wave with frequency ω within the surface element da of a conductor is given by the flux of the real part of the Poynting vector through this surface. By adopting Jackson’s convention $\exp(-i\omega t)$ for the time dependence of the field, one has

$$\frac{dP}{da} = -\frac{1}{2} \operatorname{Re}[\hat{n} \cdot (\vec{E} \wedge \vec{H}^*)], \quad (32)$$

where \hat{n} is the unit normal vector directed toward the interior of the conductor, and \vec{E} and \vec{H} are the fields at the surface. If the conductor is perfect, \vec{E} is perpendicular to the surface, \vec{H} is parallel, and there is no dissipated power — in the following, parallel or perpendicular will be understood *with respect to the surface of the conductor*. This ideal situation will cor-

respond to the zeroth order of our description of the field near the surface of the actual conductor. For a finite conductivity σ , one can compute the first-order corrections for the fields following the standard approach described, for instance, in Ref. [20].

To first order, the perpendicular electric field and the parallel magnetic field outside the conductor remain unmodified. Using appropriate boundary conditions together with Maxwell equations, it may be shown that nonvanishing parallel components of both electric and magnetic fields exist inside the conductor. These fields decrease as $\exp(-z/\delta)$, where $\delta = \sqrt{2/\mu_c\sigma\omega}$ is the skin depth (μ_c being the magnetic permeability of the conductor and σ its effective conductivity), and only depend on the zeroth-order parallel component of the magnetic field $\vec{H}_{\parallel}^{(0)}$ at the surface of the conductor. By continuity, one deduces the existence of a small parallel component of the electric field just outside the conductor,

$$\vec{E}_{\parallel}^{(1)} = \sqrt{\frac{\omega\mu_c}{2\sigma}}(1-i)\left(\hat{n} \wedge \vec{H}_{\parallel}^{(0)}\right). \quad (33)$$

Using Eq. (33), one finds

$$\frac{dP}{da} = \frac{\mu_c\omega\delta}{4} \|\vec{H}_{\parallel}^{(0)}\|^2. \quad (34)$$

To obtain the total power dissipated through Ohmic losses within a cavity, a mere integration of equation Eq. (34) over the walls is required.

In an ideal 2D cavity, the electromagnetic field does not vary along z ,

$$\vec{H}^{(0)} = \begin{cases} H_x^{(0)}(x, y) \\ H_y^{(0)}(x, y) \\ 0 \end{cases} \text{ and } \vec{E}^{(0)} = \begin{cases} 0 \\ 0 \\ E_z^{(0)}(x, y) \end{cases} \quad (35)$$

Denoting $\psi^{(0)} = E_z^{(0)}(x, y)$, the time-independent Maxwell equations are reduced to a 2D Helmholtz equation,

$$(\vec{\nabla}_t^2 + \epsilon\mu\omega^2)\psi^{(0)} = 0, \quad (36)$$

where the transverse gradient operator $\vec{\nabla}_t$ is associated to the (x, y) coordinates, and ϵ and μ are, respectively, the permittivity and the permeability inside the cavity. On the contour, $\psi^{(0)}$ obeys Dirichlet conditions,

$$\psi^{(0)} = 0 \text{ on } \mathcal{C}. \quad (37)$$

This yields a complete analogy with the free propagation of a quantum particle in a 2D infinite well. This type of system is commonly called a *quantum billiard*. For a given mode, the Ohmic dissipated power reads

$$P = \frac{1}{2\sigma\delta} \left[\oint_{\mathcal{C}} d\ell \int_0^d dz \|\hat{n} \wedge \vec{H}^{(0)}\|_{\text{cont}}^2 + \int_S da \|\hat{n} \wedge \vec{H}^{(0)}\|_{\text{ends}}^2 \right]. \quad (38)$$

One defines the integrals I_1 and I_2 so that Eq. (38) is rewritten as

$$P = \frac{I_1 + I_2}{2\sigma\delta\mu}. \quad (39)$$

Using Faraday's law, one obtains

$$I_1 = \xi \frac{Ld}{A} \epsilon \int \int_S da |\psi^{(0)}|^2 \quad (40)$$

where ξ is defined by

$$\frac{1}{\epsilon\mu\omega^2} \oint_{\mathcal{C}} d\ell |\partial_n \psi^{(0)}|^2 \equiv \xi \frac{L}{A} \int \int_S da |\psi^{(0)}|^2, \quad (41)$$

∂_n denoting $(\hat{n} \cdot \vec{\nabla})$. Here it should be remarked that ξ is a parameter, which depends on the spatial structure of the mode at hand. Likewise, one may compute I_2 ,

$$I_2 = \frac{2}{\mu\omega^2} \int \int_S da \|\vec{\nabla}_t \psi^{(0)}\|^2. \quad (42)$$

Now using the 2D Green's theorem together with Eq. (36), one gets

$$I_2 = 2\epsilon \int \int_S da |\psi^{(0)}|^2 \quad (43)$$

and, eventually,

$$P = \frac{\epsilon}{\sigma\delta\mu} \left(1 + \xi \frac{Ld}{2A} \right) \int \int_S da |\psi^{(0)}|^2. \quad (44)$$

Considering that the total electromagnetic energy stored in the cavity is given by

$$W = \frac{\epsilon}{2} \int \int_V dv \|\vec{E}^{(0)}\|^2 = \frac{\epsilon d}{2} \int \int_S da |\psi^{(0)}|^2, \quad (45)$$

the full width at half maximum (FWHM) of the resonances is given by

$$\Gamma = \frac{P}{W} = \frac{\mu_c}{\mu} \frac{1}{d} \sqrt{\frac{2\omega}{2\mu\sigma\delta}} \left(1 + \xi \frac{Ld}{2A} \right). \quad (46)$$

In our context μ_c/μ is practically equal to unity. Thus one finally has to consider two distinct types of Ohmic losses: those located at the surface of both ends, which amount to attenuation along propagation, and Ohmic losses upon reflection at the contour,

$$\Gamma^{\text{Ohm}} = \Gamma^{\text{prop}} + \Gamma^{\text{refl}}, \quad (47)$$

where

$$\Gamma^{\text{prop}} = \frac{2}{d} \sqrt{\frac{\omega}{2\mu\sigma_{\text{ends}}}} = \frac{\delta_{\text{ends}}\omega}{d}, \quad (48)$$

$$\Gamma^{\text{refl}} = \xi \frac{L}{A} \sqrt{\frac{\omega}{\pi\mu\sigma_{\text{cont}}}} = \xi \frac{L\delta_{\text{cont}}\omega}{2A}. \quad (49)$$

Here, we have introduced two different effective conductivities (σ_{ends} and σ_{cont}) and their corresponding skin depths (δ_{ends} and δ_{cont}) to account for two different types of copper

used in our experiment, and for possible different surface states for the top and bottom plates and the inner surface of the copper frame used as the contour. These two contributions to the widths are also quite distinct in their physical interpretation. Indeed, Γ^{prop} truly corresponds to losses endured by a plane wave propagating in free space between two parallel infinite metallic planes. It is a slowly varying function of frequency, depending neither on the transverse geometry of the cavity, nor on the spatial distribution of the wave function in the cavity. Γ^{refl} , on the contrary, is related to a loss mechanism located on the contour of the cavity, which clearly depends on the geometry of the latter, and chiefly, on the spatial distribution of the normal gradient of the wave function via the quantity ξ . Γ^{refl} therefore fluctuates from mode to mode and, in the case of the rectangular cavity, its explicit form will be given in the following section. By using a boundary perturbation technique to compute losses pertaining to reflections on the contour, it is shown in Appendix B that, to each correction of the imaginary part of the frequency due to Ohmic losses, there is a correspondingly equal correction of the real part. Moreover, this boundary approach sheds light on the intimate connection between the boundary conditions on the contour, leading to nonpurely real wave functions, and the fluctuating partial widths Γ^{refl} [21].

Collecting the above results with those obtained in the previous section, we are now in a position to write the S matrix between weakly coupled pointlike antennas in a 2D cavity in the presence of Ohmic losses. It reads

$$S_{ab} = \delta_{ab} - 2iT^2(\omega) \sum_{n=1}^N \frac{\psi_n(\vec{r}_a)\psi_n(\vec{r}_b)}{\omega^2 - \omega_n^2 + i\omega_n^{(0)}(\Gamma_n^{\text{Ohm}} + \Gamma_n^{\text{ant}})}, \quad (50)$$

where $\omega_n = \omega_n^{(0)} - \Gamma_n^{\text{Ohm}}/2$ and the $\{\omega_n^{(0)}\}$'s are the unperturbed eigenfrequencies of the ideal lossless cavity, and where

$$T(\omega) = c \frac{Z_0}{Z} \frac{\sin^2 \frac{\omega l_{\text{eff}}}{2c}}{\sin \frac{\omega l^*}{2c} \cos \frac{\omega l^*}{2c}}, \quad (51)$$

the contribution of antennas to the widths being given, at leading order, by

$$\Gamma_n^{\text{ant}} = \frac{T^2(\omega_n)}{\omega_n^{(0)}} \sum_{c=1}^M |\psi_n^{(0)}(\vec{r}_c)|^2. \quad (52)$$

Here it should be remarked that the second factor ψ in Eq. (50) should not be a complex conjugate. Indeed, due to Ohmic losses, the wave functions are no longer real and the S matrix cannot keep its unitarity. Nonetheless, it obviously has to remain symmetric. In the previous section, we used the Hermitian formalism for the sake of convenience, but it turns out to be inappropriate for the present purpose (see, for instance, Ref. [13] about self-adjoint systems).

IV. EXPERIMENTAL VALIDATION IN A RECTANGULAR CAVITY

A. A preliminary global test

The aim of this section is to check the pertinence of the description given above in a rectangular cavity where eigenfunctions and eigenfrequencies are easily calculated in the limit of vanishing losses. A preliminary test, which does not involve any sophisticated fitting procedure, consists in comparing the average transmission between two antennas with the corresponding quantity deduced from Eq. (50). According to this equation, the transmission coefficient ($a \neq b$) for $\omega = \omega_n$ approximately reads

$$|S_{ab}(\omega_n)| \simeq 2T^2(\omega_n) \frac{|\psi_n(\vec{r}_a)\psi_n(\vec{r}_b)|}{\omega_n^{(0)}\Gamma_n}, \quad (53)$$

where $\Gamma_n = \Gamma_n^{\text{Ohm}} + \Gamma_n^{\text{ant}}$. In a lossless rectangular cavity with sides $L_x \times L_y$, the eigenfrequencies are

$$\omega_{l,m}^{(0)} = \pi c \sqrt{\left(\frac{l}{L_x}\right)^2 + \left(\frac{m}{L_y}\right)^2}, \quad (54)$$

where l, m are integers. The corresponding eigenfunctions read

$$\psi_{l,m}^{(0)}(x,y) = \frac{2}{\sqrt{L_x L_y}} \sin \frac{l\pi x}{L_x} \sin \frac{m\pi y}{L_y}. \quad (55)$$

Assuming that $|\psi_n(\vec{r})| \simeq |\psi_{l,m}^{(0)}(x,y)|$, one deduces

$$T^2(\omega_n) \simeq \frac{L_x L_y \pi^4 \omega_n \Gamma_n}{128} \langle |S_{ab}(\omega_n)| \rangle, \quad (56)$$

where the average is performed on the positions \vec{r}_a and \vec{r}_b of the antennas. In our experiments, the average was obtained by performing the 45 distinct transmission measurements that the 10 antennas allow. The values of ω_n and Γ_n used in the experimental evaluation of the right-hand side of Eq. (56) were obtained, in a rough way, through the analysis of the *group delay*. This quantity, defined as the derivative of the phase φ_{ab} of S_{ab} with respect to ω , presents rather well defined extrema at frequencies close to eigenfrequencies. For a gross estimation of Γ_n we used $\Gamma_n \simeq 2/\langle d\varphi_{ab}(\omega_n)/d\omega \rangle$, which is exact for an isolated resonance. Note that, in the case of moderate or large modal overlap, this method generally overestimates the widths. Knowing the dimensions L_x and L_y of the cavity, the right-hand side of Eq. (56) only depends on the length parameters l_{eff} and l^* . Recall that l^* is the length of the perturbed region at the end of the coax, and that l_{eff} is the effective length over which the field inside the cavity is coupled to the antenna. One may assume, in this preliminary global test, that l_{eff} remains close to the length l of the part of the antenna which lies inside the cavity: $l_{\text{eff}} \simeq l = 2.0 \pm 0.3$ mm. In the same way, a rough estimate of l^* is given by the distance between the end of the antenna and the reference (calibration) plane of the coax: 16.5 ± 0.2 mm. Figure 3 compares T^2 as obtained through Eq. (51) with its experimental value deduced from Eq. (56) for the first 348 resonances up to 5.5 GHz. The lowest and the highest continuous curves correspond to $l_{\text{eff}} = 1.7$ mm and $l_{\text{eff}} = 2.3$ mm,

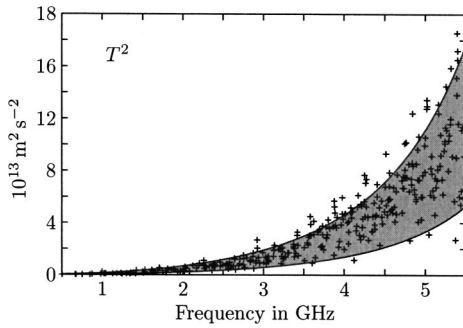


FIG. 3. Experimentally based estimation of $T^2(\omega_n)$ as given by Eq. (56) (crosses). The gray region corresponds to its theoretical expression (51) for values of l_{eff} between 1.7 mm and 2.3 mm ($l^* = 1.65$ cm).

respectively. At the resolution of the presented figure, the curves obtained for values of l^* ranging from 16.3 mm to 16.7 mm are not distinguishable. A fair agreement is observed between the experiment and our model. A first consequence of this test is to substantiate the correspondence between the length parameters of our model and the actual lengths of the coax antennas. Note also that this global preliminary test requires no sophisticated data processing of the individual resonances. In the following, we will see how our model for coupling with antennas remains quite satisfactory when put to more stringent tests.

B. A test with individual resonances

In the global test presented above, we had no need of a precise knowledge of the wave functions at the antennas. To check the validity of formula (50), we have developed an original fitting procedure (see [22]) to extract the actual complex eigenfrequencies ω_n and the complex amplitudes

$$A_n^{ab} = -2iT^2(\omega_n)\psi_n(\vec{r}_a)\psi_n(\vec{r}_b). \quad (57)$$

With this procedure, based upon a mixture of robust algorithms, we could check that the actual eigenfrequencies remain very close to the unperturbed values given by Eq. (54) in the frequency range studied here. Now we proceed to verify that the amplitudes A_n deduced from our measurements are well described by Eq. (57) with expression (51) for T and formula (55) to approximate the true eigenfunctions. Indeed, even if the existence of nonuniform losses (chiefly those associated to Γ^{refl}) leads to nonpurely real wave functions, we will see below that the corrections remain very small. From Eq. (57) it is easily deduced for three different antennas a , b , and c that

$$\frac{|A_n^{ab}| |A_n^{ac}|}{|A_n^{bc}|} = 2T^2(\omega_n)|\psi_n(\vec{r}_a)|^2. \quad (58)$$

As there are 36 different ways of combining the 45 amplitudes A^{ab} , yielding 36 slightly different values of Eq. (58), one can use the following average estimate:

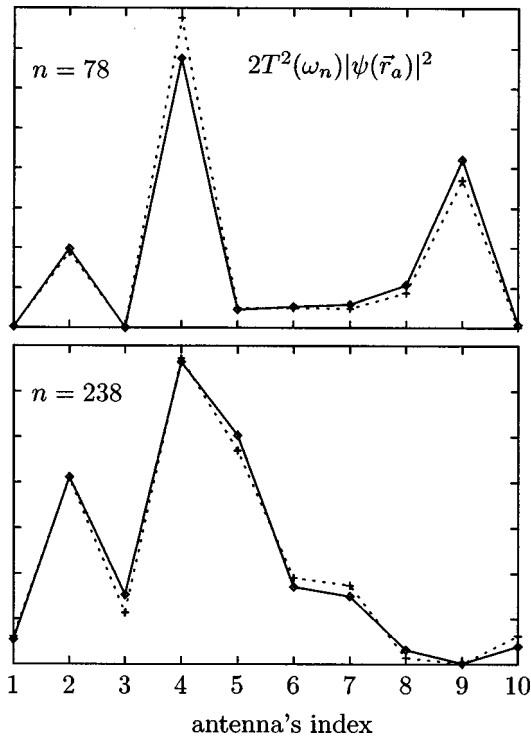


FIG. 4. Comparison of Eq. (59) with $2T^2(\omega_n)|\psi_{l,m}^{(0)}(x_a, y_a)|^2$ at the ten antennas (indices are introduced in Fig. 1) for resonances $n=78$ and $n=238$.

$$2T^2(\omega_n)|\psi_{l,m}^{(0)}(x_a, y_a)|^2 = \frac{1}{36} \sum_{\substack{b,c \neq a \\ b < c}} \frac{|A_n^{ab}| |A_n^{ac}|}{|A_n^{bc}|}, \quad (59)$$

where $|\psi_n(\vec{r})| \approx |\psi_{l,m}^{(0)}(x, y)|$ is assumed. For a given resonance, one can directly compare the above quantity with $2T^2(\omega_n)|\psi_{l,m}^{(0)}(x_a, y_a)|^2$ for the ten antennas ($a=1, \dots, 10$). This comparison is shown in Fig. 4 for two distinct resonances, namely $n=78$ at 2.655 GHz and $n=238$ at 4.558 GHz. As the great majority of resonances that we are concerned with are narrow enough to ensure a good correspondence with the unperturbed wave functions, we observe a fairly good agreement.

To extend our comparison to all resonances, one can now average over all ten locations of antenna a . For the best values of $l_{\text{eff}}=1.9$ mm and $l^*=16.5$ mm obtained in the frequency range from 2 GHz to 5.5 GHz, Fig. 5 shows the comparison between the experimental quantity $\langle \frac{1}{36} \sum_{b < c \neq a} |A_n^{ab}| |A_n^{ac}| / |A_n^{bc}| \rangle_a$ and the prediction $2T^2(\omega_n) \times \langle |\psi_{l,m}^{(0)}(x_a, y_a)|^2 \rangle_a$ up to 5.5 GHz. The agreement is excellent on the average. By a close inspection, e.g., between 2 GHz and 3 GHz as shown in the inset, one can notice that the agreement is generally excellent even at the level of individual resonances. Rare important discrepancies are observed for very close neighboring eigenfrequencies (quasidegeneracies) due to modal overlapping. Indeed, when the latter effect is not negligible, one expects that the spatial distribution of the wave function results from a linear combination of neighboring unperturbed wave functions [23]. Beyond 3 GHz, this effect deteriorates the agreement due to

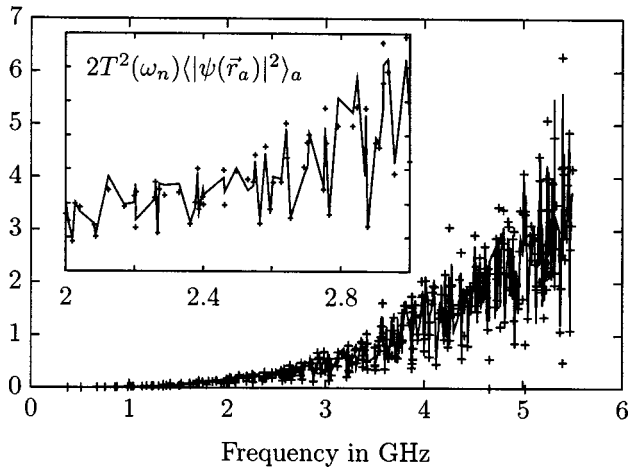


FIG. 5. Comparison between the experimental quantity $\langle \frac{1}{36} \sum_{b < c \neq a} |A_n^{ab}| |A_n^{ac}| / |A_n^{bc}| \rangle_a$ (crosses) with the prediction $2T^2(\omega_n) \times \langle |\psi_{l,m}^{(0)}(x_a, y_a)|^2 \rangle_a$ (line). Inset: enlarged view within the range 2–3 GHz.

the concomitant increase of the total width and decrease of the mean spacing, leading to an inadequacy of the zeroth-order eigenfunctions we use for our test.

C. Partial width decomposition

As seen above, the total width of a resonance can be decomposed as a sum of three partial widths associated to losses through the antennas, Ohmic losses on the contour of the cavity, and Ohmic losses at the surface of both ends which appear as damping along propagation. In a rectangular cavity, the total width of the n th resonance, characterized by the quantum numbers l and m , is given by

$$\Gamma_n = \Gamma_{l,m}^{\text{ant}} + \Gamma_{l,m}^{\text{refl}} + \Gamma^{\text{prop}}(\omega_n). \quad (60)$$

By using expression (55) for the wave functions in order to evaluate the factor ξ in Eq. (41), one obtains

$$\xi_{l,m} = \frac{Ac^2}{\omega_{l,m}^2 L} \left(\frac{l^2}{L_x^3} + \frac{m^2}{L_y^3} \right) \quad (61)$$

whence, using Eq. (49),

$$\Gamma_{l,m}^{\text{refl}} \simeq \frac{c^2 \delta_{\text{cont}}(\omega_n)}{2\omega_{l,m}^{(0)}} \left(\frac{l^2}{L_x^3} + \frac{m^2}{L_y^3} \right). \quad (62)$$

These partial widths clearly vary from mode to mode as illustrated in Fig. 6, where $\xi_{l,m}-1$ is shown for each eigenfrequency up to 5.5 GHz. Note that the $\xi_{l,m}$'s oscillate around unity and vary at most by 23%.

The widths associated to losses through antennas also vary from mode to mode,

$$\Gamma_{l,m}^{\text{ant}} = \frac{T^2(\omega_n)}{\omega_{l,m}^{(0)}} \sum_{c=1}^M |\psi_{l,m}^{(0)}(\vec{r}_c)|^2. \quad (63)$$

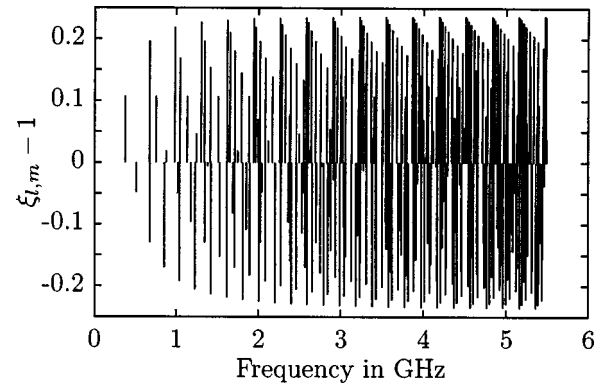


FIG. 6. Values of $(\xi_{l,m}-1)$ after Eq. (61) for all resonances up to 5.5 GHz.

In the previous subsection, we already checked the validity of the above formula for all resonances shown in Fig. 5 since $\Gamma_{l,m}^{\text{ant}}$ is essentially proportional to the sum of expression (59) over all antennas.

Thus by fitting the experimental transmission by formula (50), one obtains a direct measure of the total width and an indirect measure of Γ_n^{ant} , thus enabling us to evaluate the two effective conductivities σ_{ends} and σ_{cont} . A representation of all the Ohmic widths $\Gamma_n^{\text{Ohm}} = \Gamma_n - \Gamma_{l,m}^{\text{ant}}$ up to 3 GHz is given in Fig. 7. A comparison is shown between theoretical Ohmic widths (crosses) and experimental Ohmic widths (continuous curve). The smooth dominant contribution given by $\Gamma^{\text{prop}}(\omega)$ is indicated by the dashed curve. The agreement on the mean level and on the amplitude of fluctuations (only present in Γ_n^{refl}) is fairly good, whereas, resonance by resonance, the agreement is not systematic, essentially due to the effect of modal overlap mentioned above.

V. CONCLUSION

In conclusion, we have tried to provide a better understanding of the physical mechanisms at the origin of resonance broadening in microwave cavities. We have explicitly

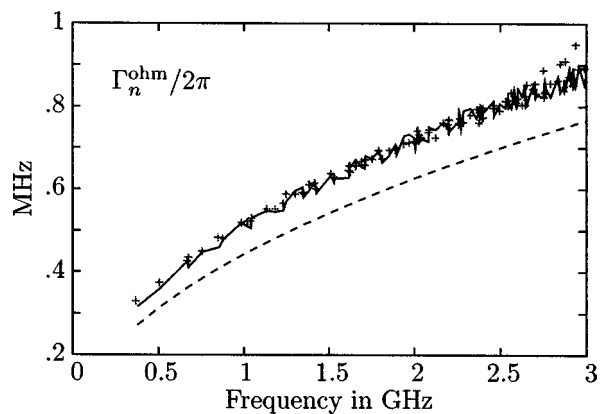


FIG. 7. Behavior of the Ohmic widths up to 3 GHz. Comparison is shown between theoretical Ohmic widths (crosses) and experimental Ohmic widths (continuous curve). The dashed curve indicates the smooth contribution $\Gamma^{\text{prop}}(\omega)$.

developed an S -matrix model including the frequency-dependent coupling of the antennas and accounting for Ohmic absorption at the boundaries of a two-dimensional cavity. We have especially emphasized the necessity to distinguish between Ohmic attenuation along propagation, leading to a smooth frequency-dependent contribution to the total width, and localized absorption at the contour of the cavity, yielding a contribution varying from mode to mode. We have performed experiments where we analyzed the transmission versus frequency in terms of a Breit-Wigner decomposition deduced from our model. In the rectangular cavity we used, all the quantities involved in our theoretical description could easily be calculated in the perturbative limit of small or moderate modal overlap. We therefore have been able to validate our approach and provide a very precise estimation of the various contributions to the total widths. In particular, the varying contribution of Ohmic losses at the contour could be quantitatively checked at the level of individual resonances, except for quasidegenerate modes. This approach has recently enabled us to relate the losses at the contour, in a chaotic cavity, to the imaginary part of the wave function [21].

We believe that our present approach is an important step to test existing or yet to come theories of open or absorptive chaotic wave systems. Indeed, such theories generally assume that losses are associated with distinct well identified coupling channels [11]. It is nonetheless not obvious that these can be used to describe different sources of loss as damping along propagation or Ohmic dissipation at the contour. For instance, absorbing boundaries may be viewed as a number (of the order of L/λ) of distributed coupling channels. Indeed, to mimic absorption, recent theoretical predictions have been proposed but only in the asymptotic limit of a large number of effective channels with vanishing coupling [24,25] (see also [10]).

ACKNOWLEDGMENTS

The authors gratefully acknowledge helpful discussions with P. Sebbah, R. L. Weaver, and H.-J. Stöckmann.

APPENDIX A: EVALUATION OF THE S MATRIX

1. Self-adjointness condition

In the Hilbert space of the complete problem (cavity and antennas), one defines the following scalar product:

$$(\Phi, \Phi') = \int \int_{\mathcal{A}} d\vec{r} \varphi_{\alpha}^*(\vec{r}) \varphi_{\alpha'}(\vec{r}) + \sum_{c=1}^M \int_0^{\infty} dz_c \varphi_{\beta_c}^*(z_c) \varphi_{\beta'_c}(z_c). \quad (\text{A1})$$

With this scalar product, the self-adjointness condition

$$(\mathcal{H}\Phi, \Phi') = (\Phi, \mathcal{H}\Phi') \quad (\text{A2})$$

reads

$$\begin{aligned} & (\mathcal{H}\Phi, \Phi') - (\Phi, \mathcal{H}\Phi') \\ &= \int \int_{\mathcal{A}} d\vec{r} [\varphi_{\alpha}^*(\vec{r}) [\Delta \varphi_{\alpha'}(\vec{r})] - [\Delta \varphi_{\alpha}(\vec{r})]^* \varphi_{\alpha'}(\vec{r})] \\ &+ \sum_{c=1}^M [T_c^*(k) \varphi_{\beta_c}^*(0) \varphi_{\alpha'}(\vec{r}_c) - \varphi_{\alpha}^*(\vec{r}_c) T_c(k) \varphi_{\beta'_c}(0)] \\ &- \sum_{c=1}^M \int_o^{\infty} dz_c [\varphi_{\beta_c}''(z_c) \varphi_{\beta'_c}(z_c) - \varphi_{\beta_c}^*(z_c) \varphi_{\beta'_c}''(z_c)]. \end{aligned} \quad (\text{A3})$$

Using Green's theorem for the first term and integrating the third one by parts, one obtains

$$\begin{aligned} & (\mathcal{H}\Phi, \Phi') - (\Phi, \mathcal{H}\Phi') \\ &= \int_{\mathcal{C}} d\hat{n} \{ \varphi_{\alpha}(\vec{r}) [\nabla \varphi_{\alpha'}(\vec{r})] - [\nabla \varphi_{\alpha}(\vec{r})] \varphi_{\alpha'}(\vec{r}) \} \\ &+ \sum_{c=1}^M [T_c^*(k) \varphi_{\beta_c}^*(0) \varphi_{\alpha'}(\vec{r}_c) - \varphi_{\alpha}^*(\vec{r}_c) T_c(k) \varphi_{\beta'_c}(0)] \\ &- \sum_{c=1}^M [\varphi_{\beta_c}''(z_c) \varphi_{\beta'_c}(z_c) - \varphi_{\beta_c}^*(z_c) \varphi_{\beta'_c}''(z_c)]_0^{\infty}. \end{aligned} \quad (\text{A4})$$

The eigenfunctions $\varphi_{\alpha}(\vec{r})$ obey boundary Dirichlet conditions, and the last term in Eq. (A4) vanishes for $z \rightarrow \infty$. The self-adjointness condition can thus be written

$$\begin{aligned} & \sum_{c=1}^M \{ [\varphi_{\beta_c}''(0) \varphi_{\beta'_c}(0) - \varphi_{\beta_c}^*(0) \varphi_{\beta'_c}'(0)] \\ &+ \varphi_{\beta_c}^*(0) T_c^*(k) \varphi_{\alpha'}(\vec{r}_c) - T_c(k) \varphi_{\alpha}^*(\vec{r}_c) \varphi_{\beta'_c}(0) \} = 0. \end{aligned} \quad (\text{A5})$$

This condition is nontrivially fulfilled by imposing

$$T_c^*(k) \varphi_{\alpha}(\vec{r}_c) = \varphi_{\beta_c}'(0). \quad (\text{A6})$$

2. The coupling matrix elements

Assuming $E_0 = k^2$, eq. (20) now reads

$$(\Delta + k^2) \varphi_{\alpha}(\vec{r}) = \sum_{c=1}^M T_c(k) \delta(\vec{r} - \vec{r}_c) \varphi_{\beta_c}(0). \quad (\text{A7})$$

Furthermore, the Green's functions of the isolated cavity are given by

$$(\Delta + k^2) G(\vec{r}, \vec{r}', k^2) = \delta(\vec{r} - \vec{r}'). \quad (\text{A8})$$

By comparing eqs. (A7) and (A8), for $\vec{r} = \vec{r}_b$, one obtains

$$\varphi_{\alpha}(\vec{r}_b) = \sum_{c=1}^M T_c(k) G(\vec{r}_b, \vec{r}_c, k) \varphi_{\beta_c}(0). \quad (\text{A9})$$

With the boundary conditions (A6) and the expression (15) of φ_{β} , relation (A9) becomes

$$\begin{aligned} \mathcal{A}_{in}^c - \frac{i}{k} T_b^*(k) \sum_{c=1}^M T_c(k) G(\vec{r}_b, \vec{r}_c, k) \mathcal{A}_{out}^c &= \mathcal{A}_{out}^c \\ + \frac{i}{k} T_b^*(k) \sum_{b=1}^M T_c(k) G(\vec{r}_b, \vec{r}_c, k) \mathcal{A}_{out}^b, \end{aligned} \quad (\text{A10})$$

or, in a matrix form,

$$\mathcal{A}_{in} - iK\mathcal{A}_{in} = \mathcal{A}_{out} + iK\mathcal{A}_{out}, \quad (\text{A11})$$

where K is an $M \times M$ matrix defined by

$$K_{ab}(k) = \frac{T_a^*(k)}{\sqrt{k}} G(\vec{r}_a, \vec{r}_b, k) \frac{T_b(k)}{\sqrt{k}}. \quad (\text{A12})$$

From $\mathcal{A}_{out} = S\mathcal{A}_{in}$ one thus makes the relation (26) between K and the S matrix explicit. By introducing in Eq. (12) the expansion of the Green's function in terms of the eigenfunctions $\psi_\nu(\vec{r}) = \langle \vec{r} | \nu \rangle$ of the isolated cavity,

$$G(\vec{r}, \vec{r}', E) = \sum_{\nu=1}^N \frac{\psi_\nu(\vec{r}) \psi_\nu^*(\vec{r}')}{k^2 - k_\nu^2}, \quad (\text{A13})$$

one finds the following expression for the K matrix:

$$K_{ab}(k) = \left(\frac{T_a(k) \psi_\nu^*(\vec{r}_a)}{\sqrt{k}} \right)^* \frac{1}{k^2 - k_\nu^2} \left(\frac{T_b(k) \psi_\nu^*(\vec{r}_b)}{\sqrt{k}} \right). \quad (\text{A14})$$

Finally, the elements of the coupling matrix W , related to K by Eq. (27), are given by

$$W_{\mu c} = \frac{T_c(k) \psi_\mu^*(\vec{r}_c)}{\sqrt{k} \pi}. \quad (\text{A15})$$

APPENDIX B: PERTURBATIVE BOUNDARY CONDITIONS

An alternative way of computing the losses at the contour is easily obtained by following a boundary perturbation technique (see, for instance, [20]). Indeed, calling ψ_0 the solution at the real eigenfrequency ω_0 of the zeroth-order problem

defined by Eqs. (36) and (37), the perturbation of the boundary conditions can be written

$$\psi \simeq -(1+i) \frac{\mu_c \delta}{2\mu} \partial_n \psi_0 \text{ on } \mathcal{C}. \quad (\text{B1})$$

Green's theorem applied to this 2D problem straightforwardly yields

$$\omega^2 - \omega_0^2 \simeq -(1+i) \frac{1}{\epsilon \mu} \frac{\mu_c \delta}{2\mu} \frac{\oint_C d\ell |\partial_n \psi_0|^2}{\int_S \int_S da |\psi_0|^2}. \quad (\text{B2})$$

Writing the perturbed eigenfrequency as $\omega = \omega_0 + \delta\omega - i\Gamma/2$, Eq. (B2) becomes

$$\delta\omega - i\Gamma/2 \simeq -(1+i) \frac{1}{\epsilon \mu} \frac{\mu_c \delta}{4\mu \omega_0} \frac{\oint_C d\ell |\partial_n \psi_0|^2}{\int_S \int_S da |\psi_0|^2}, \quad (\text{B3})$$

leading, in the case at hand, to equal corrections on both real and imaginary parts of ω . This last comment is general and applies as well to the corrections originating from Ohmic losses at the top and bottom of the cavity. Thus, this perturbative approach completely agrees with the one developed in Sec. III as long as the widths are concerned and completes it as it provides an estimation of the frequency shift of the resonances related to Ohmic losses. This was indeed remarkably well verified for all the resonances with frequencies larger than 2 GHz studied in Sec. IV of the present article, these results being detailed in Chap. V of Barthélemy's thesis (Ref. [22]). It is also particularly interesting to note that Eq. (B1) gives a quite natural hint of how Ohmic losses on the contour induce a small amount of complexity for wave functions that are purely real in the unperturbed limit. As long as a perturbative approach is valid, an immediate connection is deduced between the complex character of wave functions and the fluctuating part of the widths embodied in the quantity ξ defined in Eq. (41) [21].

-
- [1] H.-J. Stöckmann, *Quantum Chaos* (Cambridge University Press, Cambridge, 1999).
 - [2] H.-J. Stöckmann and J. Stein, Phys. Rev. Lett. **64**, 2215 (1990).
 - [3] H.-D. Gräf, H. L. Harney, H. Lengeler, C. H. Lewenkopf, C. Rangacharyulu, A. Richter, P. Schardt, and H. A. Weidenmüller, Phys. Rev. Lett. **69**, 1296 (1992).
 - [4] F. Haake, G. Lenz, P. Šeba, J. Stein, H.-J. Stöckmann, and K. Życzkowski, Phys. Rev. A **44**, R6161 (1991).
 - [5] H. Alt, H.-D. Gräf, H. L. Harney, R. Hofferbert, H. Lengeler, A. Richter, P. Schardt, and H. A. Weidenmüller, Phys. Rev. Lett. **74**, 62 (1995).
 - [6] T. Ericson, Ann. Phys. (N.Y.) **23**, 390 (1963).
 - [7] M. Schreder, J. Acoust. Soc. Am. **34**, 1819 (1962).
 - [8] J. Verbaarschot, H. Weidenmüller, and M. Zirnbauer, Phys. Rep. **129**, 367 (1985).
 - [9] R. Schäfer, T. Gorin, T. Seligman, and H.-J. Stöckmann, J. Phys. A **36**, 3289 (2003).
 - [10] I. Rozhkov, Y. V. Fyodorov, and R. L. Weaver, Phys. Rev. E **68**, 016204 (2003).
 - [11] F.-M. Dittes, Phys. Rep. **339**, 215 (2000).
 - [12] R. F. Harrington, *Time-Harmonic Electromagnetic Fields*, A Classic Reissue (Wiley-Interscience, New York, 2001).
 - [13] R. E. Collin, *Field Theory of Guided Waves, Electromagnetic Waves*, 2nd ed. (IEEE, New York, 1991).
 - [14] G. Liu and C. A. Grimes, Microwave Opt. Technol. Lett. **26**,

- 30 (2000).
- [15] Z. Shen and R. H. MacPhie, *Radio Sci.* **31**, 1037 (1996).
- [16] H. J. Eom, Y. H. Cho, and M. S. Kwon, *IEEE Trans. Antennas Propag.* **48**, 1142 (2000).
- [17] H. Feshbach, *Theoretical Nuclear Physics* (Wiley, New York, 1992).
- [18] Y. Fyodorov and H.-J. Sommers, *J. Math. Phys.* **38**, 1918 (1997).
- [19] S. Albeverio, F. Haake, P. Kurasov, M. Kuš, and P. Šeba, *J. Math. Phys.* **37**, 4888 (1996).
- [20] J. D. Jackson, *Classical Electrodynamics* (Academic, New York, 1965).
- [21] J. Barthélémy, O. Legrand, and F. Mortessagne, e-print cond-mat/0402029.
- [22] J. Barthélémy, Ph.D. thesis, Université Paris 7 - Denis Diderot (2003), URL <http://tel.ccsd.cnrs.fr/documents/archives0/00/00/41/14/>.
- [23] U. Kuhl, E. Persson, M. Barth, and H.-J. Stöckmann, *Eur. Phys. J. B* **17**, 253 (2000).
- [24] R. A. Méndez-Sánchez, U. Kuhl, M. Barth, C. H. Lewenkopf, and H.-J. Stöckmann, *Phys. Rev. Lett.* **91**, 174102 (2003).
- [25] D. V. Savin and H.-J. Sommers, *Phys. Rev. E* **68**, 036211 (2003).

C. Inhomogeneous resonance broadening and statistics of complex wave functions in a chaotic microwave cavity, Europhysics Letters 70, 162 (2005) & Inhomogeneous losses and wave function complexity, Europhysics Letters 76, 774 (2006)

Je présente simultanément ces deux articles car l'un, le deuxième, théorise ce que l'autre, le premier, avait vu et conjecturé. Les deux s'attachent donc de façon complémentaire à décrire le lien subtil qui relie la distribution de la phase d'une résonance et les pertes du système dans lequel elle s'établit. Nous ne parlons évidemment pas ici de pertes spatialement uniformes, mais de pertes inhomogènes, liées à la structure spatiale de la résonance. En effet, dans le premier cas le mode n'acquiert qu'une phase globale, spatialement homogène. En revanche, dans le second, la phase présente des variations importantes d'un point à l'autre de la résonance. Cette distinction est déjà faite dans la section III de IV.B, mais elle est exploitée dans le premier des présents articles. Il faut souligner que l'obtention des données qui permettent de construire la figure 1 de cet article tient de la gageure ; c'est grâce au remarquable outil d'ajustement développé par Jérôme Barthélémy durant sa thèse que nous avons pu la relever. Je prends le risque de faire naître chez le lecteur un soupçon de « Sabine mania », mais encore une fois l'argument qualitatif avancé pour dériver l'équation (13) repose sur la loi de Sabine. Elle semble décidément incontournable dès que l'on tolère des pertes dans le système ! Grâce à cette invocation de Wallace Clement Sabine, nous justifions physiquement la proportionnalité directe observée entre les largeurs des distributions de phases et les largeurs spectrales inhomogènes des résonances. Dans le deuxième, nous la dérivons explicitement pour le problème simple de deux résonances initialement isolées, et dont la présence de pertes induit un recouvrement.

Le projet sur l'amplification optique des scars (*cf.* II.E) a déjà dressé une passerelle vers les lasers aléatoires. Ici encore, mon travail rejoint des préoccupations actuelles de Christian Vanneste et Patrick Sebbah. En effet, leurs simulations d'un laser aléatoire fonctionnant dans un régime de diffusion loin de la localisation forte mettent en exergue des modes lasers d'une durée de vie extrêmement fugace dans le régime passif³⁹ ; la proportion d'ondes progressives dans la structure spatiale de ces résonances est donc très importante. À l'opposé d'un mode localisé, qui se comporte comme un mode stationnaire standard : tous les points oscillent en phase ou en opposition de phase, un tel mode diffus exhibe une distribution de phase très large. La thèse que débute Charles Poli sera l'occasion d'associer nos efforts pour atteindre, grâce à la conjonction de nos savoir-faire numériques, expérimentaux et théoriques (en collaboration étroite avec Dima Savin),

une meilleure compréhension de ces situations complexes.

³⁹ C. Vanneste, P. Sebbah, and H. Cao, *Lasing with resonant feedback in the diffusive regime*, soumis à Phys. Rev. Lett. (2006).

Inhomogeneous resonance broadening and statistics of complex wave functions in a chaotic microwave cavity

J. BARTHÉLEMY, O. LEGRAND and F. MORTESSAGNE

*Laboratoire de Physique de la Matière Condensée, CNRS UMR 6622
Université de Nice-Sophia Antipolis - 06108 Nice cedex 2, France*

received 24 January 2005; accepted in final form 24 February 2005
published online 16 March 2005

PACS. 05.45.Mt – Quantum chaos; semiclassical methods.

PACS. 05.60.Gg – Quantum transport.

Abstract. – The complex (non-real) character of wave functions is ubiquitous in open or dissipative wave systems. We experimentally study the various manifestations of ohmic losses in a two-dimensional microwave chaotic cavity and show that losses located at the contour of the cavity lead to resonance widths which vary from mode to mode. We describe how this *inhomogeneous* damping is responsible for a spatially non-uniform phase of the wave function. We experimentally demonstrate that the *inhomogeneous* part of the width is related to a single parameter, which measures the amount of complexity of the wave function, and provide theoretical arguments in favor of this relation.

Investigations of the morphology of wave functions in partially open chaotic wave systems have recently become an active domain of research, especially through theoretical works concerned with quantum transport in the ballistic regime [1, 2]. That the spatial properties of resonances are closely related to their spectral widths has been recognized ever since the pioneering work of Porter and Thomas [3] until more recent experimental investigations in a superconducting microwave cavity [4]. These experiments resort to a chi-squared distribution of widths based on results of Random Matrix Theory (RMT), which is known to describe spectral and spatial statistics of closed chaotic wave systems [5]. Microwave cavities turn out to be ideal model systems to study open wave systems [6, 7], since they offer the possibility of opening channels through antennas or connected waveguides. They can also be qualified as open because of dissipation through ohmic losses at their boundaries. Locally, boundaries may be viewed as distributed equivalent opening channels with *ad hoc* impedances. Through such losses, the standing waves of a closed cavity are changed into a mixture of standing and traveling waves, the latter being associated to the energy flowing out of the system [8]. *Homo-geneous* damping, *i.e.* overall uniform attenuation rate, can only lead to modes that are real (up to a global phase) and associated to the standing-wave part of the wave function. Hence, the observation of complex-valued wave functions implies *inhomogeneous* damping mechanisms giving birth to the traveling part of the wave function [8]. A thorough description of the link between *inhomogeneous* damping and the complex character of wave functions is still lacking, as recently emphasized by Lobkis and Weaver in the context of acoustical reverberant dissipative system [9].

In this letter, we present an experiment in a two-dimensional (2D) chaotic microwave cavity at room temperature where dissipation is essentially due to ohmic losses at boundaries. In such chaotic cavities, modes are generically ergodic, *i.e.* present speckle-like intensity patterns. The importance of the imaginary part of the modes implied by the presence of losses can be measured through a single statistical parameter, namely the ratio $\langle (\text{Im } \psi)^2 \rangle / \langle (\text{Re } \psi)^2 \rangle \equiv q^2$, where the wave function ψ is conventionally assumed to be real ($q = 0$) in the case of vanishing losses. The principal aim of this paper is to demonstrate the intimate relation between this parameter q and the part of the decay rate (or modal width) associated to *inhomogeneous* damping. We provide strong experimental evidences of this relationship by carefully analyzing hundreds of resonances in a Sinai-like chaotic cavity.

The cavity is the slice of a rectangular waveguide closed at both ends, with contour \mathcal{C} of length $L = 2.446$ m, section \mathcal{S} of area $A = 0.352762$ m² and thickness $d = 5$ mm. Inside this *flat* parallelepipedic cavity is inserted an obstacle with the shape of a disk of radius 6 cm and thickness d . As long as the wavelength $\lambda = 2\pi k^{-1}$ is larger than d , the cavity may be considered as two-dimensional (2D) and only admits transverse magnetic modes. If the conductor is perfect, the electric field $\vec{E} = E^{(0)}(x, y)\hat{z}$ is perpendicular to the plane (x, y) of the cavity, the magnetic field is parallel and there is no dissipated power. This ideal situation will correspond to the zeroth order of our description of the field near the surface of the actual conductor. Denoting $\psi_0 = E^{(0)}(x, y)$, the time-independent Maxwell equations are reduced to a 2D Helmholtz equation:

$$(\vec{\nabla}^2 + \epsilon\mu\omega^2)\psi_0 = 0, \quad (1)$$

where ϵ and μ are, respectively, the permittivity and the permeability inside the cavity. On the contour \mathcal{C} , ψ_0 obeys Dirichlet conditions $\psi_0 = 0$.

Ohmic losses at the contour are easily computed by following a boundary perturbation technique [10]. Indeed, the perturbed boundary conditions (BC) now read:

$$\psi \simeq -(1+i)\frac{\mu_c\delta}{2\mu}\partial_n\psi \quad \text{on } \mathcal{C}, \quad (2)$$

where $\delta = \sqrt{2/\mu_c\sigma_{cont}\omega}$ is the skin depth (μ_c being the magnetic permeability of the conductor and σ_{cont} the effective conductivity of the contour), and where ∂_n denotes $\hat{n} \cdot \vec{\nabla}$ (\hat{n} being the unit normal vector directed toward the interior of the conductor). Green's theorem applied to this 2D problem straightforwardly yields

$$\omega^2 - \omega_0^2 \simeq -(1+i)\frac{1}{\epsilon\mu}\frac{\mu_c\delta}{2\mu}\frac{\oint_{\mathcal{C}} d\ell |\partial_n\psi|^2}{\iint_{\mathcal{S}} da |\psi|^2}, \quad (3)$$

where ω is the perturbed eigenfrequency, ω_0 being the corresponding real eigenfrequency of the lossless problem. Writing $\omega = \omega_0 + \delta\omega - i\Gamma/2$, eq. (3) becomes

$$\delta\omega - i\Gamma/2 \simeq -(1+i)\frac{1}{\epsilon\mu}\frac{\mu_c\delta}{4\mu\omega_0}\frac{\oint_{\mathcal{C}} d\ell |\partial_n\psi|^2}{\iint_{\mathcal{S}} da |\psi|^2}, \quad (4)$$

leading, in the case at hand, to equal corrections on both real and imaginary parts of ω . In our context μ_c/μ is practically equal to unity. A similar perturbative approach can be applied to the ohmic losses at the top and the bottom of the cavity. One finds that they lead to spatially uniform damping. The total width due to ohmic losses Γ^Ω can thus be split into two parts [11]:

$$\begin{aligned} \Gamma^\Omega &= \Gamma^h + \Gamma^{inh} \\ &\equiv \frac{2}{d}\sqrt{\frac{\omega}{2\mu_c\sigma_{ends}}} + \xi\frac{L}{A}\sqrt{\frac{\omega}{2\mu_c\sigma_{cont}}}, \end{aligned} \quad (5)$$

where ξ is defined by

$$\frac{1}{\epsilon\mu\omega^2} \oint_{\mathcal{C}} d\ell |\partial_n \psi|^2 \equiv \xi \frac{L}{A} \iint_S da |\psi|^2. \quad (6)$$

The first term Γ^h in eq. (5) is the *homogeneous*-damping part of the width (depending only on ω without any dependence on the spatial structure of the mode) associated to an effective conductivity σ_{ends} of the top and bottom. The second term Γ^{inh} is the *inhomogeneous*-damping part of the width related to a parameter ξ , which depends on the spatial structure of the mode at the contour, and is therefore expected to vary from mode to mode.

Here, it is particularly interesting to revisit eq. (2) which turns out to give a quite natural hint of how ohmic losses on the contour induce a small amount of imaginary part for wave functions that are purely real in the unperturbed limit. Indeed, assuming an incident plane wave with unit amplitude, the BC (2) leads to a reflected wave with a small (of order $k\delta$) dephasing. The same BC leads to eq. (4) which relates the width to the quantity ξ .

For the rectangular cavity the values of ξ are readily calculated and display fluctuations around unity, as generally expected [10]. In a previous work [11], studying the case of a rectangular cavity, we actually checked the validity of formula (5) in our experimental situation. In the case of a Sinai-like chaotic cavity, one may view a typical speckle-like mode locally as the superposition of plane waves with random directions, amplitudes and phases. This led Berry [12] to conjecture that the wave functions should be *ergodic* on the average, *i.e.* should display all statistical features of a Gaussian random field. Apart from specific non-ergodic features like *scars* (local intensity enhancement along short unstable periodic orbits), in a chaotic cavity, the relative fluctuations of ξ about unity are expected to decrease with the wavelength λ as the contour \mathcal{C} encompasses a larger number $\sim L/(\lambda/2)$ of equivalent opening channels.

The cavity used for the measurements presented here is made of Oxygen-Free High Conductivity (OFHC) copper. Ten antennas are fixed through the bottom plate and are used as emitters and receivers as well. These antennas (diameter 1.27 mm) are only 2 mm inside the cavity. A rather low coupling is thus achieved, making the role of the antennas nearly negligible regarding their scattering and loss characteristics [11]. Radiation losses are also made negligible by a tight fitting of the various parts of the cavity. Losses are therefore dominated by ohmic losses on the walls of the cavity. A Vector Network Analyzer HP 8720 D is used for the measurements. We restrict our studies to frequencies ranging up to 5.5 GHz since, at higher frequencies, the modal overlap defined as $\Gamma \times n(\omega)$ ($n(\omega)$ being the modal density per unit interval of ω) becomes too important and invalidates any perturbative approach. Below 5.5 GHz, apart from few broader resonances, the modal overlap remains smaller than unity. The measurements are performed by 0.5 GHz bands, sampled with a frequency step 0.3125 MHz. The 45 possible couples of antennas are used. On the whole, it amounts to 756000 points measured between 0.25 GHz and 5.5 GHz. Beyond 2 GHz, all couples of antennas are spaced by a distance larger than λ [11].

In order to fit the transmission between two distinct antennas, we use a Breit-Wigner formula (see, *e.g.*, ref. [6]) which, in our case, reads [11]

$$S_{ab}(\omega) = \sum_n \frac{\alpha_n^{ab} + i\beta_n^{ab}}{\omega^2 - \omega_n^2 + i\omega_n\Gamma_n^\Omega}. \quad (7)$$

The Lorentzian associated to the n -th resonance for the transmission between the antennas a and b is thus characterized by its complex amplitude $\alpha_n^{ab} + i\beta_n^{ab} = -2iT^2(\omega_n)\psi_n(\vec{r}_a)\psi_n(\vec{r}_b)$, its width Γ_n^Ω and its central frequency $\omega_n = \omega_n^0 - \Gamma_n^\Omega/2$, where ω_n^0 stands for the n -th eigenfrequency of the unperturbed cavity. $T(\omega)$ is a function representing the coupling of the antennas

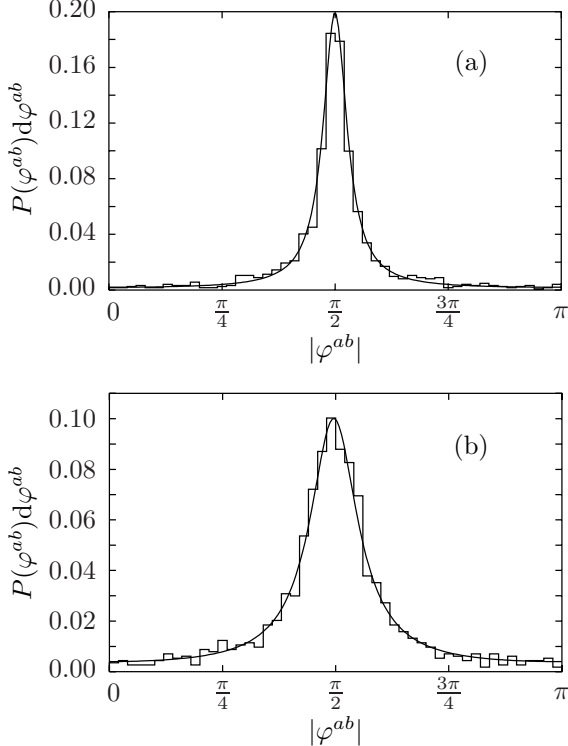


Fig. 1 – Experimental histograms of phase φ^{ab} obtained with 30 resonances in the frequency intervals (a) [3.76 GHz, 4.1 GHz] and (b) [5.24 GHz, 5.5 GHz]. Fitted distributions (9) in solid line: (a) $q = 5.0 \times 10^{-2}$ and (b) $q = 10.1 \times 10^{-2}$.

(all supposed to be identical) to the cavity whose explicit form, which essentially depends on the geometry of the antenna, has been derived in [11, 13]. We were able to test our model for antenna coupling very precisely in an empty rectangular cavity where wave functions and eigenfrequencies are readily calculated. For the present purpose, it is enough to know that T is a slowly varying function on a frequency scale much larger than the mean spacing $n^{-1}(\omega)$. This coupling is obviously also responsible for additional losses and can be accounted for by introducing corresponding partial widths. The contribution of the latter to the total widths being at most of the order of one percent for all the measurements presented here, we could safely neglect them.

Assume that the real and imaginary parts of the wave function $\psi(\vec{r})$ are Gaussian centered random variables with standard deviations $\sigma_r = \sqrt{\langle (\text{Re } \psi)^2 \rangle}$ and $\sigma_i = \sqrt{\langle (\text{Im } \psi)^2 \rangle}$. The key parameter $q = \sigma_i/\sigma_r$ is a measure of the *openness* of the system. Its value is 0 when the cavity is completely closed (real wave functions) and tends to unity for totally absorbing boundaries (complex-valued wave functions with equal σ_r and σ_i). In practice, as the spatial sampling over ten antennas for a given resonance is undersized to estimate σ_r and σ_i accurately, we are led to restrict ourselves to a coarse-grained estimation of q by grouping several contiguous resonances in frequency windows. This may be achieved by building the probability distribution of the phase φ_n^{ab} of the complex amplitude of $\alpha_n^{ab} + i\beta_n^{ab}$:

$$\varphi_n^{ab} = -\frac{\pi}{2} + \varphi_n(\vec{r}_a) + \varphi_n(\vec{r}_b), \quad (8)$$

where $\varphi_n(\vec{r})$ is the phase of the complex field $\psi_n(\vec{r})$. This distribution is readily obtained from the Gaussian hypothesis and reads [9, 14, 15]:

$$P(\varphi^{ab}) = \frac{q}{\pi} \frac{1+q^2}{4q^2 + (1-q^2)^2 \sin^2(\varphi^{ab} + \frac{\pi}{2})}. \quad (9)$$

This distribution displays a peak centered on $|\varphi^{ab}| = \pi/2$ (see fig. 1). The width of the peak increases with q so that the distribution tends to a Dirac delta as $q \rightarrow 0$ or to a uniform distribution as $q \rightarrow 1$. Distribution (9) is related to the so-called Poisson kernel [16] which has gained a renewal of interest in recent microwave experiments concerned with the S -matrix of chaotic cavities with absorption in the one-channel case [17, 18]. The distributions (a) and (b) shown in fig. 1 have been obtained by using 30 resonances lying in the frequency intervals [3.76 GHz, 4.1 GHz] and [5.24 GHz, 5.5 GHz] respectively, yielding coarse-grained estimations of q equal to 5.0×10^{-2} and 10.1×10^{-2} , respectively. The quality of the fit substantiates the Gaussian hypothesis whose validity is known to improve when a frequency average is performed (see, for instance, refs. [6, 19]). This hypothesis is intimately related to RMT, the relevance of which we could check in our experiment by exhibiting a spacing distribution of the Wigner-Dyson type [13].

In order to establish the connection between the spatial statistics of complex wave functions and their (spectral) widths due to *inhomogeneous* damping, it is useful to introduce a ray picture of losses due to reflections at the contour. For a plane wave incident on an air-metal interface with angle of incidence θ , it can be shown [20] that the relative amount of absorbed energy reads:

$$\mathcal{T} = |t|^2 = \frac{4a \cos \theta}{2a^2 \cos^2 \theta + 2a \cos \theta + 1}, \quad (10)$$

where $a = \sqrt{\omega\epsilon/(2\sigma_{cont})}$. In the case of OFHC copper, $a \sim 10^{-5}$ around 1 GHz and the previous equation reduces to

$$\mathcal{T} \simeq 4a \cos \theta. \quad (11)$$

For an *ergodic* wave function in a chaotic billiard, a contour average is equivalent to an angular average with the appropriate statistical measure $d(\sin \theta)/2$, leading to a mean absorption coefficient,

$$\langle \mathcal{T} \rangle = \pi \sqrt{\omega\epsilon/(2\sigma_{cont})}. \quad (12)$$

Having in mind the analogy of our problem with ultrasonics in a reverberant body [21] or with room acoustics [22], one may use the so-called Sabine's law [22] to deduce the average width Γ_{refl} related to absorption at the contour:

$$\Gamma_{refl} = \frac{cL}{\pi A} \langle \mathcal{T} \rangle = \frac{L}{A} \sqrt{\frac{\omega}{2\mu\sigma_{cont}}}. \quad (13)$$

This last result may be identified with the expression of Γ^{inh} in eq. (5), provided that ξ be replaced by its mean value for an ergodic mode namely unity [13]. We now propose to identify q and $\langle \mathcal{T} \rangle$, leading to the following relationship:

$$\Gamma^{inh} = \frac{cL}{\pi A} q. \quad (14)$$

We justify this heuristic identification by the fact that the spectral perturbation Γ^{inh} and the spatial perturbation q are of the same order⁽¹⁾. Indeed, the relationship (2) indicates that q

⁽¹⁾The identification leading to (14) in the limit of vanishing q is also supported by the discussion following eq. (12) in ref. [8], where the parameter δ has the same meaning as $\langle \mathcal{T}^2 \rangle \simeq \langle \mathcal{T} \rangle^2$.

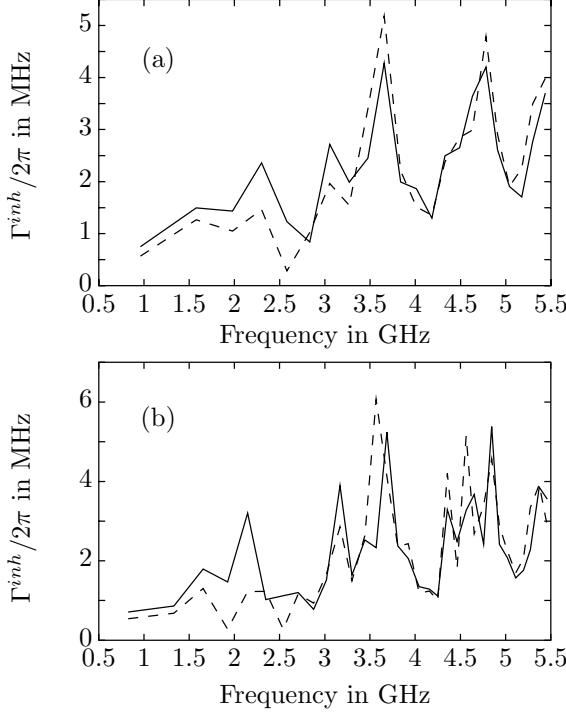


Fig. 2 – Solid lines correspond to evaluations of Γ^{inh} extracted from our measurements through expressions (7) and (5) with an average over contiguous groups of: (a) 15 resonances and (b) 10 resonances. Dashed lines show relation (14) with coarse-grained q deduced from the distribution (9).

is of order $k\delta$. Likewise, eq. (5) shows that $(A/cL)\Gamma^{inh}$ is also of order $k\delta$. This excludes any power law relationship, other than proportionality, between q and Γ^{inh} .

From our measurements, we used formulas (7) and (5) to extract, by an appropriate and original fitting procedure [13], the values of the *inhomogeneous* widths Γ^{inh} for all 330 resonances up to 5.5 GHz. These data are shown in fig. 2, where an average over contiguous groups of 15 (a) and 10 (b) resonances is performed. They are compared to expression (14) where a coarse-grained evaluation of q is deduced from the distribution (9) built with the same groups of resonances. With only 10 resonances, we have checked that fitting the experimental histograms of phase with formula (9) is still legitimate. The obvious correlation between the effective measure of imaginary parts, given by the parameter q , and the variations of the widths gives strong support to our hypothesis embodied in relation (14). The agreement is fairly good even though some small discrepancies can be observed, which can be attributed to the lack of ergodicity of certain modes (either bouncing balls or scars). Our belief is that relation (14) should hold for each truly *ergodic* mode but its verification is out of reach with our present experimental set. In our experiment, the main contribution to inhomogeneous ohmic losses is due to the interior disk. Indeed, by comparison with the bare rectangular cavity (see ref. [11]), we could deduce that its presence dramatically increased ohmic losses (whose origins are yet unclear even if we strongly suspect they have to do with the surface roughness of the disk). Therefore, that the relative variation of both Γ^{inh} and q is large is not surprising, as the circumference of the disk is only a few wavelengths leading to a rather small number of effective loss channels. For our present purpose, the essential feature shown

in fig. 2 is that both quantities follow the same variations, whether huge or not.

In this letter, for the first time to our knowledge, we propose theoretical arguments in favor of the hypothesis that the imaginary parts of the modes should correlate with the *inhomogeneous* part of the widths. Through an original analysis of transmission measurements in a lossy chaotic microwave cavity, we provide clear experimental evidence of its pertinency. It should be stressed that our point of view is complementary to RMT in that it focuses on spatial aspects whereas RMT for open systems is mainly concerned with spectral statistics [5]. We believe that the present work may have conceptual implications in transport in open mesoscopic devices [23] and also in structural acoustics [24].

REFERENCES

- [1] ISHIO H., SAICHEV A. I., SADREEV A. F. and BERGGREN K.-F., *Phys. Rev. E*, **64** (2001) 056208.
- [2] ŠEBA P., HAAKE F., KUŠ M., BARTH M., KUHL U. and STÖCKMANN H.-J., *Phys. Rev. E*, **56** (1997) 2680.
- [3] PORTER C. and THOMAS R., *Phys. Rev.*, **104** (1956) 183.
- [4] ALT H., GRÄF H.-D., HARNEY H. L., HOFFERBERT R., LENGELE R., RICHTER A., SCHARDT P. and WEIDENMÜLLER H. A., *Phys. Rev. Lett.*, **74** (1995) 62.
- [5] DITTES F.-M., *Phys. Rep.*, **339** (2000) 215.
- [6] STÖCKMANN H.-J., *Quantum Chaos: An Introduction* (Cambridge University Press, Cambridge, UK) 1999.
- [7] BARTH M. and STÖCKMANN H.-J., *Phys. Rev. E*, **65** (2002) 066208.
- [8] PNINI R. and SHAPIRO P., *Phys. Rev. E*, **54** (1996) R1032.
- [9] LOBKIS O. I. and WEAVER R. L., *J. Acoust. Soc. Am.*, **108** (2000) 1480.
- [10] JACKSON J. D., *Classical Electrodynamics* (Academic Press, New York) 1974.
- [11] BARTHÉLEMY J., LEGRAND O. and MORTESSAGNE F., *Phys. Rev. E*, **71** (2005) 016205.
- [12] BERRY M. V., *J. Phys. A*, **10** (1977) 2083.
- [13] BARTHÉLEMY J., *Chaos ondulatoire en présence de pertes: modélisation et expérience de billards micro-ondes* (Université Paris 7 - Denis Diderot, Paris) 2003 (<http://tel.ccsd.cnrs.fr/documents/archives0/00/00/41/14/>).
- [14] WEAVER R. L. and LOBKIS O. I., *Phys. Rev. Lett.*, **84** (2000) 4942.
- [15] KANZIEPER E. and FREILIKER V., *Phys. Rev. B*, **54** (1996) 8737.
- [16] BEENAKKER C. W. J., *Rev. Mod. Phys.*, **69** (1997) 731.
- [17] MÉNDEZ-SÁNCHEZ R. A., KUHL U., BARTH M., LEWENKOPF C. H. and STÖCKMANN H.-J., *Phys. Rev. Lett.*, **91** (2003) 174102.
- [18] KUHL U., MARTÍNEZ-MARES M., MÉNDEZ-SÁNCHEZ R. A. and STÖCKMANN H.-J., e-print cond-mat/0407197 (2004).
- [19] DOYA V., LEGRAND O. and MORTESSAGNE F., *Phys. Rev. E*, **65** (2002) 056223.
- [20] COLLIN R., *Field Theory of Guided Waves* (IEEE Press) 1991.
- [21] LOBKIS O. I., WEAVER R. L. and ROZHKOVA I., *J. Sound Vibr.*, **237** (2000) 281.
- [22] MORTESSAGNE F., LEGRAND O. and SORNETTE D., *Chaos*, **3** (1993) 529.
- [23] ALHASSID Y., *Rev. Mod. Phys.*, **72** (2000) 895.
- [24] LOBKIS O. I., ROZHKOVA I. and WEAVER R. L., *Phys. Rev. Lett.*, **91** (2003) 194101.

Inhomogeneous losses and complexity of wave functions in chaotic cavities

D. V. SAVIN^{1,2}, O. LEGRAND³ and F. MORTESSAGNE³

¹ Department of Mathematical Sciences, Brunel University - Uxbridge, UB8 3PH, UK

² Fachbereich Physik, Universität Duisburg-Essen - 45117 Essen, Germany

³ Laboratoire de Physique de la Matière Condensée, CNRS UMR 6622

Université de Nice-Sophia Antipolis - 06108 Nice cedex 2, France

received 2 August 2006; accepted in final form 10 October 2006

published online 1 November 2006

PACS. 05.45.Mt – Quantum chaos; semiclassical methods.

PACS. 05.60.Gg – Quantum transport.

PACS. 03.65.Nk – Scattering theory.

Abstract. – In a two-dimensional microwave chaotic cavity Ohmic losses located at the contour of the cavity result in different broadenings of different modes. We provide an analytic description and establish the link between such an inhomogeneous damping and the complex (non-real) character of biorthogonal wave functions. This substantiates the corresponding recent experimental findings of Barthélémy *et al.* (*Europhys. Lett.*, **70** (2005) 162).

Open wave-chaotic systems in the presence of energy losses (absorption) are nowadays under intense experimental and theoretical investigations, see [1, 2] for recent reviews as well as [3] for a general discussion. Most of the works concern the case of uniform absorption which is responsible for homogeneous broadening Γ_{hom} of all the modes (resonance states). However, in some experimentally relevant situations like, *e.g.*, complex reverberant structures [4, 5] or even microwave cavities at room temperature [6, 7] one should take into account also localized-in-space losses which lead to an inhomogeneous part Γ_{inh} of the widths which varies from mode to mode. As a result, the neighboring modes experience nontrivial correlations due to interference via one and the same decaying/dissipative environment that result in the complex-valued wave functions of corresponding resonance states. Such a complexity may reveal itself in long-range correlations of wave function intensity and current density [8] that were recently studied experimentally [9]. Following refs. [4, 10], it is convenient to measure the above-mentioned complexity through a single statistical parameter, namely the ratio $\langle (\text{Im}\psi)^2 \rangle / \langle (\text{Re}\psi)^2 \rangle = q^2$ of variances of the real and imaginary parts of the mode wave function ψ . The modes are real ($q = 0$) in the case of vanishing inhomogeneous losses and become complex-valued when $\Gamma_{\text{inh}} \neq 0$ (the value of Γ_{hom} has no effect on the mode complexity, as will become clear later on). The strong experimental evidences in the favor of the intimate relation between q and Γ_{inh} were recently provided by Barthélémy *et al.* [6], who analyzed hundreds of resonances in a Sinai-like chaotic microwave cavity and found a proportionality between these two quantities. Here, we present a thorough analytic description of this problem.

It is instructive to start with the discussion of the physical picture of the problematic. A typical experimental setup consists of a flat (two-dimensional) cavity fed with microwaves through attached antennas or waveguides which support M_a scattering channels (propagating modes) in total. These very channels are used to perform all the measurements and their number is finite. Dissipation through Ohmic losses at cavity boundaries gives another reason to treat our system as open, since boundaries may be viewed locally as distributed “parasitic” equivalent channels with *ad hoc* impedances [11, 12]. One should distinguish, however, between almost uniform Ohmic attenuation at the cavity plates and localized absorption at the cavity contour [6, 7]. The number of “parasitic” channels responsible for the former (“bulk”) mechanism can be naturally estimated as $M_b \sim (L/\lambda)^2$, while one has typically $M_c \sim L/\lambda$ channels at the contour (where L is the characteristic length of the cavity and λ denotes the wavelength). Both $M_b, M_c \gg 1$ but their ratio $M_c/M_b \sim \lambda/L$ is parametrically small and that will be essential for our consideration.

It is natural, therefore, to use the following model description of the problem. According to the Hamiltonian approach to scattering [13–15], see also [2], one can represent the scattering matrix in terms of the effective non-Hermitian Hamiltonian \mathcal{H}_{eff} of the open system as follows:

$$S_{\text{tot}} = 1 - iV^\dagger \frac{1}{E - \mathcal{H}_{\text{eff}}} V, \quad \mathcal{H}_{\text{eff}} = H - \frac{i}{2} VV^\dagger. \quad (1)$$

The Hamiltonian H of the closed chaotic system gives rise to N levels (eigenfrequencies) ϵ_n characterized locally in the relevant range of the energy E by the mean level spacing Δ . Those are coupled to all the open channels via the $N \times (M_a + M_b + M_c)$ matrix V of coupling amplitudes and, as a result, are converted into complex resonances $\mathcal{E}_n = E_n - \frac{i}{2}\Gamma_n$, which are given by the poles of the S -matrix. Accordingly, we propose to decompose $V = \{A, B, C\}$ into coupling to M_a antennas, M_b “bulk” and M_c “contour” parasitic channels to separate explicitly different contributions to the widths Γ_n . The total $(M_a + M_b + M_c)$ -dimensional scattering matrix (1) is, of course, unitary⁽¹⁾. However, one can access experimentally only the $(M_a \times M_a)$ subblock $S = 1 - iA^\dagger(E - \mathcal{H}_{\text{eff}})^{-1}A$ which is subunitary.

Without loss of generality one can consider the case of preserved time-reversal invariance (which was indeed the case of experiment [6]) when the coupling amplitudes V are real and H is symmetric. It is convenient first to represent \mathcal{H}_{eff} in the eigenbasis of its Hermitian part as follows:

$$(\mathcal{H}_{\text{eff}})_{nm} = \epsilon_n \delta_{nm} - \frac{i}{2} \left(\sum_{a=1}^{M_a} A_n^a A_m^a + \sum_{b=1}^{M_b} B_n^b B_m^b + \sum_{c=1}^{M_c} C_n^c C_m^c \right). \quad (2)$$

In a chaotic cavity, H is commonly described in the framework of Random Matrix Theory [3]. A (real orthogonal) rotation that diagonalizes the random Hermitian matrix H transforms the (fixed) matrix V to Gaussian-distributed coupling amplitudes with zero means and following covariances (we assume statistical independence of channels from different classes) [13, 14]:

$$\langle A_n^a A_{n'}^{a'} \rangle = 2\kappa_a \frac{\Delta}{\pi} \delta^{aa'} \delta_{nn'}, \quad \langle B_n^b B_{n'}^{b'} \rangle = 2\kappa_b \frac{\Delta}{\pi} \delta^{bb'} \delta_{nn'}, \quad \langle C_n^c C_{n'}^{c'} \rangle = 2\kappa_c \frac{\Delta}{\pi} \delta^{cc'} \delta_{nn'}. \quad (3)$$

Coupling constants κ determine transmission coefficients $T = 4\kappa/(1+\kappa)^2$ of the corresponding channels, so that $T \ll 1$ ($T = 1$) stands for weak (perfect) coupling. The strong inequality $M_b \gg M_c \gg 1$ allows us to perform now the limit of a very large number of weak fictitious bulk channels, $M_b \rightarrow \infty$ and $T_b \rightarrow 0$ with $M_b T_b \equiv 2\pi\Gamma_{\text{hom}}/\Delta$ being kept fixed [12], which singles

⁽¹⁾Unitarity of the total S -matrix as well as causality, $\Gamma_n > 0$, are automatically provided by the factorized algebraic structure of the anti-Hermitian part of \mathcal{H}_{eff} [14]

out the homogeneous absorption contribution. Indeed, by virtue of the central limit theorem one may replace in \mathcal{H}_{eff} the sum $\sum_{b=1}^{M_b} B_n^b B_m^b$ with its average value $\sum_{b=1}^{M_b} \langle B_n^b B_m^b \rangle \equiv \Gamma_{\text{hom}} \delta_{nm}$ in the limit considered that yields

$$(\mathcal{H}_{\text{eff}})_{nm} = \left(\epsilon_n - \frac{i}{2} \Gamma_{\text{hom}} \right) \delta_{nm} - \frac{i}{2} (AA^T + CC^T)_{nm}, \quad (4)$$

meaning that all the levels acquire one and the same attenuation rate. Since \mathcal{H}_{eff} comes into the scattering problem only as the resolvent $(E - \mathcal{H}_{\text{eff}})^{-1}$, uniform absorption turns out to be operationally equivalent to a pure imaginary shift of the scattering energy $E \rightarrow E + \frac{i}{2} \Gamma_{\text{hom}} \equiv E_\gamma$ [12, 16]. Thus the physical scattering matrix acquires the following form:

$$S = 1 - iA^T \frac{1}{E_\gamma - \tilde{\mathcal{H}}_{\text{eff}}} A, \quad \tilde{\mathcal{H}}_{\text{eff}} = H - \frac{i}{2} (AA^T + CC^T). \quad (5)$$

A representation similar to (5) was used in [5, 17] to study statistics of transmitted power in dissipative ergodic microstructures. Here, we concentrate rather on spectroscopic problems.

It is clear from the above consideration that only escape to antennas and inhomogeneous losses contribute to the fluctuating part $\tilde{\Gamma}_n = \Gamma_n - \Gamma_{\text{hom}}$ of the widths. The latter are given now by the imaginary parts of the complex eigenvalues of $\tilde{\mathcal{H}}_{\text{eff}}$. Since $\tilde{\mathcal{H}}_{\text{eff}}$ is non-Hermitian, the eigenvalue problem $\tilde{\mathcal{H}}_{\text{eff}}|n\rangle = \tilde{\mathcal{E}}_n|n\rangle$ and $\langle \tilde{n}| \tilde{\mathcal{H}}_{\text{eff}} = \langle \tilde{n}| \tilde{\mathcal{E}}_n$ defines two sets of right and left eigenfunctions, which satisfy the conditions of biorthogonality, $\langle \tilde{n}|m\rangle = \delta_{nm}$, and completeness, $\sum_{n=1}^N |n\rangle \langle \tilde{n}| = 1_N$. The matrix $U_{nm} \equiv \langle n|m \rangle \neq \delta_{nm}$ differs from the unit one and is known in nuclear physics as Bell-Steinberger nonorthogonality matrix [18] (see a compact description in [14]). This matrix features in two-point correlations in open systems seen, *e.g.*, in decay laws [19]. U_{nn} appears also in optics via the so-called Petermann factor of a lasing mode [20–22]. Some statistical aspects of chaotic nonorthogonal eigenfunctions were recently studied in [22–24].

For a general non-Hermitian matrix left and right eigenvectors are independent of each other. However, in our case $\tilde{\mathcal{H}}_{\text{eff}}$ is complex symmetric (due to time-reversal invariance), implying that left eigenfunctions are given by the transpose of the right ones, $\langle \tilde{n}| = |n\rangle^T$. As a result, $\tilde{\mathcal{H}}_{\text{eff}} = \Psi \tilde{\mathcal{E}} \Psi^T$ can be diagonalized by a *complex* orthogonal transformation [14], with $\tilde{\mathcal{E}} = \text{diag}(\tilde{\mathcal{E}}_1, \dots, \tilde{\mathcal{E}}_N)$ and $\Psi = (|1\rangle, \dots, |N\rangle)$, that leads to the well-known pole representation of the S -matrix, $S = 1 - iA^T \Psi (E_\gamma - \tilde{\mathcal{E}})^{-1} \Psi^T A$, or in its components:

$$S_{aa'} = \delta_{aa'} - i \sum_{n=1}^N \frac{\psi_n^a \psi_n^{a'}}{E_\gamma - \tilde{\mathcal{E}}_n}, \quad \psi_n^a \equiv A^a |n\rangle = \sum_{k=1}^N A_k^a |n\rangle_k. \quad (6)$$

The wave function component ψ_n^a of the n -th mode excited through the a -th channel is generally complex. This complexity is solely due to biorthogonal nature of the eigenfunctions and is directly related to the structure of the anti-Hermitian part of $\tilde{\mathcal{H}}_{\text{eff}}$. In particular, all ψ_n^a would be real were $(\text{Im} \tilde{\mathcal{H}}_{\text{eff}})_{nm} \propto \delta_{nm}$ or, more generally, if the anti-Hermitian part of the effective Hamiltonian commuted with its Hermitian part⁽²⁾.

We proceed now with considering the case of tunneling coupling to antennas, which was realized in experiment [6]. This allows us to neglect safely antenna contributions to Γ_n , approximating $\tilde{\mathcal{H}}_{\text{eff}} \approx H - \frac{i}{2} CC^T$. In the case of the large but finite number M_c of (contour)

⁽²⁾In this case both the Hermitian H and anti-Hermitian parts of $\tilde{\mathcal{H}}_{\text{eff}}$ can be diagonalized simultaneously, thus the eigenbasis being a conventional orthogonal one, as follows from $H^T = H$.

channels, the levels acquire on average the width given by the so-called Weisskopf's estimate

$$\Gamma_{\text{inh}} \equiv M_c T_c \frac{\Delta}{2\pi}, \quad (7)$$

well known in nuclear physics, see, *e.g.*, [14, 15]. It is worth noting that this value can be formally linked to Sabine's law of room acoustics, which determines the average width Γ_{refl} related to absorption at the cavity contour. One has $\Gamma_{\text{refl}} = cLT_c/(\pi S)$ [6, 25], where S is the cavity area, c is the speed of light and L is now the cavity perimeter. Making use of Weyl's law for the mean level spacing $\Delta = c\lambda/S$ and putting $M_c = L/(\lambda/2)$, we find that Γ_{refl} is exactly converted to Γ_{inh} . This provides us with a further link between the present model description and the microscopic treatment of [6, 7] based on Maxwell's equations.

Fluctuations of the widths around Γ_{inh} are mostly due to those of the matrix CC^T . As follows from the central limit theorem, fluctuations of off-diagonal matrix elements are suppressed as compared to diagonal ones at $M_c \gg 1$, $(CC^T)_{n \neq m} \sim (CC^T)_{nn}/\sqrt{M_c} \sim \Gamma_{\text{inh}}/\sqrt{M_c}$, so that they contribute to $\tilde{\Gamma}_n$ in the next-to-leading order in $1/M_c$. However, off-diagonal matrix elements give a dominating contribution to the mode nonorthogonality. Indeed, all essential features of the problem can be most explicitly seen in the two-state approximation. Representing $\tilde{\mathcal{H}}_{\text{eff}}$ as follows

$$\tilde{\mathcal{H}}_{\text{eff}} \approx \begin{pmatrix} \epsilon_1 & 0 \\ 0 & \epsilon_2 \end{pmatrix} - \frac{i}{2} \begin{pmatrix} \|C_1\|^2 & (C_1^T C_2) \\ (C_2^T C_1) & \|C_2\|^2 \end{pmatrix}, \quad (8)$$

where $C_{1,2}$ are the M_c -dimensional vectors of the corresponding coupling amplitudes, one can easily solve the secular equation for its two eigenvalues $\tilde{\epsilon}_{1,2}$, finding $\tilde{\epsilon}_{1,2} = (\tilde{\epsilon}_1 + \tilde{\epsilon}_2 \mp d)/2$, where $d = \sqrt{(\tilde{\epsilon}_1 - \tilde{\epsilon}_2)^2 - (C_1^T C_2)^2}$ and $\tilde{\epsilon}_{1,2} = \epsilon_{1,2} - \frac{i}{2}\|C_{1,2}\|^2$. The corresponding eigenfunctions (we assume $\epsilon_1 < \epsilon_2$) are given by

$$|1\rangle = \mathcal{N} \begin{pmatrix} 1 \\ if \end{pmatrix} \quad \text{and} \quad |2\rangle = \mathcal{N} \begin{pmatrix} -if \\ 1 \end{pmatrix}, \quad f = \frac{(C_1^T C_2)}{\tilde{\epsilon}_2 - \tilde{\epsilon}_1 + d}, \quad (9)$$

$\mathcal{N}^2 = (1 - f^2)^{-1}$ being the normalization constant. Then the nonorthogonality matrix reads $U = |\mathcal{N}|^2[(1 + |f|^2)\mathbf{1}_2 + 2\text{Re}(f)\sigma_y]$, with the Pauli matrix σ_y . The parameter f controls the mode complexity, as follows from

$$\psi_{1,2}^a = \mathcal{N}(A_{1,2}^a \pm if A_{2,1}^a) \quad (10)$$

for the mode wave functions.

In experiment [6], the complexity parameter

$$q^2 = \langle (\text{Im}\psi_n^a)^2 \rangle / \langle (\text{Re}\psi_n^a)^2 \rangle \quad (11)$$

was accessible only in the regime of the weak mode overlap due to inhomogeneous losses (we stress, however, that the total width $\Gamma_{\text{hom}} + \Gamma_{\text{inh}}$ can be larger than Δ). In this regime, $\Gamma_{\text{inh}} \ll \Delta$, the computation of q can be easily carried out by making the use of the above two-state approximation. One finds straightforwardly that $q^2 \approx \langle (\text{Re}f)^2 \rangle \approx \langle (C_1^T C_2)^2 \rangle / (2\Delta)^2$, which determines now the average nonorthogonality matrix as $\langle U_{nm} \rangle \approx (1 + 2q^2)\delta_{nm}$. The remaining Gaussian averaging over random amplitudes (3) yields $\sum_{c,c'} \langle C_1^c C_2^c C_1^{c'} C_2^{c'} \rangle = M_c (2\kappa_c \Delta / \pi)^2 \approx M_c (T_c \Delta / 2\pi)^2$, as $T_c \approx 4\kappa_c \ll 1$ in our case of large M_c and fixed Γ_{inh} . Collecting everything, we arrive at

$$q \approx \frac{1}{\sqrt{M_c}} \frac{\Gamma_{\text{inh}}}{2\Delta} \quad (12)$$

that substantiates the proportionality between q and Γ_{inh} established experimentally [6]. The mode complexity (nonorthogonality) decreases as the number of absorptive channels increases, in agreement with the general discussion presented above.

We discuss now the role of fluctuations in energy levels and contributions from the other levels neglected so far. Restricting ourselves to the same weak overlap regime, we can use the perturbation theory for wave functions to find $q^2 \approx \frac{1}{4} \sum_{m \neq n} \langle (C_n^T C_m)^2 \rangle \langle (\epsilon_n - \epsilon_m)^{-2} \rangle$. The known correlation function $R_2(\omega)$ of Gaussian orthogonal ensembles, see [3], can be now used to get $\sum_{m \neq n} \langle (\epsilon_n - \epsilon_m)^{-2} \rangle = \int d\omega \omega^{-2} R_2(\omega)$, which can be appreciated as (average square of) the so-called “level curvature” studied in [26, 27]. Since $R_2(\omega) \sim \omega$ as $\omega \rightarrow 0$, this integral has a logarithmic divergency regularized by setting the lower limit $\sim \Gamma_{\text{inh}}$ that also ensures us to stay within the perturbation theory. As a result, (12) is renormalized to yield a contribution $\sim \ln(\Delta/\Gamma_{\text{inh}})$. One should expect that such a factor would be absent in a non-perturbative treatment (see also the relevant discussion in [22]). The computation of q at arbitrary inhomogeneous absorption is still an interesting open problem to consider.

In summary, we have presented the model description for inhomogeneous (localized-in-space) losses in open chaotic systems and discussed thoroughly the resulting complexity (or biorthogonality) of the mode wave functions. In particular, the complexity parameter q determining the relative weight of the imaginary parts of the modes is found analytically to be proportional to the inhomogeneous part Γ_{inh} of the widths in full agreement with experimental results of [6]. Though the present calculation of q is perturbative in the small parameter $\Gamma_{\text{inh}}/\Delta$, it may nevertheless be valid in the intermediate or large modal overlap regime where Γ_{hom} dominates, as, for instance, in the case of room acoustics or elastodynamics [1, 25]. Our analysis may be also relevant for problems of mode nonorthogonality outside of the scattering systems as those considered recently in [23, 28].

* * *

We thank Y. V. FYODOROV and V. V. SOKOLOV for useful comments. One of us (DVS) acknowledges gratefully the generous hospitality of LPMC in Nice and the financial support of University of Nice during his stay there. The financial support by the SFB/TR 12 of the DFG (DVS) is acknowledged with thanks.

REFERENCES

- [1] KUHL U., STÖCKMANN H.-J. and WEAVER R., *J. Phys. A: Math. Gen.*, **38** (2005) 10433.
- [2] FYODOROV Y. V., SAVIN D. V. and SOMMERS H.-J., *J. Phys. A: Math. Gen.*, **38** (2005) 10731.
- [3] STÖCKMANN H.-J., *Quantum Chaos: An Introduction* (Cambridge University Press, Cambridge, UK) 1999.
- [4] LOBKIS O. I. and WEAVER R. L., *J. Acoust. Soc. Am.*, **108** (2000) 1480.
- [5] ROZHKO I., FYODOROV Y. V. and WEAVER R. L., *Phys. Rev. E*, **68** (2003) 016204.
- [6] BARTHÉLEMY J., LEGRAND O. and MORTESSAGNE F., *Europhys. Lett.*, **70** (2005) 162.
- [7] BARTHÉLEMY J., LEGRAND O. and MORTESSAGNE F., *Phys. Rev. E*, **71** (2005) 016205.
- [8] BROUWER P. W., *Phys. Rev. E*, **68** (2003) 046205.
- [9] KIM Y.-H., KUHL U., STÖCKMANN H.-J. and BROUWER P. W., *Phys. Rev. Lett.*, **94** (2005) 036804.
- [10] PNINI R. and SHAPIRO B., *Phys. Rev. E*, **54** (1996) R1032.
- [11] LEWENKOPF C. H., MÜLLER A. and DORON E., *Phys. Rev. A*, **45** (1992) 2635.
- [12] BROUWER P. W. and BEENAKKER C. W. J., *Phys. Rev. B*, **55** (1997) 4695.
- [13] VERBAARSCHOT J. J. M., WEIDENMÜLLER H. A. and ZIRNBAUER M. R., *Phys. Rep.*, **129** (1985) 367.

- [14] SOKOLOV V. V. and ZELEVINSKY V. G., *Nucl. Phys. A*, **504** (1989) 562.
- [15] FYODOROV Y. V. and SOMMERS H.-J., *J. Math. Phys.*, **38** (1997) 1918.
- [16] SAVIN D. V. and SOMMERS H.-J., *Phys. Rev. E*, **68** (2003) 036211.
- [17] ROZHKOVA I., FYODOROV Y. V. and WEAVER R. L., *Phys. Rev. E*, **69** (2004) 036206.
- [18] BELL J. S. and STEINBERGER J., *Proceedings of the Oxford International Conference on Elementary Particles, September, 1965* (Rutherford High Energy Laboratory, Chilton, Berkshire, UK) 1966, p. 195.
- [19] SAVIN D. V. and SOKOLOV V. V., *Phys. Rev. E*, **56** (1997) R4911.
- [20] PETERMANN K., *IEEE J. Quantum Electron.*, **15** (1979) 566.
- [21] SIEGMAN A. E., *Phys. Rev. A*, **39** (1989) 1253.
- [22] SCHOMERUS H., FRAHM K. M., PATRA M. and BEENAKKER C. W. J., *Physica A*, **278** (2000) 469.
- [23] CHALKER J. T. and MEHLIG B., *Phys. Rev. Lett.*, **81** (1998) 3367.
- [24] FYODOROV Y. V. and MEHLIG B., *Phys. Rev. E*, **66** (2002) 045202(R).
- [25] MORTESSAGNE F., LEGRAND O. and SORNETTE D., *Chaos*, **3** (1993) 529.
- [26] FYODOROV Y. V. and SOMMERS H.-J., *Z. Phys. B*, **99** (1995) 123.
- [27] VON OPPEN F., *Phys. Rev. E*, **51** (1995) 2647.
- [28] FYODOROV Y. V. and SOMMERS H.-J., *J. Phys. A: Math. Gen.*, **36** (2003) 3303.

D. Gel de la diffusion : modes localisés

En dépit de plusieurs décennies de recherches très actives, l'observation directe de la localisation des ondes classiques reste un formidable défi pour les expérimentateurs⁴⁰. Nous n'allons pas revenir sur les différentes voies suivies pour atteindre cet objectif, elles ont été évoquées dans l'introduction de ce chapitre. Pour être complet (et honnête), on trouve dans la littérature sur le sujet quelques articles prétendant montrer des modes localisés dans des cavités micro-ondes, au sens où nous l'entendons⁴¹. Disons-le tout net : ces articles ne me convainquent pas ! On peut d'ailleurs remarquer le très faible écho qu'ils ont eu dans la communauté de la diffusion multiple. Leur défaut principal repose soit sur l'utilisation de cavité fermée, soit sur l'absence de test de robustesse des structures observées. Lorsque l'on veut mettre en évidence un piégeage d'une onde par un effet subtil d'interférences multiples, il paraît judicieux d'éviter un piégeage trivial par des conditions aux limites strictes. Même si les modes observés par ces auteurs ne ressemblent pas à des modes réguliers, le couplage de ces derniers avec le milieu diffusant peut donner lieu à des structures spatiales très variées. Une concentration spatiale de l'énergie, surtout, comme c'est souvent le cas dans ces expériences, proche des bords de la cavité, ne prouve pas l'établissement d'un mode localisé.

Le projet est donc de proposer une expérience de diffusion dans une cavité micro-ondes désordonnée et ouverte. L'expérience réalisée s'appuie sur la même cavité micro-ondes qui a servi aux études précédentes. La grande modification réside dans la mise en place de bords à fuite. Ouvrir brutalement la cavité n'est évidemment pas une solution car la pollution électromagnétique n'est pas qu'une antienne de journaliste (ou un sujet de Bar des Sciences...) D'autre part, il faut éviter que le déplacement d'un objet, ou d'une personne, dans la salle de manip entraîne une modification des conditions aux limites au cours des (longues) mesures. La cavité est donc maintenue hermétique, mais nous délimitons une zone centrale par des couches de mousse absorbante possédant des impédances électromagnétiques différentes (ECCOSORB® LS-14 and LS-16). Concrètement, la géométrie de ce cadre absorbant est déterminée de façon à obtenir 20 dB d'atténuation du signal ré-injecté dans la zone centrale, aux fréquences utilisées. Le dispositif est schématisé sur la figure 18. Dans la zone libre, on introduit 196 diffuseurs diélectriques dont la permittivité, que nous avons mesuré, atteint $\epsilon = 37$. Ils ont une forme cylindrique de diamètre 6 mm et de hauteur 5 mm, égale à

la hauteur interne de la cavité. Outre leur haut indice, ces diffuseurs possèdent une très faible absorption : un facteur de qualité $Q = 7000$ à 7 GHz.

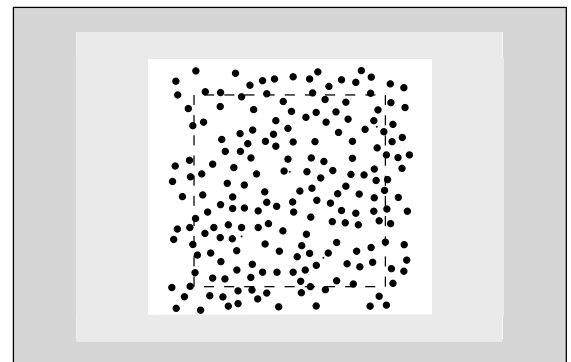


FIG. 18 Représentation schématique de la cavité utilisée : 196 diffuseurs occupent une zone centrale de dimensions $25\text{ cm} \times 25\text{ cm}$, pour certaines mesures les diffuseurs situés à l'extérieur de la zone délimitée par le carré en tirets sont retirés. En périphérie des mousses absorbantes de deux qualités différentes assurent une faible réintroduction de l'énergie dans la zone centrale.

Les positions des diffuseurs sont déterminées aléatoirement avec une fraction surfacique de 8.9 % et une distance minimale entre centres des diffuseurs, d_{\min} , de 11 mm. À la valeur donnée de la fraction surfacique, cette distance peut varier entre 8 mm (la technique de dépôt des diffuseurs interdit une distance inférieure) et 19 mm. La valeur supérieure correspond à la taille de la maille d'un réseau périodique carré. La figure 18 montre une disposition aléatoire particulière des diffuseurs, obtenue dans ces conditions. Nous disposons de 4 antennes à l'intérieur de la zone centrale. La figure 19 montre un spectre typique de transmission entre deux antennes. La représentation en échelle semi-log permet de distinguer dans la structure globale du spectre une zone de transmission quasi nulle. Il s'agit d'une réminiscence de la bande interdite (du « gap ») observée dans cette zone, pour un arrangement périodique des diffuseurs, avec la même fraction surfacique. Ce trou de transmission est fortement corrélé avec la section efficace de Mie d'un diffuseur unique⁴², représentée sur la figure par la courbe en tirets.

Pour accéder à l'intensité du champ dans la cavité, nous utilisons une technique « perturbative » qui consiste à suivre le déplacement en fréquence du maximum de transmission d'un mode donné, en réponse au déplacement d'une bille métallique à l'intérieur de la cavité⁴³. Nous utilisons une bille d'un diamètre de 2 mm,

⁴⁰ Pour une revue récente sur le sujet, voir : A. Z. Genack and A. A. Chabanov, J. Phys. A : Math. Gen. **38**, 10465 (2005).

⁴¹ R. Dalichaouch, J. P. Armstrong, S. Schultz, P. M. Platzman, and S. L. McCall, Nature **354**, 53 (1991); A. Kudrolli, V. Kudambi, and S. Sridhar, Phys. Rev. Lett. **75**, 822 (1995); Prabhakar Pradhan and S. Sridhar, Phys. Rev. Lett. **85**, 2360 (2000).

⁴² M. M. Sigalas, C. M. Soukoulis, C.-T. Chan, and D. Turner, Phys. Rev. B **53**, 8340 (1996).

⁴³ L'article séminial, souvent mal cité, est : L. C. Maier, Jr and J. C.

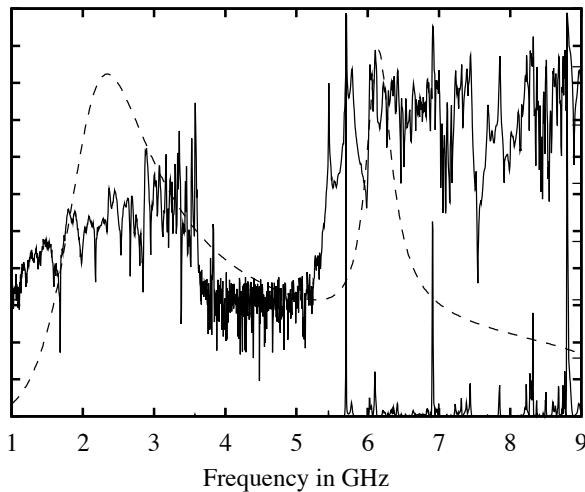


FIG. 19 En trait plein : signal de transmission mesuré pour le désordre représenté sur la figure 18, le signal est représenté en échelle linéaire et en échelle semi-log; en ligne brisée : section efficace de diffusion d'un diffuseur diélectrique unique.

pilotée par un aimant monté sur une platine de translation XY, à grande course (60 cm) et d'une précision du micron. Les points de mesure sont disposés sur une grille régulière possédant une maille carrée de 5 mm de côté. En raison de la présence des diffuseurs, la bille ne peut pas emprunter un chemin quelconque. Une procédure automatique de calcul de trajectoires, développée par Grégory Sauder, permet, pour chaque configuration de désordre, de déterminer une trajectoire « optimale », c'est-à-dire celle qui minimise la durée de la mesure, ou, pour le moins, la rend raisonnable. Malgré tout, la durée de certaines acquisitions peut dépasser les deux jours avec l'analyseur de réseaux dont nous disposons actuellement.

Nous avons isolé trois résonances dans le spectre de transmission présenté sur la figure 19 : une dans le vestige du gap à 5.45 GHz, une en bord de gap à 5.66 GHz et une dans la forêt de pics à 7.80 GHz. Les valeurs des largeurs de ces trois résonances sont de l'ordre ou légèrement supérieures aux valeurs ohmiques. Il est donc raisonnable de penser qu'elles ne « voient » pas les bords absorbants du système. Les cartes d'intensité obtenues par la technique précédemment décrite sont représentées en (a), (b) et (c) sur la figure 20. Est représentée, en fait, la racine carrée de l'intensité, ce qui permet de réduire la dynamique et de moins masquer les détails. Sans conteste possible, les trois résonances exhibent une forte localisation spatiale de l'onde électromagnétique. Tous les mots y sont : localisation, forte, onde ! Mais la prudence est

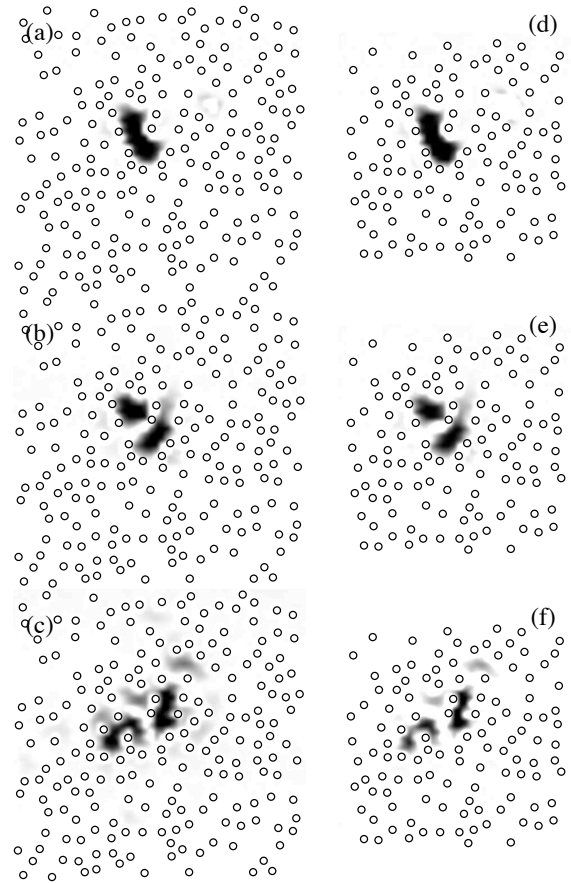


FIG. 20 Mesures expérimentales des cartes d'amplitude (racine de l'intensité) des modes localisés à 5.45 GHz, (a) et (d), 5.66 GHz, (b) et (e), et 7.80 GHz, (c) et (f), pour deux extensions de la zone diffusante. Les trois modes sont très peu sensibles à la suppression des diffuseurs périphériques.

encore de mise. Il faut noter que si le mode (a) (le mode du gap) se construit dans une sorte de microcavité, les deux autres serpentent autour des diffuseurs. Pour tester la robustesse de ces modes, nous avons modifié l'extension de la zone diffusante, en conservant la même fraction surfacique. Cette zone réduite est représentée sur la figure 18. Le spectre obtenu est globalement similaire au précédent, mais pas superposable : des pics disparaissent, d'autres s'élargissent, mais les trois résonances cartographiées y sont présentes, aux mêmes fréquences et avec des largeurs identiques. Leurs distributions d'amplitudes sont représentées sur la figure 20 en (d), (e) et (f). Les cartes obtenues ne sont pas strictement identiques aux précédentes, mais il est indéniable que la modification des conditions aux limites n'a absolument pas affectée l'intégrité de ces trois modes... qu'il devient de plus en plus légitime de qualifier de localisés.

Pour éprouver davantage nos résultats expérimentaux, nous avons réalisé, avec l'aide de Christian Vanneste, une simulation numérique basée sur la résolution directe des

Slater, J. Appl. Phys. **23**, 68 (1952); la référence suivante montre que la technique est certainement plus subtile que certains utilisateurs (dont par décence nous tairons le nom) ne semblent le (laisser) croire : A. Gokirmak, D.-H. Wu, J. S. A. Bridgewater, and S. M. Anlage, Rev. Sci. Instrum. **69**, 3410 (1998).

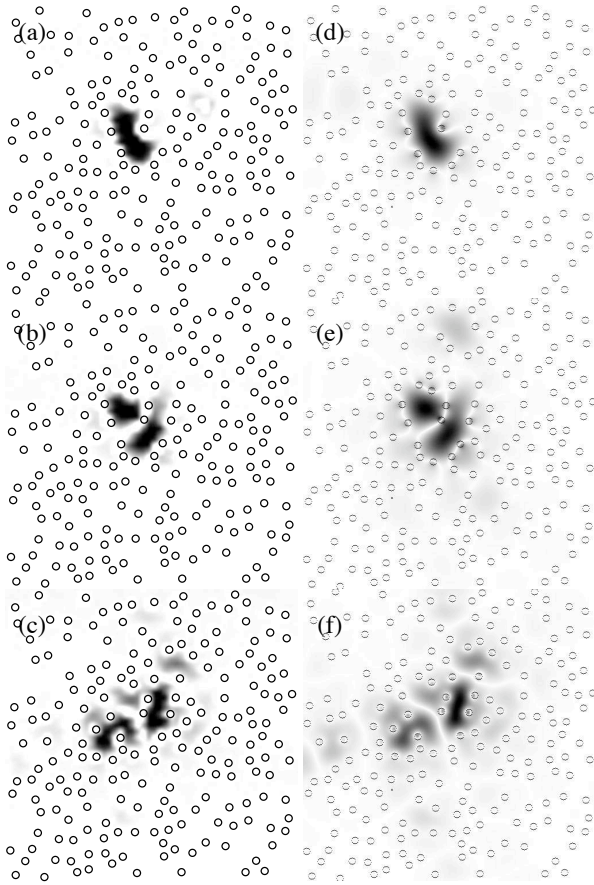


FIG. 21 Comparaison des résultats expérimentaux (a), (b) et (c) (idem figure 20) avec une simulation numérique par FDTD (conditions aux limites ouvertes) (d), (e) et (f); la comparaison est excellente.

équations de Maxwell par la méthode FDTD⁴⁴ (finite-difference time-domain). Pour simuler un milieu ouvert, des conditions dites PML (perfectly matched layer) ont été implémentées⁴⁵. Remarquons que la succession de couches aux propriétés absorbantes différentes utilisée dans l'expérience procède de la même démarche que les conditions PML. Admettons tout de même la plus grande efficacité du numérique : aucun champ n'est réintroduit dans la cavité. Autre différence, la simulation ne prend pas en compte les pertes par dissipation ohmique sur les parois inférieure et supérieure de la cavité. Pour cette raison les spectres issus de la simulation sont plus riches que les spectres expérimentaux. Mais toutes les résonances expérimentales sont présentes dans le spectre numérique, aux mêmes fréquences. La figure 21 montre les modes du système numérique obtenues en « excitant » aux

fréquences propres successives. La comparaison avec les modes localisés expérimentaux est édifiante ! Les similitudes des images (c) et (f) sont particulièrement remarquables.

Les tests de robustesse à la perturbation des conditions aux limites, et la comparaison avec la simulation numérique contribuent à conforter les résonances observées dans leur statut de modes localisés. Des tests en fonction des antennes de mesures utilisées ont également été réalisés. Ils montrent l'impossibilité d'exciter ces modes si l'une au moins des antennes n'est pas située à proximité d'une zone de fort champ. Nous procédons actuellement à des mesures de longueur de localisation et les confrontons à des prédictions théoriques⁴⁶. L'évolution des largeurs des résonances en fonction de la taille du milieu diffusant est également en cours de caractérisation. Les résultats sont indiscutablement bien orientés, mais indubitablement trop préliminaires pour être présentés ici. La conclusion de cette partie est donc la même que celle du chapitre II : la dynamique autour de ces expériences est forte, à la hauteur de leur potentiel.

⁴⁴ A. Tafove, *Computational Electrodynamics : The Finite-Difference Time-Domain Method*, Artech House, Norwood, (1995).

⁴⁵ J. P. Berenger, *J. Comput. Phys.* **114**, 185 (1995).

⁴⁶ Notamment celle présentée dans : F. A. Pinheiro, M. Rusek, A. Orlowski, and B. A. van Tiggelen, *Phys. Rev. Lett.* **69**, 026605 (2004).

V. POSTFACE

J'espère que le lecteur qui parviendra à cette postface en ayant lu l'intégralité du document aura en tête une appréciation voisine de « beau travail ! » C'est en tout cas avec passion et enthousiasme que j'ai mené mon métier d'enseignant-chercheur tout au long de ces années ; et c'est bien ainsi que je souhaite le poursuivre (j'espère avoir convaincu que je ne manquais pas de projets...)

La recherche est, en vérité, un métier difficile... pour l'entourage ! Je pense notamment au conjoint, qui doit posséder une forte dose de patience aimante pour soutenir, toujours, et supporter, parfois, cet être étrange qu'est « l'homo scientificus ». J'ai dédicacé cette thèse d'habilitation à mon épouse ; elle sait pourquoi... et moi aussi.

Je n'oublie pas d'où je viens : d'une cité ouvrière de Seine-Saint-Denis, ce « 9-3 » tristement célèbre depuis quelques années ! Si je peux aujourd'hui prétendre au plus haut diplôme du système universitaire français, il est bien évident que mes parents n'y sont pas étrangers. Merci Maman, merci Papa pour m'avoir donné le goût d'apprendre et pour les sacrifices que cela a entraîné. Merci Stéphane, aussi, pour tout.

Je voudrais profiter de cette postface pour associer, remercier, saluer certaines personnes qui ont, plus ou moins directement, contribué au travail présenté ici.

D'abord mes figures tutélaires. Jean-Pierre Romagnan, par ses immenses qualités intellectuelles et humaines, constitue un modèle qui guide ma démarche d'enseignant-chercheur, et même au-delà. Michel Le Bel-lac constitue également un modèle pour moi, par sa rigueur scientifique, sa puissance de travail et son impressionnant sens physique.

Mes copains de jeu, ensuite. Olivier Legrand, bien sûr, mais également Christian Vanneste et Patrick Sebah, avec qui je forme le POMC « canal historique », groupuscule de joyeux fondamentalistes qu'a rejoint récemment, pour le plus grand plaisir de tous, Valérie Doya. J'apprécie, au quotidien, la chance d'avoir de tels partenaires. Merci à vous quatre ! J'associe ici Christian Miniatura, qui a partagé un bout de route avec nous, et avec qui nous aurons certainement d'autres projets.

Les « thésards ». Valérie fut la première... elle a mal tourné. Jérôme, qui fera le bonheur de ses élèves de Lycée, mais quelle perte pour la recherche. David, qui m'a permis de comprendre que le bourre-pif n'est pas la seule technique possible d'encadrement. Charles, qui prendra les bourre-pifs nécessaires. Claire, très occupée par sa chasse au « lascar » (est-ce bien sérieux ?)

Les figures du laboratoire, ceux qui ont marqué mes premières années. Un hommage d'abord au trop tôt disparu Jean Coste, l'un des rares vrais intellectuels que j'ai croisé dans cette profession, Carlos Montes en étant un autre. Même passion de la « Connaissance » chez ces deux hommes, même fougue, même lyrisme, parfois. Comme lorsque Coste commençait une phrase par « à

propos.. » et finissait une heure plus tard en ayant lessivé son interlocuteur. Ou lorsque Carlos prononce avec un petit sourire « tu te rends compte... », et s'évertue à faire comprendre en 10 minutes le résultat de 3 mois de calculs acharnés... De bien passionnantes passionnés. Nicole Ostrowsky a joué pour moi un rôle de modèle d'enseignant-chercheur, j'ai toujours été impressionné (et envieux) par sa puissance de travail et sa pugnacité. Dan Ostrowsky, un gourmet-gourmand au pays des télécommunications optiques, aussi fin connaisseur des subtilités de la mécanique quantique que de la cuisine française, m'a rassuré à mes débuts : les chercheurs ne sont pas que pur esprit, ouf !

Et puis il y a les copains (beaucoup sont des amis) du labo, qui contribuent à l'ambiance détendue et intellectuellement stimulante du LPMC : Alain, Bernard, Éric, Elisabeth, Franck, François, Guy, Laurent, Marc, Nathalie, Pascal, Pierre, Sébastien, Wilfried. Évidemment j'aurais pu distinguer, pour chacun, la proportion de détente et de stimulation intellectuelle... mais j'y ai renoncé, par peur des représailles et des conséquences éventuelles sur les carrières de certains. Je n'oublie pas les « nouveaux » : Alice, Laurent (du Périgord !) et Olivier. Si les petits cochons ne les mangent pas...

Un labo ne vit pas sans une équipe technique et administrative efficace. La nôtre répond présent. Je tiens particulièrement à remercier les personnes suivantes. Jean-Claude Noiray, le champion toutes catégories de la salle de manips, je ne chercherai même pas à chiffrer les précieux conseils qu'il nous a prodigués. Le nombre de collègues, de thésards, qui lui sont redatables est à la mesure de sa patience et de son dévouement : infini ; Catherine Laye, qui a joué un rôle important dans les premières phases de la « manip fibre ». Ce fut, évidemment, avec la compétence, la disponibilité et la gentillesse qui la caractérisent ; Michèle Udé et Stan Trzesien, gardiens de la Tour... de tirage et grands maîtres du Centre... de préforme. Grégoire Sauder, qui avec une constante humeur gracieuse (j'en fais trop là ?) a brillamment automatisé la manip micro-ondes⁴⁷

Bernard, le petit blaireau de Saint Blaise, toujours disponible, toujours efficace, et toujours de bonne humeur (mais comment fait-il ?) ; Omar Bessir, qui s'est chargé avec sérieux et soin de la mécanique liée aux premières manips micro-ondes ; Yann, qui passe son temps à courir (loin) derrière moi en collant moultant... je finis par me poser des questions ! Et j'ai gardé les meilleures pour la fin : les « filles », Annette, Christine, Denise, Martine et Mika (hélas partie), qui jonglent avec les bases de données redondantes et incompatibles, s'épuisent à la gym, composent avec nos exigences, bavardent dans les couloirs, bref, sont in-

⁴⁷ D'ailleurs à ce sujet, il faudrait modifier tout le programme car « ça va pas du tout ! »

dispensables.

Le développement d'une nouvelle équipe expérimentale n'aurait pas pu se faire sans le soutien constant (et financier) et la confiance des deux directeurs qui se sont succédés depuis la naissance de l'équipe POMC : Jean-Pierre Romagnan et Gérard Monnom. Un merci sincère à eux deux.

Par leur collaboration directe, ou le simple (mais appréciable) intérêt qu'ils ont porté à mes travaux, je tiens à vivement remercier Bart van Tiggelen, Mathias Fink, Ule Kuhl, Roger Maynard, Hans-Jürgen Stöckmann, Dominique Delande, Richard Weaver, Thomas Seligman, Dima Savin, Rafael Mendez, Jean-Marc Laheurte, Oriol Bohigas, Patricio Leboeuf, ...

Il y aussi les collègues du département de Physique avec qui je prends toujours beaucoup de plaisir à travailler, discuter, refaire le monde universitaire : Pierre Coullet, Gian Luca Lippi, George Batrouni (mon estimé co-auteur), Bruno Cessac, David Wilkowski, Alain Pu-mir, Médéric Argentina, François Rocca, Jorge Vinter, Jacques-Alexandre Sépulchre... et que ceux que j'oublie me pardonnent.

Je n'oublie pas de remercier chaleureusement les membres du jury : George Batrouni, Pierre Coullet, Patricio Leboeuf, Roger Maynard, Jacques Treiner et Ri-

chard Weaver. À tous un grand merci d'avoir accepté car je sais vos emplois du temps très chargés ! Celui de Mathias Fink l'était trop, je regrette son absence, mais le remercie d'avoir tout essayé. Le cumul des mandats n'étant pas interdit chez les universitaires, Roger Maynard m'a fait l'honneur et le plaisir d'endosser le rôle de Président-rapporteur-examinateur. Patricio et Richard ont également accepté la (lourde ?) tâche de lire et d'évaluer le présent document, je les en remercie profondément ; le mérite est d'autant plus grand pour Richard Weaver qui n'a pas souvent l'occasion de pratiquer son français dans l'Illinois... Que Pierre ait réussi à « casser » ma soutenance au milieu de ses innombrables activités, relève des exploits dont il est coutumier et qui suscitent mon admiration ! J'ai apprécié la spontanéité avec laquelle Jacques a répondu favorablement à ma demande. Merci d'être là, et d'amener avec toi un peu du souvenir de ce merveilleux DEA « de Valentin ». Et merci, enfin, à George... qui va faire l'effort de traverser le Var (what did you say about our common sense of humor : it bites, huh ?)

Et pour finir, un petit coucou à mon Grand Schtroumpf et à ma Schtroumpfette, Pierre et Eugénie, qui seraient déçus de ne pas se trouver dans ces lignes... et les décevoir est bien ce que je souhaite le moins au monde.